Clustering and redshift-space distortions in QSO and galaxy surveys

Cruz da Angela, José Antonio

Clustering and Redshift-Space Distortions in QSO and Galaxy Surveys

by José António Cruz da Ângela

A thesis submitted to Durham University
in accordance with the regulations for
admittance to the Degree of Doctor of Philosophy.

Department of Physics
Durham University
June 2006

Clustering and Redshift-Space Distortions in QSO and Galaxy Surveys

by José António Cruz da Ângela

PhD Thesis, June 2006

Abstract

In this thesis, we exploit the potential of existing QSO and galaxy surveys for investigating the nature of the large scale structure in the Universe. A detailed analysis of clustering and redshift-space distortions allows us to constrain cosmological parameters. We model the anisotropies due to dynamical and geometrical effects in the measured clustering pattern of distant QSOs from the 2dF QSO Survey (2QZ) and also Lyman break galaxies. The 2QZ is then combined with the QSO sample from the 2dF SDSS LRG and QSO Survey (2SLAQ) to study the luminosity dependence of QSO clustering. Using N-body simulations, we estimate the statistical gains in the determination of cosmological parameters from future LRG surveys.

We measure the clustering of distant QSOs from the 2QZ survey by performing a correlation analysis of redshift-space (z-space) distortions. To interpret the z-space correlation function measured in orthogonal directions, $\xi(\sigma,\pi)$, we require an accurate model for the QSO real-space correlation function, $\xi(r)$. Motivated by the form for $\xi(r)$ seen in the 2dF Galaxy Redshift Survey (2dFGRS) and in standard ΛCDM predictions, we use a double power-law model for $\xi(r)$ which gives a good fit to the z-space and projected correlation functions.

By fitting functional forms of $\xi(\sigma,\pi)$ which include both dynamical and geometrical modelling, we find, as expected, that β (which parameterises the infall into overdense regions) and the density of the Universe (Ω_m^0) are degenerate. However, this degeneracy can be lifted by using linear theory predictions under different cosmological scenarios. Using the 2QZ survey, we obtain: $\beta_{QSO}(z=1.4)=0.50^{+0.13}_{-0.15}$, $\Omega_m^0=0.35^{+0.19}_{-0.13}$.

The modelling of geometrical and dynamical anisotropies in the measured $\xi(\sigma,\pi)$ pattern is then applied to a sample of distant Lyman-break galaxies. The presence of feedback mechanisms in these $z\sim 3$ star-forming galaxies heightens the importance of understanding the effects of z-space distortions. Despite the limited size of the fields, which hampers the determination of $\xi(r)$ at large scales, we find that a double-power law $\xi(s)$ parameterisation is consistent with the correlation function measurements. This double power law model is then used as an input for the $\xi(\sigma,\pi)$ fitting and subsequent constraining of cosmological parameters. This investigation reveals that: $\beta_{LBG}(z=3)=0.25^{+0.05}_{-0.06}$ and $\Omega_m^0=0.55^{+0.45}_{-0.16}$.

The combination of the 2QZ with the fainter 2SLAQ QSO sample reveals that QSO clustering

does not depend strongly on luminosity. This result is consistent with models which predict that haloes of similar mass can harbour QSOs of different luminosities. By assuming ellipsoidal models for the collapse of density perturbations, we test this hypothesis and estimate the mass of the dark matter haloes which the QSOs inhabit. We find that halo mass does not seem to evolve strongly with redshift nor depend on QSO luminosity. Having determined the black hole mass associated with the QSOs, we investigate how it correlates with luminosity and redshift and ascertain the relation between Eddington efficiency and black hole mass. Our results suggest that: (i) black hole mass does not depend strongly on accretion efficiency and (ii) black holes associated with QSOs of different luminosities have similar masses.

Finally, the *Hubble Volume* simulation is used to construct a mock sample of a future AAΩ Luminous Red Galaxy (LRG) survey. The ultimate aims of this survey are to identify the baryon acoustic features in the LRG clustering signal and to determine the equation of state of dark energy. We apply the z-space distortion analysis developed previously in the thesis to infer the statistical gain in terms of determinations of $\beta_{LRG}(z \sim 0.7)$ and Ω_m^0.

This thesis exploits the wealth of information contained in cosmological surveys, and demonstrates how the use of tools such as clustering statistics or z-space distortion analyses permit the extraction of such information.

PREFACE

The work presented in this thesis was carried out between 2002 and 2006 while the author was a research student under the supervision of Prof. Tom Shanks in the Department of Physics at Durham University.

The major part of the work presented in this thesis is the author's own work except where specifically noted in the text, as summarised below.

- Dr. Phil Outram generated the random catalogue used to compute the 2QZ correlation functions, in chapters 2 and 3.
- Dr. Fiona Hoyle wrote the software used to extract mass particles from the *Hubble Volume* simulation, in chapter 6.

Contents

List of Figures

List of Tables

Declaration

The work described in this thesis was undertaken between 2002 and 2006 while the author was a research student under the supervision of Prof. Tom Shanks in the Department of Physics at Durham University. This work has not been submitted for any other degree at Durham University or any other University.

Portions of this work have appeared in the following papers:

- da Ângela, J., Outram, P. J., Shanks, T., Boyle, B. J., Croom, S. M., Loaring, N. S., Miller, L., & Smith, R. J. 2005, MNRAS, 360, 1040, **The 2dF QSO Redshift Survey- XV. Correlation analysis of redshift-space distortions** (chapters 2 and 3)

- da Ângela, J., Outram, P. J., & Shanks, T. 2005, MNRAS, 361, 879, **Constraining $\beta(z)$ and Ω_m^0 from redshift-space distortions in $z \sim 3$ galaxy surveys** (chapter 4)

The author has also either worked on, or been involved in the following work:

- Croom, S. M., Boyle, B. J., Shanks, T., Smith., R. J., Miller, L., Outram, P. J., Loaring, N. S., Hoyle, F., da Ângela, J. 2005, MNRAS, 356, 415, **The 2dF QSO Redshift Survey - XIV. Structure and evolution from the two-point correlation function**

- Wake, D. A., Nichol,R. C., Eisenstein,D. J., Loveday,J., Edge, A. C., Cannon, R., Smail, I., Schneider, D. P., Carson, D., Ross, N. P., Brunner, R. J., Colless,M. , Couch, W. J., Croom, S. M., Driver, S. P., da Ângela, J., de Propis, R., Drinkwater, M. J., Bland-Hawthorn, J., Pimbblet, K. A., Roseboom, I. G., Shanks, T. , Sharp, R. G., Brinkmann,J., **The 2dF-SDSS LRG and QSO survey: Evolution of the luminosity function of luminous red galaxies to** $z = 0.6$, submitted to *Monthly Notices of the Royal Astronomical Society* (MNRAS)

Acknowledgements

First of all, I will start by thanking my supervisor, Tom Shanks, for his support, time and guidance. This thesis would not have been possible without his supervision, enthusiasm and vast knowledge of cosmology and general astronomy.

Phil Outram helped me out at various stages during the Ph.D.. I must thank him for all his practical advice on astronomy, computing, maths, etc. This thesis would have been much harder without his "co-supervision" during the first years.

Catarina Lobo also deserves a very special "obrigado", for encouraging me to take a Ph.D. in the first place, and for her constant support during all this time.

There are quite a few astronomers who at some point gave me a hand during the Ph.D. course, or with whom I had useful discussions. To name a few: I thank Shaun Cole, Scott Croom, Nelson Padilla, Max Tegmark and David Wake for general discussions on cosmology, AGN physics, galaxy bias, covariance matrices, etc, etc; Fiona Hoyle, Adrian Jenkins and Adam Myers for helping me with the *Hubble Volume* mocks; Carlton Baugh and Peder Norberg for valuable help, advice and discussions on correlation functions, quasar clustering, etc. Another big "thank you" to Carlton for (proof-) reading one of my thesis chapters.

I thank Alan Lotts for keeping the network up and running and for taking care of all sort of computer matters. I must also thank Shaun Cole, Lydia Heck, Nigel Metcalfe and David Stockdale for lending me laptops so I could write my thesis while sitting comfortably at home, and also for making sure that they worked!

I am grateful to all those astronomers who made the SISCO meetings so enlightening, exciting and enjoyable. A special thanks to Eelco for making my first skiing experience possible.

My time in Durham would not have been the same if it weren't for all the friends I made, and who I must thank for distracting me from the world of astrophysics. A special thanks goes to Aarti, Alistair, Angelo, António, Dajana, Daniela, David, Heather, Lucy, Marc, Mark, Nuria, Panayis, Peter, Richard, Tatiana, to name a few. "Moltes gracies" to Marc for all the discussions on life, philosophy, football, politics, music and of course, astronomy. And also Peter, for all his tips on observational astronomy, telescopes and jenga, and António, for introducing me to Brazilian cuisine.

I should also thank David, Jeanette and Marc, for their patience whilst sharing an office with me. A special thanks to David for distracting me with his latest gadgets, pictures and projects, and for letting me spread my astro-ph compilation across the floor.

I leave my warmest "thank you" to the person whom I met soon after deciding to take Salsa classes. I thank Michelle for all her love, support and inspiration during the second half of my Ph.D.. The last couple of years have been amazing. Obrigado!

And finally, my biggest "obrigadão" has to go to my parents and my "mana", for being there. This thesis would have never happened without their constant support during all my academic life.

Chapter 1 | *Introduction*

1.1 The expanding Universe

Most theoretical models in modern cosmology rest intrinsically on the *cosmological principle*. The cosmological principle tells us that the Universe is homogeneous and isotropic, *at large scales*. The "large-scale" caveat allows one to accept this principle whilst observing the uneven distribution of galaxies and the (sometimes non-linear) clustering and evolution of gravitationally-bound structures. Whereas homogeneity means that no observer has a privileged position, isotropy means that there are no preferred directions (an example of a homogeneous, non-isotropic Universe could be an empty Universe permeated with a constant, unidirectional magnetic field). Working with the assumption of the cosmological principle, H. P. Robertson and A. G. Walker established what came to be one of the cornerstones of modern cosmology (Robertson, 1935; Walker, 1935). By combining the time coordinate with space homogeneity and isotropy, they developed the following metric[1]:

$$ds^2 = -dt^2 + a(t)^2 \left(\frac{dr^2}{1 - kr^2} + r^2(d\theta^2 + \sin^2\theta d\phi^2) \right) \tag{1.1}$$

where t is the time coordinate and the spatial coordinates are represented in polar form. The constant k represents the geometry, or curvature, of the Universe. By rescaling the coordinates one can make k equal to 0 (flat Universe), 1 (for a closed Universe) or -1 (corresponding to an open Universe). $a(t)$ is the "scale factor", which represents the time dependence of cosmological distances due to the expansion of the Universe and is related to the redshift by $a_0/a = 1 + z$, and the index 0 indicates the present time.

The Universe's expansion is governed by the energy density contributions of all the constituents and, under the cosmological principle, it can be characterised by three equations.

Friedmann's equation,

$$\left(\frac{\dot{a}}{a}\right)^2 = H^2 = \frac{8\pi G}{3}\rho - \frac{k}{a^2} \tag{1.2}$$

is the differential equation relating the evolution of the scale factor to the overall energy density of the Universe (ρ). H is commonly referred to as the Hubble parameter and G is the gravitational constant. If the energy content includes contributions from different components (e.g., mass, radiation), then $\rho \equiv \sum_i \rho_i$, where the summation includes all the fluids comprising the Universe.

[1] Assuming units with $c = 1$.

The fluid equation explains the time change of the energy density as a consequence of the volume change and the thermodynamic work exerted by the pressure during the expansion:

$$\dot{\rho} + 3H(\rho + p) = 0 \tag{1.3}$$

where p and ρ are the pressure and energy density of the fluid. The third equation is actually derived from the previous two, and it describes the Universe's acceleration:

$$\frac{\ddot{a}}{a} = -\frac{4\pi G}{3}(\rho + 3p) \tag{1.4}$$

The extrapolation of the dynamical equations above to earlier times defines the standard Big Bang scenario. When we know the relation between the pressure and density of the fluids that comprise the Universe[2], it is straightforward to solve the above equations and determine the time evolution of the scale factor, especially when one of the components (e.g. matter component, with $p = 0$) dominates the energy budget. However, it has been suggested that the Universe may be slightly more complicated. In recent years, two main questions have been the focus of many theoretical and observational efforts: **1)** what accounts for the Universe's energy density? **2)** what is the equation of state of the main contributors to the energy budget?

Obvious contributions to the energy density come from non-relativistic matter (with $p = 0$) and radiation (corresponding to $p = 1/3\rho$). Recent observations have hinted at the need for an extra energy component with a not as obvious an equation of state. The evidence for this "dark energy" usually come from one of either two approaches. One is by probing directly the Universe's expansion rate, through the properties of distant objects (e.g., Cepheids, Tanvir et al. 1999, supernovae, Perlmutter et al. 1999). The other is by determining the matter density of the Universe and comparing that with the total density, inferred by measuring the Universe's geometry (e.g. Tegmark et al., 2004; Spergel et al., 2006). The convergence of independent results to a common cosmological scenario where the Universe is spatially flat and is currently experiencing an accelerated expansion has lead to the concept of *concordance model.* This model implies that the Universe is now in a phase of accelerated expansion, and that the matter content of the Universe accounts for a mere third of the complete energy budget. The energy density is also such that the Universe is very close to having a flat geometry.

If we write the equation of state of state as $p = w\rho$, it follows from Eq. 1.4 that the fluid causing the accelerated expansion (i.e., $\frac{\ddot{a}}{a} > 0$) has $w < -1/3$, and the negative pressure is the drive responsible for increasing the rate of expansion. Observations seem to indicate that the likely value of w is $w \sim -1$, which corresponds to adding an extra (constant) term to Einstein's field equations, a *cosmological constant.*

Equation 1.2 can be re-written by expressing each of the i energy contributions as a fraction of the critical density, i.e., that corresponding to a flat, $k = 0$ geometry: $\Omega_i^0 = 8\pi G\rho_i/(3H_0)$, where the index 0 represents the present value. In this case, Friedmann's equation can be written as:

[2]This relation is often labelled *equation of state.*

$$\left(\frac{H}{H_0}\right)^2 = \Omega_r^0 a^{-4} + \Omega_m^0 a^{-3} + \Omega_{DE}^0 a^{-3(1+w)} + \Omega_k^0 a^{-2} \quad (1.5)$$

where we normalised the scale factor such that at the present time $a_0 = 1$. Ω_r^0, Ω_m^0, refer to the present density values of radiation and matter, respectively. Ω_{DE}^0 is the present value of the energy density of the *dark energy* field, with equation of state $p = w\rho$, causing the accelerated expansion. $\Omega_k^0 = -kH_0^{-2}$ is the curvature term. It is therefore evident that different values for Ω_i^0 will weight differently the different contributions, and determine the dynamics of the Universe. In asymptotic cases, however, it is the dependence on the scale factor that intrinsically determines which of the energy contributors dominates the expansion of the Universe. In particular, at very early times, when a is very small, radiation plays the dominant role on the expansion. Later on, non-relativistic matter with $p = 0$ is responsible for driving the expansion, followed by the curvature term (for a non-flat cosmology) and the dark energy field, assuming that $w < -1/3$.

1.1.1 Universe and dark energy

Recent studies of the cosmic microwave background (CMB) led to a coherent picture where the Universe is very close to having a flat geometry, with $0.98 \lesssim \Omega_{tot}^0 \lesssim 1.08$ (de Bernardis et al., 2000; Bennett et al., 2003; Spergel et al., 2003, 2006). These observations, together with large-scale structure surveys (Percival, 2006), suggest a value of $\Omega_m^0 \sim 0.25 - 0.30$. In addition, the baryonic content of the Universe only accounts to $4 - 6\%$ of the total energy density (Bennett et al., 2003), leading us to conclude that even most of the matter is un-observed, non-baryonic *dark matter*. Finally, the radiation content of the Universe seems to have a negligible contribution to the energy budget, and does not yield a significant weight in the present expansion dynamics ($\Omega_{rad}^0 \sim 5 \times 10^{-5}$).

The overall parameterisation of the energy density of the Universe, is accepted to be, approximately, $\Omega_{Dark\ matter}^0 \approx 0.26$, $\Omega_{baryon}^0 \approx 0.04$, (with the total matter density, $\Omega_m^0 = \Omega_{Dark\ matter}^0 + \Omega_{baryon}^0$), $\Omega_{rad}^0 \approx 5 \times 10^{-5}$ and $\Omega_\Lambda^0 \approx 0.7$ (e.g. Padmanabhan, 2006). The suffix Λ means that we are considering an energy field in the form of a cosmological constant Λ, with $w = -1$. The existence of a cosmological constant is consistent with most cosmological observations. However, its true physical nature is still a dilemma to modern physics. The fact that the dominant fluid driving the Universe dynamics and ultimately dictating its future is so poorly understood is in fact somewhat uncomfortable.

If on one hand dark energy, and in particular the cosmological constant, is required to fit observational results under the framework of the Big Bang model, and it does explain observations successfully, it also raises deeper questions which are difficult to understand from a theoretical perspective. If the cosmological constant does exist, and is associated to a repulsive energy density associated to the vacuum, then its scale is 10^{-47} GeV, 10^{123} times smaller than that expected from fundamental physics (Movahed and Rahvar, 2006), hence requiring a considerable amount of fine-tuning in order to fit the observations. Also, and as seen in Eq. 1.5, if dark energy has indeed the

form of a cosmological constant, then it dominates the Universe's expansion at late times, after an era when matter drives most of the Universe dynamics and the expansion is decelerating. However, we seem to be living in this unique "transition" time, when both the energy contributors have comparable weight. This unexpected coincidence is the second cosmological constant problem: why is it that, precisely at this time in the history of the Universe, $\Omega_\Lambda^0 \approx \Omega_m^0$?

1.2 Clustering and evolution of large scale structure

Understanding the formation, clustering and evolution of large-scale structure (LSS) has been one of the major quests in the history of cosmology. The combination of results from large cosmological surveys (e.g., 2dF Galaxy Redshift Survey, 2dFGRS, Colless et al. (2001)) and simulations (e.g., the *Hubble Volume* simulation, Evrard et al. 2002) has shown that dark energy, usually assumed to have the form of a cosmological constant (Λ), probably plays a central role in the overall picture of cosmological structure formation and evolution. Combined with the hypothesis of a period of accelerated expansion taking place very early in the history of the Universe (commonly known as inflation), dark energy predicts a general description of large scale structure almost identical to that observed in large surveys of galaxies or quasi-stellar objects (often shortened to quasars or QSOs). The success of this now *standard paradigm* is very tightly linked to that of the cold dark matter (CDM) model. The combination of both models originated the ΛCDM model.

ΛCDM implies that the mass content of the Universe, accounting for a third of the energy budget and largely dominated by dark matter, is in the form of non-baryonic, weakly interactive massive particles (WIMPs), and it was the gravitational growth of Gaussian, primordial departures from isotropy that seeded the large scale structures observed today. These fluctuations in the energy density in the early universe were amplified during the inflationary period of the Universe (Guth, 1981), and grew hierarchically by gravitational instability, with more overdense regions attracting more matter, increasing the density contrast with time. Such a process could lead to the formation of galaxies, stars, and the large scale structures observed today. The fact that gravity is the dominant force for the growth of density perturbations, in the post-inflationary Universe, allows us to study the evolution of structure without the need to know the true nature of dark matter.

Density perturbations can be quantified as a function of the local (ρ) and background densities (ρ_b):

$$\delta(\mathbf{x}) = \frac{\rho(\mathbf{x}) - \langle\rho_b\rangle}{\langle\rho_b\rangle} \tag{1.6}$$

We can then define the autocorrelation function of the density field as

$$\xi(r) = \langle\delta(\mathbf{x})\delta(\mathbf{x}+\mathbf{r})\rangle \tag{1.7}$$

where r is a measurement of the separation between two local overdensities.

These *clustering measurements* can also be considered in Fourier space, and the density contrast can be transformed into its Fourier pair:

$$\delta(\mathbf{k}) = \int \delta(\mathbf{x}) \exp(i\mathbf{k}.\mathbf{x}) d^3x \tag{1.8}$$

and it follows that the Fourier pair of the autocorrelation function is the power spectrum ($P(k)$), which can be given by:

$$\langle \delta(\mathbf{k}) \delta(\mathbf{k}') \rangle = (2\pi)^3 P(k) \delta_D(\mathbf{k} - \mathbf{k}') \tag{1.9}$$

where $\delta_D(\mathbf{k} - \mathbf{k}')$ is the Dirac-δ function. The density power spectrum and the autocorrelation function are related as follows:

$$P(k) = \int \xi(r) \exp(i\mathbf{k}.\mathbf{r}) \mathbf{d^3r} \tag{1.10}$$

$$\xi(r) = \frac{1}{(2\pi)^3} \int P(k) \exp(-i\mathbf{k}.\mathbf{r}) \mathbf{d^3k} \tag{1.11}$$

If non-linear effects are not relevant, as should be the case if we are probing large enough scales ($\gtrsim 10\,h^{-1}$Mpc), the growth of density perturbations is given by (e.g. Peacock, 1999):

$$\ddot{\delta} + 2\frac{\dot{a}}{a}\dot{\delta} = \delta \left(4\pi G\rho - \left(\frac{c_s k}{a} \right)^2 \right) \tag{1.12}$$

where $c_s = \sqrt{\partial p / \partial \rho}$ is the speed of sound. By combining this equation with Friedmann's equation we can probe the time (or redshift) evolution of density perturbations in different cosmological scenarios. We can then measure the clustering of structure and compare with that from linear theory predictions, in order to determine the density parameters that describe the energy content of the Universe.

One of the best ways to study the clustering and evolution of the Universe and large scale structure is by performing large surveys of the cosmic web. Recent developments of observational technology and facilities (e.g., SDSS York et al. (2000), 2dF Lewis et al. (2002), DEEP2 Davis et al. (2003), AAΩ Sharp et al. (2006)) have either delivered an enormous amount of information, or should do so in the very near future. By statistically analysing the clustering of galaxies and QSOs from these redshift surveys we can probe how structure has grown and study the evolutionary properties of the Universe as it expanded and cooled down.

1.3 Redshift-space distortions

However, measuring the clustering of distant objects does not provide a direct determination of their true spatial distribution, or the *real* clustering of the underlying dark matter. The distances

are distorted by dynamical distortions due to peculiar velocities and also geometrical distortions, if a wrong cosmology is used to convert the observed redshifts into distances.

1.3.1 Dynamical distortions

To compute the distances to distant objects one needs to assume that their observed redshifts are only due to the expansion of the Universe. However, they also include contributions from the objects' peculiar motions, in their local rest-frame. Therefore, the distances estimated from their redshifts do not correspond to the "true distances" and are said to be measured in *redshift-space* (z-space). If the true positions of the objects were known, then these would have been said to be measured in *real-space*. Thus, peculiar motions will introduce distortions in the measured clustering pattern.

There are basically two mechanisms leading to the dynamical z-space distortions. As structures grow through gravity, the infall of objects to higher-density regions contributes to the measured redshifts. If these are assumed to be solely due to the Hubble flow, than the large-scale distribution will appear flatter, or thinner, along the line of sight, thus "distorting" the clustering signal. At smaller scales, the random peculiar motions of the objects will also contribute to the measured redshifts, and hence distort the measured clustering signal for close pairs of objects. If the distribution of distant objects has, on average, a spherically symmetric clustering pattern in real space, but large velocity dispersion, then the clustering signal measured in z-space will be smeared along the line-of-sight. These features are often referred to as "fingers-of-God", and are commonly seen as elongated structures in radial wedge plots of distant galaxy surveys, such as the 2dFGRS (e.g. Hawkins et al., 2003).

As shown by Peebles (1980), Kaiser (1987), or Hamilton (1992), the large scale coherent infall can be used to probe the clustering of the underlying dark matter clustering and the matter content of the Universe. The infall can be parameterised by comparing the large-scale clustering in real- and z-space. In terms of the power-spectrum:

$$P_{gal}(k_s) = P_{gal}(k_r)\left(1+\beta\mu^2\right)^2 \tag{1.13}$$

where the subscripts r and s refer to the real- and z-space measurements, respectively. μ is the cosine between the velocity vector and the line of sight, and β relates the observed large-scale infall to the clustering of the (invisible) dark matter. The equation above, if written in terms of correlation functions instead, takes the form (Kaiser, 1987):

$$\xi_{gal}(s) = \xi_{gal}(r)\left(1+\frac{2}{3}\beta+\frac{1}{5}\beta^2\right) \tag{1.14}$$

β is related to cosmology and the dark matter distribution by

$$\beta = \frac{f\left(\Omega_m(z), \Omega_\Lambda(z), z\right)}{b} \tag{1.15}$$

Here, b is the bias, which relates the luminous matter clustering to that of the underlying dark matter ($b^2 = \xi_{galaxy}/\xi_{mass}$). This relation means intrinsically that luminous objects are biased tracers of the underlying mass distribution, which dictates the overall dynamics due to gravitational effects. However, it has been found that galaxy clustering is a function of galaxy properties, such as morphology, type, luminosity, etc (e.g. Davis and Geller, 1976; Norberg et al., 2001, 2002; Madgwick et al., 2003). Therefore, the *true* bias will also depend on the physics of galaxy formation, interactions and feedback mechanisms, which are still not so well understood. However, at large enough scales where the density fluctuations are close to linear and Eq. 1.12 holds, this more deterministic approach to the bias should provide a fair description of the dark matter clustering.

$f(\Omega_m(z), \Omega_\Lambda(z), z)$ quantifies the growth of structure as a function of the cosmological parameters (Peebles, 1980):

$$f(\Omega_m(z), \Omega_\Lambda(z), z) = \frac{d\ln\delta}{d\ln a}, \tag{1.16}$$

which, in the case of a flat Universe can be approximated to (Lahav et al., 1991):

$$f \approx \Omega_m(z)^{0.6} + \frac{1}{70}\left(1 - \frac{1}{2}\Omega_m(z)(1 + \Omega_m(z))\right) \tag{1.17}$$

but is more often simply assumed as $f \approx \Omega_m(z)^{0.6}$.

The formalism for z-space to real-space mapping of the large-scale structure distribution is hardly unique. Whilst Kaiser (1987) related the real and z-space correlation functions through Eq. 1.14, Peebles (1980) uses the simpler form $\xi_{gal}(s) = \xi_{gal}(r)\,(1 + 2/3\beta)$; Heavens and Taylor (1995) used a spherical harmonic approach to relate the z-space to real-space clustering measurements. More recently the modelling of dynamical distortions has been developed under the halo occupation distribution (HOD) framework (Tinker, 2006) and non-linearities and scale dependent parameterisations of the velocity dispersion have been included (Bharadwaj, 2001; Scoccimarro, 2004).

In addition to the distinct methods developed for parameterising the z-space distortions, different ways of extracting the anisotropy information have been developed. As pointed out by Landy and Szalay (2002), three different frameworks regarding the estimation of β have been developed: **1)** by measuring the ratio of the z-space and real-space power spectrum/correlation function (e.g. Loveday et al., 1996); **2)** by measuring the ratio of the quadrupole to monopole moments of the z-space power spectrum/correlation function (e.g. Hamilton, 1993a; Cole et al., 1994); **3)** by setting the amplitude of the modes, β and the power spectrum as model parameters (e.g. Ballinger et al., 1995; Heavens and Taylor, 1995). Landy and Szalay (2002) also propose a new way of estimating β, by Fourier inverting the z-space distortions seen in the density field. Using different β values for the inversion, the one resulting in an isotropic density field should correspond to the true β value.

1.3.2 Geometric distortions

Peculiar velocities are not the only effect leading to anisotropies in the clustering pattern. As shown by Alcock and Paczynski (1979), if one assumes a cosmology different from the true, underlying cosmology of the Universe to convert redshifts into distances, the effect on separations along the line of sight differs from that affecting the separation in the sky direction. As a consequence, the clustering signal might appear elongated (or squashed) in the redshift direction. As shown by those authors these *geometric distortions* can be a powerful cosmological test, namely to determine Ω_Λ^0.

If Δz is the redshift difference between two galaxies, and $\Delta\theta$ their angular separation, then

$$\frac{\Delta z}{z\Delta\theta} = \frac{D_A(z)}{cz/H(z)}, \tag{1.18}$$

where

$$D_A = \frac{c}{H_0(1+z)} \int_0^z \frac{dz'}{\sqrt{\Omega_0^0(1+z')^3 + \Omega_\Lambda^0}} \tag{1.19}$$

is the angular diameter distance (assuming a spatially flat universe with matter and cosmological constant). This ratio is close to unity for small z, but at high redshift it deviates from unity, by an amount that depends on the cosmological parameters.

Due to their significance at high-z, these potential geometric distortions have been used to constrain cosmological parameters using QSO catalogues (e.g. Calvão et al., 2002; Outram et al., 2004); 21 cm maps of the epoch of reionisation (Nusser, 2005) or the Lyman α forest (Becker et al., 2004).

However, and as discussed in detail in Ballinger et al. (1996), it is sometimes not trivial to disentangle the effects of geometric distortions from those caused by peculiar velocities. If both the infall parameter β and cosmological density values as Ω_m^0 or Ω_Λ^0 are left as free variables, we expect to see a degeneracy between the anisotropies caused by the large scale infall and the geometric distortions. Those authors define a "flattening factor", which determines, as a function of redshift and cosmology, the level of asymmetry expected to see as a result of geometric distortions, and found that its value is degenerate with that of β. Those authors also conclude that QSO surveys should provide better constraints in Ω_m^0 and β, given both the larger volume and high redshift.

1.4 Thesis motivation and outline

1.4.1 Cosmology and z-space distortions

In this thesis, we start by performing a detailed analysis of the clustering of high-z QSOs. The aim is to better understand the effects of dynamical and geometrical distortions in the measured clustering pattern of cosmological sources. We attempt to lift the degeneracy between dynamical

and geometric distortions by using additional constraints from linear theory predictions. By combining both the constraints, we aim to determine $\beta(z)$ and Ω_m^0.

The question might arise as to why we are performing these studies, as most recent cosmological surveys already seem to converge towards a particular picture. In addition, CMB measurements combined with existing galaxy survey results (e.g. 2dFGRS) reach a level of "precision" that is unlikely to be achieved through the Alcock-Paczynski test. However, one should emphasise the number of assumptions made in analysis of CMB anisotropies and other surveys. In what concerns CMB studies, for example, the initial fluctuations are generally assumed to be 100% adiabatic. Even a small component of isocurvature fluctuations, as predicted by some braneworld models, could modify the amplitude of the peaks (Sanders 2005 and references therein) and consequently affect the resulting cosmological constraints. Similarly, if one relaxes the assumption of a scale free power-spectrum, the need for a cosmological constant to fit the CMB data vanishes (Blanchard et al., 2006).

It is therefore with the intent of performing cosmological tests that are independent of the CMB data that we use z-space distortion and clustering statistics in large scale structure surveys. In particular, we use the 2dF QSO Redshift Survey (2QZ) and a sample of 800 Lyman-break galaxies (LBGs) for the modelling of z-space distortions (chapters 3 and 4, respectively). We find, however, that in order to obtain accurate measurements of the clustering anisotropies, we need a detailed description of the real-space clustering. Hence, in chapter 2, we combine z-space and sky-projected clustering measurements to obtain a detailed model for the QSO real-space clustering. The real space QSO clustering is of great interest in itself, as is the possible existence of deviations from simple power-law parameterisations (e.g. Zehavi et al., 2004). The interpretation of these depends on the physics behind the growth and evolution of gravitationally bound structures.

1.4.2 Lyman break galaxies

There are several reasons why LBGs are a particularly interesting tool in terms of z-space distortion studies. **1)** They are easily identifiable due to the pronounced Lyman break; **2)** they are strongly clustered (e.g. Steidel et al., 1998) and **3)** they existed at a time when the Universe was just a fraction of its current age.

The statistical tools needed for the z-space distortion analysis of the LBG clustering not only allow the determination of cosmological parameters, but are also essential to understand galaxy - inter-galactic medium (IGM) interactions via feedback mechanisms. Feedback processes, such as galactic winds or ionisation, are likely to have a fundamental role in the process if galaxy formation (e.g. Theuns et al., 2001) and future observations of LBGs in the line of sight of background QSOs should have a crucial role in expanding our understanding of such processes.

Adelberger et al. (2003) probed the distribution of gas clouds at high-z by identifying redshifted Lyman α and CIV absorption lines in the spectra of distant QSOs. This allowed the *cross-*

correlation between the gas distribution and that of foreground LBGs. By measuring the clustering signal both in the redshift and sky directions, they compared the LBG auto-correlation function with the cross-correlation between LBG-Lyman α and LBG-*CIV* systems.

Their results revealed different shapes of the clustering contours in these two orthogonal directions: whereas the LBG-LBG and LBG-*CIV* systems show significant small-scale elongations of the clustering signal along the line of sight, the LBG-Lyman α clustering seems to be reasonably isotropic. Interpreting these different levels of z-space anisotropies is crucial in order to properly understand the LBG-*CIV* and LBG-Lyman α interactions. Hence, in this chapter, we use a super-sample of the dataset utilised by Adelberger et al. (2003) to determine if the elongation of the LBG-LBG clustering signal is, in fact, due to extremely high velocity dispersion of the LBGs (or associated z-uncertainty) or, instead, a statistical fluctuation, due to the lack of galaxy pairs at close separations.

1.4.3 The black hole - QSO connection

QSO clustering also allows us to study the dependence of QSO clustering on luminosity. Whereas the dependence of galaxy clustering on luminosity has been addressed (e.g. Norberg et al., 2001), the luminosity dependence of QSO clustering is still the object of study and speculation. The main difficulty in these investigations is due to the L - z degeneracy: as the most luminous QSOs lie preferentially at high redshifts, it is hard to disentangle luminosity from evolutionary effects on the QSO clustering. We address this question in chapter 5, where we combine the 2QZ sample with the fainter QSO sample from the 2dF SDSS LRG and QSO survey (2SLAQ). In this chapter, we also exploit the information contained in QSO clustering to investigate the link between black hole mass and QSO luminosity.

According to active galactic nuclei (AGN) unification models, differences between objects such as Seyfert 1, Seyfert 2 galaxies, QSOs or BL Lacs can be explained by a single "family" of highly energetic, exotic objects, characterised by the existence of a compact powerful supermassive black-hole (SMBH) in the centre. The energy release from the accretion onto the SMBH fuels the immense energy output, which depending on geometry, orientation and thickness of accretion disk and dusty torus, can lead observers to associate the different spectral properties to different classes of objects, where in fact such sources have a similar fuelling mechanism (for a detailed discussion on AGN and unified models, see Antonucci 1993).

Despite the many successes of *unification models*, the underlying processes governing black hole growth and QSO activity are still poorly understood. SMBHs seem to reside in the centres of most galaxies in the local Universe (Kormendy and Richstone, 1995; Richstone et al., 1998) and their mass correlates with either the mass of the spheroid (Magorrian et al., 1998; Marconi and Hunt, 2003) or the velocity dispersion (Ferrarese and Merritt, 2000; Tremaine et al., 2002). These observational results reveal a link between the origin of galaxies and SMBHs. As QSO activity depends on the gas available to "feed" the SMBH, its lifetime is expected to depend on the rate

of energy conversion from accretion into luminosity, as well as QSO feedback processes.

Recent studies (Hopkins et al., 2005a,b) have assumed that QSOs spend more time emitting at luminosities below their peak luminosities, thus have a high probability to be observed during this stage of their life. This is different from previous studies, where it has been assumed that QSOs radiate for a fixed luminosity during most of their lifetime (Kauffmann and Haehnelt, 2000). These two scenarios have different predictions for the QSO clustering dependence on luminosity. If QSOs radiate at a given luminosity throughout their lifetime, then one would expect faint QSOs to populate lower mass dark matter haloes, where brighter QSOs should inhabit more massive haloes. If, however, bright and faint QSOs are similar objects observed at different stages, then the same massive haloes should harbour both bright and faint QSOs, and QSO luminosity and clustering should not be strongly correlated (Lidz et al., 2006). Through the combination of the 2QZ and 2SLAQ sample we can address this subject by measuring the QSO clustering as a function of luminosity, at different redshifts, in order not to "contaminate" the results with possible evolution of QSO clustering (e.g. Croom et al., 2005).

1.4.4 Future constraints from z-space distortion analyses

In chapter 6 we address the potential of future Luminous Red Galaxy (LRG) surveys in terms of z-space distortion analysis, in particular the gain in terms of Ω_m^0 and $\beta(z)$ constraints from modelling the distortions seen in the clustering measured along and across the line of sight. LRGs are particularly good candidates to probe large-scale structure as due to being easily identifiable through the pronounced $4000\mathring{A}$ break and their high-bias. A mock LRG catalogue is built, mimicking the survey size of a future AAΩ LRG survey. The prime aim of such a survey is to measure the equation of state of dark energy by identifying baryon acoustic oscillations features in the LRG's power-spectrum/correlation function.

As previously stated, the simplest solution for dark energy, the cosmological constant, does imply a considerable level of "fine-tuning" in order to be associated with the vacuum energy. Different solutions for dark energy are therefore being sought (generally known as quintessence fields), in order to better understand the nature of dark energy and the physics driving the accelerated expansion. The baryon acoustic oscillations in the power spectrum can be used as a standard rod to measure the equation of state of dark energy, by comparing them to the oscillations seen in CMB measurements, at time of recombination ($z \sim 1100$) (e.g. Eisenstein, 2005). Therefore, large cosmological surveys are being used to measure the baryonic features in the galaxy power spectrum/ correlation function (Eisenstein et al., 2005; Cole et al., 2005).

Given that, in order to constrain w, one needs very good constraints on Ω_m^0, Ω_Λ^0, in chapter 6 we determine if these can be obtained self-consistently by z-space distortion analysis of the AAΩ LRG sample, by applying the fitting method developed in the first chapters of this thesis.

Finally, in chapter 7, we draw the conclusions of this work. Clustering analysis and z-space

distortion modelling are potentially powerful tools to probe large-scale structure. This thesis demonstrates how they can be used to address both *Cosmology* and *Astrophysics* questions, and tackle some of the most intricate mysteries in modern physics.

Chapter 2

Clustering in the 2dF QSO Survey

2.1 Introduction

If the distances to high-z QSOs are determined directly from their observed redshifts, z-space distortions due to the QSOs peculiar motions are due to influence the measured clustering signal. Small scale fingers-of-God and large scale gravitational instabilities will introduce distortions in the measured clustering pattern, hence "hiding" the true, real-space clustering of the QSO sample.

The aim of the next two chapters is to study the clustering of QSOs in the redshift range $0.3 \lesssim z \lesssim 2.2$, particularly discussing the effects of the "peculiar" velocities of the QSOs, superimposed on the expansion due to the Hubble flow, in the measured clustering properties. For this purpose, we use statistical tools such as the two-point correlation functions. In this chapter, in particular, we concentrate on estimating the real-space correlation function of the QSOs in the 2dF QSO Redshift Survey using the observed z-space and sky-projected measurements. We shall see, in chapter 3, that an accurate description of the real-space clustering is essential for the modelling of dynamical and geometrical distortions imposed on the clustering pattern measured in orthogonal directions. We also derive values of $\beta(z)$ assuming different $\xi(r)$ models. As we shall see in more detail, this parameter quantifies the coherent infall of the QSOs into the potential well caused by overdense regions.

Before continuing our study of the z-space distortions in the 2QZ survey, in chapter 3, we conclude this chapter with the comparison of what we found to be an adequate $\xi(r)$ description with results from the 2dF Galaxy Redshift Survey (2dFGRS Colless et al., 2001; Hawkins et al., 2003) and theoretical predictions from Cold Dark Matter (CDM) non-linear clustering models (Peacock and Dodds, 1996; Smith et al., 2003).

2.2 The 2dF Quasar Redshift Survey – 2QZ

2.2.1 Basics

The 2QZ survey area consists of two declination strips, $75° \times 5°$ each, one centred on $\delta_{B1950} = -30°$ and extending from $\alpha_{B1950} = 21^{\rm h}40^{\rm m}$ to $\alpha_{B1950} = 3^{\rm h}15^{\rm m}$ (SGP strip) and the other centred on

$\delta_{B1950} = 0°$ and extending from $\alpha_{B1950} = 9^h50^m$ to $\alpha_{B1950} = 14^h50^m$ (NGP strip). The 2dF Galaxy and QSO Redshift Surveys were ran simultaneously and the sky coverage is similar from both (Folkes et al., 1999).

The QSO candidates have $18.25 < b_J < 20.85$ and were selected using the ultra-violet excess technique in the plane $u - b_J : b_J - r$ with a 93% completeness (Croom et al., 2004). Around 47% of the colour - selected candidates were spectroscopically identified as QSOs, with the criterion being the presence of broad ($> 1000\,\mathrm{km\,s^{-1}}$) emission lines. The remaining objects are stars, white dwarfs, narrow-line galaxies and other objects, such as cataclysmic variables (Marsh et al., 2002). In total, 22652 QSO spectra were obtained.

The spectra were obtained using the 2-degree field instrument (2dF) at the Anglo-Australian Telescope (AAT). The design of this multi-fibre spectrograph allows obtaining 400 spectra simultaneously over a 2° diameter circular field of view (Croom et al., 2004). To cover the survey area with the 2dF field, a tiling algorithm that maximised the number of galaxies and QSOs per pointing was used. The tiling of the 2dF fields has a direct implication from the angular selection function of the survey.

2.2.2 Angular and radial selection functions

A very detailed analysis of the angular and radial QSO selection functions used in this work is given by Outram et al. (2003) and Croom et al. (2005). The selection functions must be taken into account when generating the random distribution of points in the volume probed by the QSOs. The random distribution of points must describe all the characteristics of the QSO ensemble except its clustering, and therefore it must be generated taking into account the same selection functions as the QSO sample. The random ensemble is then used in estimating the two-point correlation functions. In this work we use the same random ensemble as Outram et al. (2003).

The tiling algorithm of the 2dF fibres maximises the number of QSO candidates per pointing. The inability to place fibres in the vicinity of bright stars, weather conditions at the time of different pointings and the variable seeing between observations in different fields make the angular mask of the 2QZ quite complicated. In addition, the extinction due to Galactic dust is also taken into account, when computing the angular mask.

It is also crucial that the random ensemble follows the same redshift or radial distribution as the QSO data. As shown by Outram et al. (2003), the QSO radial number density is quite flat at intermediate distances (between $\sim 1000\ h^{-1}$Mpc and $\sim 2600\ h^{-1}$Mpc, assuming an EdS cosmology, and $\sim 1000\ h^{-1}$Mpc and $\sim 3600\ h^{-1}$Mpc, assuming a ΛCDM cosmology), it increases rapidly from $\sim 300\ h^{-1}$Mpc and has steep decrease at large distances (until $\sim 3000\ h^{-1}$Mpc, assuming an EdS cosmology, and $\sim 4400\ h^{-1}$Mpc, assuming a ΛCDM cosmology). At low redshift the contribution from the host galaxy's brightness is the greatest, which leads to the QSOs appearing as extended. The incompleteness at high redshift is due to the contribution of the

Lyman-alpha forest in the U band, which will significantly influence the ultraviolet excess QSO selection. Therefore, in order to take this deficit in the number density of QSOs at low and high z into account, the same redshift cuts were applied as in Outram et al. (2003), i.e., the QSOs in the following study lie between $0.3 \lesssim z \lesssim 2.2$. As a consequence, the final QSO catalogue used in this study comprises 19549 QSOs (8704 in the NGP strip and 10845 QSOs in the SGP strip).

2.3 The two-point correlation function

2.3.1 Definition and estimators

The two-point correlation function (ξ) measures the excess probability of finding a pair of objects, at a given separation, relative to what would be expected from a uniform distribution. In Appendix A we present the definition of ξ, and general formalism relating it to the probability function and density field of a distribution of objects.

Although correlation functions represent an extremely important statistical tool to quantify the clustering of galaxies, QSOs, or to describe large-scale structure, its measurement is not always a trivial task. Different estimators have been developed to evaluate ξ. The "standard" estimator, developed by Peebles (1979) is given by:

$$\xi(x) = \frac{< DD(x) >}{< DR(x) >} \frac{m}{n} - 1 \tag{2.1}$$

$< DD(x) >$ and $< DR(x) >$ represent the average number of pairs of objects (e.g., galaxies, QSOs) at separation x and the "crosspairs object-random", also at separation x. The factor m/n normalises the random number density to the data number density.

Following this estimator, other more complicated estimators of the correlation function were then developed. The estimator developed by Hamilton (1993b) does not require the knowledge of the ratio m/n. Considering this estimator, $\xi(x)$ is evaluated by:

$$\xi(x) = \frac{< DD(x) >< RR(x) >}{< DR(x) >^2} - 1, \tag{2.2}$$

where $RR(x)$ is the number of random-random pairs separated by x.

In addition to these, Landy and Szalay (1993) developed an estimator which is also a robust estimate of $\xi(x)$, specially at high x i.e., when $\xi(x)$ should be close to zero. There is however the same need as in the first estimator of knowing the number density of the data points:

$$\xi(x) = \frac{< DD(x) > -2 < DR(x) > (n/m) + < RR(x) > (n/m)^2}{< RR(x) > (n/m)^2} \tag{2.3}$$

2.3.2 Error estimates

There are several ways of estimating the error on the QSO two-point correlation function:

- Probably the simplest method of having an estimate of the errors and probably the easiest to compute, is by considering that the number of $< DD >$ pairs per separation interval as a Poisson process. As a consequence, the standard deviation will be $\sqrt{DD}$. It then follows that the error on ξ is given by:

$$\Delta\xi = (1+\xi)\sqrt{\frac{1}{DD}}, \tag{2.4}$$

  which is the definition of Poisson errors.

  However, there are a few reservations when considering this error estimate. One of them is the assumption that the number of pairs in each separation bin is a Poisson process. This is not the case if the pairs in each bin are not independent, and this becomes a more substantial factor at large separations, specially when the objects are strongly clustered (e.g., luminous red galaxies).

- When the the Poisson estimate is a suitable description of the uncertainty in $\xi(s)$ (e.g. QSO surveys, Hoyle 2000), the correlation of pairs in large-separation bins causes this estimate to underestimate the true ξ uncertainty. Therefore, instead of using the number of pairs as an indicator of the error on the correlation function, Shanks and Boyle (1994) found that the error could also be computed using the total number of objects in the survey. This estimate of the errors (N_o errors) is quite similar to Poisson errors, but DD is replaced by the total number objects in the survey, N_o.

- If the sample is big enough, field-to-field errors can also be used. In this case, the ensemble is divided in similar subsamples, and ξ is computed in each of them, as in the complete set of objects. The error on this last will then be given by Eq. 2.5 (Press et al., 1986; Myers, 2003), where N is the total number of subsamples of the whole ensemble, and j refers to each of those subsamples. The main problem in using this error estimate is that no additional information to the data is used: the actual data is used to get an estimate of the error on itself.

$$\Delta\xi = \sqrt{\frac{1}{N-1}\sum_{j=1}^{N}\frac{DR_j}{DR_{tot}}(\xi_j - \xi_{tot})^2}, \tag{2.5}$$

  where the index j refers to each of the N subsamples and the subscript tot to a measurement on the whole sample. The factor $\sqrt{1/(N-1)}$ should be changed to $\sqrt{1/N}$ of the the mean value ξ is known *a priori*, and not estimated from the sample (Press et al., 1986). The DR_j/DR_{tot} ratio weights each subsample depending on its size.

- Like in the previous case, by dividing the sample in separate regions, a variation of the jackknife error scheme can also be used (e.g. Scranton et al., 2002). Now, ξ is computed also N times, but in the whole sample, and removing one region each time, so that ξ is always computed in $N-1$ regions. The error is then be given by:

$$\Delta\xi = \sqrt{\frac{N-1}{N}\sum_{j=1}^{N}\frac{DR_j}{DR_{tot}}(\xi_j - \xi_{tot})^2} \tag{2.6}$$

  N being the total number of different regions and j referring to a measurement in the whole sample apart from the j subset. This error estimate suffers from the same drawback as the field-to-field errors.

- Bootstrap errors (Ling et al., 1986; Hoyle, 2000) are computed by determining ξ in several subsamples of the data. Suppose that we have measurements of ξ in N subsamples of the data. We can randomly select, with repetition, N of those subsamples and compute the average value of ξ from them. By repeating this procedure a large number of times (say, N'), we obtain a measurement of the error on the original ξ calculation, from the dispersion in our N' measurements.

- Another method of measuring the errors is to measure the correlation function in several different mock catalogues that mimic the number density of objects in the same volume and with a similar clustering amplitude. By combining the measurements of ξ in the different mocks, an estimate of the error on the measurements can be given from the dispersion of the results, also given by Eq,. 2.5. Now, N is the total number of mock catalogues, and j refers to each of these mocks. Although this is possibly the most complicated and robust method of measuring the errors, it has the disadvantage that it comes solely from mock catalogues. These have to match the true data very accurately. Even in this case, the mocks will not include all the information contained in the data. This can lead to deviations to the true error in the correlation function.

In the results presented in this chapter Poisson errors and N_q errors were considered, since at small scales the pairs are independent (Croom *et al.* 2001). At large scales, when the number of DD pairs exceeds the total number of QSOs in the survey, N_q are used, to correct for the correlation between the pairs. As shown by Hoyle (2000), these are in good agreement with the errors obtained with the other error estimates. Note that the correlation function estimates may be correlated bin-to-bin, but this will be quantified by means of covariance matrices, in the following sections.

2.4 The 2QZ redshift-space correlation function

The positions of the QSOs inferred from their observed redshift, using a certain cosmological model, are said to be measured in redshift-space (z-space). The motions of the QSOs in their local

rest-frame, due to their intrinsic velocity dispersion and coherent infall into their potential well, are superimposed in their systemic flow due to the Hubble expansion. Therefore, the measurements of QSO properties (such as their clustering) will be affected.

If the velocities of the QSOs were known, or if they were at rest in their local rest-frames, then their clustering would be measured in real-space. The difference between real- and z-space is due to the effects of the peculiar velocities of the QSOs, which can be due to the QSO small scale random motions, or the large-scale coherent infall into higher-density regions.

To convert the observed QSO redshifts into distances from the observer a cosmology must be assumed (Eq. 2.7). In the next two chapters two cosmologies will be assumed. The purposes of considering two different cosmologies are: **1)** to get a better handling of the data by measuring the clustering and comparing the effects of z-space distortions in the different cosmologies, **2)** to better visualise the effect of Ω_m^0 in our assumptions/results. Hence, we present our results using an Einstein-de Sitter ($\Omega_m^0 = 1.0$, $\Omega_\Lambda^0 = 0.0$) and a Λ cosmology ($\Omega_m^0 = 0.3$, $\Omega_\Lambda^0 = 0.7$), where Ω_m^0 is the ratio of matter density to the critical density. The superscript 0 indicates that it is the present value of Ω_m, at $z = 0$. Ω_Λ^0 is the energy density associated to the dark energy, here assumed to have the form of a cosmological constant ($p_\Lambda = -\rho_\Lambda$).

Let $D(z)$ be the distance to a QSO at redshift z. By combining the Robertson Walker metric with the Friedmann equation in a flat Universe, we have that:

$$D(z) = \frac{c}{H_0} \int_0^z \frac{dz'}{\sqrt{(1-\Omega_m^0) + \Omega_m^0 (1+z')^3}}, \tag{2.7}$$

In Fig.2.1 the z-space correlation function for the complete 2QZ catalogue is shown. The results obtained with the three different estimators presented are shown. These are self-consistent, within the errors. The errors are Poisson and N_q errors (see section 2.3.2). At small and intermediate scales, Poisson errors are computed, and N_q errors are computed when the number of DD pairs exceeds the total number of QSOs in the survey. Hoyle (2000) found that these two estimated give accurate estimates of the uncertainty in the 2QZ clustering measurements.

An obvious feature also noticeable in that plot is the non-power law shape of $\xi(s)$. This feature has been observed in several other surveys, like the 2dF Galaxy Survey – 2dFGRS – (Hawkins et al., 2003), or the Sloan Digital Sky Survey – SDSS - cluster catalogue (Basilakos and Plionis, 2004).

As demonstrated by Croom et al. (2005), the small scale flattening in the 2QZ $\xi(s)$ is not due to the fibre collisions of the 2dF instrument, which is unable to position two fibres at less than ~ 30 arcsec. The overlapping arrangement of the 2dF fields counterbalances that effect. In addition, it was found that the majority of QSO pairs at small angular separations actually have quite large radial separations, hence not affecting the shape of $\xi(s)$ at small scales.

Three factors determine the shape and amplitude of the 2QZ $\xi(s)$:

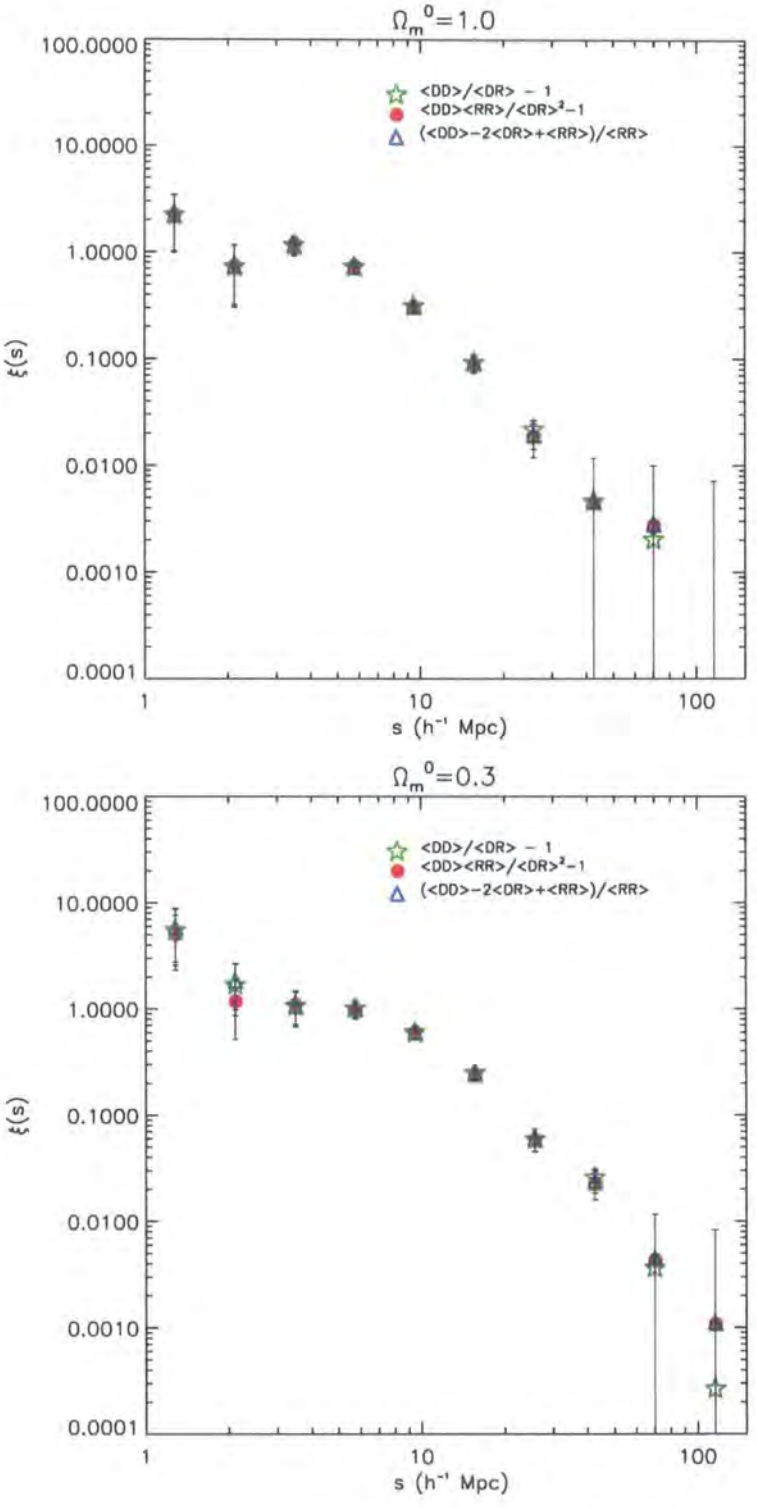

Figure 2.1: The redshift-space correlation function measured with the three different estimators. The Hamilton and the Landy-Szalay estimators give practically the same result at all scales, and there is a small discrepancy between these and Peebles' standard estimator, at large scales. However, even considering the scales where the results differ the most, they are all consistent within the errors.

- The growth of structure due to gravitational instabilities, and the initial spectrum of fluctuations,
- non-linear physics that occurs during QSO formation,
- z-space distortions due to peculiar the motions of the QSOs along the line of sight, at small scales, and due to the infall into the potential well caused by overdense regions, at large scales.

A more quantitative perception of the non-power shape of $\xi(s)$ is obtained by doing a χ^2 fit of a power-law model to $\xi(s)$. In Fig. 2.2 the best fitting power-law of $\xi(s)$ is shown. The estimator used for $\xi(s)$ is the Hamilton estimator.

The fit to the correlation function was made with a power-law model of the form $\xi(s) = \left(\frac{s}{s_0}\right)^{-\gamma}$. The best fitting values of s_0 and γ are indicated on Fig. 2.3, and tables 2.1 and 2.2.

	$\Omega_m^0 = 1.0$	$\Omega_m^0 = 0.3$
s_0	$3.2^{+0.2}_{-0.2}$	$4.5^{+0.2}_{-0.3}$
γ	$1.58^{+0.07}_{-0.06}$	$1.48^{+0.05}_{-0.07}$
χ^2_{min} (reduced)	6.52	5.78
d.o.f.	10	10

Table 2.1: The values of s_0 and γ from the best fitting power-law model to $\xi(s)$, for $1 \lesssim s \lesssim 100\, h^{-1}$Mpc (10 degrees of freedom, d.o.f.). Two explanations are possible to explain why the values of χ^2_{min} reduced are extremely large: either the errors are underestimated or the model is not a good representation of the data. A "visual" interpretation of the actual $\xi(s)$ models overploted with the data seems to suggest that the second hypothesis should be the most likely one.

	$\Omega_m^0 = 1.0$	$\Omega_m^0 = 0.3$
s_0	$5.3^{+0.2}_{-0.3}$	$6.5^{+0.3}_{-0.4}$
γ	$2.31^{+0.14}_{-0.16}$	$1.89^{+0.11}_{-0.13}$
χ^2_{min} (reduced)	1.23	3.15
d.o.f.	5	5

Table 2.2: The values of s_0 and γ from the best fitting power-law model to $\xi(s)$, considering only the points between $5 - 50\ h^{-1}$Mpc. For "common" values for the velocity dispersion of the QSOs, only the growth of gravitational instabilities and other processes in the formation of the QSOs should determine the shape of the correlation function, on these scales. The values of χ^2_{min} tend to suggest that a power-law model might still not be a very suitable model for the correlation function.

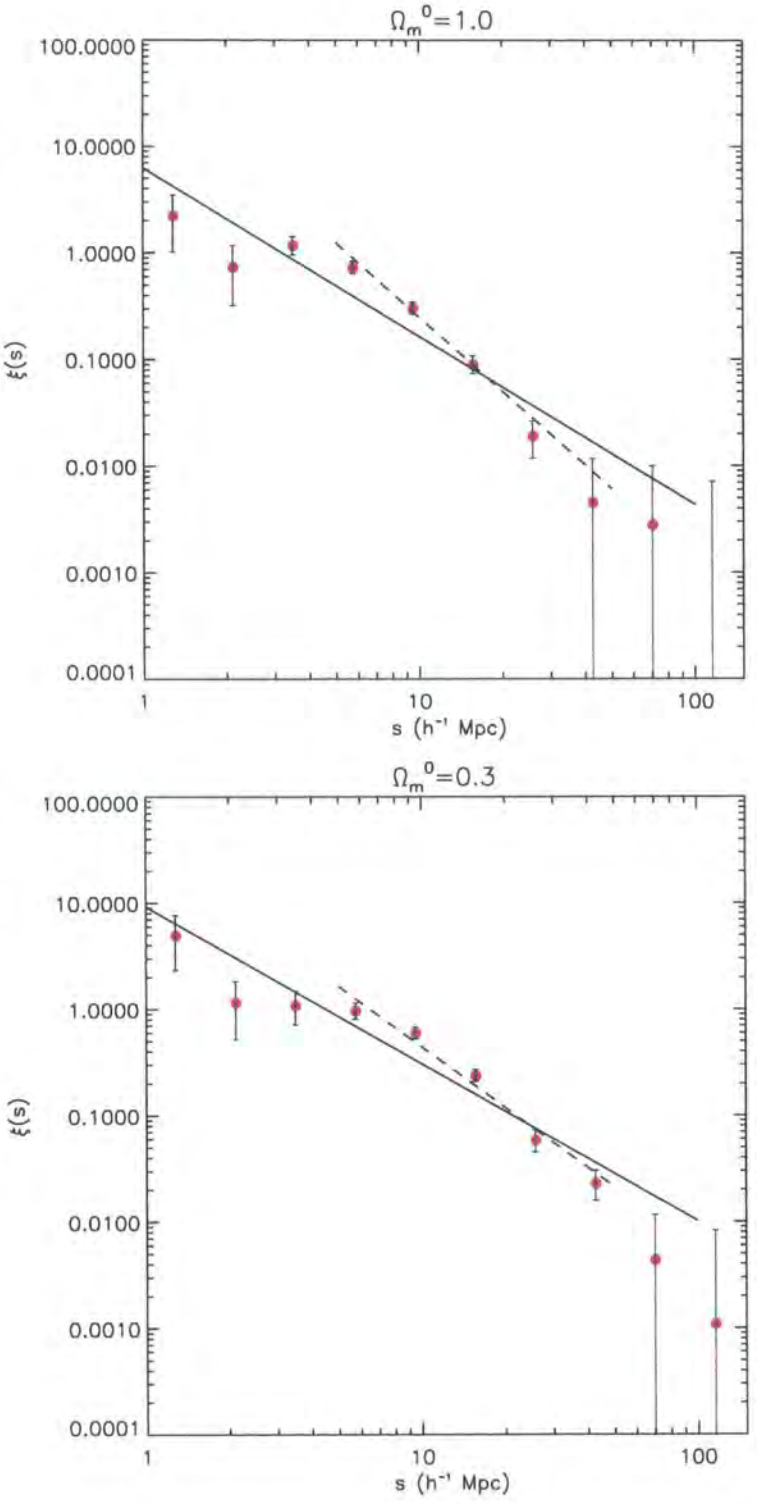

Figure 2.2: The 2QZ $\xi(s)$, measured using the Hamilton estimator for QSOs in the redshift interval $0.3 < z < 2.2$. On top is $\xi(s)$ assuming $\Omega_m^0 = 1.0$ and on bottom assuming $\Omega_m^0 = 0.3$. The solid line represents the best fitting power-law for $1 < s < 100\,h^{-1}$Mpc. The dashed line is the best fitting power-law in the range $5 - 50\ h^{-1}$Mpc.

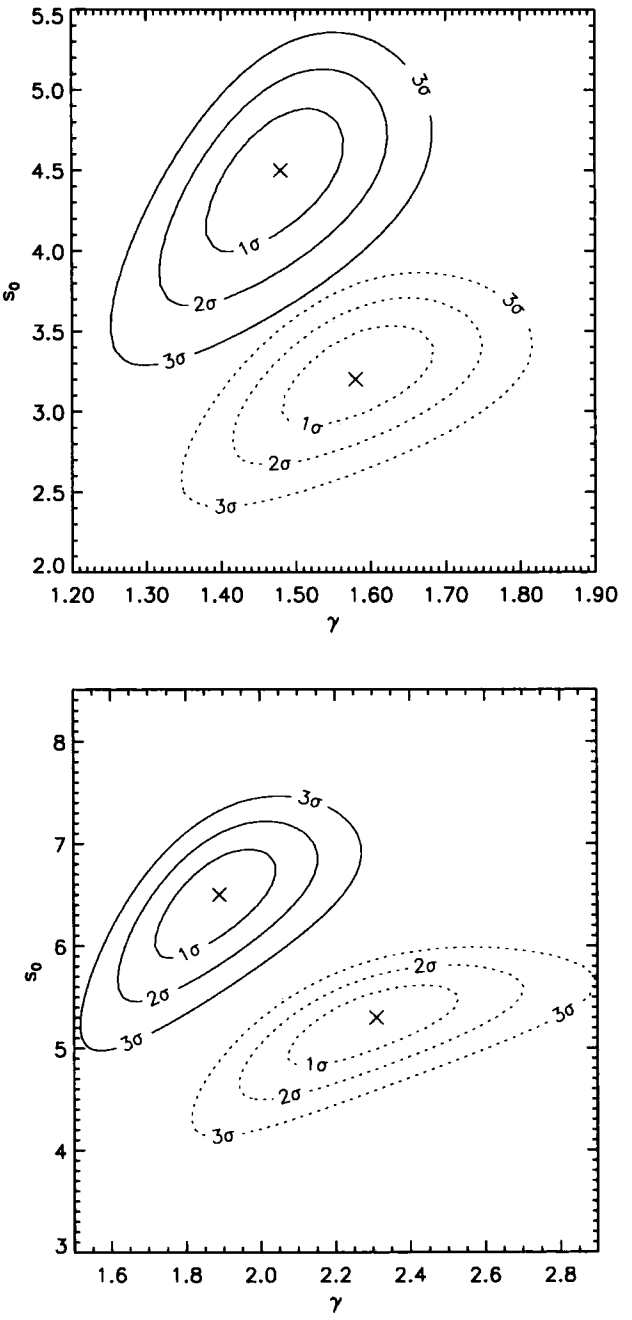

Figure 2.3: The best fitting values of s_0 and γ and the respective 2-parameter confidence levels obtained when fitting a model of the form $\left(\frac{s}{s_0}\right)^{-\gamma}$ to $\xi(s)$. On the contour plot on the top, the results refer to the confidence levels obtained when fitting the model to all scales $< 100\ h^{-1}$Mpc, and on the bottom to scales where $5 < s < 50\ h^{-1}$Mpc. The solid contour lines represent the results from fitting the function measured with an assumed value for Ω_m^0 of 0.3, and the dotted line for Ω_m^0 of 1.0. The best fitting pairs of values $[s_0, \gamma]$ are indicated with $\times$. These plots do not represent the "goodness" of the fit for the best fitting parameters. This can only be shown by the comparison of the χ^2_{min} with the number of degrees of freedom, i.e., the χ^2_{min} reduced.

The values of the χ^2_{min} reduced (χ^2_{min}/d.o.f.) indicate that the power-law model for $\xi(s)$ is not the most appropriate one. One other possibility would be that the Poisson errors are not correct. However, Hoyle (2000) compared different $\xi(r)$ error estimates from $\sim$ 10000 2dF QSOs, and found that Poisson errors should give a plausible error estimate at least until large scales, where N_q errors would be more reliable.

The error bars can also underestimate of the true error on ξ if the pairs in different bins are correlated. In this case, Poisson statistics are not a suitable estimate of the uncertainty on the $\xi(s)$ measurements. In order to determine if this is the case, we can compute the *covariance matrix*, which represents the statistical correlation between different bins. The *correlation matrix* compares the terms of the covariance matrix with the errors on each individual bin. If different bins are uncorrelated, or very weakly correlated, then the *covariance* between them should be much smaller than the errors on the ξ measurements on those bins.

To determine the correlation matrix, one can first divide the QSO sample into N regions, with similar QSO numbers, and compute $\xi(s)$ in each of those regions. The *covariance matrix* is given by:

$$Cov(i,j) = \frac{1}{N}\sum_{k=1}^{N}\left(\xi_k(s_i) - \bar{\xi}(s_i)\right)\left(\xi_k(s_j) - \bar{\xi}(s_j)\right) \tag{2.8}$$

where $\bar{\xi}(s)$ is the average value of $\xi(s)$ in the N regions, i.e., the actual $\xi(s)$ value measured from the whole quasar sample.

To obtain the *correlation matrix* we only have to divide each matrix element by the product of the errors on $\bar{\xi}(s_{i,j})$ in the separation bins corresponding to that matrix element (i,j):

$$Corr(i,j) = \frac{Cov(i,j)}{\Delta\bar{\xi}(s_i)\Delta\bar{\xi}(s_j)} \tag{2.9}$$

Therefore, if the separation bins i and j are totally correlated, we will have that $Corr(i,j) = 1$; and if they are strongly anti-correlated, that correlation matrix element will bed close to -1. Ideally, we would like that $Corr(i,j) \approx 0$, for all $i \neq j$.

Fig. 2.4 shows the correlation matrix measured for the 2QZ $\xi(s)$. We computed $Corr(i,j)$ using Eq. 2.9, and split the 2QZ sample in 30 subregions. Naturally, the matrix is symmetric and the diagonal values are 1. We can see that the separation bins are actually not very strongly correlated; adjacent bins, in particular, show a correlation usually no larger than 0.1, in absolute value, supporting the hypothesis that the Poisson formula is probably a suitable estimate of the 2QZ $\xi(s)$ errors. In addition, we have re-computed the best fitting values of s_0 and γ but taking into account the bin covariance, and compared these with the values shown in Fig. 2.3. In order to take the covariance between bins into account, the χ^2 is computed through:

$$\chi^2 = \sum_{i,j}(\xi_i^m - \xi_i^d)Corr_{ij}^{-1}(\xi_j^m - \xi_j^d)^T \tag{2.10}$$

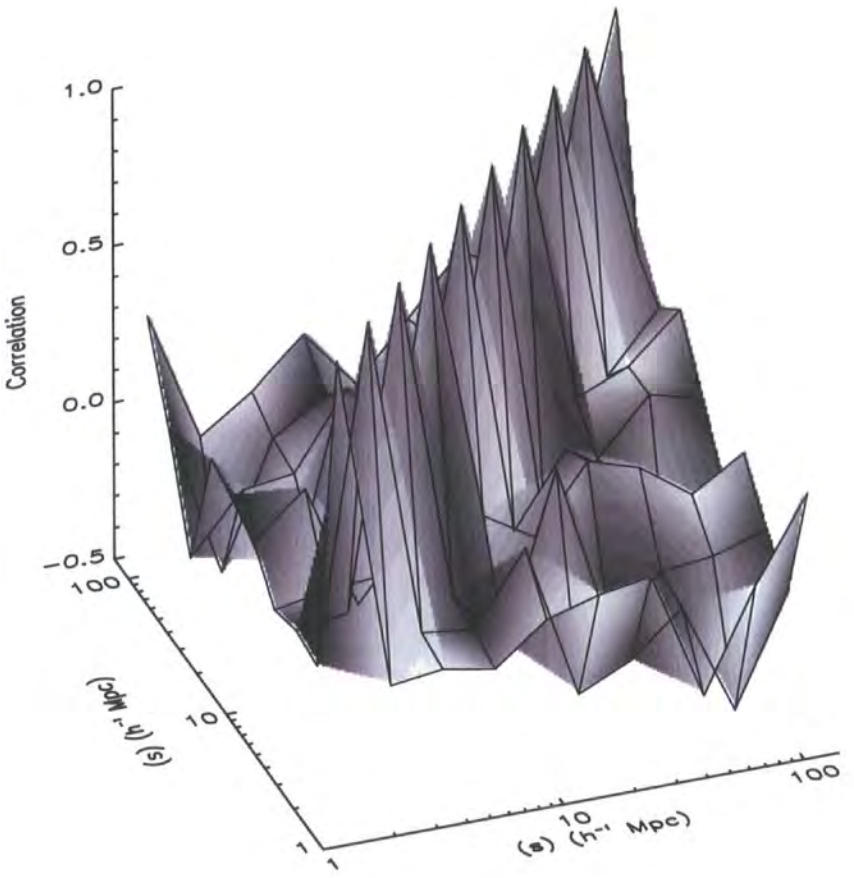

Figure 2.4: The $\xi(s)$ correlation matrix. Naturally, the diagonal elements are 1. It can be seen that the off-diagonal matrix elements are much smaller,indicating a weak correlation between $\xi(s)$ bins.

where $Corr_{ij}^{-1}$ is the inverse of the covariance matrix, ξ^d the data measurements of $\xi(s)$, ξ^m is the model for $\xi(s)$, here given by $\xi(s) = (s/s_0)^{-\gamma}$.

Fig 2.5 shows the effect of taking into account the covariance matrix in our fits, for a $\Omega_m^0 = 0.3$ cosmology. The top panel refers to the contours obtained when fitting $\xi(s)$ with $1 < s < 100\,h^{-1}$Mpc, where the bottom panel represents the contours for $5 < s < 50\,h^{-1}$Mpc. The solid contours are the same as those in Fig. 2.3, and represent the best fitting values for s_0 and γ, when a $\Omega_m^0 = 0.3$ cosmology is assumed. The dotted contours are now the same contraints once we take into account the covariance between bins and use Eq. 2.10 to compute the best fitting model. It can be seen that the "change" of the contours is small, given associated errors, and the shift between the best fitting cases is of the order of $\sim 1\sigma$.

To measure and explain the deviations from a simple power-law $\xi(s)$ model, the real-space correlation function of the 2QZ must be measured. The best way to estimate it is from the projected correlation function, which is free of z-space distortions due to line-of-sight peculiar velocity components.

2.5 A coherent picture of the QSO clustering

Studying the real-space clustering of the QSOs is, in itself, a subject of obvious interest: it allows the direct study of QSO clustering and its bias relative to the underlying dark matter distribution, providing a picture of how the formation and evolution of QSOs take place. Nevertheless, our motivation for studying $\xi(r)$ also includes the need for an adequate and trustworthy amplitude input for modelling z-space distortions, in the next chapter. Comparing the distortions in the clustering measured along and across the line-of-sight will allow the measurement of cosmological and z-space distortion parameters (chapter 3).

Let the separations along and across the line of sight be defined as:

$$\pi = |s_2 - s_1| \tag{2.11}$$

$$\sigma = \frac{(s_1 + s_2)}{2}\theta \tag{2.12}$$

where s_1 and s_2 are the distances to two different QSOs, measured in z-space, and θ the angular separation between them. See Fig. 2.6 for a visual representation.

Since the effects of z-space distortions are purely radial, the real-space clustering can be inferred from the projection of $\xi(\sigma, \pi)$ along the σ direction[1]. The projected correlation function is obtained by integrating $\xi(\sigma, \pi)$ along the π direction (Peebles, 1980):

$$w_p(\sigma) = 2\int_0^\infty \xi(\sigma, \pi) d\pi \tag{2.13}$$

When implementing this integration it must be truncated at some value π_{cut}, where ξ becomes negligible. If very large scales are included, the signal amplitude will become dominated by noise.

[1] $\xi(\sigma, \pi)$ will be considered in detail in Chapter 3

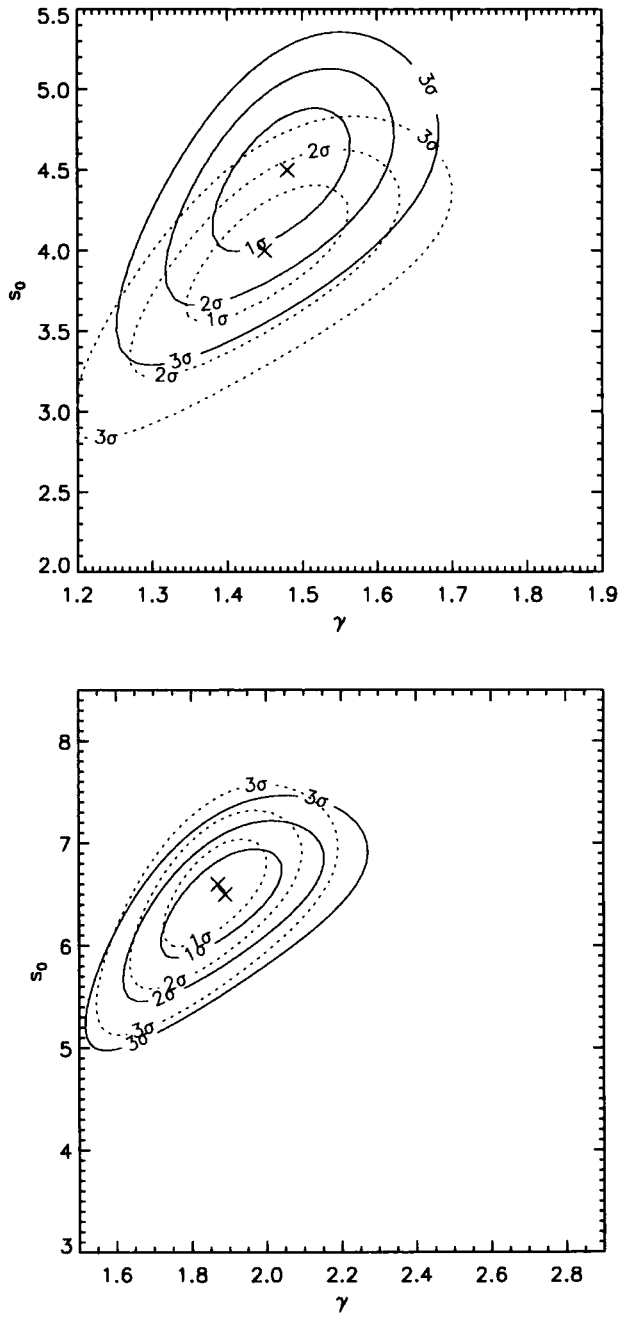

Figure 2.5: The best fitting values of s_0 and γ and 2-parameter confidence levels. The contour plot on the top shows the confidence levels obtained when fitting the model for $1 < s < 100\ h^{-1}$Mpc, and the bottom one for $5 < s < 50\ h^{-1}$Mpc. The solid contours are the same as in Fig 2.3, and represent the results for $\Omega_m^0 = 0.3$. The dotted lines shows the shift in those contours, once we take into account the covariance between bins. It can be seen that these shifts are small, whitin the errors.

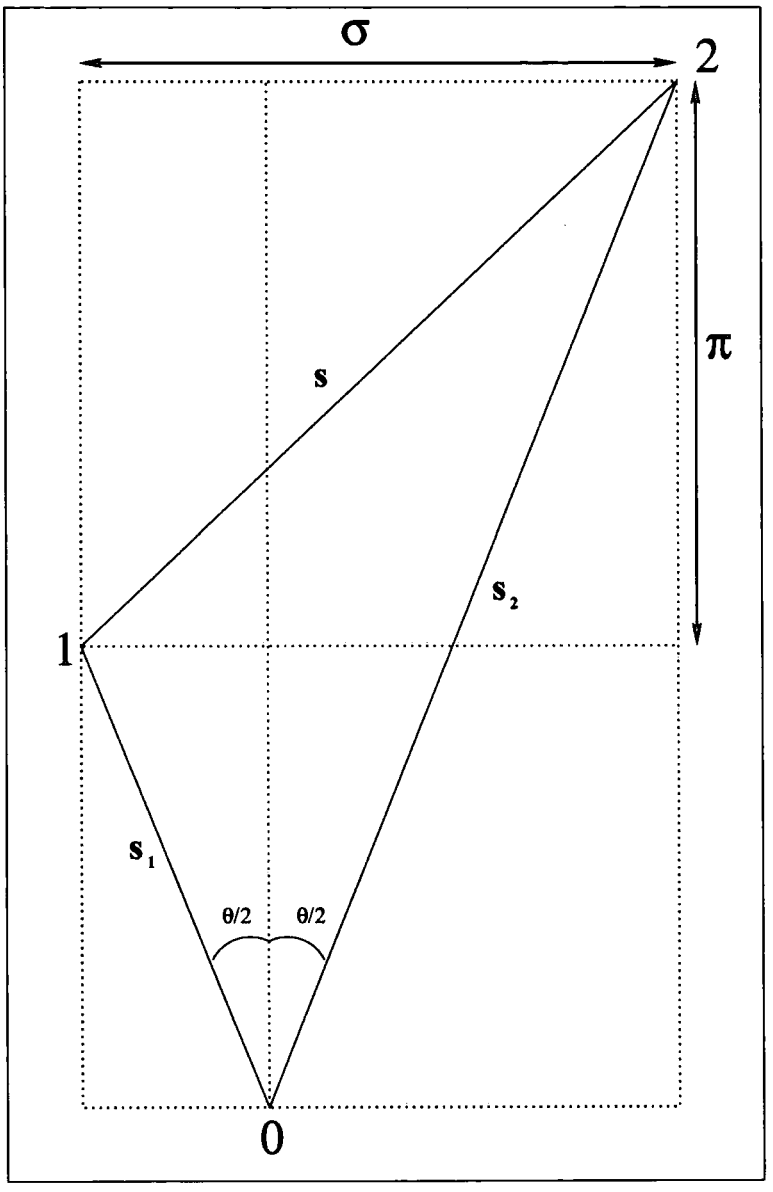

Figure 2.6: The definitions of σ and π: s_1 and s_2 are the distances in redshift-space from the observer at 0 to the QSOs at 1 and 2, respectively. s is the redshift-space separation between the two. The projection of s in the directions along and across the line-of-sight gives π and σ.

On the other hand, if the integral is only performed at very small scales, then the projected correlation function will be systematically underestimated. It was found that, in the present survey, the results did not seem sensitive to π_{cut} values around 70 h^{-1}Mpc, which was the value used. Therefore:

$$w_p(\sigma) = 2 \int_0^{\pi_{cut}} \xi(\sigma, \pi) d\pi \tag{2.14}$$

Fig. 2.7 shows $w_p(\sigma)/\sigma$ measured with the three different estimators. The error bars show Poisson and N_q errors.

In Fig. 2.8 we show the effect of taking different values for π_{cut}. It can be seen that the $w_p(\sigma)$ measurements are stable for π_{cut} close to $\sim 70\,h^{-1}$Mpc. Larger values of the upper integration limit may introduce noise, whereas taking too low a value for π_{cut} may lead to underestimate the clustering power, especially at large scales.

Since $w_p(\sigma)$ describes the clustering in real-space, the integral in equation 2.13 can be written in terms of the real-space correlation function $\xi(r)$ (Davis and Peebles, 1983):

$$w_p(\sigma) = 2 \int_\sigma^\infty \frac{r\xi(r)}{\sqrt{r^2 - \sigma^2}} dr \tag{2.15}$$

If $\xi(r)$ is well described by a power-law model, then the integral can be solved analytically and it follows that:

$$w_p(\sigma) = r_0^\gamma \sigma^{1-\gamma} \left(\frac{\Gamma\left(\frac{1}{2}\right) \Gamma\left(\frac{\gamma-1}{2}\right)}{\Gamma\left(\frac{\gamma}{2}\right)} \right), \tag{2.16}$$

where $\Gamma(x)$ is the Gamma function computed at x.

Therefore, if the real-space correlation function $\xi(r)$ is well approximated by a power-law, then its slope will be the same as in $w_p(\sigma)/\sigma$, and its amplitude proportional to the $w_p(\sigma)/\sigma$ amplitude. Fig. 2.9 shows $w_p(\sigma)/\sigma$ measured from the 2QZ catalogue. The error bars represent Poisson errors. The solid line is the best fitting power-law to the data points.

The range used is $1 < \sigma < 25\,h^{-1}$Mpc, assuming EdS, and $1.2 < \sigma < 30\,h^{-1}$Mpc, assuming Λ. The corresponding best fitting values of r_0 and γ are summarised in Table 2.3. The errors on these parameters can be inferred from the confidence levels in the [r_0,γ] plane, shown in Fig. 2.10. The close-to-unit values of the reduced χ^2 indicate that the power-law prediction for $\xi(r)$ corresponds to a reasonable description of $w_p(\sigma)$ within the limited range it was fitted. If EdS is assumed, then the best fitting $\xi(r)$ power-law model has the form: $(r/3.77)^{-2.09}$, while if Λ is assumed instead, the best fitting power-law model is: $\xi(r) = (r/4.96)^{-1.85}$. The value of $w_p(\sigma)$ at the largest scales indicates some deviation from the best-fitting power-law model, at scales larger than the ones used in the fit; the $w_p(\sigma)$ clustering amplitude is lower than predicted from the best-fitting model, for $\sigma \gtrsim 30\,h^{-1}$Mpc.

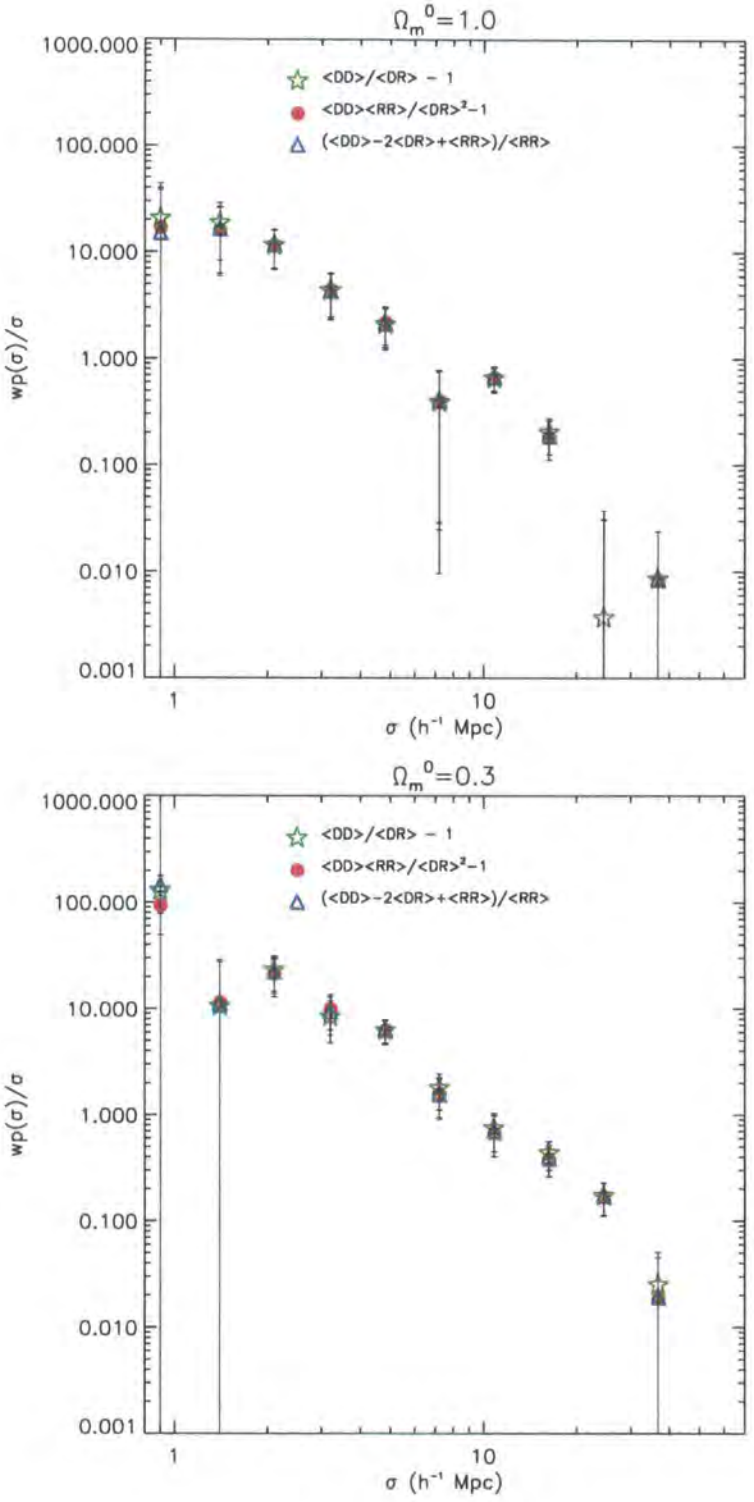

Figure 2.7: The projected correlation function measured with the three different estimators. They all give practically the same result at intermediate scales, apart from small discrepancies at small and large scales. These, however, are still included in the errors.

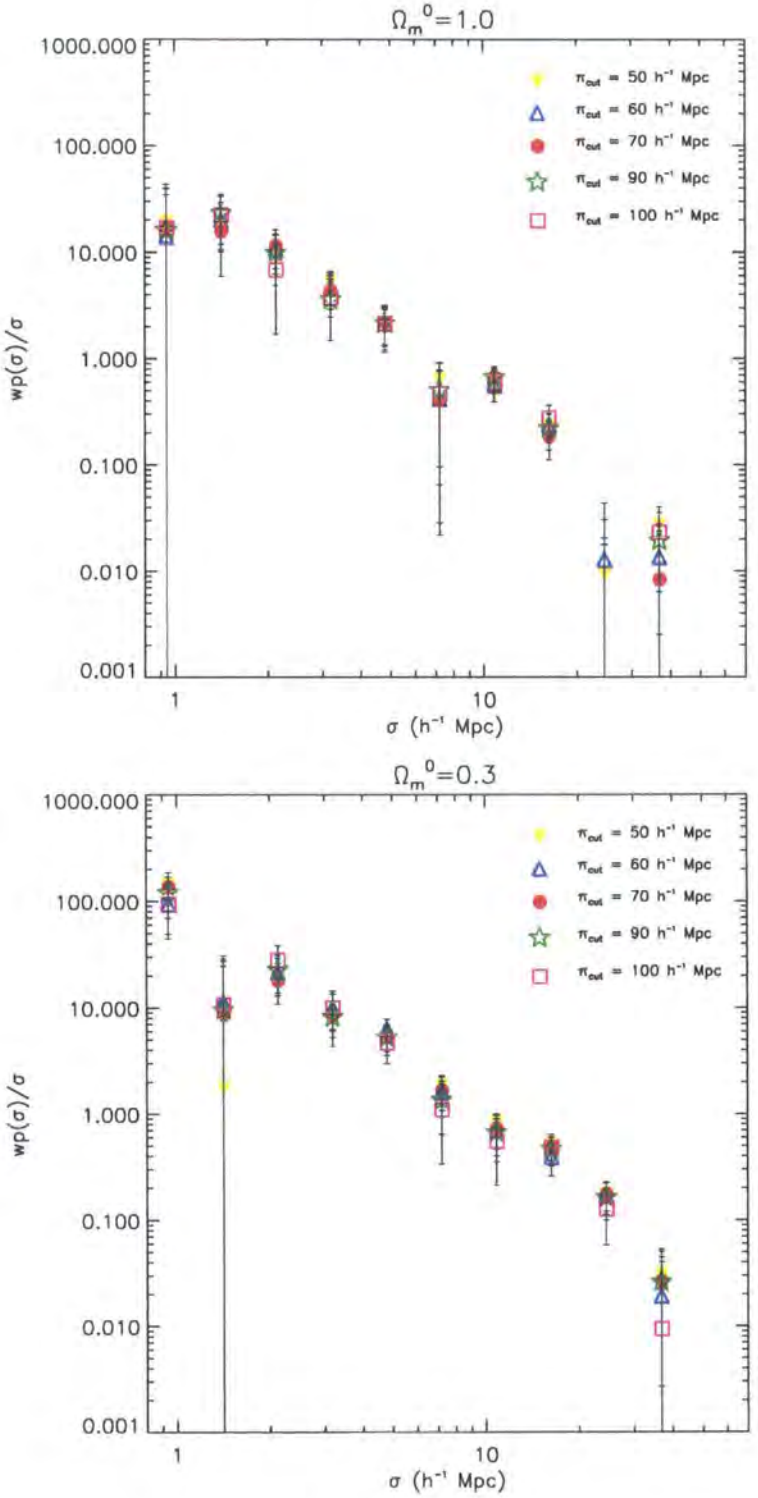

Figure 2.8: The projected correlation function for different valus of π_{cut}. One can see that the results are considerably stable for different values of π_{cut}, close to 70 h^{-1}Mpc, which was the value used.

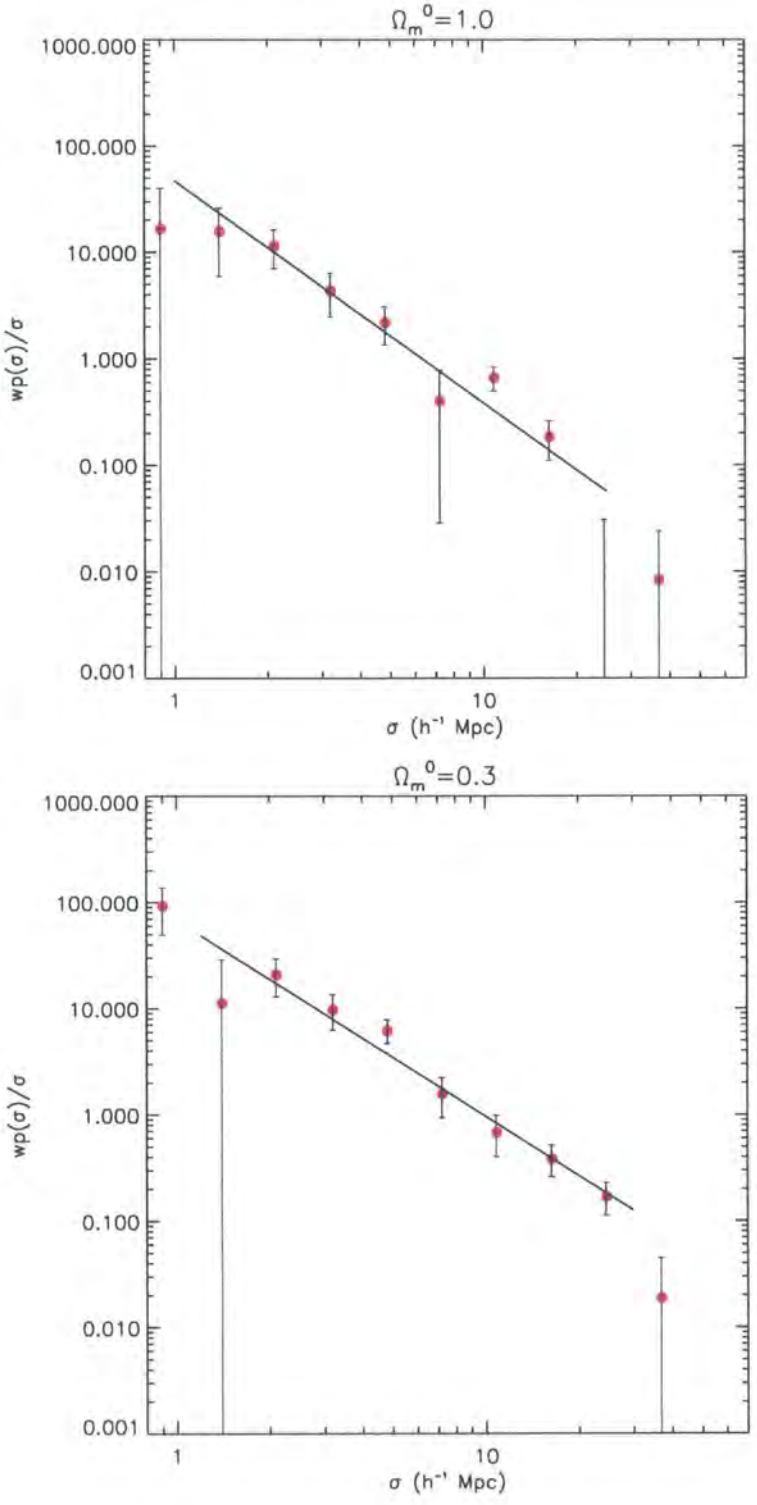

Figure 2.9: The projected correlation function measured with the Hamilton estimator and the best fitting power-law. The top panel shows the case where EdS was assumed, and the bottom panel the result assuming Λ. The solid lines represent the best fitting power-laws, that correspond to $\xi(r) = (r/3.77)^{-2.09}$ assuming EdS and $\xi(r) = (r/4.96)^{-1.85}$ assuming Λ.

	$\Omega_m^0 = 1.0$	$\Omega_m^0 = 0.3$
r_0 (h^{-1}Mpc)	$3.77^{+0.33}_{-0.47}$	$4.96^{+0.54}_{-0.56}$
γ	$2.09^{+0.21}_{-0.22}$	$1.85^{+0.13}_{-0.10}$
χ^2_{min} (reduced)	1.61	0.93
d.o.f.	6	6

Table 2.3: The values of r_0 and γ from the best fitting power-law model to $w_p(\sigma)/\sigma$, for 6 degrees of freedom (d.o.f.), corresponding to the solid lines on Fig. 2.9. If the EdS model is assumed to convert the redshifts to distances, the fit is performed between $1\,h^{-1}$Mpc and $25\,h^{-1}$Mpc. When assuming the Λ cosmology the range $1.2 < \sigma < 30\,h^{-1}$Mpc was taken.

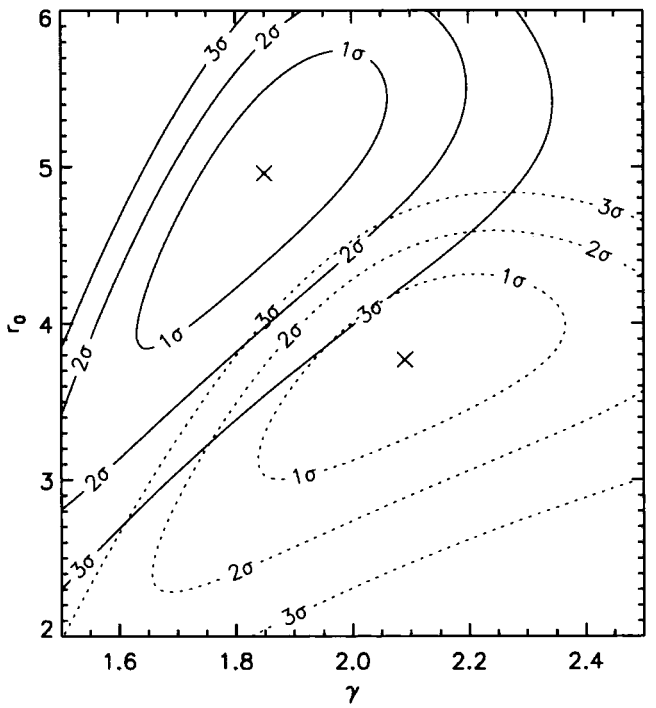

Figure 2.10: The best fitting values of r_0 and γ and the respective two-parameter confidence levels obtained when fitting a model of the form $r_0^\gamma \sigma^{1-\gamma} \left(\frac{\Gamma(\frac{1}{2})\Gamma(\frac{\gamma-1}{2})}{\Gamma(\frac{\gamma}{2})} \right)$ to $w_p(\sigma)$. The solid contour lines represent the results from fitting the function obtained assuming Λ, and the dotted line for the EdS cosmology. The best fitting pairs of values $[r_0, \gamma]$ are indicated with $\times$.

2.5.1 Does a single power-law $\xi(r)$ model explain both the $w_p(\sigma)$ and $\xi(s)$ results?

The simplest explanation to account for the different slope of $\xi(s)$ at $1 \lesssim s \lesssim 10\,h^{-1}$Mpc, compared to the slope at larger scales, is the effect of z-space distortions. The small-scale random motions of the QSOs lead to a deficit of clustering amplitude measured at scales $\lesssim 10\,h^{-1}$Mpc. In addition to this effect, the $\xi(s)$ clustering amplitude on large scales is affected by the infall of QSOs into the overdense regions.

According to linear theory, the relation between $\xi(s)$ and $\xi(r)$ is simply given by Kaiser (1987):

$$\xi(r) = \frac{\xi(s)}{1 + \frac{2}{3}\beta(z) + \frac{1}{5}\beta(z)^2}, \tag{2.17}$$

where $\beta \approx \Omega_m^{0.6}/b$.

Therefore, the ratio between the z- and real-space correlation functions gives an estimate of the infall parameter $\beta(z = 1.4)$ which, for a given cosmology, allows the determination of the bias b.

With the current data, it is not trivial to find the real-space correlation function without making some assumptions. Inversion methods of $w_p(\sigma)$ like the ones described by Saunders et al. (1992) or Ratcliffe (1996) are not feasible with this survey, as the low QSO space density would cause the errors associated with $\xi(r)$ to be extremely large.

If we approximate $\xi(r)$ by a single power-law, then the best fitting power law $w_p(\sigma)$ model can be used to constrain $\beta(z = 1.4)$. This can be done by computing the ratio between the measured values for $\xi(s)$ and the values our $\xi(r)$ model takes, at large scales. Fig. 2.11 shows the ratio $\xi(s)/\xi(r)$ as a function of separation. For a given value of the separation, the error on $\xi(s)$ can be quantified using the Poisson estimate. The uncertainty in the $\xi(r)$ model is determined from that in the parameters r_0 and γ. However, as these parameters are correlated (see contours in Fig. 2.10), the value found underestimates the true uncertainty. We therefore rescale the error in $\xi(r)$ by comparison with the $\xi(s)$ Poisson errors. We assume that the relation between the true $\xi(r)$ error and the one obtained with this method is the same as for $\xi(s)$, for which we already have Poisson/N_q errors and are also able to compute them as we have done for $\xi(r)$. To estimate the error in the ratio $\xi(s)/\xi(r)$, we then add in quadrature the error in $\xi(r)$ and the Poisson errors in $\xi(s)$. The dashed line in Fig. 2.11 shows the best fitting $\xi(s)/\xi(r)$ value at scales larger then 10 h^{-1}Mpc, and the shaded region is the 1 σ confidence interval in the fit. The best fit produces $\beta(z = 1.4) = 0.87^{+0.30}_{-0.31}$. At scales $\gtrsim 10\,h^{-1}$Mpc, non-linear effects due to peculiar velocities have a negligible effect and the z-space contribution comes only from the gravitational infall quantified by $\beta(z)$. This value of $\beta(z = 1.4)$ is larger than other results also from the 2QZ survey, found by Hoyle et al. (2002) and Outram et al. (2004). We should point out that, using single power-law fits to the $w_p(\sigma)$ result of the 2dF Galaxy Redshift Survey (2dFGRS; Hawkins *et al.* 2003) also gives high values of β from computing $\xi(s)/\xi(r)$.

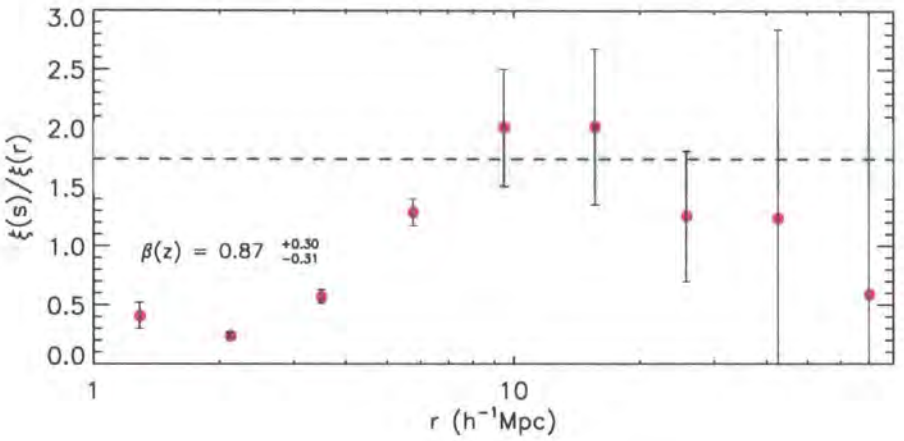

Figure 2.11: $\xi(s)/\xi(r)$ measured from the 2QZ survey, taking the measured $\xi(s)$ values and the single power-law $\xi(r)$ model derived, assuming Λ. See text for a full description of how the errors are computed. The fit to the function was performed on scales where the z-space distortions are only affected by the large-scale infall and are not contaminated by random peculiar motions of the QSOs. The dashed line and the shaded region represent this best fit and its 1 σ confidence level. This fit corresponds to a value of $\beta(z = 1.4) = 0.87^{+0.30}_{-0.31}$.

A model for $\xi(s)$ can then be constructed by decomposing the separation in σ and π and adding the z-space distortions in $\xi(\sigma, \pi)$. Then, in order to obtain $\xi(s)$, $\xi(\sigma, \pi)$ is averaged in annuli of constant $s = \sqrt{\sigma^2 + \pi^2}$. The model used to compute $\xi(\sigma, \pi)$ is discussed in Section 3.3.1. Fig. 2.12 shows the comparison of $\xi(s)$ models with the 2QZ $\xi(s)$. The circles in the plot show the 2QZ $\xi(s)$, assuming the Λ cosmology. The dotted line shows the input $\xi(r)$ model, which is the best-fitting power-law to the $w_p(\sigma)$. Note that this model lies well below the observed $\xi(s)$ at all values $s \gtrsim 10\, h^{-1}$Mpc. The dashed line represents that same power-law, scaled using equation 2.17, taking the value of $\beta(z) = 0.87$ to quantify the effect of the linear z-space distortions. Including the distortions due to small scale pairwise velocity dispersion of the QSOs, will lead to the solid or the dash-dotted lines. The solid line shows the effect of small-scale peculiar velocity dispersion $< w_z^2 >^{1/2} = 800$ km s^{-1} where the intrinsic QSO velocity dispersion is assumed to be dominated by the effect of redshift measurement errors (Outram et al., 2003; Croom et al., 2005). The effect of a larger velocity dispersion of 1500 km s^{-1} is shown as the dash-dotted line.

It can be seen that the value of 800 km s^{-1} for the velocity dispersion gives an adequate fit to the data in the $s \lesssim 10$ h^{-1}Mpc region; the tendency of this model to overestimate the points at $2 \lesssim s \lesssim 4$ h^{-1}Mpc is not resolved by moving to a bigger velocity dispersion which is seen to degrade the fit at $s \approx 10$ h^{-1}Mpc. Although the χ^2 is acceptable, the slope of $\xi(s)$ at $s \gtrsim 10$ h^{-1}Mpc is steeper than the single power-law model derived from $w_p(\sigma)$. It proved impossible to increase the slope in $\xi(r)$ in this range while maintaining an acceptable fit to $\xi(s)$. We therefore observe that a simple single power law model is not entirely an adequate description of the z-space measurements.

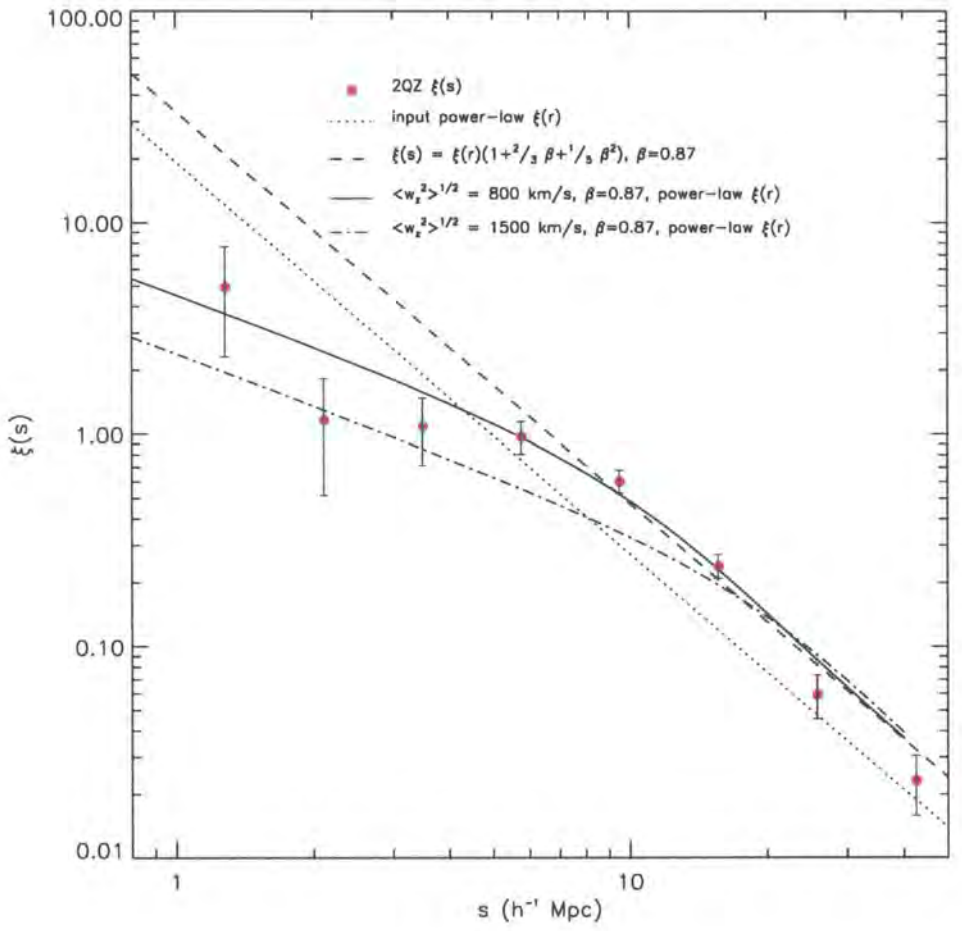

Figure 2.12: The circles show the measured $\xi(s)$ from the 2QZ, assuming Λ. The dotted line is the best fit single power-law $\xi(r)$ model to $w_p(\sigma)$. The dashed line is the same model scaled to account for the linear bias ($\beta(z) = 0.87$). The solid and dash-dotted lines also include the small-scale peculiar velocities with velocity dispersion of the order $< w_z^2 >^{1/2} = 800\,\mathrm{km\,s^{-1}}$ and $< w_z^2 >^{1/2} = 1500\,\mathrm{km\,s^{-1}}$, respectively.

This tendency of single-power law $\xi(r)$ models to give poor fits to $\xi(s)$ has been seen in previous galaxy redshift surveys such as Durham/UKST (Ratcliffe et al., 1998) and more recently in the 2dFGRS (Hawkins et al., 2003), where a non-power-law shoulder is seen rising above the small-scale power-law at $s \approx 10\ h^{-1}$Mpc, before steepening again at larger scales.

2.5.2 A double power-law $\xi(r)$ model: another explanation of the $w_p(\sigma)$ and $\xi(s)$ results

Hawkins et al. (2003) presented the correlation function analyses of the 2dFGRS, both in real- and z-space. Including data from 166000 galaxies with a mean redshift of $z \approx 0.11$, this study has a statistical weight significantly higher than the 2QZ. By inverting the projected correlation function, they found that the slope of the real-space correlation function of the 2dF galaxies varies with scale. In order to quantify the change in slope as a function of scale, we re-fitted their $\xi(r)$ data. At scales $\lesssim 1\,h^{-1}$Mpc the shape is similar to the commonly observed $\gamma \approx 1.8$ small-scales slope (Peebles, 1974a). However, at intermediate scales ($1 - 10\,h^{-1}$Mpc), which are accessible with the 2QZ survey, the $\xi(r)$ data is fitted by a shallower $\gamma = 1.45$ power-law, while at larger scales the correlation function is again steeper. Motivated by these results we now assess if the addition of a break in the $\xi(r)$ shape at $\sim 10\,h^{-1}$Mpc can still provide a good description of the QSO $w_p(\sigma)$ and $\xi(s)$ results, whilst accounting for the issues discussed in the previous section.

We thus perform a new parametric fit to $w_p(\sigma)$, considering a double power-law $\xi(r)$ model with a break at $10\,h^{-1}$Mpc (for the Λ cosmology). Then, for a grid of parameters that characterise the slope and amplitude of the power-laws, we project the functions describing $\xi(r)$ using equation 2.15 to get the respective $w_p(\sigma)$. The best fitting model is found by performing a χ^2 fit. The results are shown in Fig. 2.13. The value used for the upper limit of the integral in equation 2.15 was computed from the π_{cut} value used in equation 2.14, to determine $w_p(\sigma)$ from the data.

The top plot shows the best fitting $\xi(r)$ model to $w_p(\sigma)$ (solid line). The parameters that describe the two power laws are: for scales $r < 10\ h^{-1}$Mpc, $r_0 = 6.0^{+0.5}_{-0.6}\ h^{-1}$Mpc and $\gamma = 1.45^{+0.27}_{-0.27}$; for $r > 10\ h^{-1}$Mpc, $r_0 = 7.25\ h^{-1}$Mpc and $\gamma = 2.30^{+0.12}_{-0.03}$. The fit is performed in the range $1.0 < \sigma < 40\,h^{-1}$Mpc. We fit the slope and amplitude of the two power-laws, keeping the break between the two-power laws at $10\,h^{-1}$Mpc and ensuring that the function is continuous across the break. The reduced χ^2_{min} of this fit is 0.89 (6 d.o.f.). The bottom plot is the measured 2QZ $w_p(\sigma)/\sigma$ overploted on the projection of the best fitting $\xi(r)$ model (solid line).

This model is in very good agreement with the 2dFGRS $\xi(r)$ data, especially with the slope at intermediate scales ($1 \lesssim r \lesssim 10\,h^{-1}$Mpc). Again, we point out that with the current data we do not have enough signal at scales $\lesssim 1\,h^{-1}$Mpc, so unfortunately we can not assess whether the 2QZ $\xi(r)$ steepens at small scales, as seen in the 2dFGRS data.

These results also show that possible deviations from a power-law $\xi(r)$ in the 2QZ are such that they do not become evident after being projected along the σ direction.

The determination of β assuming the double power-law $\xi(r)$ model can be done as described

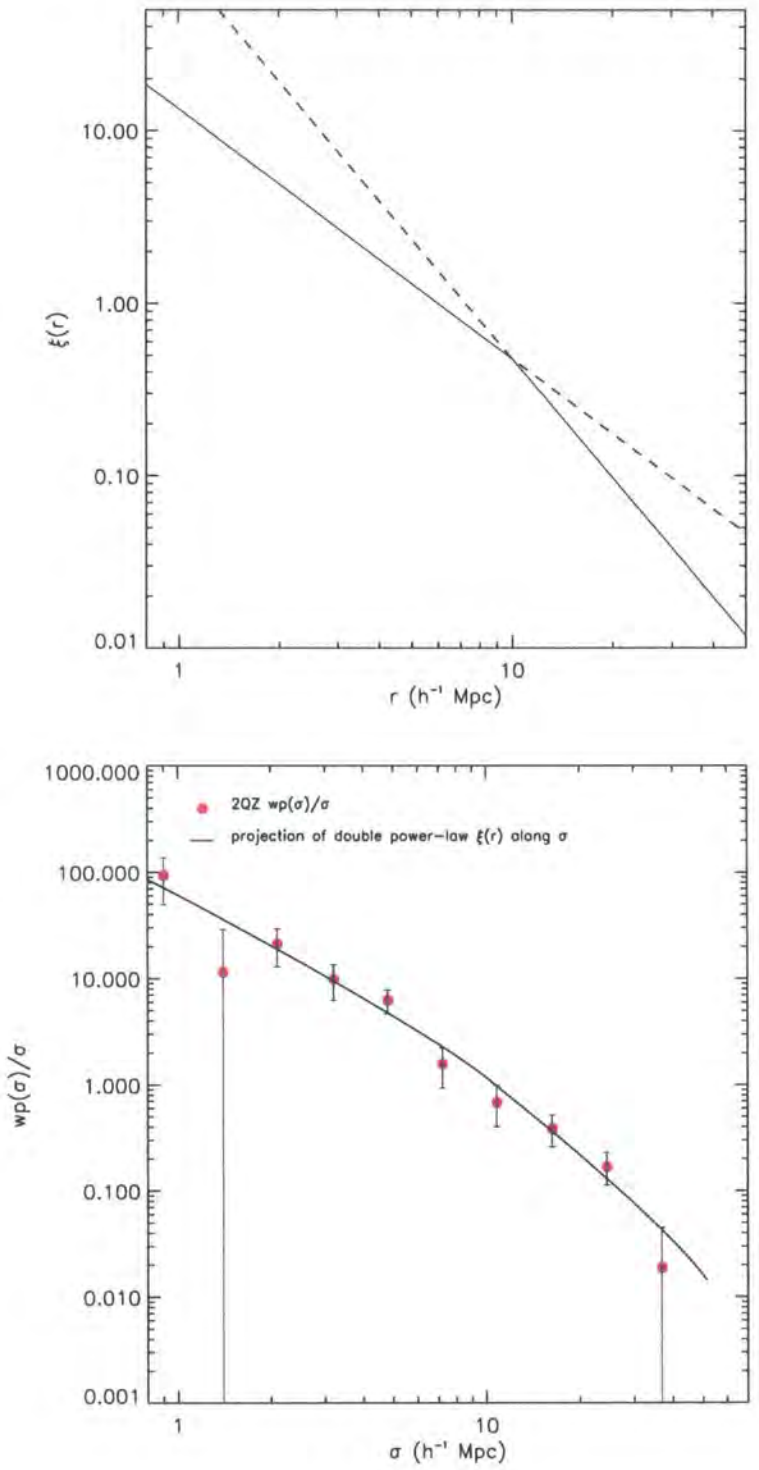

Figure 2.13: The top plot shows the best fitting two power-law $\xi(r)$ model to the $w_p(\sigma)$ data, assuming the Λ cosmology (solid line). For scales $r < 10\,h^{-1}$Mpc, the power-law has the form: $\xi(r) = (r/6.0)^{-1.45}$, while for scales $r > 10\,h^{-1}$Mpc, it has the form $\xi(r) = (r/7.25)^{-2.30}$. The dashed lines show the extrapolation of the two power-laws to small and large scales. On the bottom, the plot shows $w_p(\sigma)/\sigma$ as measured from the data (circles), overploted on the projection of the $\xi(r)$ model from the top panel (solid line).

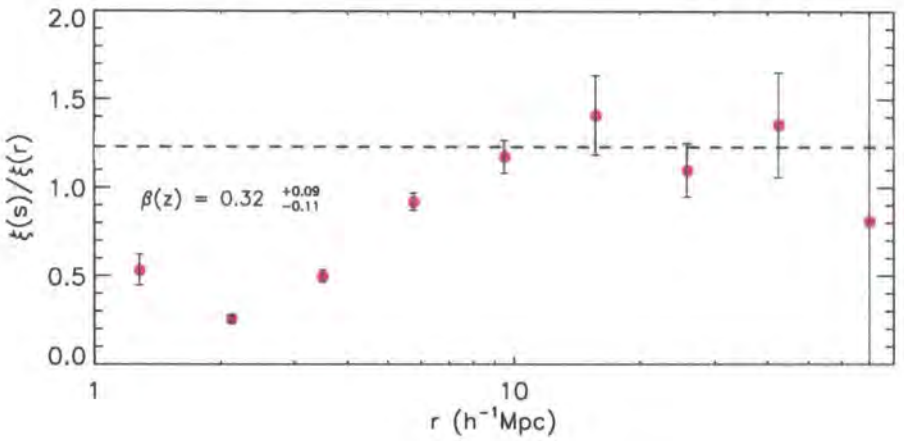

Figure 2.14: $\xi(s)/\xi(r)$ measured from the 2QZ survey, taking the measured $\xi(s)$ values and the two power-law $\xi(r)$ model we derived. As previously, the fit was made on scales where the z-space distortions are only affected by the large-scale infall and not by random peculiar motions of the QSOs. The dashed line and the shaded region represent this best fit and its 1 σ confidence level. This fit corresponds to a value of $\beta(z = 1.4) = 0.32^{+0.09}_{-0.11}$.

in Section 2.5.1. The resulting ratio $\xi(s)/\xi(r)$ obtained as a function of separation is shown in Fig. 2.14. By fitting $\xi(s)/\xi(r)$ we find that $\beta(z = 1.4) = 0.32^{+0.09}_{-0.11}$. The quoted errors are statistical only, and do not take into account the systematic uncertainty in the β measurement due to uncertainty in the form of the $\xi(r)$ model. This is potentially large, as demonstrated by the difference in the β values obtained assuming the single and double power-law $\xi(r)$ models.

The value of $\beta(z = 1.4)$ found is in agreement with the values computed from previous estimates, with different methods and also based on QSO samples taken from the 2QZ survey (Hoyle *et al.* 2002; Outram *et al.* 2004). The linear bias $b(z = 1.4) = 2.84^{+1.49}_{-0.57}$, assuming a flat $\Omega^0_m = 0.3$ cosmology. This value is slightly higher than what would be expected from linear perturbation theory, assuming that QSOs are random tracers of the galaxy distribution (Basilakos and Plionis, 2001). However, the comparisons between our results and those theoretical predictions will significantly depend on the normalisation used when computing $b(z)$.

Taking the real- and z-space clustering properties, the effect of β is to change the amplitude of the correlation function at large scales. If, on top of this effect, we add the distortions due to the small-scales peculiar motions and z-errors, we find that the predicted $\xi(s)$ from our model is a good description of the measured $\xi(s)$ (Fig. 2.15). The reduced χ^2_{min} is 0.95 (8 d.o.f.), thus indicating a very reasonable fit.

It should be pointed out, though, that the double power law parameterisation is solely a description of the shape of the correlation function within the range of scales considered, and it should not be regarded as a physically motivated model for $\xi(r)$. Outside the fitting range it is likely that the $\xi(r)$ shape will strongly deviate from the double power law description, and the

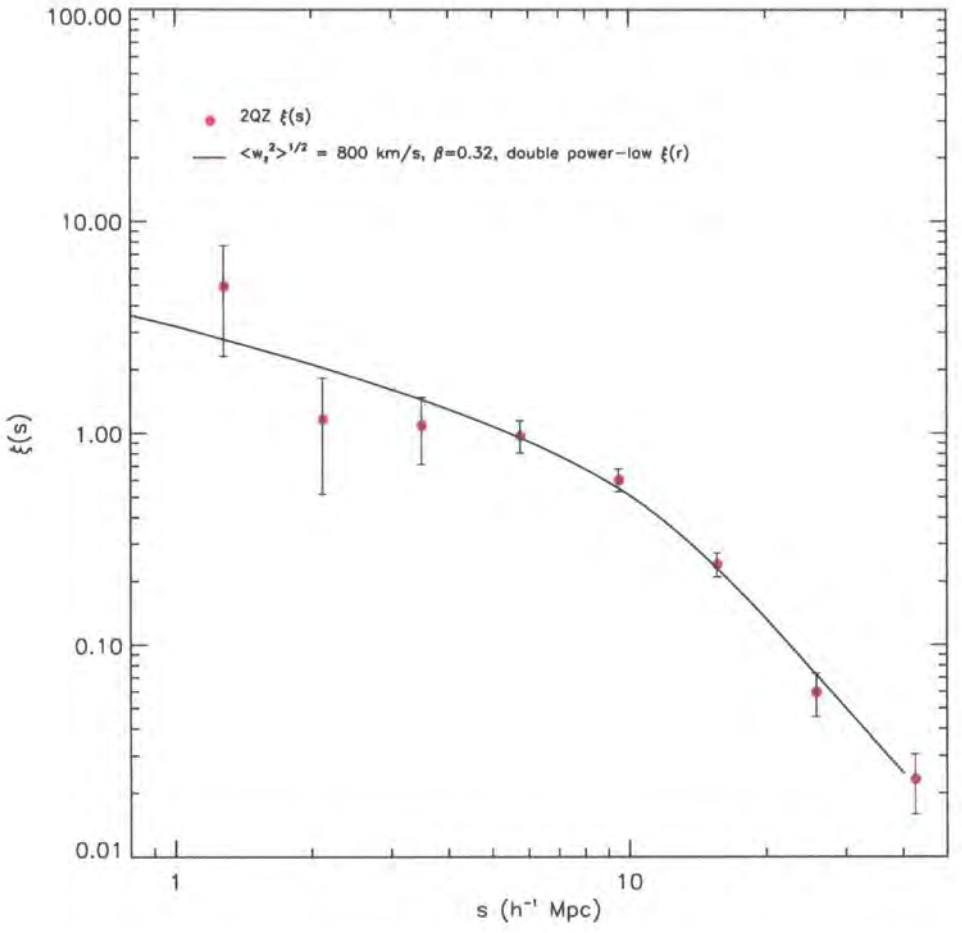

Figure 2.15: The plot shows the $\xi(s)$ results from the 2QZ overploted with the $\xi(s)$ predicted by the double power-law $\xi(r)$ model, after adding the z-space distortions due to peculiar motions. To quantify these, we took values for $< w_z^2 >^{1/2}$ and $\beta(z = 1.4)$ of $800\,\mathrm{km\,s^{-1}}$ and 0.32, respectively.

existence of the "break" at $10\,h^{-1}$Mpc can lead to non-physical (sometimes negative) forms of the associated power-spectrum, determined by computing the Fourier transform of $\xi(r)$.

2.6 Comparison with results from other surveys

The high statistical significance of the 2dFGRS sample makes it unique, and an excellent sample with which to compare our results. Hawkins et al. (2003) measured the z-space correlation function $\xi(s)$ and the projected correlation function, $w_p(\sigma)$. Unlike the case of the 2QZ, direct inversion of $w_p(\sigma)$ of the 2dFGRS allowed measuring the real-space correlation function $\xi(r)$ with great accuracy, up to scales of $\sim 20\,h^{-1}$Mpc. $\xi(s)$ is very well defined by a double power-law model, up to scales $\sim 20\,h^{-1}$Mpc, where the data stops following the two power-law fit and rapidly tends towards zero. The flatter behaviour at small scales ($\lesssim 4\,h^{-1}$Mpc) can be explained by the effects of peculiar velocities with dispersion $\sim 500\,\mathrm{km\,s^{-1}}$. From $\xi(s)/\xi(r)$ and $\xi(\sigma, \pi)$ fitting, a value of

$\beta(z) = 0.49^{+0.09}_{-0.09}$ was found.

Although the double power-law model was motivated by the form of the 2dFGRS $\xi(r)$, we have proceeded by fitting the model to the 2QZ $w_p(\sigma)$ and $\xi(s)$. Therefore, it is now worthwhile checking how the double-power law model fitted to the 2QZ data compares to the 2dFGRS correlation functions. Of course, the form of the high-z QSO correlation function need not be consistent with the low-z galaxy correlation function. However, assuming that the bias is scale independent and that the range of scales fitted are not affected by non-linear effects, it should be expected the form of $\xi(r)$ to be the same. We compare the measured 2dFGRS $w_p(\sigma)$ and $\xi(s)$ with the predictions from the $\xi(r)$ 2QZ model. This is represented in Fig. 2.16.

The shaded region, in both plots, represents the 1σ errors from the results presented in Hawkins et al. (2003). The circles are the measured $w_p(\sigma)/\sigma$ and $\xi(s)$ from the 2QZ. The dashed and solid lines show the predictions from the single and double power-law $\xi(r)$ models that best fit the 2QZ $w_p(\sigma)$ data. The upper plot shows their projection along σ and the lower plot the respective $\xi(s)$ functions, with distortions parametrised by $< w_z^2 >^{1/2} = 800$ km s^{-1} and $\beta = 0.87$ (for the dashed line) and $\beta = 0.32$ (for the solid line). It can be seen that the 2dFGRS $w_p(\sigma)$ results are very similar to the 2QZ and hence to the projection of our $\xi(r)$ double power-law model, even at scales ($\gtrsim 20\,h^{-1}$Mpc) where the 2dFGRS data does not follow the best-fitting single power-law model. Croom et al. (2005) found that the 2dFGRS and 2QZ samples have the same clustering amplitude. Our results corroborate this conclusion: the $w_p(\sigma)$ comparison between the two data sets does not show any evident discrepancy.

There is an offset between the 2QZ $\xi(s)$ models and the 2dFGRS data, at small scales. This is due to the different z-space distortions in the two data-sets. At large scales, a great level of consistency is seen between the results of both surveys and the double power-law model. The dotted and dash-dotted lines in this plot are the predicted $\xi(s)$ functions for the 2dFGRS, taking the two $\xi(r)$ models derived for the 2QZ (the single and double power-law $\xi(r)$ models respectively) and adding the distortions quantified by the values of $\beta(z = 0.11)$ and $< w_z^2 >^{1/2}$ found by Hawkins et al. (2003).

The dotted line is not a good representation of the 2dFGRS data since, at $6 \lesssim s \lesssim 20\,h^{-1}$Mpc scales, as it underestimates the 2dFGRS clustering, considering the 1σ errors. The dash-dotted line, that corresponds to the 2dFGRS $\xi(s)$ prediction assuming the double power-law model, is a better description of the clustering of the 2dF galaxies at large scales, although it underestimates the clustering at scales $\lesssim 3\ h^{-1}$Mpc.

2.7 Comparison with CDM model predictions

Peacock and Dodds (1996) presented a model to describe the evolution of the power-spectra ($P(k)$) of density fluctuations in the non-linear regime. This work was then followed by Smith et al. (2003), who derived a more accurate method of including non-linear effects in the power-

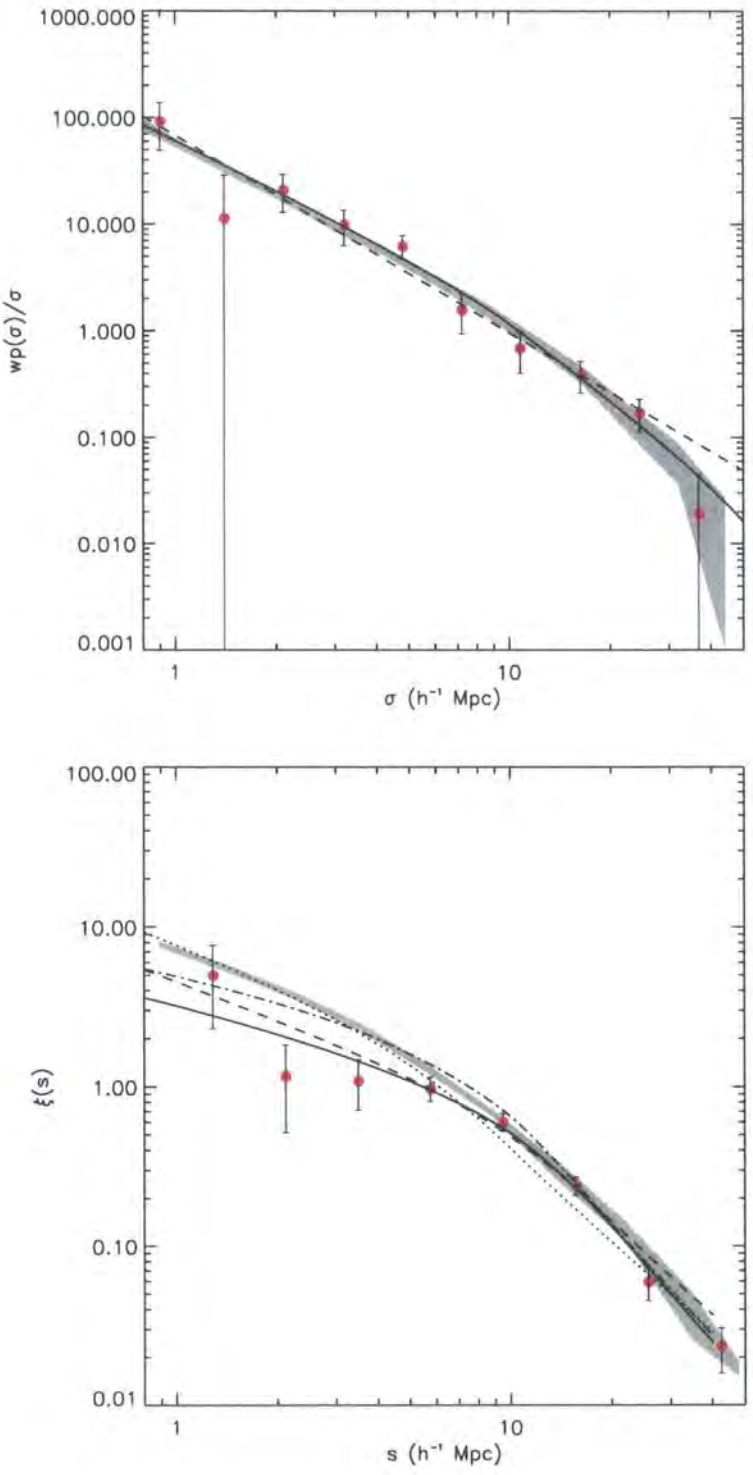

Figure 2.16: The top plot shows the $w_p(\sigma)$ results for the 2dFGRS and 2QZ surveys, together with the predictions from the single and double power-law $\xi(r)$ models previously derived for the 2QZ. The shaded region represents the 1σ error margin for the 2dFGRS $w_p(\sigma)/\sigma$. The circles are the $w_p(\sigma)/\sigma$ values measured for the 2QZ. Similarly, the bottom plot shows the $\xi(s)$ results, where the shaded region is again the 1σ error margin for the 2dFGRS results and the circles the 2QZ data. Refer to the text for a complete description of the models here represented.

spectrum, which can be applied to more general power spectra. This new method of modelling the power-spectrum is based on a fusion of the halo model with the scaling between linear and non-linear scales proposed by Hamilton et al. (1991). Smith and collaborators also presented a set of high-resolution N-body simulations that they used to test their mass power-spectrum formula. Their results suggest that the model for the mass power-spectrum is a good description of its clustering in a very wide range of scales, $k \sim 0.1 - 100\ h\mathrm{Mpc}^{-1}$.

Here we compute the real-space non-linear power-spectrum for the mass using the method described in Smith et al. (2003). By scaling the obtained power-spectrum with a linear bias b, we can obtain the predicted CDM power-spectrum for the 2QZ catalogue. We also compute the z-space power-spectrum by adding the z-space distortions to the model, as described in Padilla and Baugh (2002). After computing the real- and z-space power-spectrum, the respective correlation functions can be derived by a simple Fourier transform of the $P(k)$ output.

The top plot in Fig. 2.17 shows the $\xi(r)$ prediction derived from a ΛCDM power-spectrum, computed using the method of Smith et al. (2003) (dashed line) with parameters: $\Omega_m^0 = 0.3$, $\Omega_\Lambda^0 = 0.7$, $\sigma_8 = 0.85$, $\Gamma = 0.17$, $b = 2.3$, $< w_z^2 >^{1/2} = 800\,\mathrm{km\,s^{-1}}$ and $z = 1.4$. The solid line is our double power-law model that we derive solely based on the 2QZ $\xi(s)$ and $w_p(\sigma)$ measurements. The dotted line is the single power-law model derived for the 2QZ. As it can be seen, there are reasonable similarities between the ΛCDM prediction and the double power-law model. The slopes of the two power-laws that describe $\xi(r)$, fitted from the $w_p(\sigma)$ data, are close to the predictions from ΛCDM. The single power-law model does not appear to be as close to the ΛCDM prediction. The bottom plot shows the $\xi(s)$ results, after the distortions due to $\beta = 0.32$ and $< w_z^2 >^{1/2} = 800\,\mathrm{km\,s^{-1}}$ are included. Again, the dashed line represents the ΛCDM $P(k)$ prediction. The solid line is the $\xi(s)$ derived from our double power-law $\xi(r)$ model, and the dotted line the $\xi(s)$ derived from the single power-law model, once the z-space distortions are added. The circles represent the $\xi(s)$ measured directly from the 2QZ, and the corresponding error bars. The value of χ^2_{min} between the $\xi(s)$ ΛCDM prediction and the $\xi(s)$ data is 0.87 (8 d.o.f.). Thus, we can conclude that the ΛCDM clustering predictions provide a good description of the data, and that the ΛCDM real-space clustering shows more resemblance to the double power-law model then with the single power-law model for the QSO $\xi(r)$.

2.8 Conclusions

We have measured the correlation functions both in real- and z-space from the 2QZ survey. A simple power-law model gives a reasonable fit to $w_p(\sigma)$, indicating that the real-space correlation function might be well approximated by a single power-law model. This is not the case for the z-space correlation function, where the clustering signal is weaker than the expected from a simple power-law model, at scales below 10 h^{-1}Mpc. The effects of z-space distortions can, as a first interpretation, account for the shape of the z-space correlation function, namely its

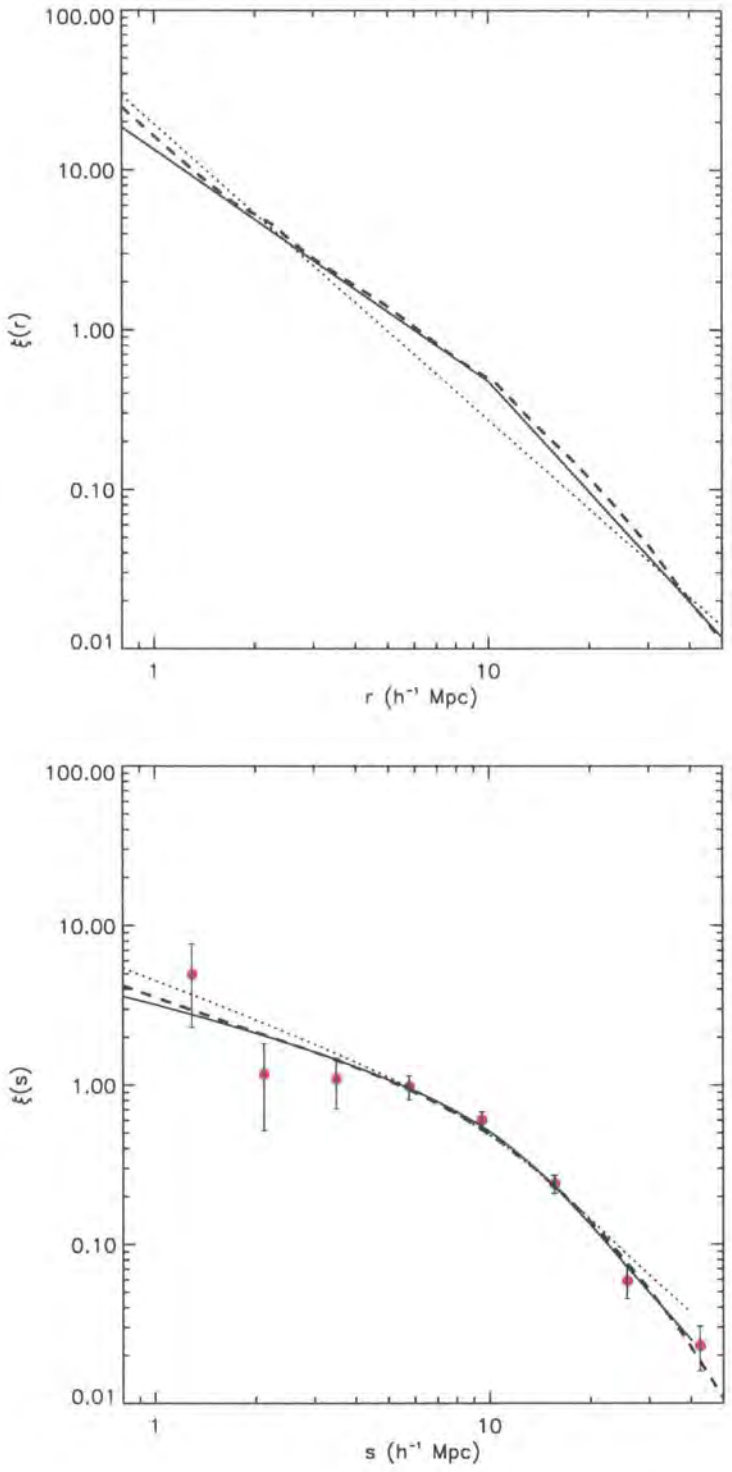

Figure 2.17: The top plot shows the derived biased $\xi(r)$ model from a ΛCDM $P(k)$ prediction (dashed line), overplotted on the best fitting double and single power-law $\xi(r)$ model fits to our $w_p(\sigma)$ data (solid line and dashed line, respectively). In the bottom plot are the respective $\xi(s)$ functions from the models above, when the distortions parametrises by $< w_z^2 >^{1/2} = 800\,\mathrm{km\,s^{-1}}$ and $\beta = 0.32$ (for the double power-law model) or $\beta = 0.87$ (for the single power-law model) are added. The dashed, solid and dotted lines represent the same models as in upper plot, but now the z-space distortions are included. The circles are the measured $\xi(s)$ from the 2QZ data. The ΛCDM $P(k)$ predicted $\xi(s)$ shows good agreement with the data, considering the errors.

non-power-law behaviour. However, small deviations from a power-law model appear to exist, at large scales, in the projected correlation function. Also, the $\xi(r)$ power-law suggested by the $w_p(\sigma)$ results seems shallower then the $\xi(s)$ function at large scales, where the difference between $\xi(r)$ and $\xi(s)$ should be only given by an amplitude shift and not include any difference in the slopes. Motivated by the non-power-law $\xi(r)$ shape measured in other redshift surveys, such as the 2dFGRS, we also test if a similar $\xi(r)$ models can explain the observed 2QZ $\xi(s)$ and $w_p(\sigma)$. We thus fit a double power-law $\xi(r)$ model to the $w_p(\sigma)$ data. The parameters of the best-fitting model are: $r_0 = 5.9^{+0.5}_{-0.6}\,h^{-1}$Mpc and $\gamma = 1.51^{+0.27}_{-0.27}$, for $r < 11\,h^{-1}$Mpc, and $r_0 = 6.92\,h^{-1}$Mpc and $\gamma = 2.03^{+0.12}_{-0.03}$, for $r > 11\,h^{-1}$Mpc (assuming Λ).

We then compared both the single and double power-law $\xi(r)$ models with the 2dFGRS results and theoretical predictions from CDM clustering models. When comparing the projected correlation function results in the 2dFGRS and the 2QZ, we found that both our data and the proposed double power-law model lie within the 2dFGRS errors, which suggests that this 2QZ $\xi(r)$ model is an acceptable description of the 2dFGRS $\xi(r)$.

With the assumed Λ cosmology, the amplitudes of the 2QZ and 2dFGRS correlation functions are similar; with the assumed EdS cosmology the 2QZ amplitude is a factor of two smaller at $\sim 10\,h^{-1}$Mpc scales. The mass correlation function amplitude evolves with redshift, and the same is true for galaxies and QSOs (Croom et al., 2005). Therefore, the agreement of the amplitudes in the Λ case is probably a coincidence. However, the 2QZ and 2dFGRS correlation functions are certainly similar in their shape.

The ΛCDM $\xi(s)$ prediction appears to be a good fit to the 2QZ $\xi(s)$. We also found that the $\xi(r)$ double power-law model that we derived from the 2QZ clustering results is a very good match to ΛCDM $\xi(r)$. On the other hand, the single power-law 2QZ $\xi(r)$ model, derived from the $w_p(\sigma)$ data, produces a poorer match to the 2dFGRS data and the ΛCDM predictions.

Using the double power-law $\xi(r)$ model and the $\xi(s)$ measurements, we estimated $\beta(z = 1.4) = 0.32^{+0.08}_{-0.11}$, by computing and fitting $\xi(s)/\xi(r)$. This result contrasts with the higher value of $\beta(z = 1.4) = 0.87^{+0.30}_{-0.31}$, found when we consider the single power-law $\xi(r)$ model.

Chapter 3

Cosmological constraints from z-space distortions in the 2QZ $\xi(\sigma, \pi)$

3.1 Introduction

In Chapter 2 we estimated $\beta(z = 1.4)$ from a direct comparison between the 2QZ $\xi(s)$ and the $\xi(r)$ models derived from the $w_p(\sigma)$ measured from the 2QZ data. We then concluded that the $\beta(z = 1.4)$ value is strongly dependent on the $\xi(r)$ model assumed. The modelling of z-space distortions and their use for parameter constraints can be taken a step further, based on the 2-D z-space correlation function $\xi(\sigma, \pi)$, developing the method of Hoyle et al. (2002) used for the 2QZ $10k$ catalogue.

We have seen that the study of dynamical distortions in the measured clustering pattern of high-z objects allows the determination of parameters such as β, which not only quantifies the amount of "infall" that drives the large-scale dynamics, but also relates to the *bias* of the objects, and hence determines the relation between their clustering and that of the underlying dark-matter. In the present chapter we use that fact that, besides the dynamical distortions, geometric distortions in the z-space clustering pattern also occur if the cosmology assumed to convert the observed QSO redshifts into distances is not the same as the true, underlying cosmology of the Universe. The reason is because the cosmology dependence of the separations along the redshift direction is not the same as for the separations measured in the perpendicular direction (Alcock and Paczynski, 1979).

QSO peculiar velocities lead to distortions in the $\xi(\sigma, \pi)$ shape. At small scales in σ, the random peculiar motions of the QSOs cause an elongation of the clustering signal along the π direction. The predominant effect at large scales is the coherent infall that causes a flattening of the $\xi(\sigma, \pi)$ contours along the π direction and some elongation along σ.

In the 2QZ sample it was found that, at small scales, there is not enough signal in the data to constrain the velocity dispersion of the 2dF QSOs with this method. Nevertheless, it should

be possible to determine constraints not only on $\beta(z)$, which parametrises the large-scale infall of the QSOs, but also on the value of Ω_m^0.

The use of geometric distortions to study cosmology was pioneered by Alcock and Paczynski (1979), who demonstrated that they are potentially a powerful cosmological test for a non-zero Λ. However, Ballinger et al. (1996) noted that the geometric and dynamical effects may be degenerate.

To break this degenerate constraint between Λ and bias, complementary constraints on these parameters can be considered simultaneously. As shown by Hoyle et al. (2002), or Outram et al. (2004), orthogonal constraints can be obtained from linear evolution theory of cosmological density perturbations. In this chapter we develop a similar analysis using the 2QZ survey data. We aim to obtain constraints on the QSO bias at $z \approx 1.4$ and on the value of the matter density of the Universe from a detailed analysis of the z-space distortions in the 2QZ clustering, combined with bias constraints from linear theory.

3.2 The 2QZ $\xi(\sigma, \pi)$

The measurement of $\xi(\sigma, \pi)$ is done the same way as $\xi(s)$, except that now the number of pairs is binned in two variables, rather than one. In Fig. 3.1 we display $\xi(\sigma, \pi)$ determined for the 2QZ catalogue.

The $\xi(\sigma, \pi)$ contours appear elongated along π, which can be attributed to the effects of peculiar velocities. The data is also quite noisy, particularly at small scales in σ. The errors are computed using the Poisson estimate. It is therefore easy to understand the reason for the noisier contours, at those scales: since the σ direction actually represents two dimensions, while π only one, the volume of each bin, and hence the number of pairs, increases as the separation σ increases, leading to a decrease in the Poisson error.

3.3 Comparison between two z-space distortions models

To understand and quantify the effects that are actually shaping the $\xi(\sigma, \pi)$ contours, we develop models for the z-space distortions and compare them to the observations. Different models exist to explain and describe z-space distortions in $\xi(\sigma, \pi)$, based on different assumptions and approximations. Nevertheless, they rest on a key assumption, which is the non-scale-dependence of the bias.

Here, two models are described and compared. The basis for the construction of the two models is the same: we start with a model for the real-space correlation function $\xi(r)$, include the effects of the coherent large-scale infall, and then convolve the result with the distribution of the small-scale pairwise peculiar velocities.

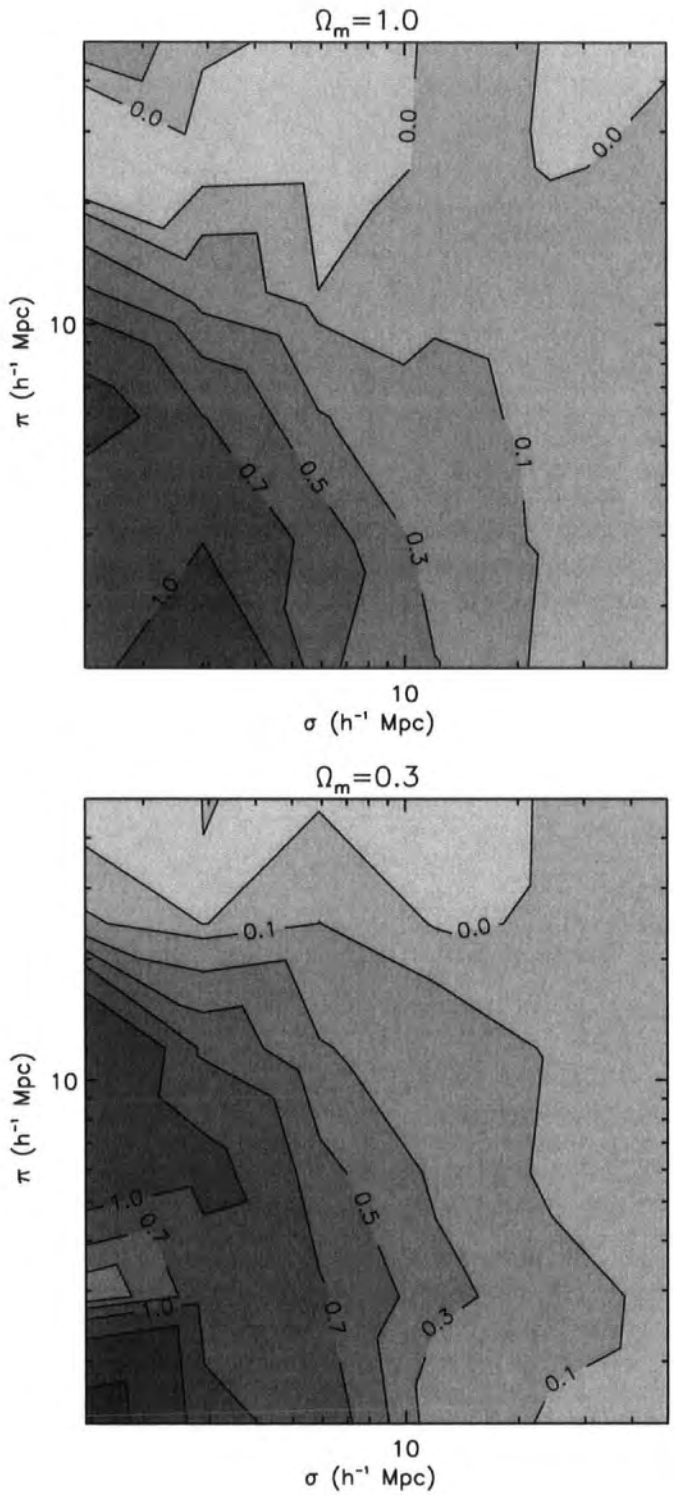

Figure 3.1: $\xi(\sigma, \pi)$ measured with the Hamilton estimator. On top is the result obtained if an EdS cosmology is assumed, on the bottom if the Λ one is assumed, instead.

3.3.1 z-space distortions: Model I

The large-scale coherent infall of the QSOs, is described in Fourier space by (Kaiser 1987; Hawkins *et al.* 2003):

$$P_s(k) = (1 + \beta(z)\mu_k^2)P_r(k), \tag{3.1}$$

where $P_s(k)$ and $P_r(k)$ are the power-spectrum in redshift and real-space, respectively, and μ_k is the cosine of the angle between the wavevector $\mathbf{k}$ and the line-of-sight. Translated to real-space, these results take the form (Hamilton 1992; Matsubara & Suto 1996):

$$\xi(\sigma,\pi) = \left(1 + \frac{2}{3}\beta(z) + \frac{1}{5}\beta(z)^2\right)\xi_0(r)P_0(\mu) \tag{3.2}$$

$$- \left(\frac{4}{3}\beta(z) + \frac{4}{7}\beta(z)^2\right)\xi_2(r)P_2(\mu) \tag{3.3}$$

$$+ \frac{8}{35}\beta(z)^2\xi_4(r)P_4(\mu), \tag{3.4}$$

where μ is now the cosine of the angle between r and π and $P_l(\mu)$ are the Legendre polynomials of order l. $\xi_0(r)$, $\xi_2(r)$ and $\xi_4(r)$ are the monopole, quadrupole and hexadecapole components of the linear $\xi(r)$ and their form will depend on the $\xi(r)$ model adopted. In general, they are given by (Matsubara and Suto, 1996):

$$\xi_{2l}(r) = \frac{(-1)^l}{r^{2l+1}}\left(\int_0^r x dx\right)^l x^{2l}\left(\frac{d}{dx}\frac{1}{x}\right)^l x\xi(x) \tag{3.5}$$

The $\xi(\sigma,\pi)$ model is then convolved with the pairwise peculiar velocity distribution to include the small scale z-space effects due to the random motions of the QSOs. Here we assume that this can be well described by a Gaussian distribution (Ratcliffe, 1996):

$$f(w_z) = \frac{1}{\sqrt{2\pi} < w_z^2 >^{1/2}} \exp\left(-\frac{1}{2}\frac{|w_z|^2}{< w_z^2 >}\right) \tag{3.6}$$

Hence, $\xi(\sigma,\pi)$ is then given by:

$$\xi(\sigma,\pi) = \int_{-\infty}^{\infty} \xi'(\sigma, \pi - w_z(1+z)/H(z))f(w_z)dw_z, \tag{3.7}$$

where $\xi'(\sigma, \pi - w_z(1+z)/H(z))$ and $f(w_z)$ are given by equations 3.4 and 3.6.

3.3.2 z-space distortions: Model II

$\xi(\sigma,\pi)$ can be defined as (Peebles 1980 ; Hoyle 2000):

$$1 + \xi(\sigma,\pi) = \int_{-\infty}^{\infty} (1 + \xi(r))f(w_z)dw_z \tag{3.8}$$

Here, it is assumed that the pairwise peculiar velocity distribution $f(w_z)$ is a slowly varying function with r. The form of $f(w_z)$ is the same as in Model I and is given on equation 3.6. The effects of the bulk motions can be included in the following way:

$$1+\xi(\sigma,\pi)=\int_{-\infty}^{\infty}(1+\xi(r))f(w_z(1+z)-v(r_z))dw_z, \tag{3.9}$$

where $v(r_z)$ is the model used for the bulk motions, as a function of the real-space separation along the π direction - r_z. Following Peebles (1980) and Hale-Sutton (1990), the infall velocity can be derived from the equation of conservation of particle pairs within a comoving separation r, from a randomly chosen mass particle:

$$\frac{\delta}{\delta t}\int_0^r x^2\xi^m(x,t)dx+\frac{1}{a(t)}r^2\left(1+\xi^m(r,t)\right)v(r,t)=0 \tag{3.10}$$

Solving the equation above to find $v(r,t)$ and assuming that $\xi(r)$ is well described by a power-law model, Hoyle (2000) obtained the following expression for the infall velocity of biased particles:

$$v(r_z)=-\frac{2}{3-\gamma}\Omega_m(z)^{0.6}H(z)r_z\frac{\xi(r)}{b^2+\xi(r)} \tag{3.11}$$

$\xi(\sigma,\pi)$ computed with these two models is shown in Fig. 3.2. The solid line refers to Model I and the dashed line to Model II. The input $\xi(r)$ form is the same for both models ($\xi(r)=(r/5.0)^{-1.8}$). For the plot on the right the model is computed considering $<w_z^2>^{1/2}=0\,\mathrm{km\,s^{-1}}$ and $\beta(z)=0.4$. The overall effect is the same for the two models, and consists of a compression of the $\xi(\sigma,\pi)$ contours along the π direction and a small elongation along the σ direction. The plot on the left displays the case with $<w_z^2>^{1/2}=800\,\mathrm{km\,s^{-1}}$ and $\beta(z)=0.4$. One can see that, at small scales, the distortions caused by the velocity dispersion dominate, while at large scales, the distortions due to a non-zero $\beta(z)$ dominate. The adopted redshift for these models is $z=1.4$, which is the median redshift of the 2QZ survey. These plots also show significant differences in the shape of the distortions caused by $\beta(z)$ between the two models.

3.3.3 Are models I and II self-consistent?

One simple test can be performed to check if a given model is self-consistent. Averaging $\xi(\sigma,\pi)$ in several annuli will give $\xi(s)$. In addition, at large scales, z-space distortions are mainly affected by the large-scale coherent infall, which implies the relation between $\xi(s)$ and $\xi(r)$ given by equation 2.17. Hence, if a model is self-consistent, after averaging $\xi(\sigma,\pi)$ at constant s, the final result should be the same as the initial input $\xi(r)$, scaled with $(1+2/3\beta(z)+1/5\beta(z)^2)$. If not, then the model must be wrong. Here, this test is done for Models I and II.

Fig. 3.3 shows the result of this test. The circles refer to Model I and the diamonds to Model II. In both cases a $\xi(\sigma,\pi)$ model is computed using an input power-law $\xi(r)=(r/5.0)^{-1.8}$, $\beta(z)=0.4$ and $<w_z^2>^{1/2}=800\,\mathrm{km\,s^{-1}}$. Then, the average $\xi(\sigma,\pi)$ is computed in constant annuli of s, thus obtaining $\xi(s)$. The output $\xi(s)$ is then divided by the predicted $\xi(s)$ using equation 2.17. One can see that Model I seems self-consistent, as the predicted $\xi(s)$ from $\xi(r)$ matches with the linear scaling of $\xi(r)$, through $\beta(z)$, at large scales. However, this is not the case for Model II. There is a discrepancy between the predicted $\xi(s)$ and the one derived from averaging the z-space

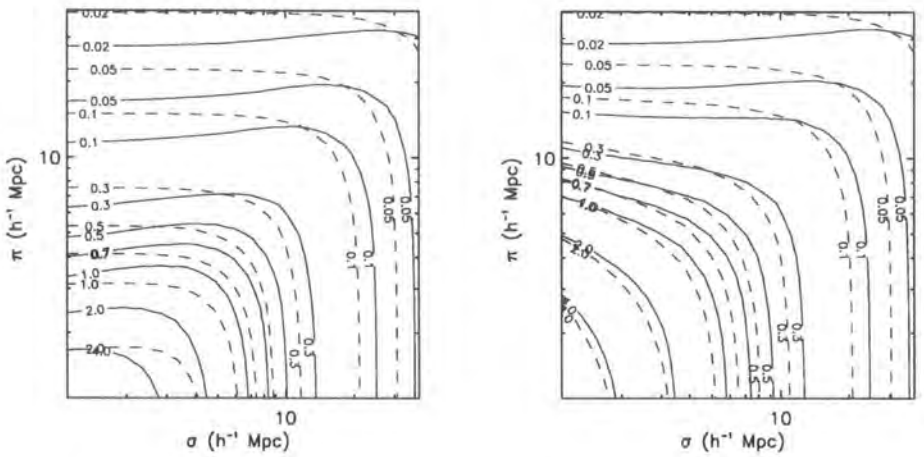

Figure 3.2: $\xi(\sigma,\pi)$ computed with Model I (solid line) and Model II (dashed line). The plot on the left shows the difference between the two models when the distortions are quantified by $< w_z^2 >^{1/2}= 0\,\mathrm{km\,s^{-1}}$ and $\beta(z) = 0.4$. The plot on the right also accounts for the distortions caused by a non-zero velocity dispersion, and the values $< w_z^2 >^{1/2}= 800\,\mathrm{km\,s^{-1}}$ and $\beta(z) = 0.4$ were used. The $\xi(r)$ model is in all cases a simple power-law of the form $(r/5.0)^{-1.8}$.

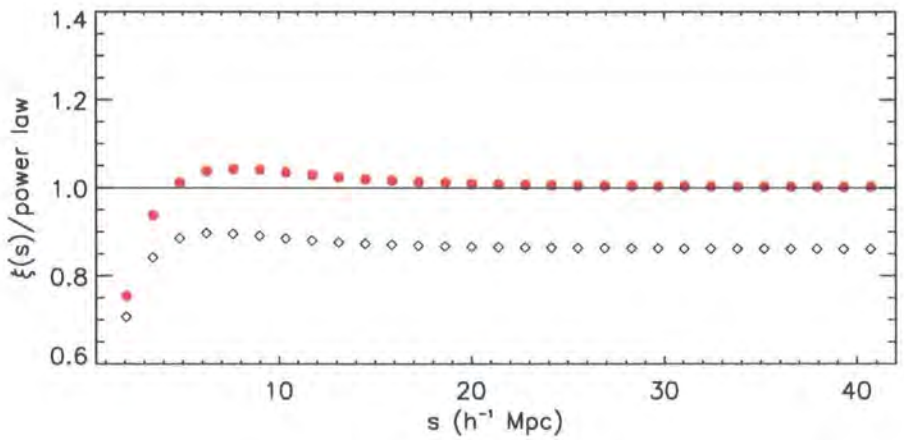

Figure 3.3: $\xi(s)$ computed from averaging $\xi(\sigma,\pi)$ in annuli of constant $s = \sqrt{\sigma^2+\pi^2}$ and divided by the power-law predicted at large-scales. The circles correspond to Model I and the diamonds to Model II. It was assumed $\xi(r) = (r/5.0)^{-1.8}$, $\beta(z) = 0.4$ and $< w_z^2 >^{1/2}= 800\,\mathrm{km\,s^{-1}}$. $\xi(s)$ computed from Model I seems to agree very well with the prediction from the linear regime scaling from $\xi(r)$, given by equation 2.17. The same does not happen with Model II, where an offset between the predicted and the derived $\xi(s)$ is observed. It can also be seen for both models the effect of the velocity dispersion, that causes a flattening of $\xi(s)$ at small scales.

distortions on $\xi(\sigma,\pi)$. This offset corresponds to an offset on the value of $\beta(z)$ of ~ 0.25, which is quite significant.

There are two main reasons which account for the offset between Model II and the predicted large-scale z-space clustering amplitude from Eq. 2.17. As pointed out by Kaiser (1987), the relation between the averaged real- and z-space correlation functions differs for Models I and II. While Model I is consistent with the relation given by Eq. 2.17, assuming Model II leads us to the following relation between $\xi(s)$ and $\xi(r)$:

$$\xi(s) = \left(1 + \frac{2}{3}\beta\right)\xi(r) \tag{3.12}$$

If one takes this into account, and substitutes b^2 by b in Eq. 3.11, then this revised version of Model II becomes self-consistent. Following Hale-Sutton (1990), the gravitational infall velocity for mass particles is given by (at $z = 0$):

$$v(r_z) = -\frac{2}{3-\gamma}\Omega_m^{0.6} H(0) r_z \frac{\xi^m(r)}{1+\xi^m(r)} \tag{3.13}$$

where ξ^m is the two point correlation function for mass particles. A more general form, valid for different values of z, and biased particles, was obtained by Hoyle (2000). However, the extrapolation of that equation to biased particles is not correct by simply inserting the relation between the luminous and dark matter correlation functions:

$$\xi^g = \xi^m b^2 \tag{3.14}$$

Hence, we have that the ratio in Eq. 3.13 is:

$$\frac{\xi^m(r)}{1+\xi^m(r)} = \frac{\xi^g(r)/b^2}{1+\xi^g(r)/b^2} = \frac{\xi^g(r)}{b^2+\xi^g(r)}$$

ie, the same as in Eq. 3.11. Thus, for $z = 0$, both Eqs. 3.11 and 3.13, give the same value of $v(r_z)$, regardless of the value of b, if ξ^g ξ^m are scaled accordingly.

Eq. 3.10 represents the conservation of the number of pairs at separation x from a random *mass* particle. If we use that equation when determining the infall velocity associated to the biased particles, we are considering pairs between mass and biased particles and the relation between the excess numbers of mass-mass and mass-biased particle pairs ($\xi(r)$) will not be b^2, as in Eq. 3.14, but b. We therefore replaced the term b^2 by b in Eq. 3.11 and repeated the test described above. This difference inplies that the bulk motions of biased particles differ from those of mass particles. We leave for future a complete determination of the streaming velocity for a general biased particle.

Fig. 3.4 shows the spherically-averaged $\xi(\sigma,\pi)$, generated with this revised version of Model II, divided by the expected z-space $\xi(s)$ amplitude (Eq. 3.12). The input $\xi(r)$ model is, in all cases, given by $\xi(r) = (r/5.0)^{-1.8}$. Table 3.1 gives the different values for the redshift and bias, used to generate each model. In all cases, we took $< w_z^2 >^{1/2} /(1+z) = 300\,\mathrm{km\,s^{-1}}$, in order to obtain similar small-scale distortions independent of z.

	•	+	◇	△
z	0.0	1.4	0.0	1.4
$b(z)$	1.0	1.0	2.0	2.0

Table 3.1: The values of z and b in each of the realisations shown in Fig. 3.4.

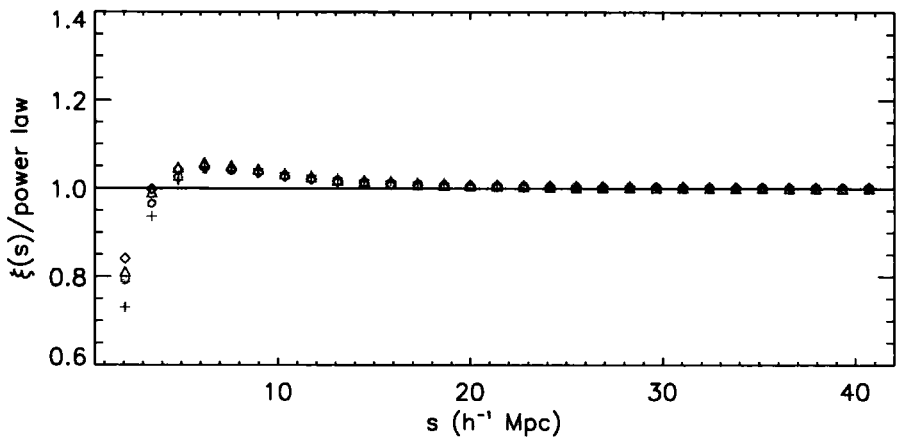

Figure 3.4: $\xi(s)$ computed from averaging $\xi(\sigma, \pi)$ in annuli of constant $s = \sqrt{\sigma^2 + \pi^2}$ and divided by the power-law predicted at large-scales, from Eq. 3.12. All symbols refer to the revised version of Model II presented here. It was assumed $\xi(r) = (r/5.0)^{-1.8}$. Refer to Table 3.1 for the values of z and $b(z)$ used in each model.

It can be seen that, once we correct the contribution of the bias in the velocity associated with the bulk flow, Model II appears to be self consistent, independently of redshift and bias.

However, in order to correctly compare our results in this chapter with those in the previous chapter and others from other surveys, such as the 2dFGRS (e.g. Hawkins et al., 2003), we will continue using Model I, in our z-space distortion analysis.

3.3.4 Including geometric distortions

It is useful to make some definitions before describing the cosmology fitting through geometric distortions. Following Hoyle et al. (2002), let the true, underlying cosmology of the Universe be the *true cosmology*, the cosmology used to build the model $\xi(\sigma, \pi)$ the *test cosmology*, and the cosmology assumed to derive the $r - z$ relation, both in the model and the data to measure the correlation function, the *assumed cosmology*.

Since we are comparing the geometric distortions in both the data and the model relative to the same assumed cosmology, the test cosmology used in the model that best matches the data should be the true cosmology of the Universe, in the absence of noise.

We here assume a spatially flat cosmology, and choose to fit the variable Ω_m^0, hence fixing $\Omega_\Lambda^0 = 1 - \Omega_m^0$.

The relation between the separations σ and π in the test and assumed cosmologies (referred to by the subscripts t and a, respectively) is the following (Ballinger et al., 1996; Hoyle, 2000):

$$\sigma_t = f_\perp \sigma_a = \frac{B_t}{B_a}\sigma_a \tag{3.15}$$

$$\pi_t = f_\parallel \pi_a = \frac{A_t}{A_a}\pi_a \tag{3.16}$$

where A and B are defined as follows (for spatially flat cosmologies):

$$A = \frac{c}{H_0}\frac{1}{\sqrt{\Omega_\Lambda^0 + \Omega_m^0(1+z)^3}} \tag{3.17}$$

$$B = \frac{c}{H_0}\int_0^z \frac{dz'}{\sqrt{\Omega_\Lambda^0 + \Omega_m^0(1+z')^3}}. \tag{3.18}$$

In the linear regime, the correlation function in the assumed cosmology will be the same as the correlation function in the test cosmology, given that the separations are scaled appropriately. i.e.:

$$\xi_t(\sigma_t, \pi_t) = \xi_a(\sigma_a, \pi_a). \tag{3.19}$$

In Fig. 3.5 the geometric distortions due to assuming a cosmology different from the true, underlying cosmology are represented. On the left plot is $\xi(\sigma, \pi)$ derived from Model I using an $\Omega_m^0 = 0.3$ test cosmology, while an EdS cosmology was assumed to derive the comoving distances. The plot on the right shows the case where the underlying cosmology has $\Omega_m^0 = 1.0$ but a Λ cosmology was assumed. So, assuming a value of Ω_m^0 higher than the true one will cause a compression of the $\xi(\sigma, \pi)$ contours along the line of sight, whilst if a too small value for Ω_m^0 is assumed, it will cause an elongation of the contours along the line of sight and a high clustering amplitude to be observed. Redshift-space distortions due to the effects of peculiar velocities were not included in these models.

Ignoring for the moment the distortions caused by the peculiar velocities and the effects of noise, the observed shapes of the measured and modelled $\xi(\sigma, \pi)$ will be the same when the test cosmology matches the true, underlying cosmology of the Universe (for whatever cosmology is assumed to convert the redshifts to comoving distances). Hence by fitting the geometric distortions in the data one should be able to determine the true cosmology, though in observed data sets, the distortions will also be due to dynamical processes, thus causing a degeneracy between the cosmological and dynamical constraint (Ballinger et al., 1996).

3.4 Fitting procedure

The fitting procedure was developed from the one used by Hoyle et al. (2002). In summary, for a given value of $\beta(z)$, a $\xi(\sigma, \pi)$ model is generated in a chosen test cosmology. Then, the separations σ and π are scaled to the same cosmology that was assumed to measure the actual data. The

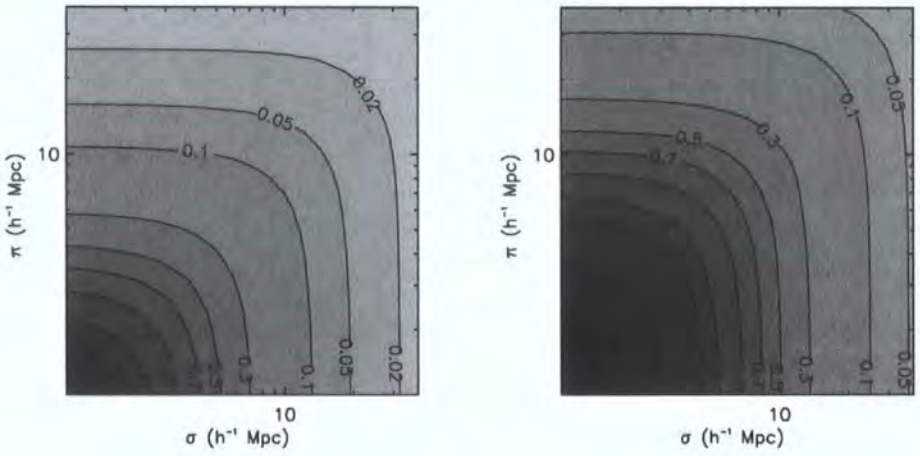

Figure 3.5: $\xi(\sigma, \pi)$ computed using Model I for different assumed and test cosmologies. The left plot shows the case where an EdS cosmology was assumed, to measure the correlation function, but the underlying cosmology of the Universe has $\Omega_m^0 = 0.3$ and $\Omega_\Lambda^0 = 0.7$. On the plot on the right is the case where the assumed cosmology is a flat cosmology with $\Omega_m^0 = 0.3$ but the underlying cosmology has $\Omega_m^0 = 1.0$. Assuming values for Ω_m^0 higher/smaller then the true ones, will cause a flattening/elongation of the $\xi(\sigma, \pi)$ along the line-of-sight, besides the overall effect on the amplitude of the correlation function, also visible in these plots. In these cases, z-space distortions due to peculiar velocities were disregarded.

final model for $\xi(\sigma, \pi)$ is then compared to the data. This method is repeated for different test cosmologies and values of $\beta(z)$.

Since we are fitting distortions in the *shape* of the z-space correlation function, the correct *spherically-averaged amplitude* of $\xi(r)$ must be given as an input to the model. Otherwise the fit will be driven by offsets in the amplitude of the $\xi(\sigma, \pi)$ model from the data, rather than the shape distortions, which would introduce systematic errors in the constraints obtained for Ω_m^0 and $\beta(z)$.

The following steps are taken in the fitting procedure:

- Assume a cosmology and measure $\xi(s)$, $w_p(\sigma)$, $\xi(\sigma, \pi)$.
- Take a model for the real-space correlation function, e.g. a double power-law model. This model should be a good description of the observed data, $\xi(s)$ and $w_p(\sigma)$.
- Choose a pair of test values of Ω_m^0 and $\beta(z)$.
- The model for $\xi(r)$ is a good description for the data in the assumed cosmology. What is actually needed at this stage is a $\xi(\sigma, \pi)$ model in some test cosmology, hence the correct input for this model is $\xi(r)$ in that same test cosmology. Since, in the linear regime, $\xi_t(r_t) = \xi_a(r_a)$, one has only to compute the real-space separation in the assumed cosmology to get $\xi_t(r_t)$. r_t is given by $r_t = \sqrt{\sigma_t^2 + (\pi_t - w_z/H_t)^2}$ and the relation between r_a and r_t is: $r_a = r_t/(f_\perp^2 f_\parallel)^{1/3}$.

- Using that model for $\xi_t(r_t)$, compute $\xi_t(\sigma_t, \pi_t)$. Then, include the geometric distortions by scaling $\xi_t(\sigma_t, \pi_t)$ back to the assumed cosmology, in a similar way as described in the previous step. To get $\xi_a(\sigma_a, \pi_a)$, one needs to scale the separations σ_t and π_t to σ_a and π_a, using equations 3.15 and 3.16.

- Adding the effects of large-scale infall not only introduces distortions in $\xi(\sigma, \pi)$ but also shifts the amplitude of the correlation function, by an amount that depends on the value of $\beta(z)$ taken. Since the amplitude of the spherical-averaged correlation function must remain the same (i.e. match the $\xi(s)$ data), whatever β and Ω_m^0 are used as *test* values, the amplitude of the input $\xi(r)$ model is allowed to vary in the fit, guaranteeing that the fit is being made to the *distortions* in $\xi(\sigma, \pi)$, since the averaged *amplitude* remains the same for whatever combination of β and Ω_m^0.

- For the best fitting value of this amplitude factor, determine the χ^2 value for the fit of this model to the data.

- Repeat this procedure for different combinations of Ω_m^0 and $\beta(z)$.

The number of degrees of freedom in the χ^2 fit is the total number of bins where $\xi(\sigma, \pi)$ from the model is fitted to the data minus the number of free parameters. If the fit is to Ω_m^0 and $\beta(z)$ and the averaged amplitude of $\xi(\sigma, \pi)$ is allowed to float so it matches $\xi(s)$, the number of free parameters will be three. The velocity dispersion was fixed in these fits: taking into account the z-errors of the survey and the intrinsic velocity dispersion of the QSOs, we assumed $< w_z^2 >^{1/2} = 800$ km s^{-1} (Outram et al., 2003).

3.5 Further constraints on Ω_m^0 and $\beta(z)$ from QSO clustering evolution

All the other factors being the same, the greater the value of the true, underlying Ω_m^0, the more elongated the $\xi(\sigma, \pi)$ will be along π; and the greater the value of $\beta(z)$, the flatter these contours will be. Hence, a degeneracy is expected to occur in the confidence levels in the $[\Omega_m^0, \beta(z)]$ plane. In order to get better constraints on Ω_m^0 and also $\beta(z)$, this degeneracy needs to be broken.

A possible way to break the degeneracy is to combine these results with a constraint derived from consideration of QSO clustering evolution. From the value of the mass correlation function, at $z = 0$, linear perturbation theory can be used, in a given test cosmology, to compute its value at $z = 1.4$. Then, considering that the bias ($b(z = 1.4)$) is given by the ratio of the QSO $\xi(r)$ and the mass $\xi(r)$, and that the former is, at large scales, related to the measured QSO $\xi(s)$ through $\beta(z = 1.4)$, estimates of this parameter can be obtained for a given test cosmology.

To compute the mass correlation function amplitude at low z, we can use the values of $\xi(s)$ and β found for the 2dFGRS survey. Using the values found by Hawkins et al. (2003), the first step is to compute the respective value of $b(z = 0)$.

For each test cosmology, the bias parameter of the galaxies at $z = 0$ is:

$$b(z=0) = \frac{(\Omega_m^0)^{0.6}}{\beta(z=0)} \tag{3.20}$$

Consider now the volume averaged two-point correlation function $\bar{\xi}^s$ given by:

$$\bar{\xi}^s = \frac{\int_0^s 4\pi s'^2 \xi(s') ds'}{\int_0^s 4\pi s'^2 ds'}. \tag{3.21}$$

For the 2dFGRS, $\xi(s)$ is found to be well described by a double power-law model (Hawkins et al., 2003). To compute equation 3.21 for the 2dFGRS, that model can be used in the integral on the numerator. Non-linear effects due to peculiar velocities in the sample should be insignificant by taking the upper limit of the integral $s = 20\ h^{-1}$Mpc.

Then, the equivalent averaged correlation function in real-space can be determined by:

$$\bar{\xi}^r(z=0) = \frac{\bar{\xi}^s(z=0)}{1 + \frac{2}{3}\beta(z=0) + \frac{1}{5}\beta(z=0)^2} \tag{3.22}$$

Now the real-space mass correlation function is obtained with:

$$\bar{\xi}^r_{mass}(z=0) = \frac{\bar{\xi}^r(z=0)}{b(z=0)^2}, \tag{3.23}$$

where $b(z=0)$ is given by equation 3.20.

Once determined the real-space correlation function of the mass at $z = 0$, its value at $z = 1.4$ is obtained using linear perturbation theory. Hence, at $z = 1.4$, the real-space correlation function of the mass will be:

$$\bar{\xi}^r_{mass}(z=1.4) = \frac{\bar{\xi}^r_{mass}(z=0)}{G(z=1.4)^2}, \tag{3.24}$$

where $G(z)$ is the growth factor of perturbations, given by linear theory and depends on cosmology (in this case the test cosmology) (Carroll et al., 1992).

Once the value of $\bar{\xi}^r_{mass}(z=1.4)$ is obtained for a given test cosmology, the process to find $\beta(z=1.4)$ is similar to the one used to find $\bar{\xi}^r_{mass}(z=0)$, but now the steps are performed backwards:

$\bar{\xi}^s(z=1.4)$ can be measured in a similar way as $\bar{\xi}^s(z=0)$. The bias factor at $z \approx 1.4$ is given by:

$$b(z=1.4)^2 = \frac{\bar{\xi}^r(z=1.4)}{\bar{\xi}^r_{mass}(z=1.4)}, \tag{3.25}$$

where $\bar{\xi}^r_{mass}$ is given by equation 3.24 and $\bar{\xi}^r(z=1.4)$ is obtained by:

$$\bar{\xi}^r(z=1.4) = \frac{\bar{\xi}^s(z=1.4)}{1 + \frac{2}{3}\beta(z=1.4) + \frac{1}{5}\beta(z=1.4)^2} \tag{3.26}$$

The value of $\beta(z=1.4)$ can then be determined by:

$$\beta(z=1.4) = \frac{(\Omega_m(z=1.4))^{0.6}}{b(z=1.4)}, \tag{3.27}$$

where $b(z = 1.4)$ is given by equation 3.25 and $\Omega_m(z = 1.4)$ is the value of the matter density at $z = 1.4$, given by:

$$\Omega_m(z) = \frac{\Omega_m^0(1+z)^3}{\Omega_m^0(1+z)^3 + \Omega_\Lambda^0}, \tag{3.28}$$

for a flat universe.

In the end, for a given value of Ω_m^0 in the test cosmology, $\beta(z)$ will be obtained by solving a second order polynomial equation.

The confidence levels on the computed values of $\beta(z = 1.4)$ can be obtained by considering the errors on this calculation. These are found by identifying the factors that contribute to the error, and adding the components in quadrature. Here, the components contributing to the error on $\beta(z = 1.4)$ are $\beta(z = 0)$, $\bar{\xi}^s(z = 0)$ and $\bar{\xi}^s(z = 1.4)$.

3.6 Results

We assume the double power-law $\xi(r)$ model to compute the constraints on Ω_m^0 and $\beta(z)$ from the $\xi(\sigma, \pi)$ shape. By substituting this function in Eq. 3.5 we find the subsequent expressions for the moments of the correlation function and hence the form of $\xi(\sigma, \pi)$ (see Appendix B).

It should be noted that there is some sensitivity in the $\xi(\sigma, \pi)$ fits to the detailed form of the assumed QSO $\xi(r)$. If the model for $\xi(r)$ is inaccurate then instead of fitting the distortion's *shape* in the $[\sigma, \pi]$ plane, the fits will be dominated by small differences in the average *amplitude*. As has been seen already in Section 4, the β constraints from the $\xi(s)/\xi(r)$ ratio are also sensitive to the assumed $\xi(r)$ form. In both cases, assuming single power-law models for $\xi(r)$ would lead to higher fitted values of $\beta(z = 1.4)$. We have argued that the single power-law model narrowly fails to fit the observed QSO $\xi(s)$ and $w_p(\sigma)$ results. As well as improving the fits to these data, the double power-law model for $\xi(r)$ is also a better representation of the correlation function results in the 2dFGRS (and Durham/UKST) galaxy survey and also in ΛCDM simulations.

The solid lines and the shaded areas in Fig. 3.6 represent the results from fitting $\xi(\sigma, \pi)$ models to the z-space distortions. The plots show similar likelihood contours for both the assumed cosmologies. This is as expected, since they should in theory be independent of the assumed value of Ω_m^0. The small differences that are seen are due to differences in binning the pairs between the two assumed cosmologies. It can be seen that the constraints on $\beta(z = 1.4)$ are much stronger than the constraints on Ω_m^0. Also, the lower the value of Ω_m^0, i.e. higher Ω_Λ^0, the more significant the effects of the geometric distortions are. This is reflected in the increased curvature of the contours for low Ω_m^0. This positive slope of these contours helps breaking the degeneracy between Ω_m^0 and β, when combining the results with constraints from linear growth theory (see below).

The dashed lines represent the 1σ and 2σ levels obtained from the bias evolution with redshift. We note that there is excellent overlap with the 1σ constraints from z-distortions. Essentially, it shows that the amplitudes of mass clustering at $z \approx 1.4$, allowed by 2dFGRS dynamical analysis

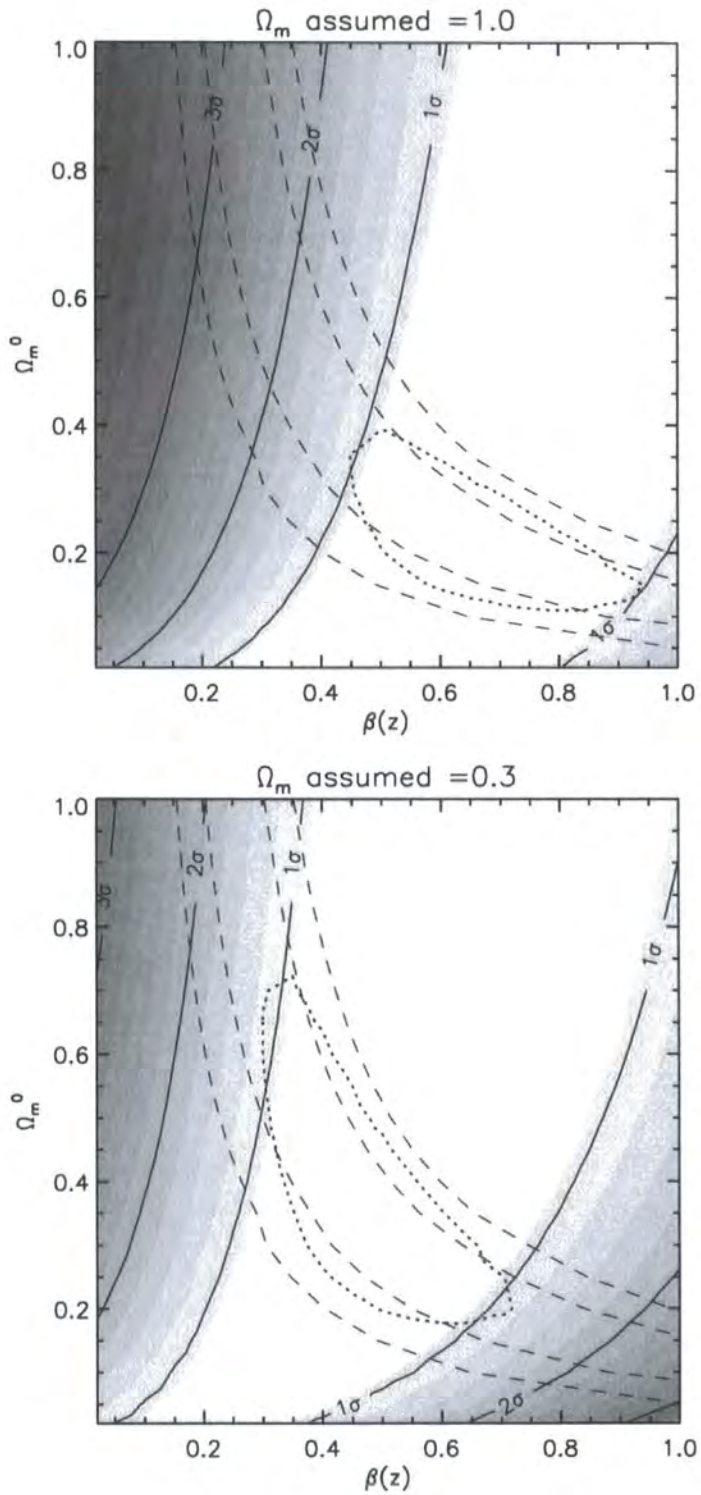

Figure 3.6: The confidence levels in the $[\Omega_m^0, \beta(z)]$ plane obtained if $\xi(r)$ is described by the double power-law model, obtained from fitting the distortions in the $\xi(\sigma, \pi)$ contours (grey-scale and solid confidence levels) and from QSO clustering evolution derived from linear theory (dashed 1σ and 2σ confidence levels). The dotted line shows the joint two-parameter 1σ confidence level obtained from combining both methods.

at $z \approx 0.1$, are consistent with the z-space distortions results from the QSOs, also at $z \approx 1.4$.

Finally we combine both the constraints from z-distortions and evolution to obtain the joint constraint represented by the dotted line. It shows the joint two-parameter 1σ confidence level obtained with both methods.

If the EdS cosmology is assumed, the best fitting values for Ω_m^0 and $\beta(z = 1.4)$ from the joint constraints are: $\Omega_m^0 = 0.20^{+0.06}_{-0.11}$ and $\beta(z = 1.4) = 0.70^{+0.15}_{-0.18}$, with a reduced χ^2_{min} of 1.10 (12 d.o.f). If the Λ cosmology is assumed instead, the best fitting values for Ω_m^0 and $\beta(z = 1.4)$ will be: $\Omega_m^0 = 0.35^{+0.19}_{-0.13}$ and $\beta(z = 1.4) = 0.50^{+0.13}_{-0.15}$, with a reduced χ^2_{min} of 1.05 (17 d.o.f.). Making the assumption of a double power-law model and the Λ cosmology, the $\beta(z)$ constraint obtained from fitting the shape of $\xi(\sigma, \pi)$, $\beta(z = 1.4) = 0.50^{+0.13}_{-0.15}$, is slightly higher than the value of $\beta(z = 1.4) = 0.32^{+0.09}_{-0.11}$ obtained from fitting $\xi(s)/\xi(r)$, but these results are consistent within the margin of error.

Our results are also consistent with previous estimates of $\beta(z = 1.4)$ and Ω_m^0 from the 2QZ. This can be seen by comparing Fig. 3.6 with Fig. 9 of Hoyle et al. (2002). However, the $\xi(\sigma, \pi)$ analysis presented here supersedes that of Hoyle et al. (2002), not only because of the $\approx 2\times$ larger QSO data set but also because of our improved z-space distortion analysis. More recently Outram et al. (2004) used the power spectrum to study the z-space distortions in the 2QZ clustering. Their method probes larger scales than those in this work. Their constraints of $\beta(z = 1.4) = 0.45^{+0.09}_{-0.11}$ and $\Omega_m^0 = 0.29^{+0.17}_{-0.09}$ are also in very good agreement with our estimate.

3.7 Conclusions

Modelling the z-space distortions in $\xi(\sigma, \pi)$ allows constraints on Ω_m^0 and $\beta(z = 1.4)$ to be derived. For the analysis we have assumed a pairwise velocity dispersion of $800\,\mathrm{km\,s^{-1}}$. Since this is dominated by z-errors ($\pm 600\,\mathrm{km\,s^{-1}}$ pairwise) our results should be robust to reasonable variations in this parameter; the pairwise velocity dispersion for the mass, for $\Omega_m^0 = 0.3$ at $z = 1.4$, is $< w_z^2 >^{1/2} \approx 400\,\mathrm{km\,s^{-1}}$ (Hoyle, 2000) and under simple assumptions this may only increase to $\approx 700\,\mathrm{km\,s^{-1}}$, for $\Omega_m^0 = 1.0$.

We compared the $\xi(\sigma, \pi)$ z-space distortions model with that previously used by Hoyle et al. (2002), and found that the latter suffers from a systematic offset between the amplitude of the input $\xi(s)$ and the $\xi(\sigma, \pi)$ amplitude. This does not seem to occur in the model used in the current work (Matsubara and Suto, 1996).

Although the $\xi(\sigma, \pi)$ fitting is sensitive to the form of the $\xi(r)$ model, assuming the double power-law model derived above, we have obtained useful constraints on $\beta(z = 1.4)$ from the z-space distortions analysis. The constraint on Ω_m^0 is not as strong from z-space distortions alone, being quite degenerate with the constraints on $\beta(z = 1.4)$. Combining these z-space distortions results with those from QSO bias evolution helps to break this degeneracy and provides much stronger constraints. The resulting constraints are $\Omega_m^0 = 0.35^{+0.19}_{-0.13}$ and $\beta(z = 1.4) = 0.50^{+0.13}_{-0.15}$,

assuming the Λ cosmology. Assuming the EdS cosmology instead produces similar results. These values are in very good agreement with the results found by Outram et al. (2004).

Chapter 4

Constraining $\beta(z)$ and Ω_m^0 from z-space distortions in $z \sim 3$ galaxy surveys

4.1 Introduction

Lyman-break galaxies are detected at $z \sim 3$ and, due to their high sky density ($\sim$ 1 LBG per arcmin^2) and scientific interest, such as the study of galaxy formation/evolution at early times in the history of the Universe or the existence/role of feedback mechanisms at $z \sim 3$, they are an excellent class of objects to study z-space distortions. They can be selected by identifying the Lyman continuum discontinuity which, at the galaxy's redshift, will determine their location in the $[U-B, B-R]$ plane.

By observing the LBGs in the line-of-sight of higher-z QSOs, the LBG distribution allows us to study of galaxy-IGM interactions, through LBG - Lyα system and LBG-CIV system cross-correlations (e.g. Adelberger et al., 2003). The spatial distribution of the Lyα and CIV systems can be probed via the redshifted 1216$\AA$ and 1549$\AA$ absorption features on the QSO spectra. Cross-correlating the LBG and gas distribution is a powerful way to determine the effects of feedback mechanisms in the process of galaxy formation and large-scale structure evolution. Such feedback effects have been observed in the form of galactic winds, due to violent star formation episodes, in $z \sim 3$ galaxies (Pettini et al., 2002). These interactions affect both galaxy formation (Theuns et al., 2001; Scannapieco et al., 2002) and the metal enrichment of the IGM (Theuns et al., 2002). $\xi(\sigma, \pi)$ measurements of both the LBG - LBG autocorrelation (e.g. da Ângela et al., 2005) and LBG - Lyα, LBG - CIV systems will also allow us to place dynamical constraints on the infall of Lyα systems onto the potential well of the protoclusters where the LBGs live.

It is therefore of crucial importance to understand the LBG-LBG z-space distortions. The galaxy - gas cross-correlation will be significantly affected by the LBG dynamics. As a first step in order to understand these distortions imprinted in the LBG autocorrelation function, we use a sample of $\sim$ 800 LBGs to model the LBG z-space distortions and infer the values of Ω_m^0 and $\beta(z)$

from these.

4.2 The LBG data

The LBGs used in this work are included in the sample of Steidel et al. (2003). The survey presented in their work comprises 17 fields, covering an area of 0.38 deg^2, and the total number of $2.67 < z < 3.25$ LBGs spectroscopically confirmed is 940.

The details of the complete survey and the data used can be found in Steidel et al. (2003). $[U, G, \mathcal{R}]_{AB}$ imaging was obtained at several telescopes and used to select the LBGs via the Lyman break technique. The spectroscopic follow-up was performed at both the Keck I and Keck II telescopes. The size of the largest field is 15.6 arcmin and the smallest 3.7 arcmin. These limited sizes compromise any clustering analysis that depends on the information on the sky direction. Seven of these fields contain a background QSO, whose spectrum can be used to probe the spatial distribution of Lyman α and metal systems.

The photometric catalogue from which the LBGs were selected includes 2347 photometrically selected candidates. These have an apparent $\mathcal{R}_{AB}$ magnitude limit of 25.5 and satisfy the colour criteria: $G_{AB} - \mathcal{R}_{AB} \leq 1.2$, $(U_{(n,AB)} - G_{AB}) \geq (G_{AB} - \mathcal{R}_{AB}) + 1.0$.

The determination of the redshift of these candidates was, in many cases, derived from the interstellar absorption lines of strong transitions, at $1200 - 1700\mathring{A}$ rest-frame. In some cases, the identification of the LBGs was also possible by identifying the Lyman-α line. In order to reduce effects due to redshift errors that would influence our clustering analysis, especially at small scales, we decided to include in our sample only the LBGs with class 1 redshift, as defined by Steidel et al. (2003). The choice of considering only class 1 redshift LBGs and the redshift range $2.6 < z < 3.4$ leaves us with 813 selected galaxies. Table 4.1 shows the number of selected LBGs in each of the fields. The field names are the same as adopted by Steidel et al. (2003).

The Lyman-α line and the absorption lines are usually separated by a factor of a few hundred $\mathrm{km\,s^{-1}}$, a feature that is often considered as evidence of powerful outflows from LBGs. It is prudent to account for this effect, in order to have a more precise estimation of the galaxies' redshifts. Following Adelberger et al. (2003) we assume a simple outflow model as an explanation for this, where the interstellar absorption lines are produced "in front" of the outflow and hence are *blueshifted* relative to the galaxy; whereas the Lyman-α line is produced in the opposite side of the outflow, "behind" the galaxy in the observer's line of sight. Assuming this simple picture, the systemic redshifts of the LBGs can be determined as follows:

If no absorption features are easily identified and the redshift is determined from the Lyman-α line only, then the following correction is applied:

$$z_{LBG} = z_{Ly\alpha} - \frac{v_{Ly\alpha}}{c}, \tag{4.1}$$

Field Name	Dimension (arcmin^2)	Number of LBGs
Q0000-263	3.69 × 5.13	15
CDFa	8.80 × 8.91	34
CDFb	9.05 × 9.10	20
Q0201+1120	8.69 × 8.72	21
Q0256-000	8.54 × 8.46	42
Q0302-003	15.59 × 15.71	40
B20902+34	6.36 × 6.57	30
Q0933+2854	8.93 × 9.28	58
HDF-N	8.62 × 8.73	53
Westphal	15.02 × 15.10	176
Q1422+2309	7.28 × 15.51	109
3C 324	6.65 × 6.63	11
SSA22a	8.74 × 8.89	50
SSA22b	8.64 × 8.98	35
DSF2237a	9.08 × 9.08	39
DSF2237b	8.99 × 9.08	42
Q2233+1341	9.25 × 9.25	38

Table 4.1: The dimensions of each of the LBG fields in this survey and the number of selected LBGs in each field. The field names are the same as adopted by Steidel et al. (2003). When the field contains a bright higher-z QSO, the name of the field is the same as that of the QSO. Some of the fields are adjacent (CDFa and CDFb; SSA22a and SSA22b; DSF2237a and DSF2237b).

where z_{LBG} is the "corrected" redshift of the galaxy, $z_{Ly\alpha}$ the redshift measured from fitting a Gaussian to the Lyman-α line's profile, $v_{Ly\alpha}$ the mean velocity of the Lyman-α relative to the galaxy's nebular lines and c is the speed of light. Following Adelberger et al. (2003), we take $v_{Ly\alpha} = 310\,\mathrm{km\,s^{-1}}$.

Similarly, if the redshift is only estimated from the absorption lines, then the correction will be:

$$z_{LBG} = z_{abs} - \frac{v_{abs}}{c}, \tag{4.2}$$

where z_{abs} is the redshift measured from the centroids positions of well-defined absorption lines and v_{abs} is the mean velocity of the interstellar absorption lines relative to the nebular lines. As we consider the absorption lines to be "blueshifted" relative to the galaxy, v_{abs} will be negative. Following Adelberger et al. (2003), we take $v_{abs} = -150\,\mathrm{km\,s^{-1}}$.

In some cases, when both $z_{Ly\alpha}$ and z_{abs} are measured, we apply the following correction (Adelberger et al., 2003):

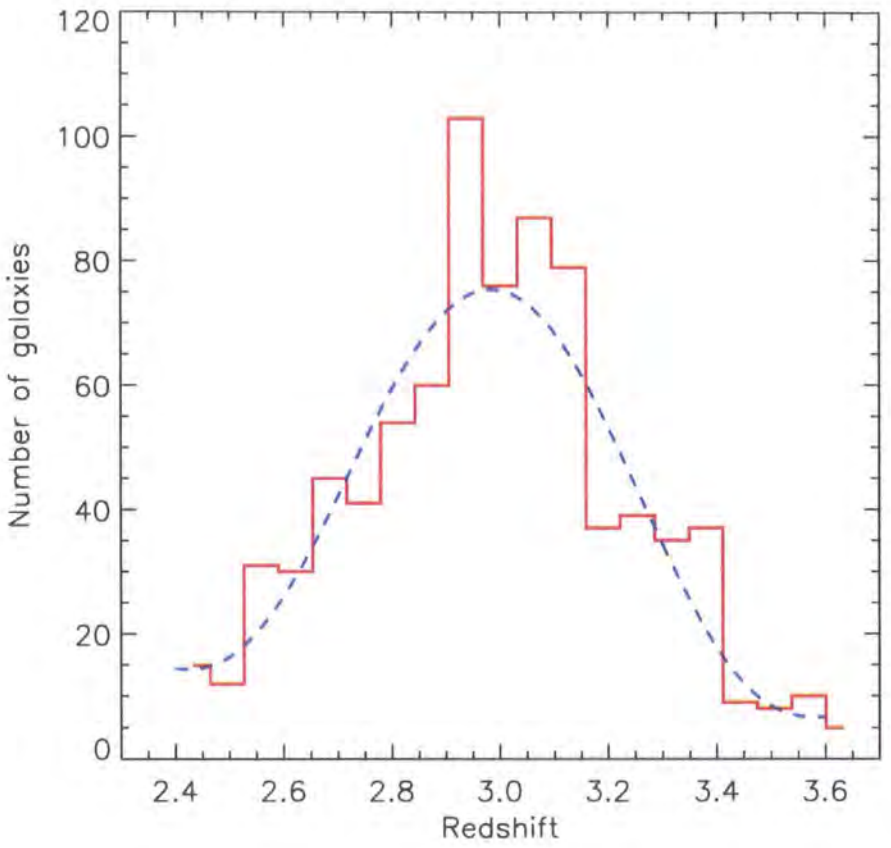

Figure 4.1: The solid line is an histogram showing the redshift distribution of the 813 LBGs taken from the catalogue of Steidel et al. (2003). The dashed line is a 4^{th} order polynomial fit to the distribution.

$$z_{LBG} = \frac{z_{Ly\alpha} + z_{abs}}{2} - \frac{-0.114\Delta v + 230}{c}, \tag{4.3}$$

where $\Delta v = v_{Ly\alpha} - v_{abs}$.

Adelberger et al. (2003), from a subsample of the LBGs used in this work, found a value of $< \Delta v >= 614 \pm 314\,\mathrm{km\,s^{-1}}$ for the average separation between $v_{Ly\alpha}$ and v_{abs}. The "velocity error" of $314\,\mathrm{km\,s^{-1}}$ corresponds to an uncertainty of $\sim 5.6\,h^{-1}$Mpc (comoving separation), that, in terms of z-space distortions, produces a similar effect to the small-scale galaxy velocity dispersion.

Fig. 4.1 shows the redshift (z_{LBG}) distribution of our sample (solid red line), after computing the corrections discussed. This distribution is similar to the redshift distribution presented by Steidel et al. (2003) (see their Fig. 10). The dashed line is a 4^{th} order polynomial fit to the redshift distribution.

To quantify the clustering, we must generate a "random" distribution occupying the same volume as the LBGs in the survey. In order not to wrongly interpret any completeness issue as

a feature in the clustering, the random distribution must follow the same completeness as the galaxy survey. Therefore, we generated a random set of points in each the fields of the survey. We generated 20 randoms for each LBG in each field. For each of the fields, the redshift distribution of this new ensemble is described by the 4^{th} order polynomial fit to the LBGs' distribution. Unfortunately, we do not have full information about the sky completeness of the individual fields. Hence, values for the declination and right ascension are randomly generated, within the field-of-view of each field. The distribution of the number of LBGs as a function of angular distance to the centre of the field (or, in some cases, the position of the background QSO) is consistent with the non-existence of radial gradients. It is possible that normalising the random distribution to the number density of galaxies in each field causes some clustering features to be "washed out". If one or more specific fields lie directly in regions with particularly high (or low) clustering signal, then by generating random sets independently of the space density in other fields will cause this structure to become unnoticeable. In order to understand how significantly our measurements are affected by this we re-computed the calculations described in Sections 3, 4, and 5, but using a random set of points generated for all the fields simultaneously. The difference between the two results was within the 1 σ confidence level. Similarly, by repeating these calculations using different polynomial fits to the LBG $N(z)$ as models for the randoms' redshift distribution, we concluded that different $N(z)$ models lead to very similar clustering measurements.

4.3 The redshift-space two-point correlation function, $\xi(\sigma, \pi)$

Consider the projection of the z-space separation s, between two LBGs, along and across the line-of-sight. The z-space correlation function can be measured in these two directions, which are given by:

$$\pi = |s_2 - s_1| \tag{4.4}$$

$$\sigma = (s_2 + s_1)\theta/2 \tag{4.5}$$

where s_1 and s_2 are the distances to two different galaxies, measured in z-space, and θ the angular separation between them.

As mentioned above, to estimate the correlation function, a random set of points probing the same volume as the LBGs must be generated. This ensemble must have all the characteristics as the LBGs, such as the sky and redshift distributions, although it can not reproduce their clustering.

Then, the correlation function $\xi(\sigma, \pi)$ can be computed using the estimator (Landy and Szalay, 1993):

$$\xi(\sigma, \pi) = \frac{< DD(\sigma, \pi) > -2 < DR(\sigma, \pi) > + < RR(\sigma, \pi) >}{< RR(\sigma, \pi) >}, \tag{4.6}$$

where $< DD(\sigma, \pi) >$ is the number of LBG-LBG pairs, $< RR(\sigma, \pi) >$ the number of random-random pairs and $< DR(\sigma, \pi) >$ the number of LBG-random pairs with separations along and

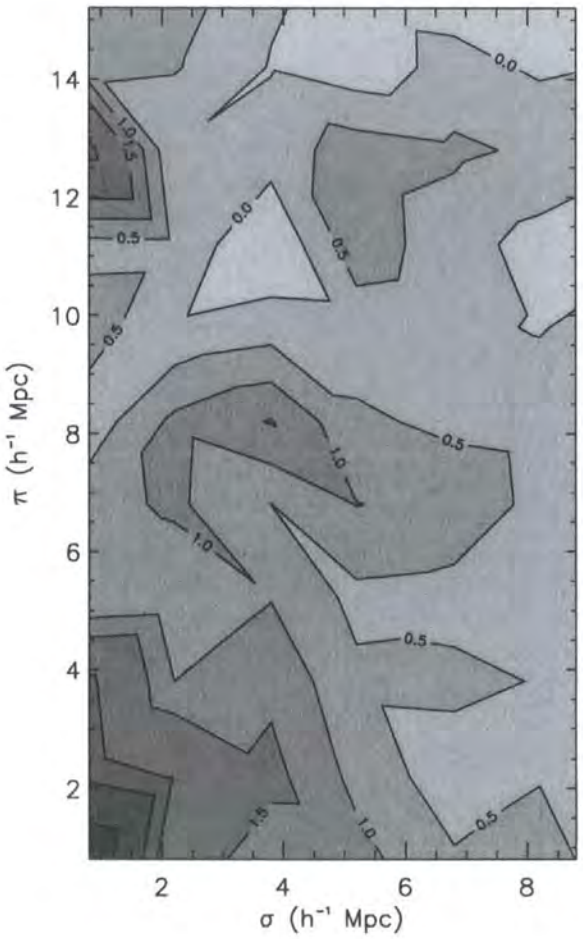

Figure 4.2: $\xi(\sigma, \pi)$ measured for the sample of 813 LBGs, assuming a flat, $\Omega_m^0 = 0.3$ cosmology.

across the line-of-sight given by σ and π, respectively.

Fig. 4.2 shows $\xi(\sigma, \pi)$ measured for our LBG sample. As previously discussed, the shape of the $\xi(\sigma, \pi)$ contours depends greatly on dynamical and geometrical effects, whose effects on the clustering can be highly anisotropic.

The LBGs' peculiar velocities lead to distortions in the $\xi(\sigma, \pi)$ shape, mainly at small scales. The random peculiar motions of the QSOs will cause an elongation of the clustering signal along the π direction. The predominant effect at large scales is the coherent infall of the LBGs into the potential well of overdense regions, which causes a flattening of the $\xi(\sigma, \pi)$ contours along the π direction and some elongation along σ.

Geometric distortions also occur if the cosmology assumed to convert the observed QSO redshifts into distances is not the same as the true, underlying cosmology of the Universe. The reason is because the cosmology dependence of the separations along the redshift direction is not the same as the one of the separations measured in the perpendicular direction (chapter 3, Alcock and Paczynski 1979).

Our result does not reproduce the extreme elongation along the line-of-sight seen in Fig. 20

of Adelberger et al. (2003), measured from a subsample of the LBGs used here, indicating that the feature was probably due to noise, arising from the small number of LBG pairs at small separations. The effects of the velocity error of $\sim 314\,\mathrm{km\,s^{-1}}$ quoted by Adelberger et al. (2003) are therefore not evident in this plot, possibly due to the cancelling of "finger-of-God" effects and infall, but more probably due to the effects of noise.

4.4 Obtaining the projected correlation function

The z-space correlation function consists of a "distorted" measurement of the clustering properties of the LBGs. Our goal is to use these distortions to derive constraints on $\beta(z=3)$ and Ω_m^0 and draw conclusions on the bias and infall of the galaxies at an early stage in the history of the Universe, as well as discuss the improvement that can be achieved with larger, future LBG surveys. However, the study of the real-space correlation function has, just for itself, an obvious interest, as it gives direct information about how galaxies cluster, independently of z-space distortion effects.

A picture of the real-space clustering can be obtained considering the clustering measured along the σ direction, since it will not be affected by the z-space distortions. This can be obtained by projecting $\xi(\sigma,\pi)$ along the σ direction, which will give information about the real-space correlation function, $\xi(r)$. As we have seen:

$$w_p(\sigma) = 2\int_0^\infty \xi(\sigma,\pi)d\pi, \tag{4.7}$$

Fig. 4.3 shows $w_p(\sigma)/\sigma$, obtained from integrating the already shown $\xi(\sigma,\pi)$ along the π direction. To compute the errors, we used the Poisson estimate: $\Delta\xi = (1+\xi)\sqrt{1/ < DD >}$. The circles are the measured values in the present survey. The diamonds are the values found by Adelberger et al. (2003), using a subsample of the LBG ensemble for the current work. For a better comparison with their results, we used the same values for the upper limit of the $\xi(\sigma,\pi)$ integration. Hence, this upper limit is the greater of 1000 $\mathrm{kms^{-1}}(1+z)/H(z)$ and 7σ. The fact that the values found by Adelberger et al. (2003) are systematically below our results is probably mainly due to differences in the random catalogue generated. However, this discrepancy is smaller than the error-bars in both results.

If $\xi(r)$ can be approximated by a power-law function with the form $\xi(r) = (r/r_0)^{-\gamma}$, it then follows from equation 4.7 that:

$$w_p(\sigma) = r_0^\gamma \sigma^{1-\gamma}\left(\frac{\Gamma\left(\frac{1}{2}\right)\Gamma\left(\frac{\gamma-1}{2}\right)}{\Gamma\left(\frac{\gamma}{2}\right)}\right), \tag{4.8}$$

where $\Gamma(x)$ is the Gamma function computed at x. Hence, $w_p(\sigma)/\sigma$ will also be given by a power-law with the same slope as $\xi(r)$. The best fitting power-law to the measured $w_p(\sigma)/\sigma$ is represented on the plot by a solid line, and it is parameterised by: $r_0 = 4.48^{+0.17}_{-0.18}\,h^{-1}\mathrm{Mpc}$ and $\gamma = 1.76^{+0.08}_{-0.09}$. Our $\xi(r)$ measurement has a higher amplitude and it is also steeper than that found by Adelberger et al. (2003) (they found $r_0 = 3.96^{+0.29}_{-0.29}$, $\gamma = 1.55^{+0.15}_{-0.15}$). Foucaud et al. (2003),

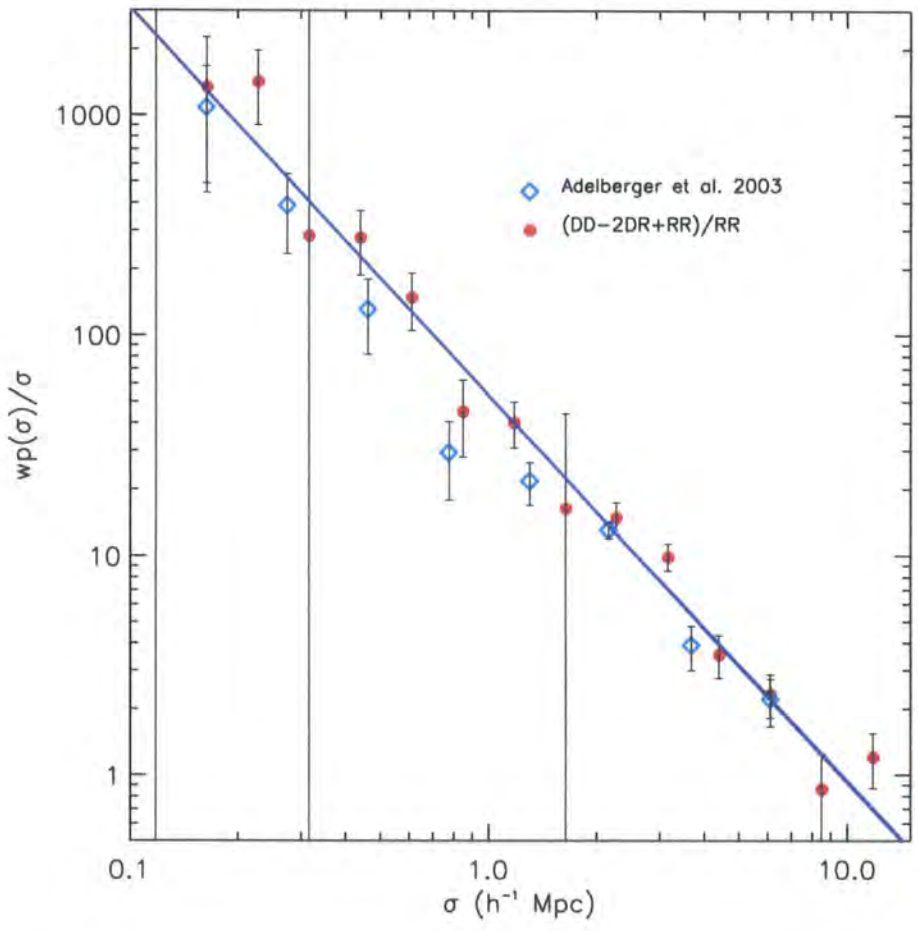

Figure 4.3: The projected correlation function measured for the LBG sample. The circles show the result obtained with the respective 1σ error bars. The solid line shows the best fitting power-law and the open diamonds the result obtained by Adelberger et al. (2003).

from a sample of 1294 LBG candidates from the Canada-France Deep Field Survey, measured r_0 for a fixed value of $\gamma = 1.8$ – which is in agreement with the slope measured here. Our amplitude is still smaller than their $w(\theta)$ measurements, which indicate $r_0 = 5.9^{+0.5}_{-0.5}\,h^{-1}$Mpc.

4.5 Obtaining the redshift-space correlation function, $\xi(s)$

In order to fit a model to the z-space distortions in $\xi(\sigma,\pi)$, the correct amplitude of the correlation function must be given as an input, in the fitting procedure. Since the fit is sensitive to the distortions in the shape of the z-space correlation function, its correct amplitude must be given as an input. Otherwise, the constraints obtained for Ω_m^0 and $\beta(z)$ will be such that their values are those needed to compensate the input $\xi(s)$, so that the *amplitude* of the model $\xi(\sigma,\pi)$ fits the *amplitude* of $\xi(\sigma,\pi)$ from the data, rather then being a good fit to the *distortions* in $\xi(\sigma,\pi)$. In principle, one could use the best-fitting $\xi(r)$ power-law as an input to the $\xi(\sigma,\pi)$ model, by decomposing it in two dimensions and adding the distortions. However, due to the limited size of the fields used in the survey, the behaviour of $\xi(r)$ at scales larger than $\sim 10\,h^{-1}$Mpc is unknown and, even considering that the power-law approximation is sufficiently good up to $\sim 10\,h^{-1}$Mpc, deviations from a simple power-law model at large scales, where $\xi(\sigma,\pi)$ is fitted, would cause shifts to the best-fitting values of $\beta(z)$ and Ω_m^0. The best way of introducing the amplitude of the correlation function correctly in the $\xi(\sigma,\pi)$ model is to input a very good description of the z-space correlation function's large-scale shape: $\xi(s)$.

$\xi(s)$ reflects the spherical average of $\xi(\sigma,\pi)$, since $s = \sqrt{\pi^2+\sigma^2}$. Fig. 4.4 shows our $\xi(s)$ measurements from the data.

To avoid underestimating the errors from contamination of correlated pairs of galaxies in the same separation bin, when the number of pairs is larger than the total number of galaxies the ratio $1/ < DD >$ in the Poisson error estimate is replaced by $1/N_{gal}$, N_{gal} being the total number of galaxies in the survey (Shanks and Boyle, 1994). The circles show the measured $\xi(s)$. The error bars represent the 1σ confidence level. The dashed line represents the best fitting power-law model to $\xi(s)$. Considering that the line is parameterised by $(s/s_0)^{-\gamma}$, then the best fitting values of s_0 and γ are given by $s_0 = 5.1^{+0.2}_{-0.1}\,h^{-1}$Mpc and $\gamma = 1.71^{+0.06}_{-0.09}$. Given the observed deviations from a simple power-law model on the $\xi(s)$ shape (the reduced χ^2_{min} of the fit is 4.07, with 16 degrees of freedom), a double power-law model for $\xi(s)$ was also fitted to the data. It was found that the best fitting model corresponded to having the two power-laws joining at $9\,h^{-1}$Mpc. Then, the amplitude of the power-law probing the large scales and the slope of both the power-laws were fitted. The amplitude of the innermost power-law was fixed in such a way that the "break" in the $\xi(s)$ shape was at $9\,h^{-1}$Mpc. The parameters characterising the two power-laws are: $s_0 = 5.673\,h^{-1}$Mpc and $\gamma = 1.30^{+0.06}_{-0.07}$, for $s < 9\,h^{-1}$Mpc and $s_0 = 7.5^{+0.4}_{-0.3}\,h^{-1}$Mpc and $\gamma = 3.29^{+0.21}_{-0.31}$, for $s > 9\,h^{-1}$Mpc. This function is represented by the solid line, in Fig. 4.4.

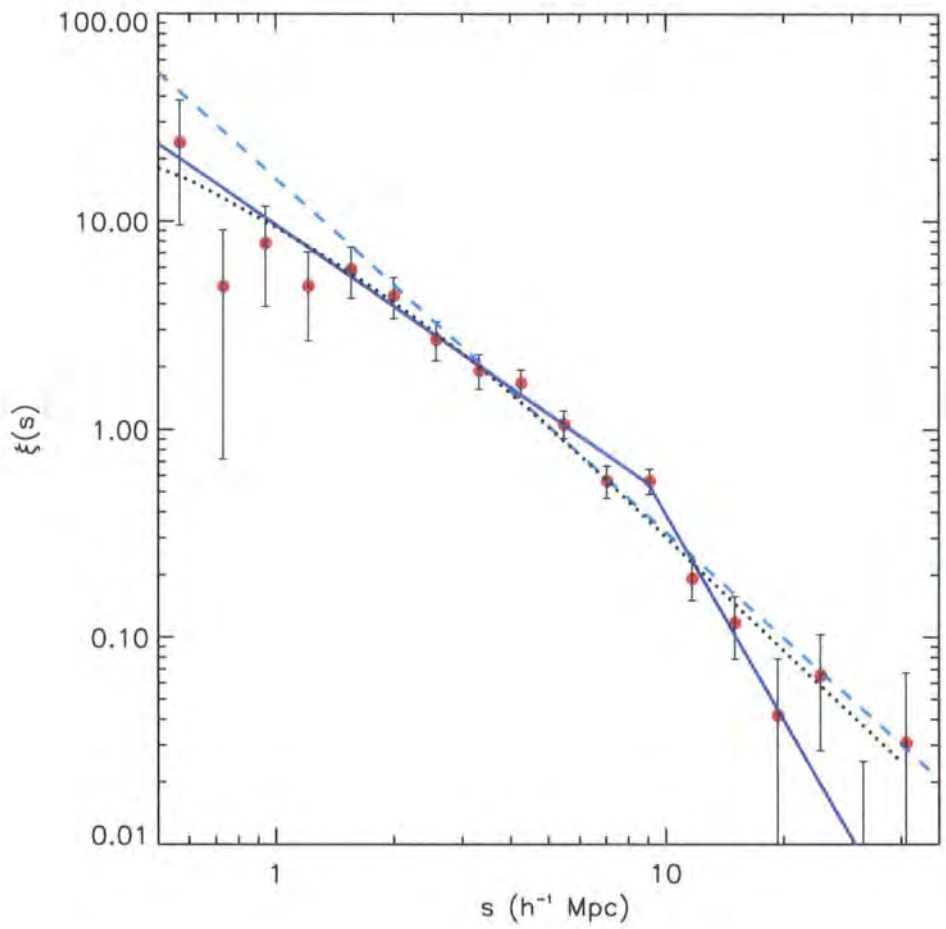

Figure 4.4: The z-space correlation function measured for the LBG sample. The circles show the result obtained with the respective 1σ Poisson error bars. The dashed line shows the best-fitting power-law to the data and the solid line the best fitting double power-law model. The dotted line is the predicted $\xi(s)$, derived from the power-law $\xi(r)$ model that best describes the $w_p(\sigma)$ data.

The shape of $\xi(s)$ suggests significant deviations from a simple power-law model. The interpretation of this result could include the effects of z-space distortions, affecting a power-law $\xi(r)$, whose form is derived from the $w_p(\sigma)$ results, as the small-scale random motions of the QSOs lead to a deficit of clustering amplitude measured at small scales. To confirm this hypothesis, we derived a $\xi(s)$ model from the best fitting power-law $\xi(r)$ to the $w_p(\sigma)$ results, by adding the distortions parameterised by $\beta(z=3)=0.25$ and $< w_z^2 >^{1/2}= 400\,\mathrm{km\,s^{-1}}$. These are likely values for those parameters (e.g., see Foucaud et al. (2003) and Adelberger et al. (2003)). To include the distortions in $\xi(r)$ and derive a prediction for $\xi(s)$, a $\xi(\sigma,\pi)$ model was derived from the $\xi(r)$ input form, and then this was integrated in annuli to obtain $\xi(s)$. The $\xi(\sigma,\pi)$ model and this method are described in detail in section 3.3.1 (Model 1) and appendix B. The dotted black line in Fig. 4.4 represents the obtained $\xi(s)$ result. This is still a good description of the data, within the errors, as it can be seen not only from the graph but also from the value of the reduced χ^2_{min}, which is 1.25, for 16 degrees of freedom. Given that these are high-redshift galaxies, the z-space distortions in $\xi(s)$ caused by the small-scale random motions are not very significant, and hence the observed flattening of $\xi(s)$ can hardly be explained by z-space distortions only.

Results from several other galaxy and QSO surveys, such as the 2dF Galaxy and QSO Redshift surveys, have indicated the possible existence of a shoulder, at $\sim 8-12\,h^{-1}$Mpc, in the respective correlation functions (see Hawkins et al., 2003; da Ângela et al., 2005). These results are also backed by the shape of the correlation function as suggested from CDM model predictions, or Halo Occupation distribution (HOD) models (da Ângela et al., 2005; Tinker et al., 2006b).

The double power-law model fitted to the data is a very good representation of the $\xi(s)$ results (the reduced χ^2_{min} of the fit is 0.66). The fact that the single power-law model for $\xi(r)$ also represents a good fit to the data, means that we can not prefer the double power-law model solely from the results of this work. However, when we take into account results from other surveys and theoretical models, the double power-law $\xi(s)$ model is more likely to be closer to the correct shape. Future LBG surveys will probe the projected correlation function at large separations.

The double power-law $\xi(s)$ model can therefore be used as the input for the amplitude of the z-space correlation function, provided that the fit is only performed on scales where the non-linear distortions caused by the random peculiar motions have a negligible contribution. As it can be seen from the dotted black line, which represents the $\xi(s)$ obtained from a simple power-law $\xi(r)$ model, this is clearly not a problem at scales greater than $6\,h^{-1}$Mpc, where the function follows very closely a power-law form (assuming the value $< w_z^2 >^{1/2}= 400\,\mathrm{km\,s^{-1}}$).

4.6 Constraints on β and Ω_m^0 from redshift-space distortions

Once we have a model describing how the amplitude of the correlation function varies with radial separation, in average, then the higher-order distortions observed on $\xi(\sigma,\pi)$ can be modelled.

The first step in modelling the z-space distortions is to build a $\xi(\sigma,\pi)$ model given an input $\xi(r)$. The latter can be obtained from a $\xi(s)$ form, if the $\xi(\sigma,\pi)$ fitting will be performed at scales where the main contribution for the distortions comes from the coherent infall. Then, the input $\xi(r)$ can be obtained by:

$$\xi(r) = \frac{\xi(s)}{1 + \frac{2}{3}\beta(z) + \frac{1}{5}\beta(z)^2} \tag{4.9}$$

If we assume a value for the velocity dispersion (we used $< w_z^2 >^{1/2} = 400\,\mathrm{km\,s^{-1}}$, following Adelberger et al. 2003) we can determine constraints on $\beta(z=3)$ and Ω_m^0, by applying the $\xi(\sigma,\pi)$ z-space distortion model described in chapter 3. As previously, the Ω_m^0 constraint follows from fitting the geometrical distortions in $\xi(\sigma,\pi)$, and adopting the definitions of *test* and *assumed cosmology* presented in chapter 3. Hence, the relations between the galaxy separations in both cosmologies are related as follows (Ballinger et al., 1996):

$$\sigma_t = f_\perp \sigma_a = \frac{B_t}{B_a}\,\sigma_a \tag{4.10}$$

$$\pi_t = f_\parallel \pi_a = \frac{A_t}{A_a}\,\pi_a \tag{4.11}$$

where again A and B are defined as:

$$A = \frac{c}{H_0}\frac{1}{\sqrt{\Omega_\Lambda^0 + \Omega_m^0(1+z)^3}} \tag{4.12}$$

$$B = \frac{c}{H_0}\int_0^z \frac{dz'}{\sqrt{\Omega_\Lambda^0 + \Omega_m^0(1+z')^3}} \tag{4.13}$$

and the subscripts t and a refer to the test and assumed cosmology, respectively.

If the same cosmology is assumed in the data and the model, then the observed shapes of the measured and modelled $\xi(\sigma,\pi)$ will be the same when the test cosmology is the same as the true, underlying cosmology of the Universe. Therefore, constraints on $\beta(z=3)$ and Ω_m^0 are obtained from simply doing a χ^2 fit between the data and the a series of different $\xi(\sigma,\pi)$ models, derived with different test cosmologies and values of $\beta(z=3)$.

The steps taken for this fitting procedure are similar to those described when fitting the $\xi(\sigma,\pi)$ z-space distortions in the 2QZ sample. Here however, we use the $\xi(s)$ amplitude and shape directly to derive a $\xi(r)$ model, rather than use the $w_p(\sigma)$ results to obtain a suitable $\xi(r)$ model. This is due to the limited size of the survey fields, which do not allow significant constraints in the $w_p(\sigma)$ clustering signal at scales $\sigma \gtrsim 10\,h^{-1}\mathrm{Mpc}$.

The number of degrees of freedom in the χ^2 fit is the total number of bins where $\xi(\sigma,\pi)$ from the model is fitted to the data minus the number of free parameters. If the fit is to Ω_m^0 and $\beta(z)$, the number of free parameters will be two. Although it can be argued that the $\xi(\sigma,\pi)$ bins may not be independent, the accuracy of these errors is supported by N-body simulations (Hoyle, 2000). The velocity dispersion was fixed to $400\,\mathrm{km\,s^{-1}}$ (Adelberger et al., 2003).

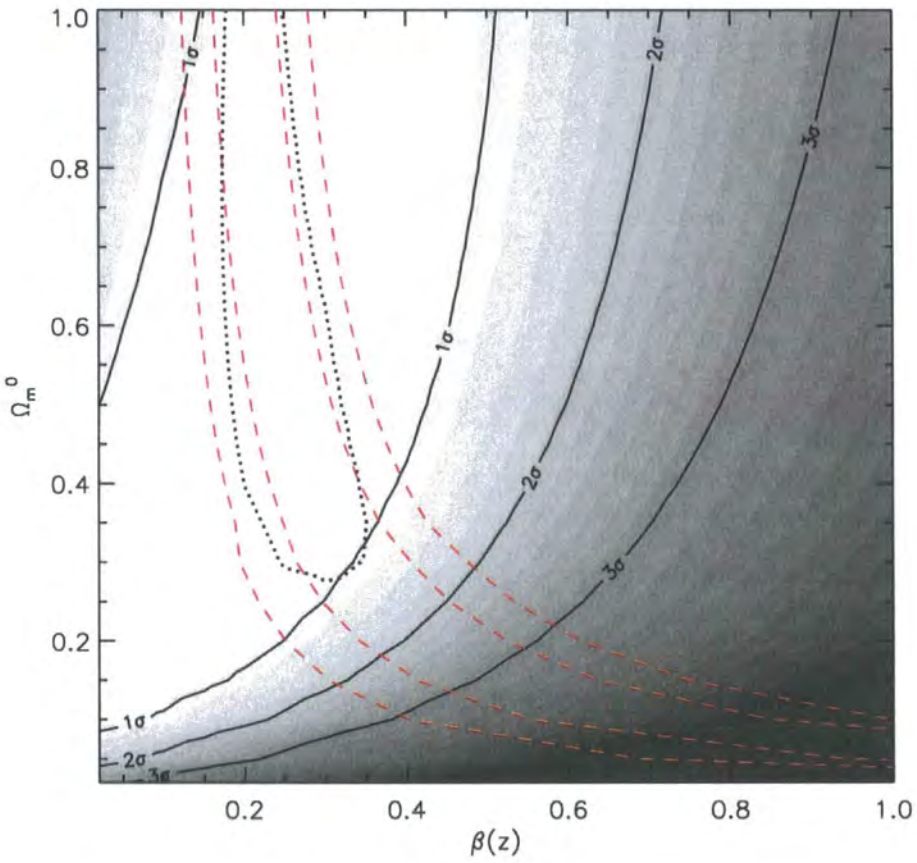

Figure 4.5: The confidence levels on the $[\Omega_m^0, \beta(z)]$ plane from fitting the z-space distortions in $\xi(\sigma, \pi)$ (grey scale and solid lines). The dashed lines show the 1σ and 2σ confidence levels obtained from linear growth theory, considering the value of β for local galaxies surveys. The joint 1σ confidence level is given by the dotted line.

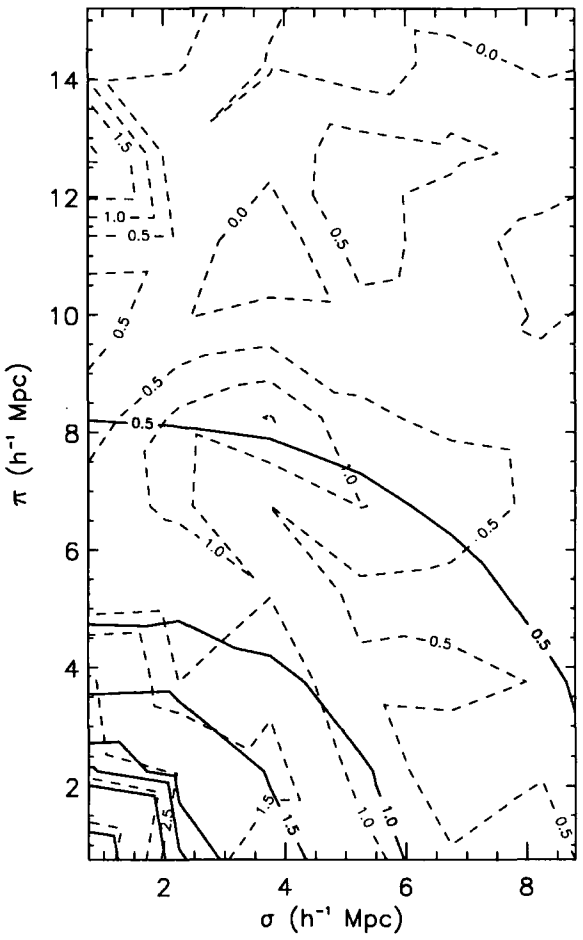

Figure 4.6: The best fitting model for $\xi(\sigma,\pi)$, obtained using the best fitting values of $\beta(z=3) = 0.25^{+0.05}_{-0.06}$ and $\Omega_m^0 = 0.55^{+0.45}_{-0.16}$ (solid line) and $\xi(\sigma,\pi)$ measured from the data (dashed line).

The result of doing this fit in the present data is shown in Fig. 4.5.

The shaded regions and the solid line refer to the confidence levels obtained from fitting the z-space distortions. These constraints alone correspond to best fitting values of $\beta(z=3) = 0.15^{+0.20}_{-0.15}$ and $\Omega_m^0 = 0.35^{+0.65}_{-0.22}$. The dashed lines are the 1σ and 2σ confidence levels obtained from clustering evolution, from applying linear growth theory and predicting the values of $\beta(z=3)$ for different cosmologies, using as an input the value of β at $z \sim 0.1$, obtained from the 2dFGRS survey (Hawkins et al., 2003). This method is described in detail in chapter 3. The dotted line represents the 1σ two parameter joint confidence level. The best fitting values are $\beta(z=3) = 0.25^{+0.05}_{-0.06}$ and $\Omega_m^0 = 0.55^{+0.45}_{-0.16}$. Fig. 4.6 shows the LBG $\xi(\sigma,\pi)$ (dashed line) and the best fitting $\xi(\sigma,\pi)$ model (solid line), obtained from the joint constraints on $\beta(z=3)$ and Ω_m^0. A visual comparison between the solid and the dashed contours also shows that the model is a good description of the $\xi(\sigma,\pi)$ data.

4.7 Discussion and Conclusions

Here we have used the z-space distortions on the clustering pattern of a sample of LBGs to derive constraints on $\beta(z=3)$ and Ω_m^0. The method used requires the spherical average amplitude of the correlation function to be accurately known and given as an input to the model. Due to the small size of the fields used in the survey, the clustering measured across the line-of-sight is not probed at scales larger than $10\,h^{-1}$Mpc. For this reason, and given that at $z=3$ only the smallest scales are significantly affected by non-linear distortions caused by the random motions of the galaxies, the input amplitude of the spherically averaged correlation function should be obtained from $\xi(s)$.

The $\xi(s)$ shape suggests that the real-space correlation function of the LBGs might deviate significantly from a simple power-law model, and these deviations are not evident in the projection $w_p(\sigma)$. Future LBG surveys where larger scales across the line-of-sight are probed, will allow a coherent picture of the clustering to be drawn from the $w_p(\sigma)$ and $\xi(s)$ measurements, similarly to what has been done for the 2dF QSO Redshift Survey (da Ângela et al., 2005).

Once a suitable model for describing the amplitude of the correlation function as a function of scale is obtained (a double power-law model was found to be a good description of the data, in the present case), then the z-space and geometric distortions can be modelled and constraints on $\beta(z=3)$ and Ω_m^0 drawn. The combination of these constraints with orthogonal confidence levels from linear growth of density perturbations, indicates that $\beta(z=3)=0.25^{+0.05}_{-0.06}$ and $\Omega_m^0=0.55^{+0.45}_{-0.16}$. These values are consistent with previous measurements of the bias. Foucaud et al. (2003) found, for a ΛCDM cosmology, $b=3.5\pm0.3$, using a sample of LBGs from the Canada-France Deep Field Survey. Considering the WMAP results (Spergel et al., 2003), if we take $\Omega_m^0=0.3$, which is within our computed error bars, their obtained value of b corresponds to $\beta(z=3)=0.27$, which is well within our derived error bars and hence consistent with our results. However, results from our $\xi(\sigma,\pi)$ fits strongly rely on the amplitude and shape of the input correlation function. If our input $\xi(s)$ shape is uncertain, then this may introduce errors in the measured constraints of Ω_m^0 and $\beta(z=3)$. We found that the derived constraints are very robust to 1 σ changes in the parameters describing the double power-law $\xi(s)$ model. However, changes to the assumed $\xi(s)$ (or $\xi(r)$) shape, will lead to more significant changes in the derived Ω_m^0 and $\beta(z=3)$ constraints. Unfortunately, with the present data it is difficult to measure the real-space correlation function. This handicap is basically due to two factors: the size of fields used; and the number of LBGs in the survey. Even though the latter is, in part, balanced by the high space density of these galaxies, the former prevents any real-space clustering measurement at scales $\gtrsim 10\,h^{-1}$Mpc, except via the $\xi(s)$ form. This hampers any attempt to build such a coherent picture of LBG clustering. We believe we have done the best that is possible with the current data. It is important to stress the advantage of the LBGs' high spatial density for z-space distortion analyses. The constraints in Ω_m^0 and $\beta(z)$ from the $\xi(\sigma,\pi)$ fitting alone are comparable to those achieved with the 2QZ sample (chapter 3, da Ângela et al. 2005), which includes $\sim$ 20000 QSOs. The much smaller number of LBGs is counterbalanced by their higher-spatial density, which dramatically increases

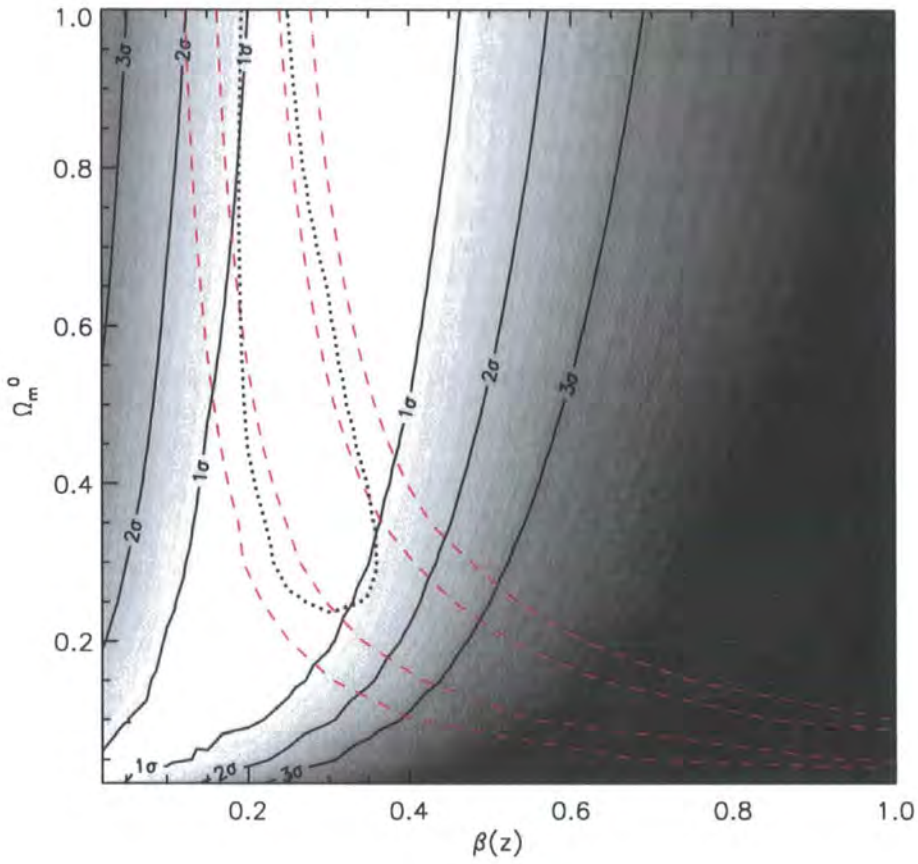

Figure 4.7: Constraints on Ω_m^0 and β from a mock *Hubble Volume* survey of $\sim$ 2300 LBGs. Again, the solid lines and shaded contours show the constraints obtained from the $\xi(\sigma, \pi)$ z-space distortion fitting. The dashed lines are the confidence levels obtained from linear theory constraints on $\beta(z = 3)$ and the dotted contour is the 1σ joint confidence level.

the clustering signal. Our results not only reflect what can be achieved in cosmological and dynamical constraints from z-space distortions, but they also foreshadow future work, based on larger LBG surveys. In particular, mock LBG catalogues built from the *Hubble Volume simulation* do show the improvement on the Ω_m^0, $\beta(z)$ confidence levels obtained from larger LBG surveys. In Fig. 4.7 it can be seen the expected confidence limits in Ω_m^0 and $\beta(z)$ from a mock LBG survey containing $\sim$ 2300 galaxies. The joint best fitting values are $\beta(z = 3) = 0.25^{+0.05}_{-0.02}$ and $\Omega_m^0 = 0.50^{+0.27}_{-0.23}$. Unfortunately, due to the low value of $\beta(z = 3)$ and the curvature of the constraints from linear evolution of density perturbations, the degeneracy between Ω_m^0 and $\beta(z)$ is not completely lifted, leading to a smaller constraint on the value of Ω_m^0 than that obtained in the previous chapter.

Chapter 5

QSO clustering in the 2SLAQ survey

5.1 Introduction

There is a significant amount of observational evidence for the existence of supermassive black holes in the centre of galactic haloes. This is based on studies which span a wide z-range. Whilst at low-z, the evidence for the presence of black holes comes from dynamical surveys of galaxies in the local Universe (Kormendy and Richstone, 1995; Richstone et al., 1998; Magorrian et al., 1998), at high-z, black hole – host galaxy studies are pursued by using the width of QSO broad emission lines to estimate black hole masses and the host galaxy's narrow emission lines to determine stellar velocity dispersion (e.g. Shields et al., 2006a,b). These results hint at a correlation between the growth and physics of the bulge and dark matter halo and the physics of accretion of mass onto the central black hole and subsequent growth (Tremaine et al., 2002; Baes et al., 2003; Wyithe and Loeb, 2005a; Wyithe and Padmanabhan, 2006). The relation between the bulge and its black hole is the subject of intense observational and theoretical interest (Kauffmann and Haehnelt, 2000; Ferrarese and Merritt, 2000; Gebhardt et al., 2000; Ferrarese, 2002; Wyithe and Loeb, 2005b). Many uncertainties still exist when trying to interpret this black hole - bulge connection. One possible scenario is that the mechanism that "feeds" black hole growth is the same, or is correlated to, those responsible for bulge growth, such as mergers or instabilities, which may also lead to enhanced star formation. Some of the gas may instead "fuel" the black hole, and consequently lead to quasar (QSO) activity (e.g. Bower et al., 2006). This picture is supported by the similar "shape" of the cosmological star formation history of the Universe and the evolution of the QSO number density, as a function of redshift (e.g. Schmidt et al., 1995; Madau et al., 1996; Dunlop et al., 2003).

In the standard scenario, QSO activity is triggered by accretion onto a supermassive black hole (SMBH, e.g. Hopkins et al., 2006). Given that the growth of the SMBH relates to that of the underlying dark matter halo (Baes et al., 2003; Wyithe and Loeb, 2005a; Wyithe and Padmanabhan, 2006) and this correlates to the local density contrast, clustering measurements provide an insight into QSO and black hole physics.

QSO clustering measurements allow determinations of halo masses and how they relate to black hole mass (e.g. Kauffmann and Haehnelt, 2000; Haehnelt and Kauffmann, 2000). QSO life-

times, which have been the basis of interpretations of QSO luminosity functions (Hopkins et al., 2005b) can also be inferred from clustering measurements (e.g. Croom et al., 2005), and hence permit us to discriminate between QSO evolutionary models, such as a cosmologically long-lived population (e.g. Boyle et al., 2000). Miller et al. (2005) addressed the change of accretion efficiency with redshift, arguing that, even though the mass of the black holes grows with time as galaxies grow hierarchically, the mean accretion rate decreases with decreasing redshift, hence leading to a decrease on the QSO luminosity with time. This picture is supported by theoretical models, such as that of Kauffmann and Haehnelt (2000).

The evolution of QSO clustering with redshift has been subject of recent study. In particular, the wealth of information contained in the Sloan Digital Sky Survey (SDSS) and the 2QZ survey data have allowed studies such as those of Myers et al. (2006), and Croom et al. (2005), who measured the redshift dependence of QSO clustering. In particular, the latter inferred the evolution of halo mass with redshift, besides estimating black hole masses and accretion efficiencies, based on QSO clustering measurements from the 2QZ sample. However, and as pointed out by those authors, these studies do not take into account any potential luminosity dependence of QSO clustering.

It is not trivial to address the possible dependence of QSO clustering on luminosity. This is due to the fact that, as result of the luminosity evolution and the fact that the 2QZ survey is flux-limited, the most luminous QSOs lie at high redshifts, while the faintest ones have low redshifts. The lowest and highest redshift objects on the 2QZ sample extend throughout separate luminosity ranges, hence hampering any attempt to study the effects of luminosity on QSO clustering, black hole masses and accretion efficiencies, free from any possible evolutionary biases.

This necessary caveat in any study of luminosity dependence of QSO clustering was one of the main motivations for the 2SLAQ (2dF -SDSS LRG and QSO) QSO survey. Using faint, photometric QSO candidates from the SDSS QSO survey, the observations at the 2dF facility result in an extension of the previous 2QZ survey to fainter magnitudes. The faint magnitude limit of $g = 21.85$ is ~ 1 magnitude fainter than that of the 2QZ, and the new data, spanning a similar z-range as the 2QZ, constitute a new, potentially powerful tool to disentangle the effects of luminosity and redshift on the clustering of QSOs, thus providing a new test of current QSO, black hole and bias models.

5.2 The 2SLAQ QSO Survey

The 2SLAQ QSO survey is an extension of the previous 2QZ survey to fainter magnitudes. The main aspects and description of this survey can be found in Richards et al. (2005), who report on the first 3 semesters of the data collection and present luminosity function results from the sample of ~ 5600 QSOs obtained at the time. Now that the survey has been completed and the analysis

of the data is being developed, there are a total of ~ 9000 ($z \lesssim 3$) QSOs. Both the imaging and spectroscopic data, obtained by the Sloan telescope and at the AAT respectively, are extensively described by those authors.

5.2.1 Photometric selection

The colour selection of the QSO candidates is described in detail by Richards et al. (2005). In particular, the following colour cuts were applied to the overall QSO sample: $A \wedge ((B \wedge C \wedge D) \vee E)$, where the letters refer to the conditions:

$$A: \ -1.0 < u-g < 0.8 \tag{5.1}$$

$$B: \ -0.8 < g-r < 0.0 \tag{5.2}$$

$$C: \ -0.6 < r-i < -0.1 \tag{5.3}$$

$$D: \ -1.0 < i-z < -0.1 \tag{5.4}$$

$$E: \ -1.5 < g-i < -0.3 \tag{5.5}$$

Further cuts are applied, with a form which depends on the candidate's magnitude. One selection was adopted for candidates with $18.0 < g < 21.15$ and a different one for objects with $21.15 \leq g < 21.85$. Since, in our clustering analysis, we will consider faint QSOs with $20.5 < g < 21.85$, both colour cuts are relevant for selecting QSO candidates. In addition to the colour cuts, we also discard objects with high r-band galaxy probability, according to the Bayesian star-galaxy classifier (Scranton et al., 2002), which, following Richards et al. (2005), we refer to as *galprob*. Hence, the additional cuts for $18.0 < g < 21.15$ candidates are $A \wedge \bar{B} \wedge \bar{C} \wedge \bar{D} \wedge \bar{E}$, and these conditions stand for:

$$A: \quad u-g<0.8 \ \wedge \ g-r<0.6 \ \wedge \ r-i<0.6 \tag{5.6}$$

$$B: \quad u-g>0.6 \ \wedge \ g-i>0.2 \tag{5.7}$$

$$C: \quad u-g<0.45 \ \wedge \ g-i>0.35 \tag{5.8}$$

$$D: \quad galprob>0.99 \ \wedge \ u-g>0.2 \ \wedge \ g-r>0.25 \ \wedge \ r-i<0.3 \tag{5.9}$$

$$E: \quad galprob>0.99 \ \wedge \ u-g>0.45 \tag{5.10}$$

These cuts specifically select the UVX candidates, while excluding F stars with low metallicity and NELGs which extend into the r band.

The fainter $21.15 < g < 21.85$ candidates satisfy the same $A \wedge \bar{B} \wedge \bar{C} \wedge \bar{D} \wedge \bar{E}$ conditions, but now these letters refer to:

$$A: \quad u-g<0.8 \ \wedge \ g-r<0.5 \ \wedge \ r-i<0.6 \tag{5.11}$$

$$B: \quad u-g>0.5 \quad \wedge \quad g-i>0.15 \tag{5.12}$$

$$C: \quad u-g<0.4 \quad \wedge \quad g-i>0.3 \tag{5.13}$$

$$D: \quad u-g>0.2 \quad \wedge \quad g-i>0.45 \tag{5.14}$$

$$E: \quad galprob>0.99 \quad \wedge \quad g-r>0.3 \tag{5.15}$$

These cuts are similar to the ones used for the brighter candidates, but are somewhat more restrictive, in order to prevent contamination from faint, main sequence stars. The colour cuts will also cause some photometric incompleteness. The reader is referred to Richards et al. (2005) for a discussion of these cuts.

5.2.2 Spectroscopic follow-up

The spectroscopic observations were performed using the 2dF instrument at the AAT. For details of the 2dF facility, see Lewis et al. (2002). The regions surveyed by the 2dF consist of two 2° – wide equatorial strips. Not all of the full strips were observed, but rather "sections" of them. Fig. 5.1 shows the two strips, on the NGC and SGC. The NGC photometric candidates are shown in green and the SGC ones in pink. The blue (red) circles are all the spectroscopically identified QSOs in the NGC (SGC). The 2dF pointings are shown as black circles. The "sections" in the NGC were indexed "a, b, c, d, e" and the one in the SGC "s". Each 2dF pointing was labelled the index of the region where it fell followed by a number, which refers to its position along the strip.

The QSO observations were performed simultaneously with those of the LRGs. 200 2dF fibres were allocated to the LRGs and 200 to the QSO observations. The LRG fibres then link to the 2dF "red spectrograph" and the QSO fibres to the "blue spectrograph". Each block of 10 fibres along the edge of the 2dF field connects to a different spectrograph, alternately blue and red. Therefore, the QSO completeness in each 2dF pointing shows a "dented structure" along the edge of the field, due to the fact that the fibres are limited to an angle of 14° (see, e.g. Richards et al., 2005). The probability of a given QSO/LRG candidate being assigned a 2dF fibre depends on its priority. The assigned priorities of the objects in the input catalogue (see table 5.1) will affect the likelihood that those objects will be observed. Objects with higher priority will have a higher likelihood to be assigned a 2dF fibre.

Tables 5.2 and 5.3 show the number of QSOs, narrow emission line galaxies (NELGs) and stars that were observed. $Q1$ and $Q2$ refer to the identification quality: $Q1$ are objects with good identification quality and $Q2$ refer to objects with lower identification quality (see section 2.3 of Croom et al. (2004) for further details on quality identification flags). Overall, the sky density of QSO candidates in 138.4 deg^{-2} and that of confirmed QSOs is 44.7 deg^{-2}.

As we are observing faint QSOs, we also expect them to have a higher space density than that achieved from other, previous surveys, such as the 2QZ or the SDSS. This is evident from the wedge plots in Figs. 5.2 and 5.3 (both courtesy of Peter Weilbacher), which show the radial

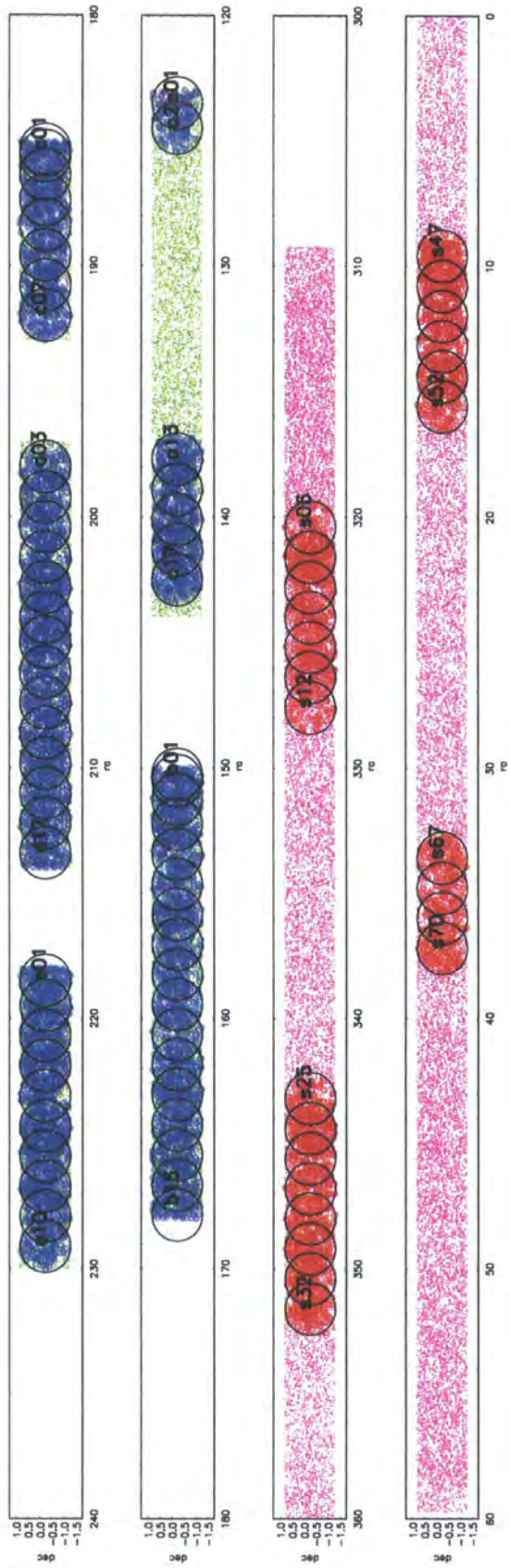

Figure 5.1: The 2SLAQ QSO strips. The black circles represent the 2dF fields observed. Green and pink points are the NGC and SGC QSO candidates, respectively. The small (blue and red) circles represent the positions of the (NGC and SGC) spectroscopically confirmed QSOs.

Objects	Priority
Guide stars	9
Main sample LRGs, sparsely sampled	8
Remaining main sample LRGs	7
$g > 20.5$ QSOs, sparsely sampled	6
Remaining $g > 20.5$ QSOs	5
Extra LRGs and high-z QSOs	4
$g < 20.5$ QSOs	3
Previously observed objects with good id	1

Table 5.1: 2dF priorities. Objects with higher priorities have a higher likelihood of being assigned a 2dF fibre.

ID	All	Q1	Q2
QSOs	6680 (57.89%)	6482 (56.17%)	198 (1.72%)
NELGs	2077 (18.00%)	2043 (17.71%)	34 (0.29%)
stars	1829 (15.85%)	1604 (13.90%)	225 (1.95%)
TOTAL	10586 (92.20%)	10129 (88.15%)	457 (4.05%)

Table 5.2: Number of QSOs in the NGC 2SLAQ strip.

projection of the 2SLAQ strips.

5.3 QSO clustering

Completeness issues within a 2dF pointing must be taken into account when constructing the angular mask used to generate a random set of points, which is necessary to measure QSO clustering from the 2SLAQ survey. The fraction of QSO candidates that were assigned a fibre and have a good redshift measurement varies from field to field, and this needs to be considered when building the mask. In addition, one needs to calculate the excess probability of finding a QSO in overlapping 2dF pointings. This excess probability is quantified by determining the ratio between the observed number of QSO candidates and the total number of candidates in the parent catalogue. This *fractional completeness* is then used to weight the probability of a QSO being

ID	All	Q1	Q2
QSOs	2378(49.68%)	2282(47.67%)	96(2.01%)
NELGs	905(18.91%)	881(18.40%)	24(0.50%)
stars	835(17.44%)	739(15.44%)	96(2.01%)
TOTAL	4118(86.02%)	3902(81.51%)	216(4.51%)

Table 5.3: Number of QSOs in the SGC 2SLAQ strip.

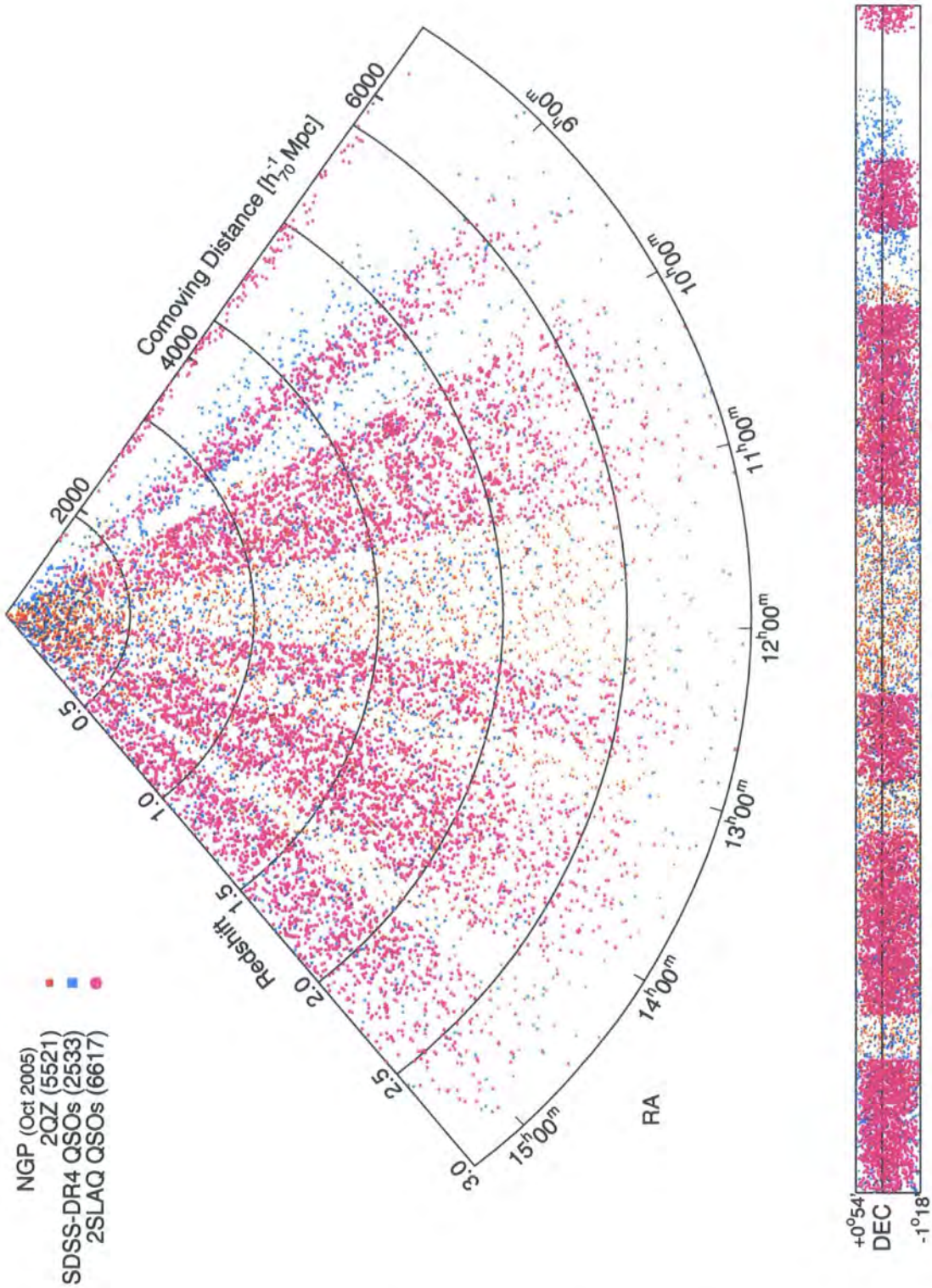

Figure 5.2: 2SLAQ QSO NGC wedge plot (Courtesy of Peter Weilbacher). The comoving distance is computed assuming a $\Omega_m^0 = 0.3$, $\Omega_\Lambda^0 = 0.7$, $h = 0.7$ cosmology.

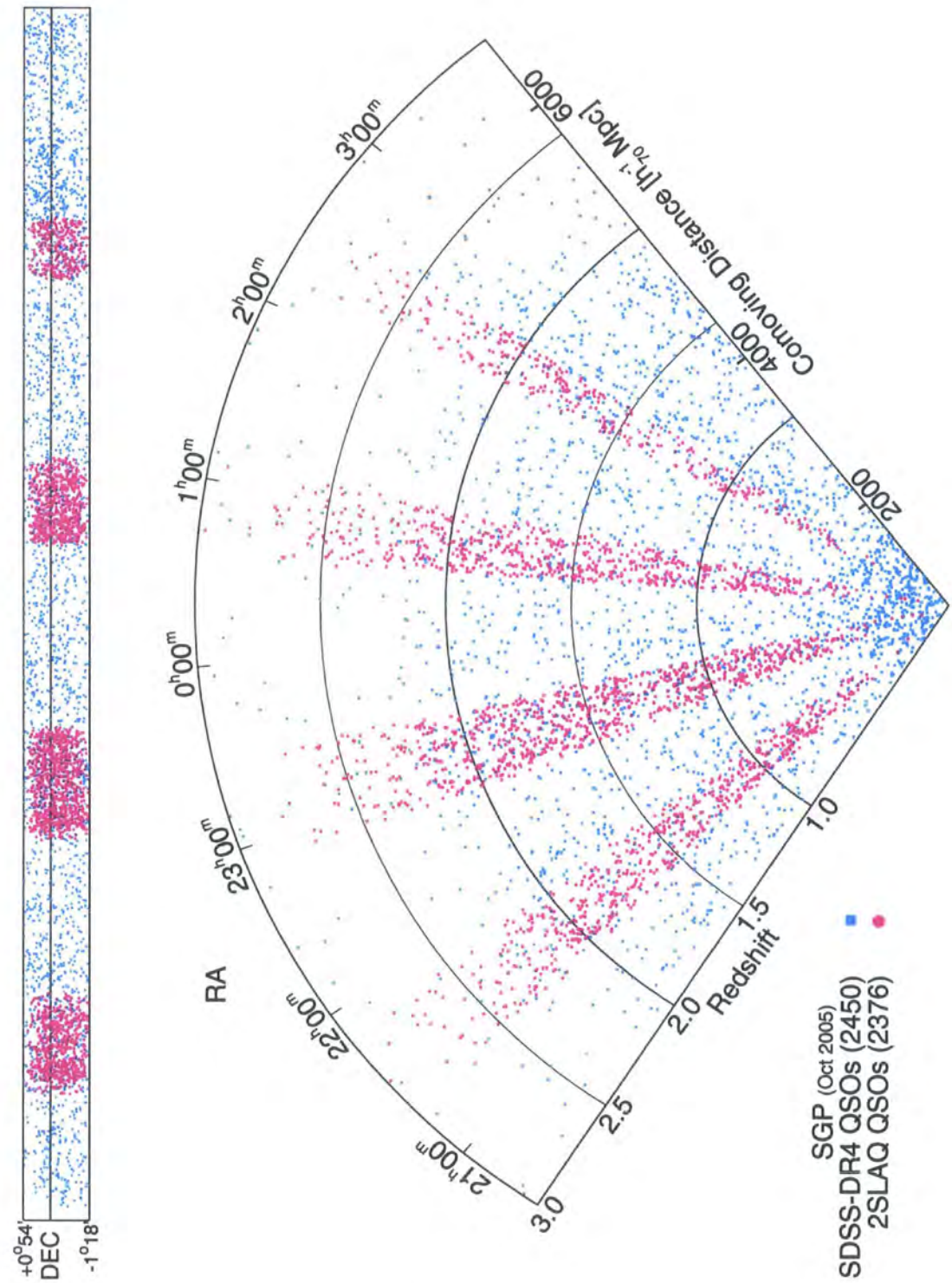

Figure 5.3: 2SLAQ QSO SGC wedge plot (Courtesy of Peter Weilbacher). The comoving distance is computed assuming a $\Omega_m^0 = 0.3$, $\Omega_\Lambda^0 = 0.7$, $h = 0.7$ cosmology.

observed in that region and, as a consequence, it corrects for the different angular completeness in overlapping 2dF pointings.

The fact that the 2dF instrument cannot place two fibres any closer than ~ 30 arcsec means that an additional incompleteness can potentially lead to an artificial deficit of close QSO pairs in 2dF surveys. In addition to this effect, one should also take into consideration that 2dF fibres cannot overlap or cross. To make an approximate correction for these effects, one can measure the angular correlation function, $w(\theta)$ (e.g. Hawkins et al., 2003). Comparing this to the angular correlation measured in the total input catalogue allows one to estimate the average deficit of close pairs at small angular separations. As shown by Croom et al. (2001), this deficit is negligible in the 2QZ sample. In the 2SLAQ sample, however, the deficit of pairs can, potentially, constitute a bigger bias. This is due to the fact that, in contrast to what happens in the 2QZ survey, the 2SLAQ QSOs are assigned a low observational priority and have a lower priority than the main sample LRGs. Therefore, the QSO-assigned fibres will only be positioned in areas allowed by the underlying angular distribution of the LRG fibres. Fig. 5.4 shows the $w(\theta)$ measurements of the 2QZ+2SLAQ sample and the 2SLAQ and 2QZ samples separately. In order to better distinguish between the errorbars, the 2SLAQ values are offset by a factor of $+0.02$ and the 2QZ $w(\theta)$ points by a factor of -0.02. Due to the large z-range of the QSO samples, we would expect $w(\theta) \sim 0$, at all scales. To account for the fibre-collision effects in the clustering of the 2SLAQ QSOs, we followed the method applied in previous work to the 2dFGRS survey data (Hawkins et al., 2003): the number of QSO pairs at a given separation is assigned a weight that depends on the QSO's angular separation $(1/(1 + w(\theta)))$. The "imprint" of the LRG angular distribution on the QSO fibres, due to these having been assigned a low 2dF priority, is also accounted for: when generating the random catalogue for the determination of the correlation functions of the 2SLAQ QSO sample, any random point has a zero probability of lying closer than 30 arcsec to any observed LRG. Although these effects have been considered, we have also noted that they have negligible effect on our clustering results.

Equally as relevant is the radial completeness, which also needs to be accurately described by the unclustered, or "random" distribution. Fig. 5.5 shows the $(0.3 < z < 2.9)$ redshift distribution of the 2QZ and 2SLAQ QSOs, in $\Delta z = 0.13$ bins. The red line represents the 2SLAQ NGC while the blue line the 2SLAQ SGC. The green and pink lines are the z-distributions of the 2QZ NGC and 2QZ SGC QSOs, respectively. Dashed lines also show the polynomial fits that were used to generate the random distribution. Later in the present chapter, we aim to study the dependence of QSO clustering on luminosity and also its redshift evolution. Hence, we extended our previously chosen $0.3 < z < 2.2$ 2QZ z-range to $0.3 < z < 2.9$, in order to better determine the clustering signal at the highest redshifts and also for the most luminous QSOs. This extension leaves the 2QZ QSO sample with 22416 objects (9982 in the NGC and 12434 in the SGC). The 2SLAQ QSO sample, when imposing faint magnitude cuts $(20.5 < g < 21.85)$ in addition to these z-cuts, comprises a total of 6374 QSOs (4574 in the NGC and 1800 in the SGC). The fact that the

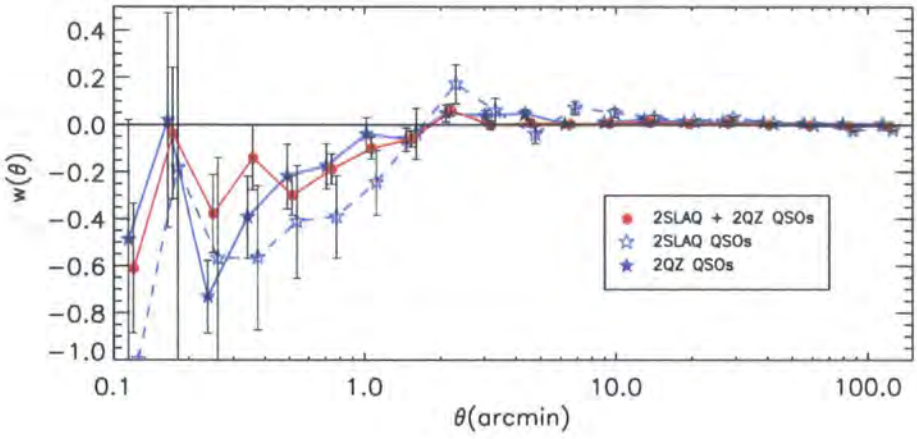

Figure 5.4: The angular correlation function measured for the 2QZ survey (solid blue stars and solid blue line), the 2SLAQ QSO survey (open blue stars and dashed blue line) and the 2QZ and 2SLAQ QSO surveys combined (red circles and line). The $w(\theta)$ measurements are very similar in both cases and show that the deficit of pairs seen at the smallest scales is not significant at typical QSO-QSO comoving separations. Note that the 2QZ values are offset by factor of -0.02 and the 2SLAQ values by a factor of $+0.02$.

2SLAQ $N(z)$ is steeper, at low-z, is possibly due to contamination of host galaxies colours, affecting the selection of fainter QSOs. The median redshift of the 2QZ+2SLAQ sample is $< z >= 1.50$.

After generating a random catalogue we can then combine the new 2SLAQ QSO sample with the 2QZ sample, and compute the QSO clustering by means of correlation functions. We start by estimating $\xi(s)$, the 2-point correlation function measured in z-space. This is presented in Fig. 5.6 (filled red circles). The estimator used to measure $\xi(s)$ is the Hamilton estimator:

$$\xi(s) = \frac{< DD(s) >< RR(s) >}{< DR(s) >^2} - 1, \tag{5.16}$$

where $< DD(s) >$, $< DR(s) >$, $< RR(s) >$ are the mean number of QSO-QSO, QSO-random and random-random pairs at separation s. For comparison, also shown is the previously determined 2QZ $\xi(s)$ (chapter 2, da Ângela et al. 2005), the 2SLAQ QSO $\xi(s)$ and also the $\xi(s)$ measurements of the 2SLAQ LRG sample (Ross et al., in prep.).

Including the 2SLAQ QSO sample does not affect the shape of the previously measured 2QZ $\xi(s)$. The $\xi(s)$ measured from both samples, including or not the 2SLAQ QSOs, are indeed very identical. We have verified the statistical weight of including the 2SLAQ sample by comparing the number of QSO-QSO pairs at separations $< 20\,h^{-1}$Mpc, and verified that the combined 2QZ+2SLAQ sample has $\sim 65\%$ more QSO-QSO pairs within $20\,h^{-1}$Mpc than the 2QZ sample alone. This gain also includes the contribution of the cross pairs between the 2SLAQ and 2QZ samples, on the NGC strip. The 2SLAQ LRGs have a higher clustering amplitude than the 2SLAQ

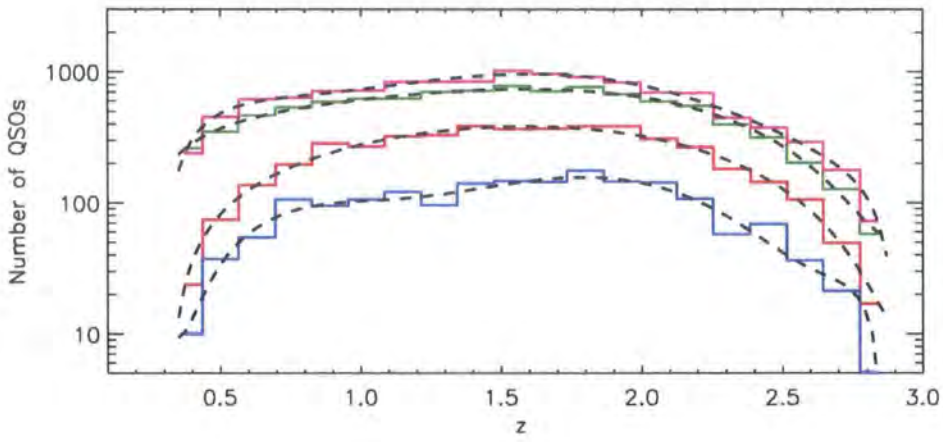

Figure 5.5: 2SLAQ QSO and 2QZ $N(z)$. Red line is the NGC and the blue line the SGC. The green line represents the 2QZ NGC and the pink line the 2QZ SGC. Also shown, as dashed lines, are the polynomial fits that were used to model the radial distribution of the random points.

QSOs. At smaller scales the two samples also differ in the shape of their correlation functions. This difference is probably due to the different z-space distortions that affect the LRGs and the 2QZ and 2SLAQ QSOs.

Also shown are two different $\xi(s)$ models, previously described in Chapter 2. The dashed line is the best fitting 2QZ power-law model, in the range $5 < s < 50\,h^{-1}$Mpc ($\xi(s) = (s/6.50)^{-1.89}$), and the solid line is the $\xi(s)$ model obtained from convolving a double power-law $\xi(r)$ model (Eq. 5.17) with the z-space distortions parameterised by $< w_z^2 >^{1/2} = 800\,\mathrm{km\,s^{-1}}$ and $\beta(z) = 0.32$.

$$\xi(r) = \begin{cases} (r/6.00)^{-1.45}, & r < 10\,h^{-1}\mathrm{Mpc} \\ (r/7.25)^{-2.30}, & r > 10\,h^{-1}\mathrm{Mpc} \end{cases} \tag{5.17}$$

It can be seen that the model is still a good description of the joint QSO $\xi(s)$ measurements, indicating that the 2SLAQ QSOs should have a similar real-space clustering and be subjected to the same dynamical distortions as the 2QZ QSOs.

The errors shown in Fig. 5.6 are "jacknife" estimates, estimated by splitting the 2QZ+2SLAQ sample in 16 subsamples. We compared the jacknife and Poisson error estimates in our $\xi(s)$ computation. The Poisson error estimates should, in principle, provide a fair description of the uncertainty for the 2QZ QSO clustering measurements (Hoyle, 2000; da Ângela et al., 2005). Here we test this hypothesis for the new sample containing the 2QZ and 2SLAQ QSOs. We divide up the overall 2QZ+2SLAQ dataset into 16 subsamples and compute $\xi(s)$ in the overall set minus each of the 16 subsamples in turn[1]. The 16 measurements of $\xi(s)$ are then combined as follows, in order to obtain the jacknife error (e.g. Scranton et al., 2002):

[1]This $\xi(s)$ computation was performed using the kd-tree algorithm of Moore et al. (2001).

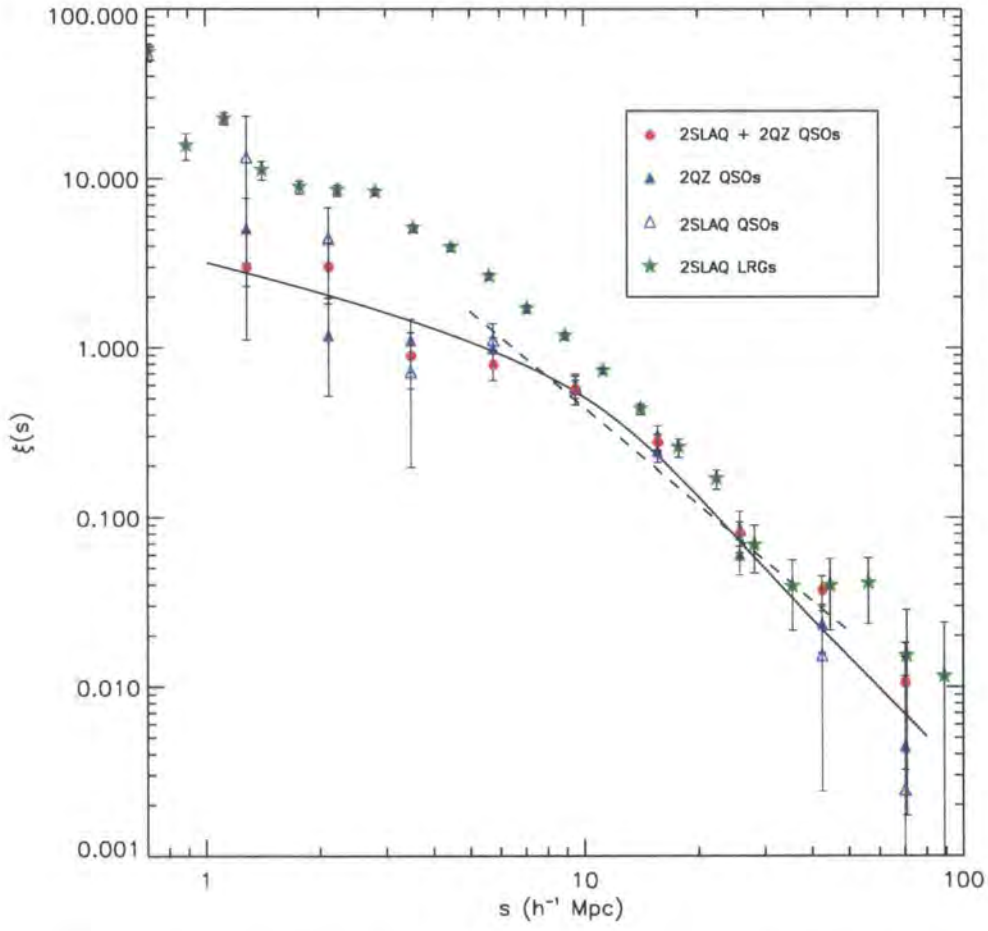

Figure 5.6: The red circles show the $\xi(s)$ measured from the 2SLAQ and 2QZ samples and the blue triangles the 2QZ results (see chapter 2). The $\xi(s)$ measurements are very similar, both in amplitude and shape. The green stars show the 2SLAQ LRG measurements (Ross et al., in prep.). The dashed and solid lines show two models: the best fitting 2QZ $5 < s < 50\,h^{-1}$Mpc power law (dashed); and the double power law $\xi(r)$ model, "distorted" by dynamical motions parameterised by $< w_z^2 >^{1/2} = 800\,\mathrm{km\,s^{-1}}$ and $\beta(z) = 0.32$.

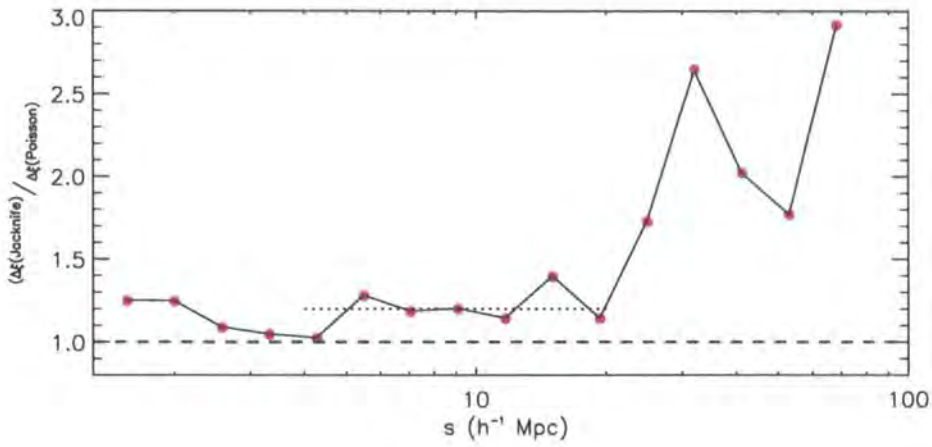

Figure 5.7: Red circles and solid line show the ratio jacknife and Poisson $\xi(s)$ errors. Poisson errors seem to under-predict the uncertainty in $\xi(s)$ at all scales, and considerably at the largest scales. At intermediate, $4 \lesssim s \lesssim 20\,h^{-1}$Mpc scales, the ratio of the two error estimates is approximately constant and ~ 1.25 (dotted line).

$$\sigma_{jacknife} = \sqrt{\frac{N-1}{N}\sum_{i=1}^{N}\frac{DR_i(s)}{DR_{tot}(s)}(\xi_i(s)-\xi_{tot}(s))^2} \tag{5.18}$$

where N is the total number of subsamples (16, in this case); the subscript i refers to the whole dataset minus subsample i; and *tot* refers to the whole 2QZ+2SLAQ QSO sample. The "DR ratio" accounts for the fact that the subsamples may not necessarily contain exactly the same number of QSOs. Fig 5.7 shows the ratio between the jacknife and the Poisson errors. It can be seen that, on all scales, Poisson errors underestimate the uncertainty on the clustering measurements, especially at the largest scales. On scales $2 \lesssim s \lesssim 4\,h^{-1}$Mpc, the two estimates are quite similar, but on $4 \lesssim s \lesssim 20\,h^{-1}$Mpc scales, where most of the clustering signal is obtained, the jacknife errors are, on average, 1.25 times bigger than Poisson errors (dotted line). At larger scales, where there are fewer QSO independent pairs, the Poisson estimates largely under-predict the true error estimate.

We have also studied the evolution of the shape of the correlation function with redshift. It has been suggested that the evolution of the $\xi(s)$ amplitude could be parameterised by

$$\xi(s) = \left(\frac{s}{s_0}\right)^{-\gamma}(1+z)^{-(3+\epsilon)} \tag{5.19}$$

assuming a power-law ξ model (e.g. Peebles, 1980; Myers et al., 2006). By determining changes in the shape of $\xi(s)$ with z, we can also determine the possible z-dependence of QSO z-space distortions and dynamics. Fig. 5.8 shows the ratio of the correlation function measured in four redshift bins divided by the overall $\xi(s)$, for the complete 2QZ+2SLAQ sample. There is not much evidence for z-evolution of the QSO correlation function amplitude or shape, within the errors.

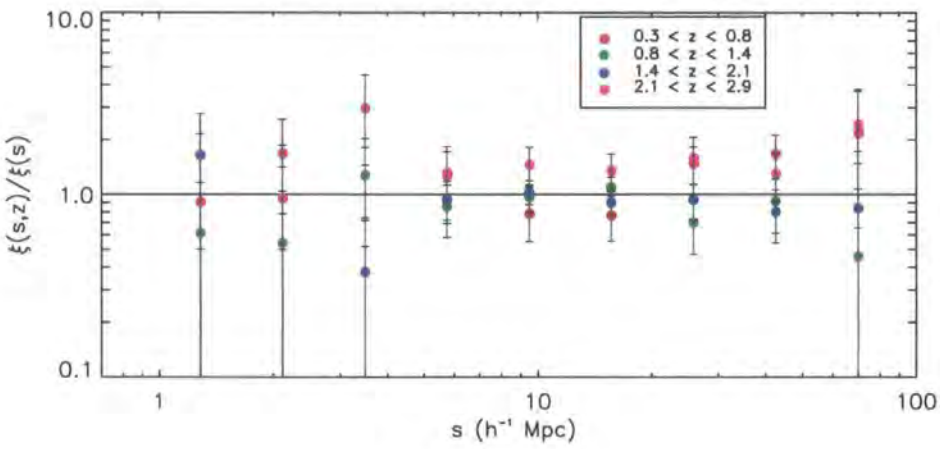

Figure 5.8: The circles show the ratio of the QSO $\xi(s)$ in one given redshift bin to the $\xi(s)$ of the whole 2QZ+2SLAQ sample. Red are the lower-z, $0.3 < z \leq 0.8$ sample. The $0.8 < z \leq 1.4$ QSOs are shown in green, the $1.4 < z \leq 2.1$ QSOs in blue and the higher-z, $2.1 < z \leq 2.4$ QSOs in pink. There is no evident evolution of the QSO $\xi(s)$ amplitude and shape. The higher-z sample hints at a higher $\xi(s)$ amplitude, but this trend is with the measured errors.

There is a hint that the higher-z QSOs (in pink) might show higher clustering amplitude, but this is not a significant result, within the measured errors.

Fig. 5.9 shows the projected correlation function measured from the 2QZ+2SLAQ sample (red circles). This is very similar to the previous 2QZ measurement (blue triangles). The open blue triangles represent the $w_p(\sigma)/\sigma$ values for the 2SLAQ ensemble alone and the green stars represent the more strongly clustered 2SLAQ LRGs (Ross et al., in prep.). The solid line is the σ-projection of the double power-law $\xi(r)$ model which was found to be a good description of the 2QZ $\xi(r)$. The dashed line corresponds to the projection of a power law $\xi(r)$ model, given by $\xi(r) = (r/4.96)^{-1.85}$ (see chapter 2).

The fact that the 2SLAQ survey targeted faint QSOs is not only an advantage for studies of the luminosity-dependence of QSO clustering, but also for z-space distortion analyses. The higher spatial density of the combined QSO sample should, in principle, improve our statistics when studying z-space distortions, and, in particular, the estimation of Ω_m^0 and $\beta(z)$ from dynamical and geometrical $\xi(\sigma, \pi)$ distortions. The $\xi(\sigma, \pi)$ measured from the whole QSO sample is shown in Fig. 5.10 (solid contours). The dashed lines refer to the 2QZ measurement, presented in chapter 3. As in the previous clustering measurements presented in this chapter, the assumed cosmology is Λ.

Given the similarities between the two contours, in addition to very similar $\xi(s)$ and $w_p(\sigma)$ measurements, we would not expect the constraints put on $\beta(z)$ and Ω_m^0 from the 2QZ+2SLAQ dynamical distortions to differ from those obtained in chapter 3, assuming that all the underlying assumptions remain the same (e.g., $\xi(r)$ shape and amplitude, velocity dispersion, scale-independent

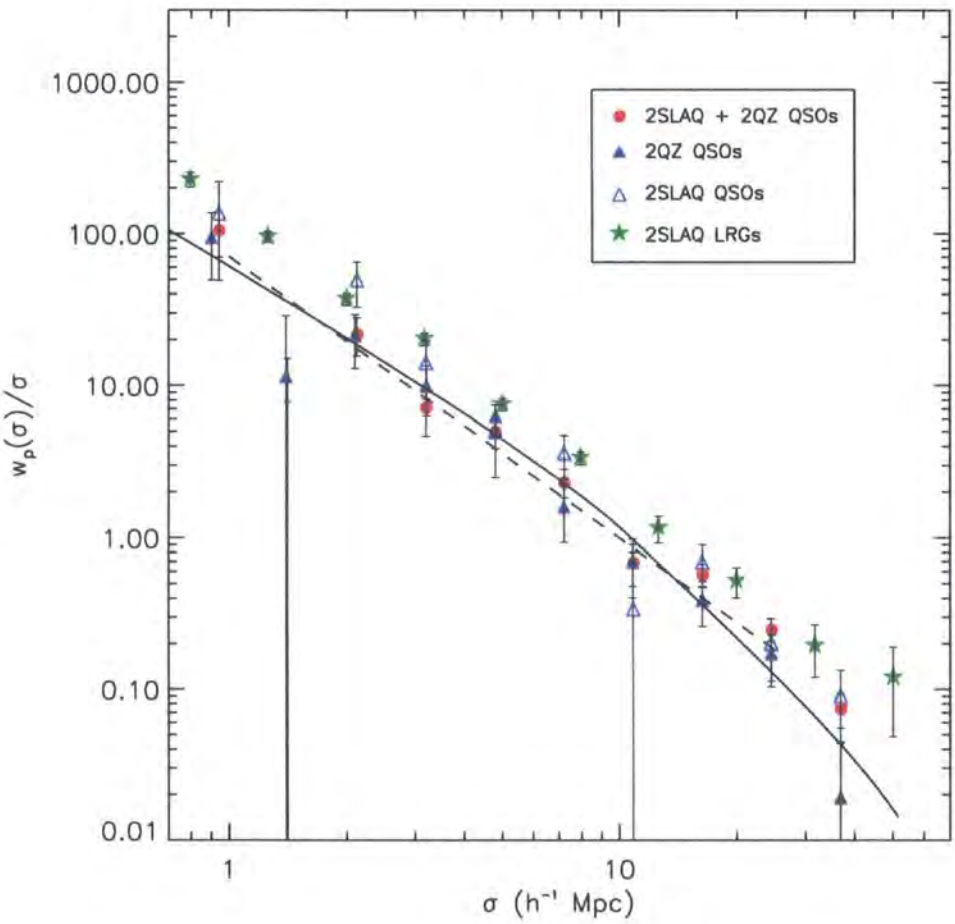

Figure 5.9: The red circles are the $w_p(\sigma)/\sigma$ measurements for the 2QZ+2SLAQ sample. These are very similar to those of the 2QZ sample alone (blue triangles). The green stars represent the higher clustered LRG sample from the 2SLAQ survey (Ross et al., in prep). The models shown represent the projection of a single (dashed line) and a double (solid line) power law models.

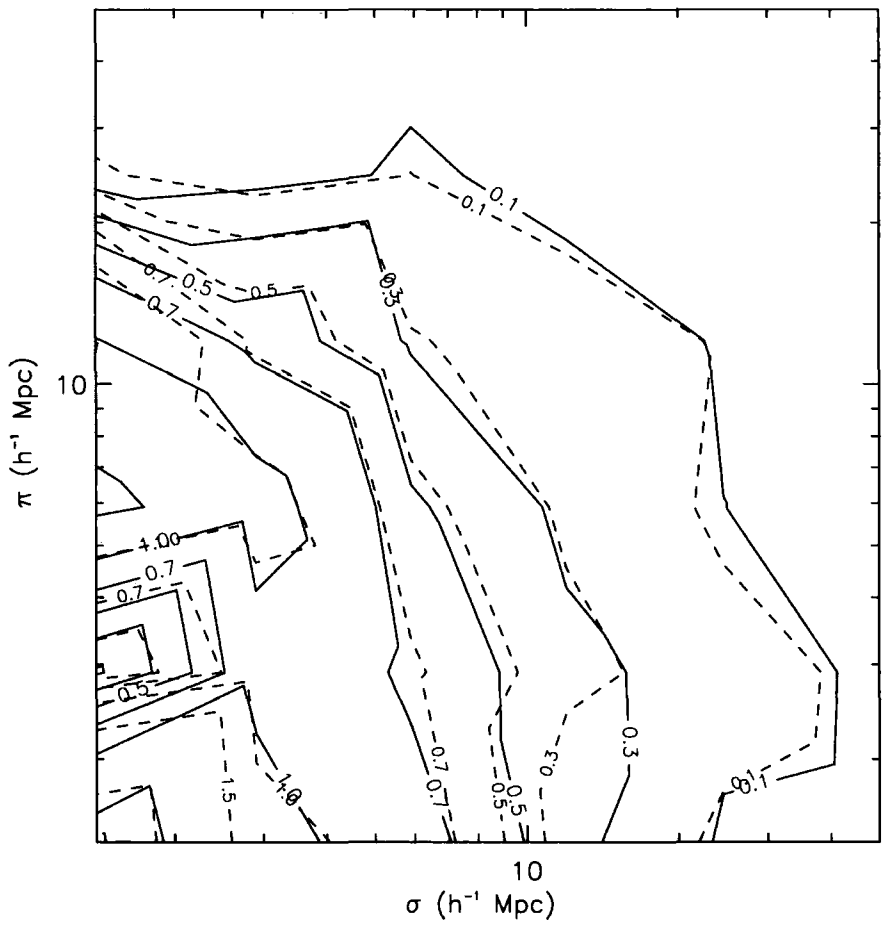

Figure 5.10: $\xi(\sigma, \pi)$ measured for the 2QZ+2SLAQ sample (solid contours) and for the 2QZ sample alone (dashed contours). The two measurements show significant similarities.

bias). We now repeat the method adopted for fitting the 2QZ dynamical and geometrical distortions, but also utilising the new 2SLAQ ensemble. The question now arises if the same $\xi(r)$ model should be assumed, or if the velocity dispersion of the QSOs should still be fixed at $800\,\mathrm{km\,s^{-1}}$. It can be seen that the 2QZ double power-law $\xi(r)$ model is still a good description of both $\xi(s)$ and $w_p(\sigma)$ measurements for the combined sample. As the 2QZ and 2SLAQ samples have similar $N(z)$ we would not expect to see clustering differences between them which would be due to redshift evolution. Any potential clustering difference between both sets would be due to the different luminosity of the samples. However, as suggested by both observations (e.g. Croom et al., 2005; Adelberger and Steidel, 2005; Myers et al., 2006), and simulations (Lidz et al., 2006) and, more importantly, as we shall see later in this chapter, QSO clustering is very weakly luminosity dependent. We therefore assume the same $\xi(r)$ prescription as used previously in chapter 3. We also assume the same velocity dispersion as for the 2QZ sample alone. It is not unlikely that the 2SLAQ QSOs would have, on average, a different velocity dispersion. As pointed out by Berlind et al. (2003), Yoshikawa et al. (2003), or Tinker et al. (2006a), galaxies can be a biased tracer of the dark matter velocity distribution, just as they are of the dark matter spatial distribution. However, as found for the 2dFGRS galaxies and predicted by HOD models (Tinker et al., 2006a), the expected difference for $M_{b_J} \lesssim -20$ is not significant. In addition, as most of the z-error is due to measurement error rather than intrinsic velocity dispersion (Croom et al., 2005), we chose to continue assuming $< w_z^2 >^{1/2} = 800\,\mathrm{km\,s^{-1}}$.

The fit to the distortions in $\xi(\sigma,\pi)$ was performed with the same assumptions and over the same range of scales as in the previous 2QZ analysis (assuming the Λ cosmology). The result is shown in Fig. 5.11. As expected, the contours are indeed tighter than the ones obtained when fitting only the 2QZ $\xi(\sigma,\pi)$. This is due to the increased number of pairs, not only from the 2SLAQ sample alone but also from the cross-pairs in the NGC between the two ensembles, as they probe overlapping volumes. Also shown are the 1σ and 2σ confidence levels predicted from clustering evolution and linear theory of density perturbations (dashed lines). The dotted line is, as usual, the 1σ joint confidence levels from both constraints. The best fitting values are $\Omega_m^0 = 0.25^{+0.09}_{-0.07}$, $\beta(z) = 0.60^{+0.14}_{-0.11}$, corresponding to a a $\chi^2_{min} = 1.02$ (12 d.o.f.). Although these results favour a somewhat higher value of β than the previous 2QZ only $\xi(\sigma,\pi)$ constraint, both obtained results are self-consistent, within the associated errors. Again, we should point out that the size of the error bars does not take into account any potential correlation between $\xi(\sigma,\pi)$ bins.

5.4 The L-z degeneracy

A few recent works have looked at the evolution of QSO clustering (e.g. Croom et al., 2005; Porciani et al., 2004; Myers et al., 2006). These suggest an increase of QSO clustering amplitude with redshift, a trend which is more significant at $z \gtrsim 1.6$. This evolution contrasts with that expected from a long-lived QSO population model, or linear theory predictions, which generally predict a

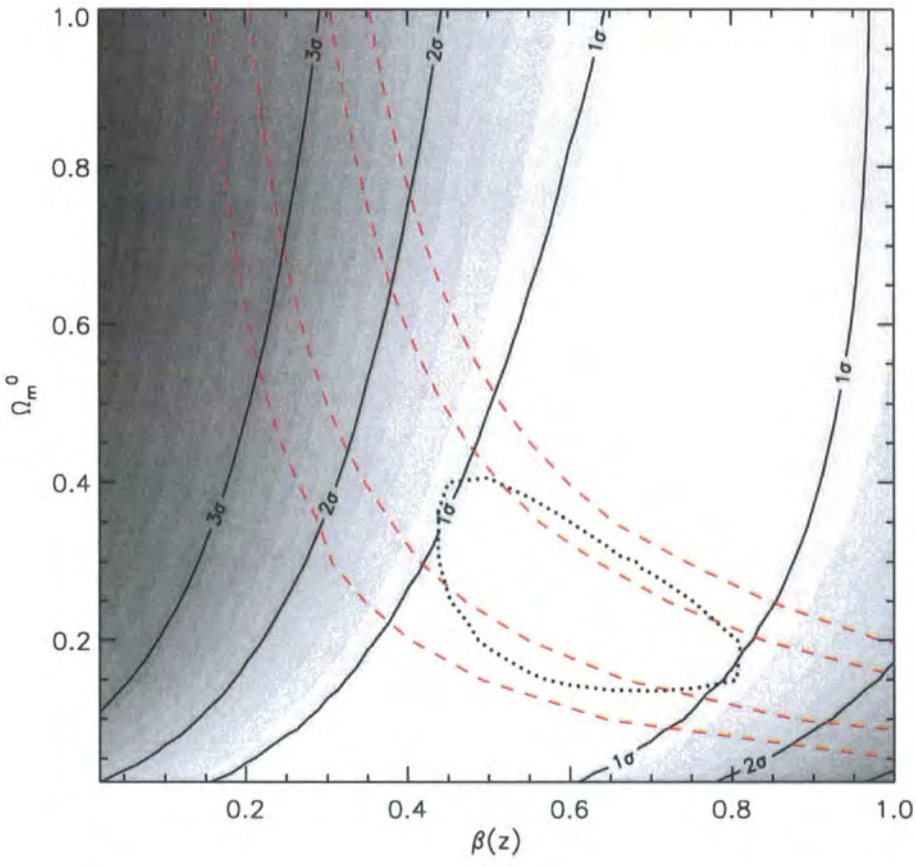

Figure 5.11: Confidence levels in the $[\Omega_m^0, \beta(z)]$ plane from obtained from fitting the 2QZ and 2SLAQ $\xi(\sigma, \pi)$ z-space distortions (solid lines and shaded contours). Dashed lines show the 1 σ and 2 σ constraints from linear theory evolution. The dotted contour is the 1 σ joint confidence level.

decrease of clustering amplitude with increasing redshift (Croom et al., 2001, 2005). The range of magnitudes covered by the QSO surveys used in these studies has not fully permitted the study of the luminosity dependence of QSO clustering. However, the combination of the 2QZ and 2SLAQ samples probably sees its greatest scientific contribution precisely in the range of luminosities it probes and for the first time allows a more rigorous determination of the QSO clustering dependence on luminosity. Croom et al. (2002) have used the 2QZ sample alone for this purpose. Their results do hint that additional data, at fainter magnitudes, such as those obtained with the 2SLAQ effort, should be essential in the pursuit of this goal.

To estimate the b_J band absolute magnitude, M_{b_J}, we compute:

$$M_{b_J}(z) = b_J - K_{b_J}(z) - A_{b_J} + 5 - 5\log(d), \tag{5.20}$$

where b_J is the apparent magnitude, K_{b_J} the k-correction in the b_J magnitude, A_{b_J} the dust correction and d the luminosity distance that corresponds to the redshift z, measured in parsecs. The value of the k-correction was taken from Cristiani and Vio (1990). The galactic dust correction, A_{b_J} is determined through: $A_{b_J} = 4.035E(B-V)$ (Schlegel et al., 1998).

The above formula is used to determine the absolute magnitude of the 2QZ QSOs. To include the dust correction when determining the absolute magnitude of the 2SLAQ QSOs, one subtracts the g magnitude galactic extinction (g_{red}) at the QSO's coordinates from the observed apparent magnitude (g): $g' = g - g_{red}$, where g' is the dust-corrected g-band QSO magnitude. The other subtlety in combining the two QSO samples is accounting for the relation between the observed b_J and g magnitudes. However, this becomes quite simple as the transmissivity curves of the filters have a significant overlap and the same zero-point. Thus, we can treat these bands as being equivalent (Richards et al., 2005). Hereafter, and for the sake of simplicity, we shall refer to the QSO absolute magnitudes for both samples as if they had been measured in the b_J band, and represent both of them as M_{b_J}. Therefore, the 2SLAQ QSOs absolute magnitude is determined by:

$$M_{b_J}(z) \approx g' - K_{b_J}(z) + 5 - 5\log(d), \tag{5.21}$$

where g' already includes the dust correction in the g band.

Fig. 5.12 shows how the 2QZ and 2SLAQ distribute in the $[M_{b_J}, z]$ plane. The 2QZ QSOs are shown in red and the 2SLAQ in blue. The cyan lines represent the adopted 2QZ $b_J < 20.85$ and 2SLAQ $20.5 < g < 21.85$ magnitude cuts. The QSO samples span the z-range $0.3 < z < 2.9$. The yellow line shows how $M^*_{b_J}$ changes with z. We adopted a second-order polynomial model to determine $M^*_{b_J}(z)$ (Boyle et al., 2000; Croom et al., 2004; Richards et al., 2005):

$$M^*_{b_J}(z) = M^*_{b_J}(0) - 2.5(k_1 z - k_2 z^2) \tag{5.22}$$

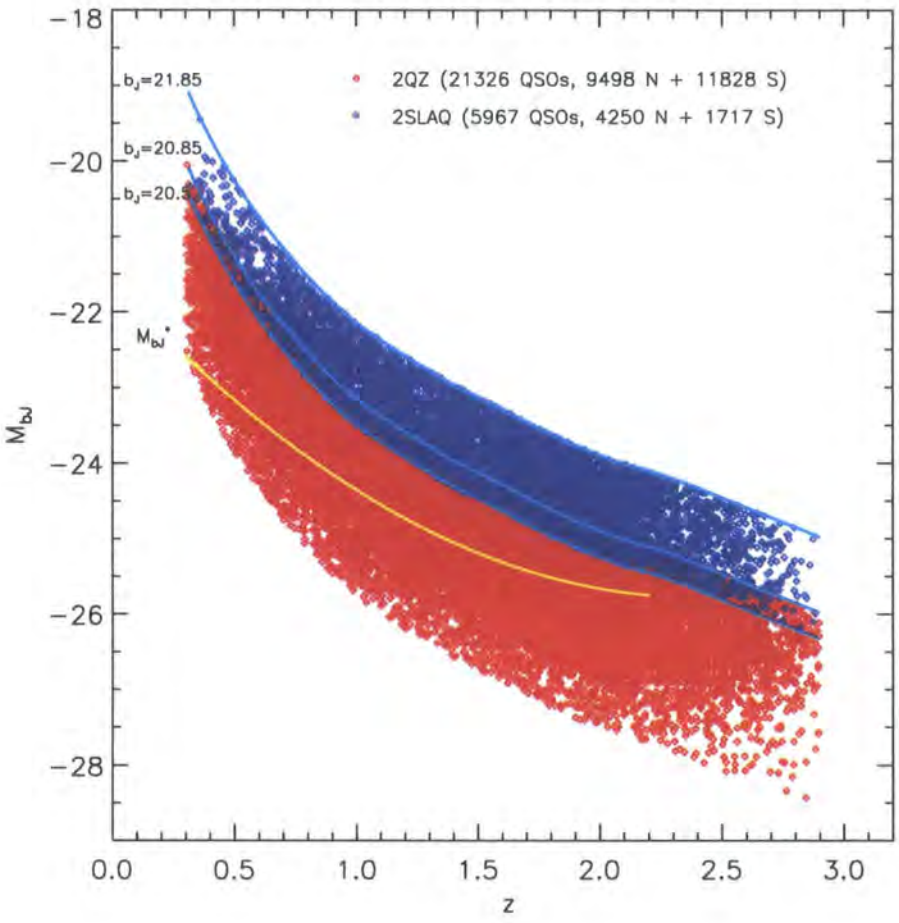

Figure 5.12: Distribution of 2QZ (red) and 2SLAQ (blue) QSOs in the $M_{b_J} - z$ plane. The yellow line extending to $z = 2.2$ shows the second order $M^*_{b_J}(z)$ model of Croom et al. (2004). The cyan lines represent the apparent magnitude b_J limits: the $b_J = 21.85$ and $b_J = 20.5$ lines are the magnitude limits on the 2SLAQ sample, and $b_J = 20.85$ is the faint magnitude cut on the 2QZ catalogue.

We adopt the values obtained by Croom et al. (2004): $M^*_{b_J}(0) = -21.61, k_1 = 1.39, k_2 = -0.29$. Richards et al. (2005) showed that the parameterisation of the $M^*_{b_J}(z)$ model is only marginally affected by including or not the 2SLAQ QSOs. The yellow line in Fig. 5.12 only extends to $z = 2.2$ given the fitting range used in this parameterisation.

The flux-limited nature of these two surveys is evident in this plot. More luminous QSOs lie at higher redshifts while fainter ones have lower redshifts. This means that, unless we probe a wide window in magnitude-space with our QSO surveys, it will be intrinsically hard to determine how QSO physical properties change with luminosity, for a fixed redshift. By combining the 2SLAQ and 2QZ samples we are widening the magnitude window and hence making it possible to determine the dependence on QSO clustering with luminosity, free of any evolutionary effects.

Fig. 5.13 shows how, using the two surveys together, we can look at a specific redshift range

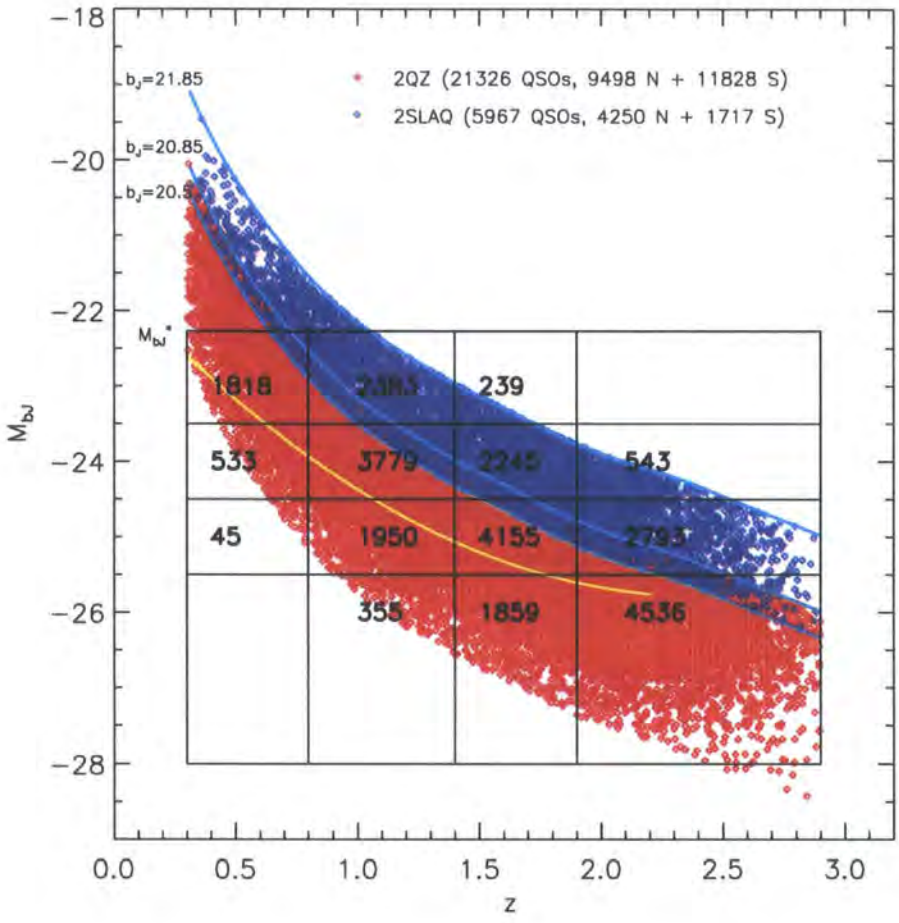

Figure 5.13: Magnitude and redshift bins adopted for 2QZ and 2SLAQ QSOs. The numbers in each division of the "grid" are the numbers of 2QZ and 2SLAQ QSOs in the specific z and M_{b_J} ranges.

and determine the QSO clustering in different magnitude samples. This "vertical approach" to the $[M_{b_J}, z]$ distribution is possibly more physically justifiable than a "horizontal" one. Given the observed evolution of the luminosity function of 2QZ and 2SLAQ QSOs (Boyle et al., 2000; Richards et al., 2005), which can be described by pure luminosity evolution (PLE) scenarios, different z QSOs with the same absolute magnitude should be, in principle, unrelated. Even assuming a simple cosmologically long-lived model (Boyle et al., 2000) (even though this is not supported by clustering measurements, Croom et al. 2005), we would expect a fading population of QSOs, and high-z objects with a given luminosity would correspond to a lower luminosity, lower-z population. However, if we concentrate on one particular epoch, by looking at given small redshift interval, we can study how clustering depends on luminosity, independently of any potential evolution effect. We use the upper absolute magnitude limit of $M_{b_J} < -22.3$ to decrease the effect of host galaxy contamination when selecting fainter QSOs (Boyle et al., 2000).

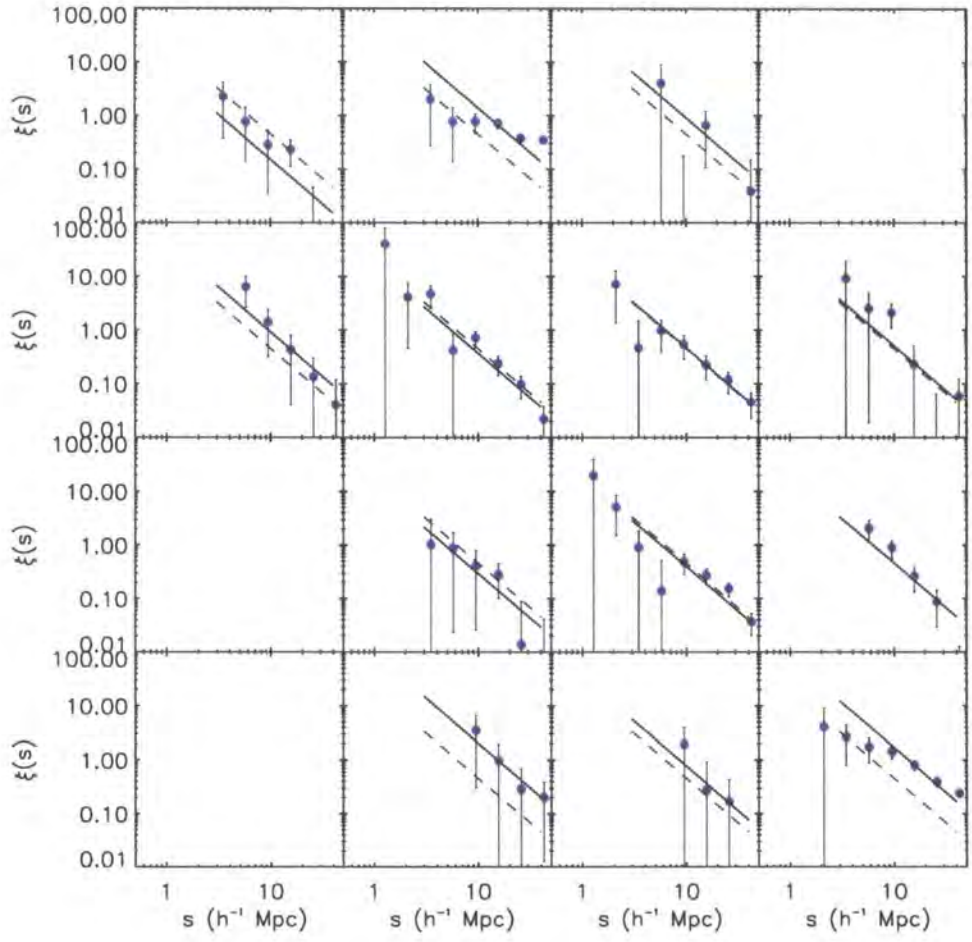

Figure 5.14: QSO $\xi(s)$ measured in different magnitude and redshift bins. The order of the panels is the same as that of the $[M_{bJ}, z]$ intervals in Fig. 5.13. The dashed line shows the best fitting power-law to the $\xi(s)$ of the full sample. The solid line is the $\xi(s)$ power-law fit to the data in each individual panel.

5.5 Clustering as a function of magnitude and redshift

Dividing up the QSO samples into magnitude and redshift bins significantly increases the error on our clustering measurements, simply due to the much smaller number of objects in each bin compared to the total number of QSOs (numbers in Fig. 5.13). This is also evident in Fig. 5.14, where we plot the $xi(s)$ measurements in each of the panels in Fig. 5.13. The dashed line shows the best fitting power-law model to the overall 2QZ+2SLAQ sample, over the $3 < s < 50$ h^{-1}Mpc range ($\xi(s) = (s/6.20)^{-1.66}$). The solid lines are the best power-law models to each individual $[M_{bJ}, z]$ interval, fixing the $\xi(s)$ slope to $\gamma = 1.66$ and performing a χ^2 fit to determine the amplitude. The order of the panels in Fig. 5.14 is the same as in the panels presented in the $[M_{bJ}, z]$ plane in Fig. 5.13.

By visually comparing the dashed and solid lines, we observe no dependence of QSO clustering on luminosity nor redshift. However, the size of the errorbars motivates the further use of more

statistically robust tools. We therefore use the integrated correlation function up to $20\,h^{-1}$Mpc in order to quantify the clustering amplitude in each magnitude-z bin. This quantity is then normalised to the volume contained in a $20\,h^{-1}$Mpc sphere:

$$\xi_{20} = \frac{3}{20^3}\int_0^{20} \xi(s)s^2 ds \tag{5.23}$$

The choice of using $20\,h^{-1}$Mpc as the radius of the spheres to compute the averaged correlation function is due to the fact that this is a large enough scale for linear theory to be applied and, as shown by Croom et al. (2005), small-scale z-space distortions do not significantly affect the clustering measurements, when averaged over this range of scales. In addition, and as seen in Fig. 5.7, we can estimate the uncertainty through computing Poisson errors, and scale this by a factor of 1.25. This estimate should provide a fair description of the uncertainty on the correlation function measurements, and significantly reduce the computing time.

We computed ξ_{20} using the Hamilton estimator in each of the bins shown in Fig. 5.13. The results for each redshift slice are shown in the four panels in Fig. 5.15. Red circles show the measurements in each magnitude bin. The shaded grey area shows the 1σ ξ_{20} measurement for QSOs of all luminosities in that specific redshift slice and its length indicates the total range of magnitudes included. The dashed line represents the average value of ξ_{20}, for all redshift and magnitude ranges. It should be pointed out that the bin sizes were chosen in such a way that the precision of the clustering measurements was maximised, and therefore the distribution of QSOs in a given z-slice is not constant for all magnitudes. Thus, we do not expect our ξ_{20} measurements to be equidistant along the horizontal axis, as these are centred on the median values in M_{b_J} of each bin. The top axis indicates the magnitude difference with respect to $M^*_{b_J}(< z >)$, at the median redshift of that specific "z - slice". The "rising" of the grey area as we move to higher redshifts is consistent with the results of Croom et al. (2005), who also found an increase of clustering amplitude with redshift, for the 2QZ QSOs.

The number of QSOs in each $M_{b_J} - z$ bin, indicated in Fig. 5.13, is now reflected in the sizes of the ξ_{20} error bars. In the first, lower-z panel, for instance, the $M_{b_J} - z$ bin with only 533 QSOs corresponds to the ξ_{20} measurement with the largest error bar. The two intermediate z-slices are the ones where most of the gain of the 2SLAQ is observed and the ones with highest statistical value. Especially in the three highest-z panels, where it is possible to make ξ_{20} measurements in at least three of the four magnitude intervals adopted, a possible weak dependence of QSO clustering on luminosity is observed. The ξ_{20} measurement in the faintest bin seems to be higher than in the brighter magnitude bins that follow, whilst the brightest QSOs seem to have, again, higher clustering amplitude. This "curved" feature is somehow hinted in the three highest-z panels, but the size of the error bars do not allow a statistically significant conclusion to be drawn, at least any other than our results being consistent with luminosity-independent QSO clustering. The possibility of luminosity dependence comes only from the fact that the deviations from a flat ξ_{20} vs. M_{b_J} trend do not seem stochastic, as the lowest and highest magnitude bins have,

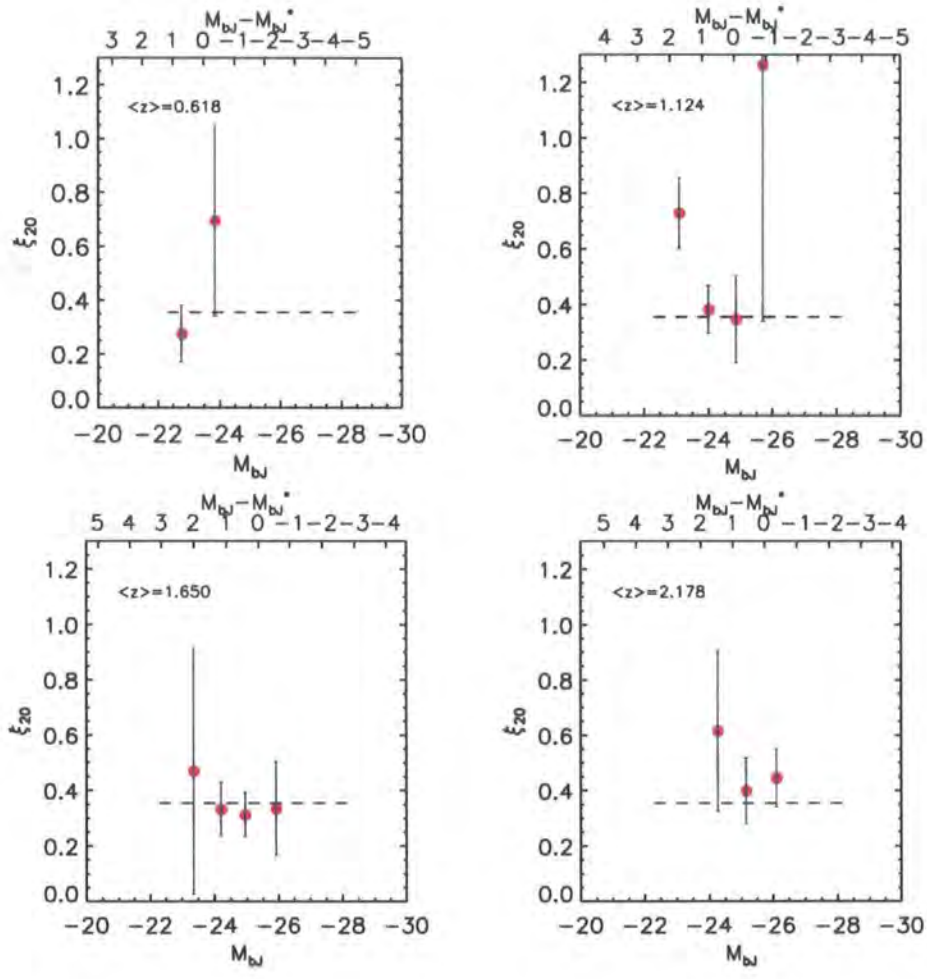

Figure 5.15: The four panels represent the ξ_{20} measurements in different redshift bins. The median redshift of each z-interval is indicated in the top left of each graph. The top horizontal axis shows the absolute magnitude difference, relative to $M^*_{bJ}(< z >)$. The red circles are the ξ_{20} measurements in different absolute magnitude bins, and are centred on the median values of each bin. The shaded area is the 1σ ξ_{20} interval for all the QSOs in that specific redshift interval. The horizontal length of the shaded area represents the range of M_{bJ} values of QSOs in that redshift interval.

systematically, higher clustering amplitude than the intermediate M_{b_J} bins, even though below 1σ significance, in most cases. As the mass of the dark matter haloes correlates with clustering amplitude, the fact that the faintest QSOs at $z \sim 1.124$ are strongly clustered could motivate new QSO clustering models. Although our results are in agreement with the hypothesis of a luminosity-independent clustering ($\chi^2_{red} = 1.16$, over 12 d.o.f.), the hypothesis of QSO clustering being constant with redshift and luminosity is not supported by the data ($\chi^2_{red} = 2.50$).

5.6 Bias and halo masses

The ξ_{20} vs. M_{b_J} results motivate the analysis of the dependence of bias on luminosity and redshift. Croom et al. (2005) investigated the redshift evolution of QSO bias, using the 2QZ survey data. They found that the QSO bias does evolve very strongly with redshift; as the mass clustering amplitude decreases with increasing redshift, the slight upward trend observed in the 2QZ ξ_{20} reveals a strong increase of bias with z.

We have seen that, under the assumption of a scale-independent bias, the bias can be obtained through (e.g. Peebles, 1980):

$$b = \sqrt{\frac{\xi_Q(r)}{\xi_\rho(r)}} \approx \sqrt{\frac{\xi_Q(r,20)}{\xi_\rho(r,20)}}, \tag{5.24}$$

where $\xi_Q(r,20)$ and $\xi_\rho(r,20)$ represent the QSO and matter real-space correlation functions, respectively, averaged in $20\,h^{-1}$Mpc spheres. We have also seen that the relation between the z-space and real-space correlation functions can be given by (Kaiser, 1987):

$$\xi_Q(s,20) = \left(1 + \frac{2}{3}\beta + \frac{1}{5}\beta^2\right)\xi_Q(r,20) \tag{5.25}$$

Combining both equations and taking into account that $\beta = \Omega_m^{0.6}/b$ leaves us with a quadratic equation in b. Solving it leads to:

$$b(z) = \sqrt{\frac{\xi_Q(s,20)}{\xi_\rho(r,20)} - \frac{4\Omega_m^{1.2}(z)}{45}} - \frac{\Omega_m^{0.6}(z)}{3} \tag{5.26}$$

Therefore, we can use our $\xi_Q(s,20)$ measurements, represented in Fig. 5.15 and, together with a theoretical estimate of $\xi_\rho(r,20)$, determine the bias that corresponds to that theoretical assumption and the observed clustering measurements, on the assumption of a cosmological model. Our results are shown in Fig. 5.16. To estimate $\xi_\rho(r,20)$, we use the $P(k)$ non-linear estimate of Smith et al. (2003). To determine $\xi_\rho(r)$ we Fourier transform this $P(k)$ estimate, and integrate the result up to $s \leq 20\,h^{-1}$Mpc to compute $\xi_\rho(r,20)$. The parameters used to generate the $P(k)$ model were: $\Omega_m^0 = 0.3$, $\Omega_\Lambda^0 = 0.7$, $\Gamma = 0.17$ and, for a better comparison with Croom et al.'s (2005) results, $\sigma_8 = 0.84$. This value is consistent with recent studies (e.g. Tytler et al., 2004), even though recent measurements also tend to suggest somewhat lower values (Spergel et al., 2006).

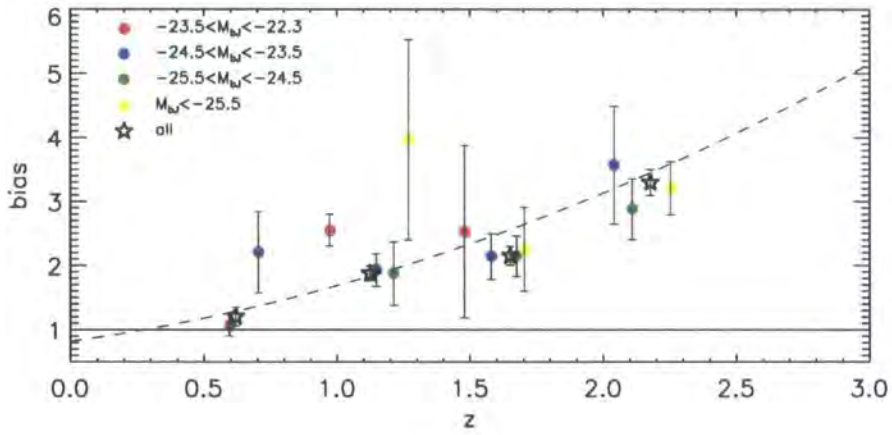

Figure 5.16: Bias evolution for different luminosity QSOs. The different colours refer to different absolute magnitude bins. The stars are the result for all the QSOs in each specific redshift bin. The dashed line is the empirical model of Croom et al. (2005). Each point is represented in the median redshift of all the QSOs in the specific M_{b_J} and z-ranges.

The stars in Fig. 5.16 represent the b estimates for the magnitude-integrated samples, corresponding to the shaded areas in Fig. 5.15. These values are very much in agreement with those found by Croom et al. (2005), using a similar method. The dashed line is the empirical description of $b(z)$ found by those authors. It corresponds to $b(z) = 0.53 + 0.289(1+z)^2$.

The circles refer to our measurements in different magnitude bins. The red ones correspond to the faintest, $M_{b_J} > -23.5$ QSOs; the blue ones to the $-24.5 < M_{b_J} < -23.5$ range; the green circles represent the QSOs with $-25.5 < M_{b_J} < -24.5$ and the brightest, $M_{b_J} < -25.5$ QSOs are represented by the yellow circles. Given the size of the error bars, which are related to the errors on the associated $\xi(20)$ measurements, no categorical conclusion can be drawn, regarding the possibility of a luminosity dependent QSO bias. The uprise in the bias values with redshift is unrelated to the different QSO luminosities, as a somewhat positive trend occurs for all QSOs irrespective of their magnitude. This is not entirely true for the brightest, $M_{b_J} < -25.5$, QSOs, (in yellow) for which the bias at $z \sim 1.3$ seems higher than at higher redshifts. However, given the small number of QSOs (355) within that redshift/magnitude range, this result would need further study.

The same "curved trend" seen for each redshift slice in Fig. 5.15 is also now apparent in this $b(z)$ plot. The b values for each magnitude are centred in the median redshift of the QSO subsample from which b was determined. Hence, in each redshift bin, the z-displacement of different magnitude points is due to the non-uniform distribution of the QSOs in the $[M_{b_J}, z]$ plane. That z-displacement, together with the colour-code in the left side of the plot, eases the interpretation of the different luminosity samples. If we concentrate on the $0.8 < z < 1.4$ interval, we see this "curved" feature when comparing the bias of consecutively brighter QSOs. This feature is

enhanced by the red, 2SLAQ-dominated, fainter bin, and its relatively small error bar. In the redshift intervals that follow, the same "curved feature" is observed, and again supporting the hypothesis that it might not be a simple stochastic variation of some luminosity - dependent variable, centred in 0. But again, the magnitude of the error bars does present the major caveat in this analysis, and a more quantitative, "Occam's razor" approach, would see the current results as conservatively consistent with a luminosity - independent QSO bias.

The bias of the QSOs is related to the mass of the dark matter halo they inhabit. The formalism of the relation between the two quantities was firstly developed by Mo and White (1996), who assumed a spherical collapse model. This was then extended to more complicated geometries, such as ellipsoidal collapse, by Sheth et al. (2001). In the analysis in this work the latter will be the adopted formalism. According to these authors, the bias can be related to the dark halo mass by:

$$b(M_{DMH},z) = 1 + \frac{1}{\sqrt{a}\delta_c(z)}\left(\sqrt{a}(a\nu^2) + \sqrt{a}b(a\nu^2)^{1-c} - \frac{(a\nu^2)^c}{(a\nu^2)^c + b(1-c)(1-c/2)}\right) \quad (5.27)$$

with $a = 0.707$, $b = 0.5$ and $c = 0.6$. ν is defined as $\nu = \delta_c(z)/\sigma(M_{DMH},z)$. δ_c is the critical density for collapse, and is given by: $\delta_c = 0.15(12\pi)^{2/3}\Omega_m(z)^{0.0055}$ (Navarro et al., 1997). $\sigma(M_{DMH},z) = \sigma(M_{DMH})G(z)$, where $\sigma(M_{DMH})$ is the *rms* fluctuation of the density field on the mass scale with value M_{DMH} and $G(z)$ is the linear growth factor (Peebles, 1984; Carroll et al., 1992). $\sigma(M_{DMH})$ can hence be computed as:

$$\sigma(M_{DMH})^2 = \frac{1}{2\pi^2}\int_0^\infty k^2 P(k) w(kr)^2 dk \quad (5.28)$$

where $P(k)$ is the power spectrum of density perturbations and $w(kr)$ is the Fourier transform of a spherical top hat, which can be given by (Peebles, 1980):

$$w(kr) = 3\frac{\sin(kr) - kr\cos(kr)}{(kr)^3} \quad (5.29)$$

where the radius r is related to the mass by:

$$r = \left(\frac{3M_{DMH}}{4\pi\rho_0}\right)^{1/3}, \quad (5.30)$$

and $\rho_0 = \Omega_m^0\rho_{crit}^0$ is the present mean density of the Universe, given by $\rho_0 = 2.78\times10^{11}\Omega_m^0 h^2 M_\odot$ Mpc^{-3}.

Here, we adopt a linear form of the power spectrum, $P(k) = P_0 T(k)^2 k^n$, where P_0 is simply a normalisation parameter that depends on σ_8 and $T(k)$ is the transfer function, which we describe through the analytical formula of Bardeen et al. (1986):

$$T(k) = \frac{\ln(1+2.34q)}{2.34q}\left(1 + 3.89q + (16.1q)^2 + (5.46q)^3 + (6.71q)^4\right)^{-1/4} \quad (5.31)$$

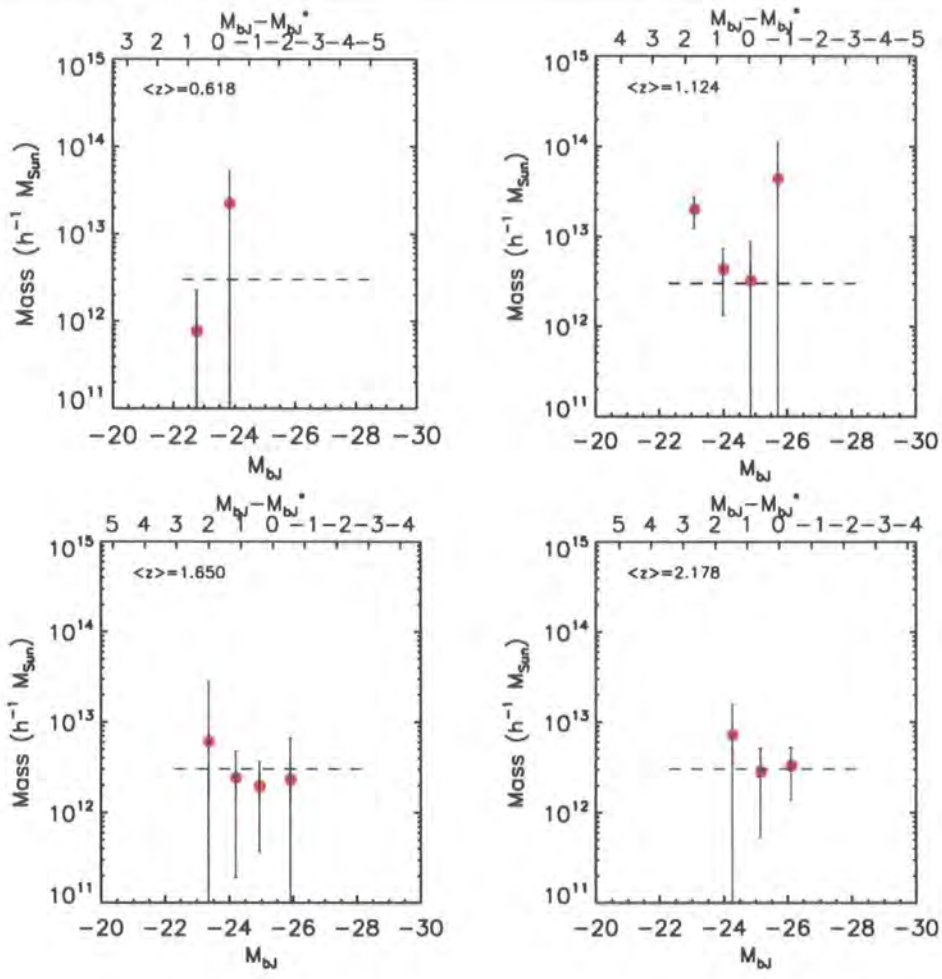

Figure 5.17: The four panels show the M_{DMH} estimates in different redshift bins. The median redshift of each z-interval is indicated in the top left of each graph. The top horizontal axis shows the magnitude difference relative to $M^*_{b_J}(< z >)$. The red circles show the dark matter halo mass measurements in different absolute magnitude bins, and are centred on the median values of each bin. The shaded area is the 1σ interval for the M_{DMH} value of all QSOs in that specific redshift interval. The horizontal length of the shaded area represents the range of M_{b_J} values for the QSOs in the redshift interval. The dashed line shows the average M_{DMH} at all redshifts.

where $q = k/\Gamma$ h Mpc^{-1}. As usual, Γ represents the shape parameter, which, taking into account the effects of the baryons, is approximately given by (Sugiyama, 1995):

$$\Gamma = \Omega_m^0 h \exp\left(\Omega_b^0 - \sqrt{h/0.5}\Omega_b^0/\Omega_m^0\right) \tag{5.32}$$

The results of performing this analysis using our determination of the bias is shown in Fig. 5.17.

The panels show the dark matter halo mass associated with different luminosity QSOs, in the same redshift intervals as those plotted in Fig. 5.15. The horizontal axes show the QSO absolute magnitude (bottom), and its difference relative to $M^*_{b_J}$ (top axis), similarly to Fig. 5.15. In each

panel, the red circles represent the M_{DMH} measurements in different magnitude bins, with error bars being the uncertainties corresponding to those obtained in our previous $b(z)$ estimates. The shaded areas represent the 1σ M_{DMH} confidence levels when estimating the masses associated to all QSOs, irrespective of their luminosities.

We find that, at all redshifts, QSOs seem to inhabit $M_{DMH} \sim 3.02 \times 10^{12} h^{-1} M_{\odot}$ haloes (dashed line), very much in agreement with what was found by Croom et al. (2005). As pointed out by those authors, this result disfavours the picture of a long-lived QSO population. As the dark matter halo masses grow, with decreasing redshift, we would expect to see lower-z QSOs in more massive haloes, if that were the case. The fact that we do not means that, at consecutive redshift intervals, we are not observing the same QSO population, but rather distinct sets of objects.

We also find, through our results, no evidence for M_{DMH} segregation with QSO magnitude. All the values seem to be consistent with a flat $M_{DMH} - M_{b_J}$ trend, indicating that QSOs seem to live in $\sim 10^{12} h^{-1} M_{\odot}$ haloes, independently of their luminosity. The only exception is at $z \sim 1.214$, where there is some indication that the faintest QSOs are associated with $\gtrsim 10^{13} h^{-1} M_{\odot}$ haloes. The "curved feature" seen in both ξ_{20} and bias determinations, is even less significant in this analysis, largely due to the size of the error bars inherent to the dark matter halo mass determination.

5.7 Estimating black-hole masses for different luminosity QSOs

Several models and theoretical studies have been developed to try to determine the relation between the mass of the dark matter halo and the mass of the black holes associated with the observed QSOs. Here we will consider two possible scenarios: **1.** a correlation exists between the dark matter halo mass (M_{DMH}) and the black hole mass (M_{BH}) (Ferrarese, 2002); **2.** instead, a correlation can be established between the bulge velocity dispersion and the black hole mass (Ferrarese and Merritt, 2000; Gebhardt et al., 2000). If we assume that these relations do not evolve strongly with redshift, we can then estimate the black hole masses associated with different luminosity QSOs, given that we know the mass of the haloes that they inhabit. We can then determine if indeed more luminous QSOs are associated with more massive black holes. For each of the two scenarios, and following Ferrarese (2002) and Croom et al. (2005), we will consider three possibilities for the dark matter halo profile, which affect each of assumed scenarios differently. We will consider: **a)** an isothermal dark matter profile; **b)** a NFW (Navarro et al., 1997) profile and **c)** a profile inferred from weak lensing studies (Seljak, 2002), which, for the sake of simplicity, we will refer to as the "lensing" profile.

When assuming a z-independent $M_{BH} - M_{DMH}$ correlation, the three possible (**a**), **b)** and **c**)) halo profiles correspond to the following relations (Ferrarese, 2002):

1. a) Isothermal profile:

$$\frac{M_{BH}}{10^8 M_\odot} \sim 0.027 \left(\frac{M_{DMH}}{10^{12} M_\odot}\right)^{1.82} \tag{5.33}$$

1. b) NFW profile:

$$\frac{M_{BH}}{10^8 M_\odot} \sim 0.1 \left(\frac{M_{DMH}}{10^{12} M_\odot}\right)^{1.65} \tag{5.34}$$

1. c) "Lensing" profile:

$$\frac{M_{BH}}{10^8 M_\odot} \sim 0.67 \left(\frac{M_{DMH}}{10^{12} M_\odot}\right)^{1.82} \tag{5.35}$$

These three possible solutions only differ by a factor which "normalises" the relation between M_{BH} and M_{DMH}, and ranges from 0.027 (for an isothermal profile) to 0.67 (for a "lensing" profile).

If we assume a z-independent correlation between the black hole mass and the circular velocity in the associated bulges (Shields et al. 2003, **2.**), then other relations are obtained.

Following Croom et al. (2005) and Wyithe and Loeb (2005a), the consequent relation between the dark matter halo mass and the black hole mass is given by:

$$M_{BH} = e \left(\frac{M_{DMH}}{10^{12} M_\odot}\right)^{2/3} \left(\frac{\Delta \Omega_m^0}{18\pi^2 \Omega_m(z)}\right)^{5/6} (1+z)^{5/2} \tag{5.36}$$

where Δ has the form:

$$\Delta = 18\pi^2 + 82\left(\Omega_m(z) - 1\right) - 39\left(\Omega_m(z) - 1\right)^2 \tag{5.37}$$

The constant e is related to the halo density profile. Different values of e will correspond to the same scenarios as considered in case **1.**. Hence, and following Wyithe and Loeb (2005a), we have that:

2. a) For an isothermal profile:

$$e \sim 10^{-5.1} \tag{5.38}$$

2. b) For a NFW profile:

$$e \sim 3.7 \times 10^{-5.1} \tag{5.39}$$

2. c) For the "lensing" profile:

$$e \sim 25 \times 10^{-5.1} \tag{5.40}$$

Again, as in case **1.**, the three different possibilities considered for the density profile differ only in terms of a normalisation parameter, in this case, given by the constant e.

We now use relations **1.** - **2.**, **a)**, **b)** and **c)**, to determine the mass of the black holes that correspond to our M_{DMH} measurements, under different assumptions, and determine if, with the current data, we can relate the the black hole mass to the QSO luminosity.

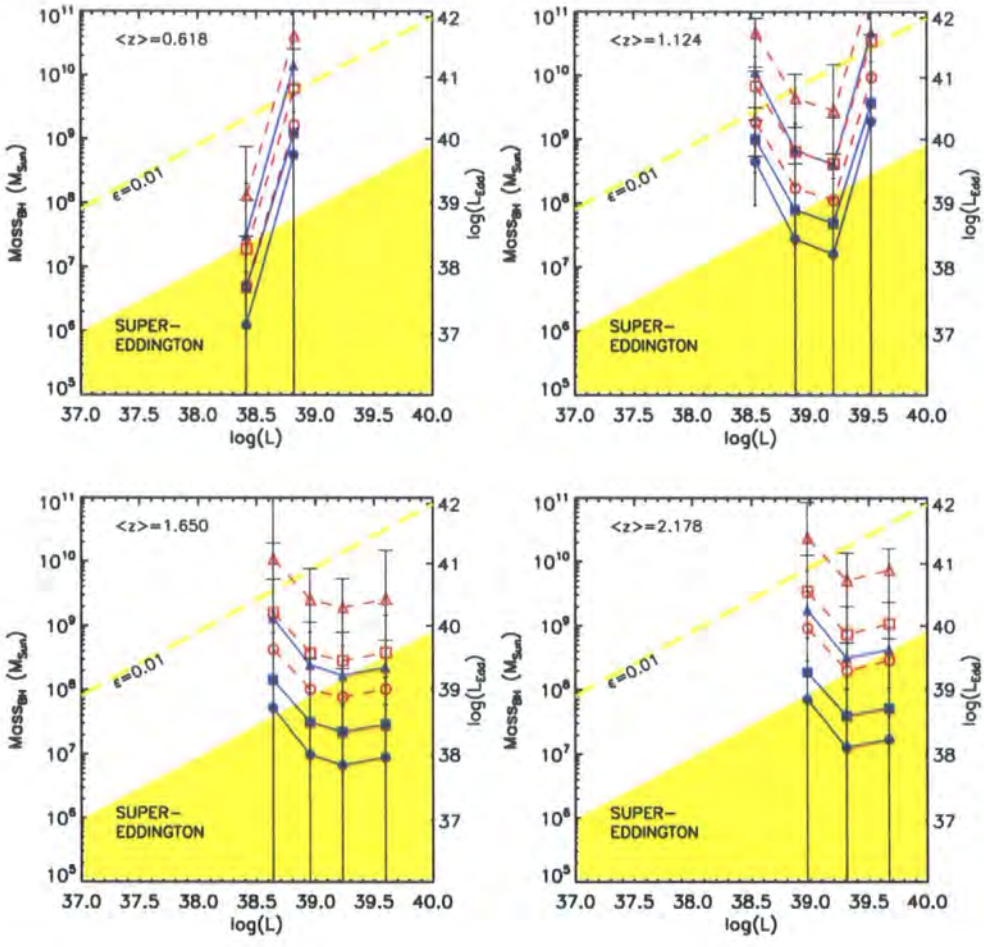

Figure 5.18: Black-hole mass as a function of luminosity, in different redshift bins. The filled symbols and solid lines are obtained assuming a M_{BH} - M_{DMH} relation which is independent of z. The dashed lines and open symbols, which also correspond to the errorbars with larger tickmarks, assume a z-independent M_{BH} - σ_c relation. In both cases, the circles, squares and triangles correspond to isothermal, NFW and lens-studies-based halo density profile, respectively. The points are located at the median luminosity value of the QSO subsample they correspond to. On the vertical axis on the right of each panel is the equivalent Eddington luminosity scale to that on M_{BH}, on the left. The yellow area represents the super-Eddington, $L/L_{Edd} > 1$, regime. The dashed yellow line corresponds to a Eddington efficiency $\epsilon = 0.01$. It can be seen that some models imply super-Eddington solutions, and hence are unlikely to occur. Most of the models though, correspond to $0.01 \lesssim \epsilon \lesssim 1.0$ values.

Our results are shown in Fig. 5.18. Each panel shows the results obtained in a given redshift bin. Plotted is the black hole mass as a function of QSO luminosity. To determine the bolometric luminosity from M_{b_J} we use (Croom et al., 2005):

$$L_{bol} = 10^{(79.42-M_{b_J})/2.66} W \tag{5.41}$$

The blue filled symbols and solid lines refer to hypothesis **1.**, where we assume a $M_{BH}-M_{DMH}$ z-independent relation. The red open symbols and dashed lines relate to hypothesis **2.**, where we assume a $M_{BH}-\sigma_c$ relation independent of z. The filled and open circles show the **a)** estimates, in Eqs. 5.33 and 5.38, respectively, on which we assume an isothermal density profile. The squares show the results if we assume a NFW profile (**b**)) and the triangles if we assume the lensing profile (**c**)). The error bars are the corresponding uncertainties to those on the M_{DMH} measurements, plotted in Fig. 5.17. To distinguish between the error bars, the ones that refer to hypothesis **1.** are represented with short tick marks, whereas the ones that refer to hypothesis **2.** have longer tick marks.

For both of the assumptions, **1.** or **2.**, the dark matter halo "lensing" density profile corresponds to more massive black holes, and the isothermal density profile corresponds to the least massive black holes, as expected. Also, it becomes evident that assuming different profiles, being it under z-independent $M_{BH}-M_{DMH}$ or $M_{BH}-\sigma_c$ scenarios, simply "shifts" the $M_{BH}-\log(L)$ relation vertically. Even though the errors associated with the M_{BH} are large, we can say that our values are consistent with those of Croom et al. (2005), who studied the evolution of M_{BH} with redshift.

The "curved feature" seen in the second and third panels is due to a similar trend being observed in our ξ_{20} clustering analysis, where we reported a higher clustering amplitude at the lowest and highest magnitudes than at intermediate luminosities.

Also shown, on the right-hand side vertical axis in each panel, is the Eddington luminosity. This is determined directly from the black hole mass as follows:

$$L_{Edd} = 10^{39.1}\left(\frac{M_{BH}}{10^8 M_\odot}\right) W \tag{5.42}$$

The yellow area in the bottom of each panel represents the value of M_{BH} that correspond to "super-Eddington" solutions ie, $L/L_{Edd} > 1$. The dashed line represents the $M_{BH}-\log(L)$ relation for an Eddington efficiency of $\epsilon = L/L_{Edd} = 0.01$. It can be seen that, for some of the scenarios considered, the mean efficiency is super-Eddington, in particular for models **1.a)** and **1.b)**, ie, assuming an isothermal profile and an NFW profile, when considering that the $M_{BH}-M_{DMH}$ relation that does not evolve with redshift. These relations are therefore unlikely to occur. Most of the remaining models suggest accretion efficiencies of $0.01 \lesssim \epsilon \lesssim 1$. It is somewhat unfortunate that the size of error bars do not allow us to draw conclusions regarding the significance of potential

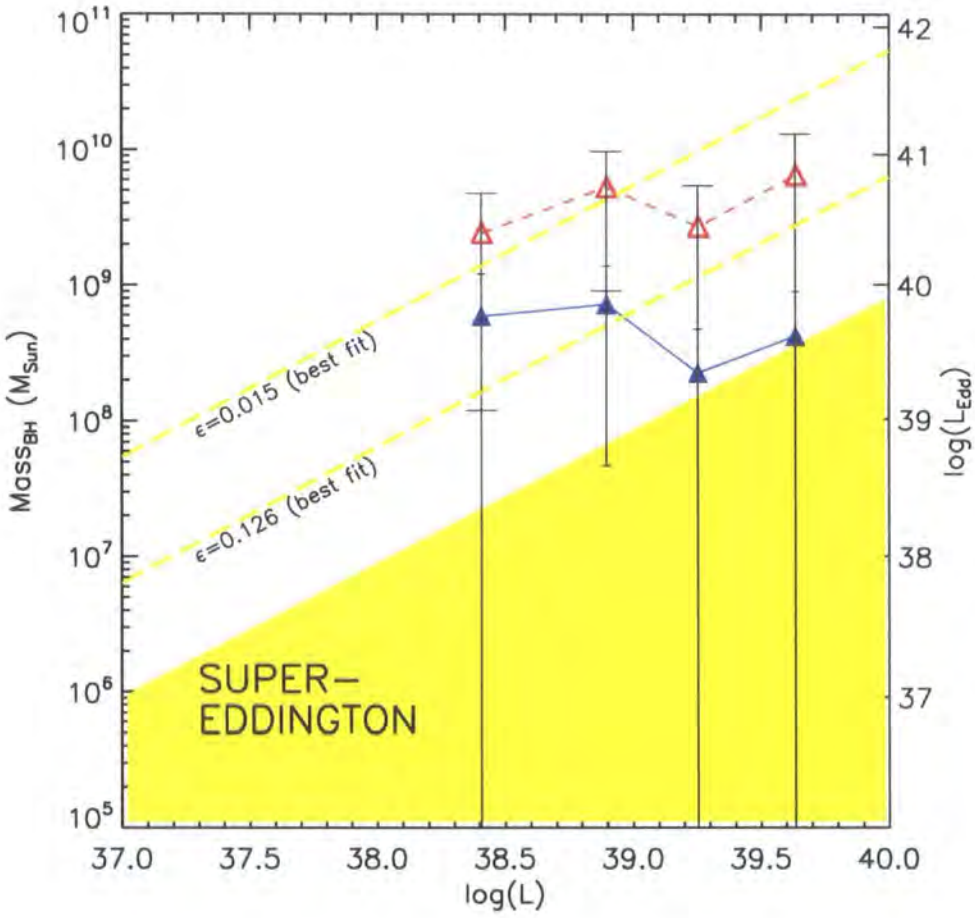

Figure 5.19: Black-hole mass as a function of luminosity, over all redshifts. We here assume the "lensing" halo density profile. The filled blue triangles refer to a z-independent M_{BH} - M_{DMH} relation, and the open red triangles to a z-independent M_{BH} - σ_c relation. The best fitting value of ϵ in both cases are shown by the dashed yellow lines.

changes of black-hole mass with luminosity of the associated QSO.

We averaged the data over the whole redshift range, and determined if we can exclude the hypothesis that QSOs do not accrete at a fixed fraction of Eddington through a simple χ^2 analysis. Fig. 5.19 represents the results, by assuming a the "lensing" density profile and a z-independent M_{BH} - M_{DMH} (filled blue triangles) and M_{BH} - σ_c (open red triangles) relations. Also shown are the best fitting values of ϵ for both assumptions.

It can easily be seen, from the M_{BH} measurements, that the black-hole mass seems independent of QSO luminosity. In addition, the black-hole mass does not correlate tightly with the Eddington efficiency ϵ, as a "flat" trend is observed in the $M_{BH} - L$ relation, which means that both luminous and fainter QSOs are associated to equally as massive black-holes, leading to higher values of accretion efficiency for brighter QSOs and lower for fainter QSOs. Hence, there seems to exist a

wide range of values for accretion efficiency consistent with a fixed black-hole mass. This dispersion of values favours the hypothesis that bright and faint QSOs are similar sources, but observed at different stages of their activity, as argued by the model of Hopkins et al. (2005a) and Lidz et al. (2006).

Our analysis is supported by a χ^2 fit to the measured efficiencies. We found that, assuming a z-independent M_{BH} - M_{DMH} relation, $\epsilon = 0.126^{+0.056}_{-0.037}$, with $\chi^2_{reduced} = 4.34$ (3 degrees of freedom), corresponding to a rejection of 99.9954%. If we instead assumed that the M_{BH} - σ_c relation does not evolve with redshift, we obtain $\epsilon = 0.015^{+0.006}_{-0.004}$, with $\chi^2_{reduced} = 2.10$ (3 degrees of freedom), corresponding to a rejection probability of 99.9017%. Given the χ^2 values, it is still possible to reject a model where the QSOs of a given mass accrete at a fixed ratio ϵ. Hence, although halo mass and black hole mass are probably closely correlated, black hole mass is almost independent of QSO luminosity and accretion efficiency.

5.8 Conclusions

The 2SLAQ QSO sample is an important tool for QSO clustering studies.

Firstly, the 2SLAQ QSO survey complements the previous 2QZ sample in terms of z-space distortion analyses. We have shown that a double-power law $\xi(r)$ model, which was previously shown to be a good description of the 2QZ real-space clustering, still describes well both the z-space and projected clustering measurements of the 2QZ and 2SLAQ samples combined. We fit the dynamical and geometrical distortions of the $\xi(\sigma, \pi)$ contours, extending the formalism developed by Hamilton (1992) and Matsubara and Suto (1996) to include a double-power law $\xi(r)$ model (Section 3.3.1, Model 1, and Appendix B) and fitting different "test" cosmologies (Alcock and Paczynski, 1979; Ballinger et al., 1996; da Ângela et al., 2005). We find that the subsequent confidence levels obtained in Ω^0_m and $\beta(z)$ are similar to those obtained when using solely the 2QZ data, but tighter due to the increased statistics from extra 2SLAQ QSO pairs, and also the additional cross-correlation pairs in the NGC 2SLAQ and 2QZ overlapping volumes. When combining these results with orthogonal contours obtained from linear theory of density perturbations, we find that $\Omega^0_m = 0.25^{+0.09}_{-0.07}$, $\beta(z) = 0.60^{+0.14}_{-0.11}$, similar to the values obtained from the 2QZ data alone.

Secondly, the 2SLAQ QSO constitutes a new dataset with a potentially central role in terms of breaking the L-z degeneracy. The sample extends 1 magnitude fainter than the 2QZ, and spans the same z-range. Hence, the combination of both provides a unique dataset, as the overall magnitude range probed is similar, both at low and high-z. This allows us to interpret clustering results and possible luminosity dependent measurements in different redshift bins, hence reducing any evolutionary biases. Our results are consistent with luminosity-independent QSO clustering. Apart from at the lowest redshift bin where there we do not have very luminous QSOs, all redshift

bins indicate a "curved" feature in terms of clustering measurements: the faintest and brightest QSOs seem to have a higher clustering amplitude than intermediate luminosity QSOs. This feature however, is not statistically significant. From the QSO bias we estimate the mass of the halos the 2QZ and 2SLAQ QSOs inhabit. Our results are consistent with those of Croom et al. (2005); QSOs seem to inhabit $\sim 3 \times 10^{12} h^{-1}\ M_{\odot}$ halos, independently of their redshift *or* luminosity. This is in contrast to what would be expected with a long-lived QSO population model. Also, our results do not show a tight correlation between halo mass and QSO luminosity, as would be expected from models where fainter QSOs populate lower mass haloes.

By assuming different density profiles for the dark matter halo and z-independent relations (such as M_{BH} - M_{DMH} or M_{BH} - σ_c) we can estimate the masses of the black holes associated with the QSOs. If the Eddington limit is a relevant limit for the accretion rate, and if one assumes that the M_{BH} - M_{DMH} relation is z-independent, then isothermal and NFW density profiles are not likely to be appropriate for the haloes these QSOs inhabit, as they predict super-Eddington accretions. This is no longer true if one assumes that the M_{BH} - σ_c is independent of redshift, instead. Most of the other assumptions imply $\sim 10^8$ – $10^{10} M_{\odot}$ black holes, and accretion efficiencies of $0.01 \lesssim \epsilon \lesssim 1$. These results are very much in agreement with those of Croom et al. (2005), and McLure and Dunlop (2004). In particular the latter measured the masses and Eddington efficiencies of high-z black holes using data from the SDSS DR1, through modelling the QSO spectra. Their analysis, significantly different from the one in the current chapter, results in M_{BH} and efficiency ϵ values similar to those we obtained. Different relations between the black hole and dark halo masses differ only by a scaling factor. Therefore, the trend observed in the $M_{BH} - \log(L)$ plot is the same irrespective of the halo density profile and M_{BH} - M_{DMH};M_{BH} - σ_c relation. The observed flat trend could suggest that QSOs do not accrete at a fixed fraction of Eddington.

The current analysis leaves room for future improvement. Future studies could relax the assumption that the error on the average correlation function, ξ_{20}, scales in a similar way as that on $\xi(s)$, and similarly to $w_p(\sigma)$. A principal component analysis on our clustering measurements could be an interesting complement, which we will leave for future.

Chapter 6

z-Space distortions in future luminous red galaxy surveys

6.1 Introduction

The wealth of information contained in cosmological surveys has been object of intense study, during the last decades. The three dimensional distribution of galaxies unveils the underlying large scale structure of the Universe and the physics behind galaxy formation, evolution of gravitationally bound structures and the dynamics of the Universe. Recent surveys (e.g., 2dFGRS, SDSS) carry a statistical weight that has permitted the estimation of cosmological parameters with unprecedented confidence levels (e.g. Tegmark et al., 2004; Hawkins et al., 2003; Cole et al., 2005; Huetsi, 2006). Results from different studies seem to converge in a "standard scenario" in which two thirds of energy content of the Universe is accounted by "dark energy", which is leading to an accelerated rate of expansion (Perlmutter et al., 1999; Spergel et al., 2006). As the dynamics of the Universe and its matter content are well constrained with available data, it is due for new, future surveys to tackle "deeper", more detailed characteristics of the physics determining the expansion of the Universe.

Recent measurements of the scale of baryon acoustic features in the galaxy correlation function and power spectrum (Cole et al., 2005; Eisenstein et al., 2005) have pioneered the determination of the equation of state of dark energy via clustering measurements on large datasets from cosmological surveys. However, the determination of w, where $p = w\rho$ is the dark energy equation of state, relies on the precise determinations of the total amount of dark energy (Blake and Glazebrook, 2003), and even more when we try to estimate redshift variations of w, using different parameterisations to quantify this z-dependence (Glazebrook and Blake, 2005; Jassal et al., 2005; Liberato and Rosenfeld, 2006).

With the aim of estimating the dark energy equation of state and further understand the cosmic expansion history of the Universe, different surveys are being prepared. Amongst them are LRG surveys, such as the AAΩ LRG survey (UK PI: T. Shanks), which aims to gather data from 350000 LRGs at $< z > \sim 0.7$. The volume of information contained in such datasets will also constitute an

enormous potential in terms of z-space distortion analysis. In this chapter it is argued if the level of precision on Ω_Λ^0 required to place constraints on w can be achieved from those same datasets, in particular from the AAΩ LRG survey, by modelling the z-space distortions imprinted on the galaxy $\xi(\sigma,\pi)$ contours. To do this, we construct a LRG mock catalogue, mimicking the main characteristics of the AAΩ LRG survey, using the *Hubble Volume* simulation. We then apply the $\xi(\sigma,\pi)$ fitting method described on this thesis to constrain the values of Ω_m^0 and $\beta(z)$ in the simulation, and quantify the uncertainty expected on these parameters, when the method is applied to the full LRG dataset.

We also intend to validate the method presented on this thesis via *Hubble Volume* simulation results. In previous work, (Hoyle, 2000) used the *Hubble Volume* to create mock QSO catalogues and apply their $\xi(\sigma,\pi)$ fitting method, but the their method differed in the dynamical distortion model used to the one adopted here (they adopted Model II, section 3.3.2). Since they also used the input clustering amplitude directly from the $\xi(s)$ measurements and not from parameterising $\xi(r)$, suggests that we need to corroborate further our $\xi(\sigma,\pi)$ z-space distortion analysis in a simulated dataset.

6.2 The *Hubble Volume* simulations

To build mock galaxy catalogues we use the *Hubble Volume* simulations. For details on these the reader is referred to Evrard et al. (2002), for example. Quite briefly, the *Hubble Volume* simulations are large N-body simulations, containing $\sim 10^9$ particles and were run by the Virgo Consortium (e.g. Jenkins et al., 1998). Two different cosmologies were assumed, when generating the simulations, a $\Omega_m^0 = 1$, τCDM cosmology and a $\Omega_m^0 = 0.3$, $\Omega_\Lambda^0 = 0.7$, ΛCDM model. We here use the latter run, whose model parameters are outlined in table 6.1. The simulation is initialised at z_0, and the particles are "perturbed" with a Harrison -Zeldovich ($P(k) \propto k$) power spectrum, with transfer function derived from CMBFAST (Seljak and Zaldarriaga, 1996). The simulation lightcone output was used, as required to mock high-z surveys. The output simulation geometry consists of an octant extending from 0 (observer on the octant vertex) to the comoving length L. At 45° from the side of the octant there is a deep, 75° × 15° wedge, extending out to $\sim 5000\,h^{-1}$Mpc ($z \sim 4$).

Ω_m^0	Ω_Λ^0	σ_8	Γ	z_0	$L(h^{-1}\mathrm{Mpc})$
0.3	0.7	0.9	0.17	35	3000

Table 6.1: The model parameters of the ΛCDM run of the *Hubble Volume* simulation.

6.3 Building a mock catalogue

The lightcone output of the *Hubble Volume* simulation contains mass particles extending throughout a very large volume/wide redshift range. To build a given galaxy mock catalogue we need to adopt a suitable bias prescription, allowing us to distinguish mock galaxies from the simulation mass particles. As previously seen, the bias can be given by the ratio of the galaxy correlation function to that of the underlying dark matter. Thus, and in particular, it reflects the different rms fluctuations of luminous and dark matter particles, in spheres of a given radius r (Kaiser, 1984; Cole et al., 1998):

$$b_r = \sigma_r^{gal}/\sigma_r^{mass} \tag{6.1}$$

Consider an underlying mass density field. The probability of local fluctuations to be associated with galaxies should depend on the density contrast. Naturally, one would expect that the relation between the local density, bias and the probability of forming galaxies to depend on the physics of galaxy formation. In the present study it is not our goal to determine a bias prescription based on processes such as gas dynamics and feedback mechanisms, which will lead to a simulated galaxy distribution (e.g. Frenk et al., 1996; Pearce et al., 2001). Instead, our motivation is to predict the gains in terms of parameter estimation from $\xi(\sigma, \pi)$ fitting in future redshift surveys. As such, and following Cole et al. (1998), Hoyle (2000) or Myers (2003), we use a parametric determination of the galaxy probability and bias prescription, from the underlying mass density distribution.

To determine the local density associated with a given particle we have assumed that this would depend only on its neighbouring particles, smoothed with a Gaussian kernel over a $3\,h^{-1}$Mpc scale. The bias prescription will determine the probability of a galaxy being associated with a given particle. When the prescription is such that the clustering measurements match those of existing surveys, after correcting for the radial completeness, we are then left with a mock catalogue of those galaxies.

6.4 Mock of a $z \sim 0.7$ galaxy survey

Luminous Red Galaxies (LRGs) are a privileged tracer of large scale structure. In addition to being intrinsically bright and strongly clustered (e.g. Zehavi et al., 2005), they are relatively spectroscopically homogeneous and straightforward to identify photometrically (Cannon et al., in prep). These qualities are the basis of the *AAΩ LRG survey*, which aims to gather observations of ~ 350000 LRGs out to $z \sim 0.8$. The (riz) colour and $(19.8 < i_{AB} < 20.2)$ magnitude selection results on a radial distribution of the LRGs extending from $z \sim 0.4$ and peaking at $z \sim 0.7$, as demonstrated at the survey pilot run. This was run at the AAΩ facility, a multi-object and integral field spectrograph. In particular the MOS mode, through using the 2dF top end, allows obtaining spectra from 392 objects, with spectral resolutions of 1200 - 10000. The imaging data

at the pilot run was obtained from SDSS DR4 (Adelman-McCarthy et al., 2006) imaging, but ultimately this will be obtained from the VST ATLAS Survey (PI: T. Shanks, Durham University, UK), an imaging survey to be performed at the VLT Survey Telescope (VST, Belfiore et al., 2005).

The scientific goals of these LRG surveys are multi-fold. The prime aim is to make a precise measurement of the LRG power spectrum and determine the scale of the acoustic oscillations imprint. This feature has recently been detected in the $z \sim 0.35$ SDSS LRG $\xi(s)$, as an excess of clustering power at $s \sim 100\,h^{-1}$Mpc (Eisenstein et al., 2005) and in the power-spectrum of 2dFGRS galaxies (Cole et al., 2005). Precise measurements of these "baryon wiggles" allow the determination of constraints in the baryon content of the Universe and the equation of state of dark energy (Cooray et al., 2001; Blake and Glazebrook, 2003; Eisenstein, 2005; Blake et al., 2006)). Based on simulation results of Blake and Glazebrook (2003), and taking into account the high bias of LRGs, the AAΩ LRG survey should produce measurements of the dark energy equation of state parameter, w, with a 10% uncertainty (T. Shanks, priv. comm.). Other scientific motivations for the survey include the determination of upper limits on the neutrino mass (e.g. Elgarøy et al., 2002; Elgarøy and Lahav, 2005); the building of a LRG cluster catalogue, using the LRGs to identify galaxy clusters; the measurement of the LRG - QSO cross-correlation, enabling studies of QSO environment and LRG - QSO evolution; stellar population studies, through the stacking of LRG spectra as a function of redshift. However, and in addition to all these scientific results, one main scientific gain of the survey is the expected tightness of the confidence levels in Ω_m^0 and $\beta(z)$ through $\xi(\sigma,\pi)$ z-space distortion analysis. The large number of LRGs, combined with the expected high clustering amplitude should significantly decrease any uncertainty in the determination of those values. In particular, they will complement the baryon acoustic oscillation analysis through a self-consistent determination of the energy density of the Universe, as the determination of w requires very precise determinations of Ω_m^0 (Blake and Glazebrook, 2003).

We here build a LRG mock catalogue using the *Hubble Volume* simulation, mimicking the total survey size and expected clustering of the $z \sim 0.7$ LRGs. We applied a bias prescription to the mass particles, in order to determine the probability of each to correspond to an LRG. In order to build the LRG mock catalogue, we found that the bias prescription that produced the best results was to consider a "smoothed version" of the high-peaks model (e.g. Davis et al., 1985). In this case, the probability of forming a galaxy depends on ν and is characterised by two parameters (a and b):

$$P(\nu) = \begin{cases} 0, & \nu < -b/a \\ a\nu + b, & -b/a < \nu < (1-b)/a \\ 1, & \nu > (1-b)/a \end{cases} \tag{6.2}$$

where $\nu(\mathbf{r}) = \delta(\mathbf{r})/\sigma$, with $\delta(\mathbf{r}) = (\rho(\mathbf{r}) - \bar{\rho})/\bar{\rho}$ being the density contrast and $\sigma^2 =< |\delta|^2 >$.

Cole et al. (1998) outlines several possible bias prescriptions. In particular, we also tested their *Model 2*. In this case, the bias probability is again characterised by two parameters (α and β):

$$P(\nu) \propto \begin{cases} \exp(\alpha\nu), & \nu \leq 0 \\ \exp(\alpha\nu + \beta\nu^{3/2}), & \nu > 0 \end{cases} \tag{6.3}$$

however, it was found that the previous $P(\nu)$ formalism (Eq. 6.2) provided a more suitable description of the LRG clustering than this latter one.

For a given combination of values of a and b, in Eq. 6.2, the radial distribution of the biased particles is convolved with a "truncated" Gaussian $N(z)$, peaking at $z = 0.7$ and extending from $z = 0.4$ to $z = 0.8$, and the sample is restricted to an area of ~ 3200 square degrees, normalising the final catalogue to a sky density of 110 deg^{-2}. In the end, we are left with 353492 mock LRGs, with the expected radial distribution and sky density as in the AAΩ LRG survey. The values of the a and b that correspond to the analysis presented here are $a = 20.0$ and $b = 0.2$.

Fig. 6.1 shows the final $N(z)$ of the biased particles, that constitute the LRG mock catalogue (blue dashed line). The solid line shows the Gaussian $N(z)$ used to mock the LRG distribution. The LRG $N(z)$ peaks at $z = 0.7$, and the wings of the distribution follow that of the bell-shaped $N(z)$ used for normalisation. Whereas both the distributions extend from $z = 0.4$, the mock LRGs only extend to $z = 0.8$. This happens due to our initial intention of building a 2SLAQ LRG mock catalogue, with a Gaussian $N(z)$, extending from $z \sim 0.4$ to $z \sim 0.8$. As the observations of the 2SLAQ survey have now been completed and the data is being analysed, an AAΩ LRG mock catalogue was instead constructed, and using the same input from the *Hubble Volume* , extending to $z \sim 0.8$. It is not expected that, had the $0.8 \leq z \leq 1.0$ been included, our z-space distortion analysis would have been different. If all clustering measurements are performed consistently and the random points correctly mimic the LRG distribution, the non-inclusion of the high-z tail of the Gaussian $N(z)$ should not affect the conclusions on this chapter. For this reason, the extrapolation of the Gaussian curve for $0.8 < z < 1.0$ is shown by the dashed line.

Fig. 6.2 shows the projected correlation function of the mock LRG sample (red circles). Also shown are the $w_p(\sigma)$ results from the ($< z > \sim 0.35$) SDSS DR2 LRGs (Zehavi et al., 2004) (open blue stars) and those of the ($< z > \sim 0.55$) 2SLAQ LRGs (Ross et al., in prep, filled green stars). It can be seen that the mock LRG sample indicates a somewhat higher clustering amplitude then the two other LRG survey results. Utilising a different bias prescription will change this result considerably. It is not our aim to provide a clustering measurement that will exactly mimic the SDSS or 2SLAQ results. Given the higher redshift and different selection of these LRGs, we would not expect to measure exactly the same clustering amplitude as in these two surveys. Instead, we intend to determine the relative constraints on Ω_m^0 and $\beta(z)$ that should be obtained from the AAΩ LRG survey, rather than the actual values of these parameters, from the mock catalogue, and hence the exact amplitude of the clustering should not be of crucial importance, given that the shape and magnitude resembles those of existing LRG surveys. The error bars shown represent

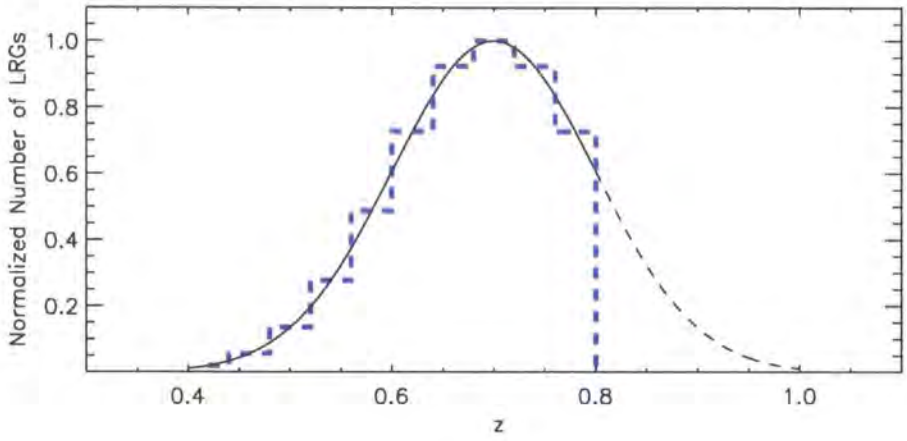

Figure 6.1: The dashed blue line is the $N(z)$ of the mock LRGs, extending from $z = 0.4$ to $z = 0.8$. Shown by the solid black line is the Gaussian $N(z)$ peaking at $z = 0.7$, used to convolve the LRG radial distribution. The dashed black line is the extrapolation of this curve for $0.8 < z < 1.0$.

field-to-field errors. The 2SLAQ sample was divided into 16 different regions and the variation of the $w_p(\sigma)$ measurements in each of those was used to determine the error on $w_p(\sigma)$. It should be pointed out that, in this case, since the LRGs are so strongly clustered, the correlation between pairs in one given separation bin will be large, and the use of the Poisson formula to estimate the errors would lead to an underestimated value of the true uncertainty. Given the simulation resolution we are only considering the results for $\sigma > 1\,h^{-1}$Mpc.

We used the $w_p(\sigma)$ measurements to estimate the LRG real-space correlation function, $\xi(r)$. For a statistically robust sample, $\xi(r)$ can be obtained directly from $w_p(\sigma)$ through (Von Zeipel, 1908; Lilje and Efstathiou, 1988; Saunders et al., 1992):

$$\xi(r) = -\frac{1}{\pi}\int_r^\infty \frac{1}{(\sigma^2 - r^2)^{1/2}}\frac{dw_p(\sigma)}{d\sigma}d\sigma \tag{6.4}$$

However, we here infer $\xi(r)$ through the method previously adopted for the 2QZ survey (chapter 2; da Ângela et al. 2005) in order to further test the application of $w_p(\sigma)$ parametric fits and their robustness in the determination of $\xi(r)$. The $w_p(\sigma)$ measurements of the mock LRGs suggest a double power-law parameterisation for $\xi(r)$. The best fitting $\xi(r)$ model to the $w_p(\sigma)$ points corresponds to:

$$\xi(r) = \begin{cases} \left(\frac{r}{14.31}\right)^{-1.60}, & r \leq 10\,h^{-1}\text{Mpc} \\ \left(\frac{r}{12.70}\right)^{-2.40}, & r > 10\,h^{-1}\text{Mpc} \end{cases} \tag{6.5}$$

and its projection is shown by the solid line in Fig. 6.2.

Given that in the mock LRG sample we can directly measure the "true" correlation function, free from any dynamical distortions, we can compare the $\xi(r)$ model above, obtained by fitting the $w_p(\sigma)$ data and the real-space correlation function measurements, computed from the simulation

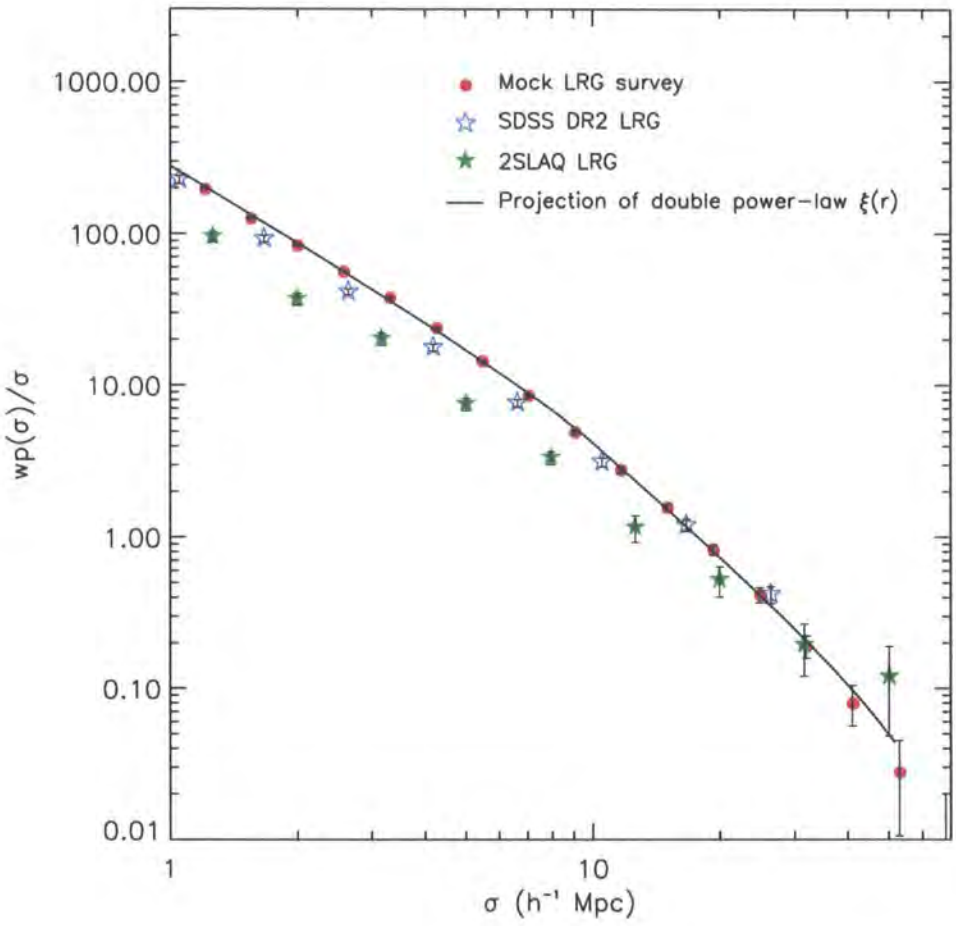

Figure 6.2: The red circles show the $w_p(\sigma)/\sigma$ measurements from a mock LRG survey. The errorbars represent jacknife errors. Also shown as open blue stars are the $w_p(\sigma)/\sigma$ from the ($< z >= 0.35$) SDSS DR2 LRG sample (Zehavi et al., 2004) and the $< z >= 0.35$ 2SLAQ LRG sample as green stars. The solid line shows the projection of a double-power law $\xi(r)$ model.

directly. This is shown in Fig. 6.3. The red circles are the LRG real-space $\xi(r)$, measured directly from the real-space positions of the LRGs in the mock catalogue, using the Hamilton estimator. The errors shown are field-to-field errors from the 16 subsamples. The dashed line shows the best fitting double power law model to the $\xi(r)$ measured directly from the mocks, and is parameterised by:

$$\xi(r) = \begin{cases} \left(\frac{r}{13.84}\right)^{-1.80}, & r \leq 10\,h^{-1}\mathrm{Mpc} \\ \left(\frac{r}{12.80}\right)^{-2.20}, & r > 10\,h^{-1}\mathrm{Mpc} \end{cases} \tag{6.6}$$

The solid line shows the double power law $\xi(r)$ model obtained by fitting $w_p(\sigma)$ (Eq. 6.5), whose projection is represented in Fig. 6.2. The similarities between the dashed and solid lines illustrates that the two different parameterisations give similar overall $\xi(r)$ descriptions. Also shown, as open pink triangles, are the $\xi(r)$ measurements obtained by deprojecting $w_p(\sigma)$. The $w_p(\sigma)$ inversion is calculated by assuming a step function for $w_p(\sigma)$, and performing a linear interpolation between the σ values (Saunders et al., 1992; Hawkins et al., 2003). For $r = \sigma_i$:

$$\xi(\sigma_i) = -\frac{1}{\pi} \sum_{j \geq i} \frac{w_{p_{j+1}} - w_{p_j}}{\sigma_{j+1} - \sigma_j} \ln \left(\frac{\sigma_{j+1} + \sqrt{\sigma_{j+1}^2 - \sigma_i^2}}{\sigma_j + \sqrt{\sigma_j^2 - \sigma_i^2}} \right) \tag{6.7}$$

It can be seen that the inversion technique does provide very reliable measurements of $\xi(r)$, as found by Hawkins et al. (2003) using 22 2dFGRS mock catalogues also from the *Hubble Volume* simulation. However, we find that the above formula is sensitive to the binsize of $w_p(\sigma)$. For larger bins, Eq. 6.7 is likely to underestimate $\xi(r)$. This effect should also depend on the clustering strength of the galaxies, and the fact that our mock sample is highly clustered will, in principle, amplify this dependence on the binsize.

Also shown by the dash-dotted line, is the non-linear prediction of the dark matter clustering at $z \sim 0.7$. This was computed using the $P(k)$ model of Smith et al. (2003), with the same model parameters as the *Hubble Volume* simulation (in table 6.1). The amplitude difference between the mass $\xi(r)$ and that of the mock LRGs reveals the high-bias of the mock sample. This difference changes very slightly with scale, hence indicating that our bias prescription does not imply a highly scale-dependent bias.

It is not surprising the fact that deviations from a $\xi(r)$ power-law model are seen in our mock sample. The shape of the correlation function will naturally depend on the bias prescription used. Ultimately, however, it will also be a function of the physics behind the mass clustering (e.g. Smith et al., 2003) and that of galaxy bias (e.g. Rees, 1985). The power-law form is a popular description of correlation functions, and it does hold as a suitable description over a limited separation range (Peebles, 1974b; Fisher et al., 1994; Norberg et al., 2001). However, and as suggested by our QSO clustering analysis on chapter 2, correlation functions do show deviations from simple power-law models, as corroborated by other observational results (e.g. Groth and Peebles, 1977; Shanks et al., 1983; Maddox et al., 1990; Baugh, 1996; Zehavi et al., 2004). In particular, the change of slope suggested by our results could be due to the curvature of the $\xi(r)$ contribution from galaxy pairs

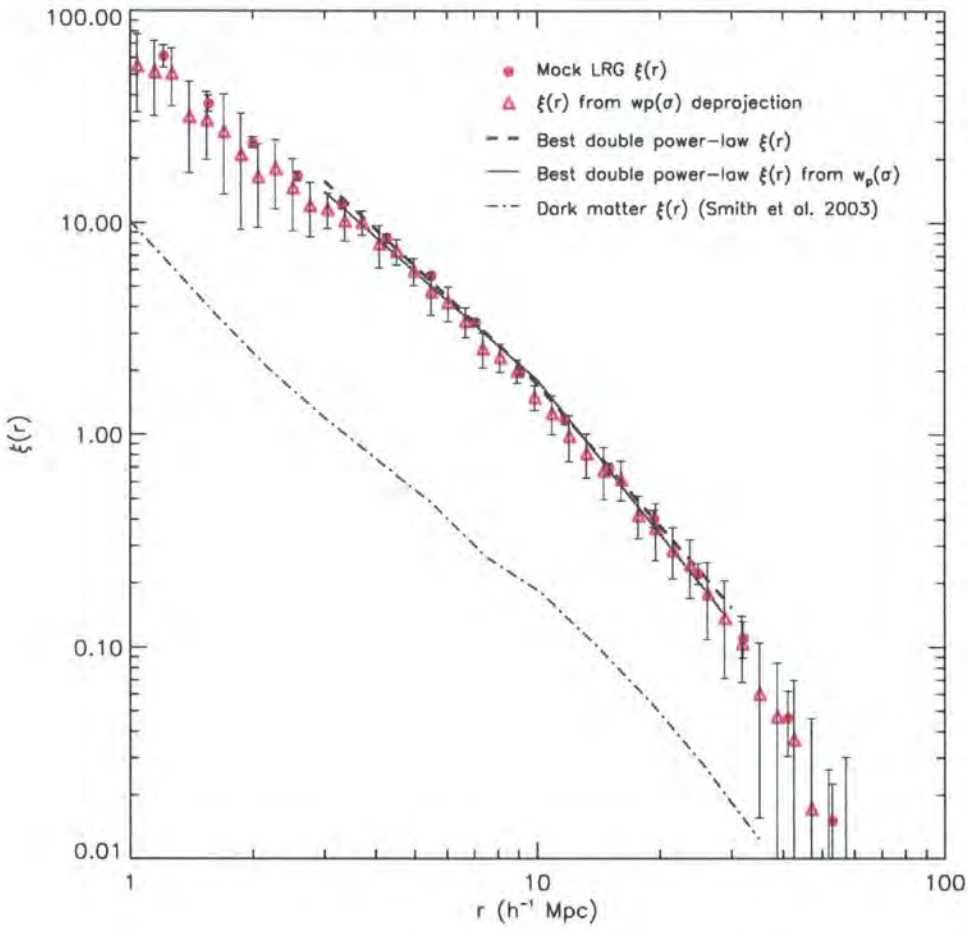

Figure 6.3: The red circles shows the $\xi(r)$ measured directly from the *Hubble Volume* mock LRG survey. The open pink triangles are the $\xi(r)$ values obtained by inverting $w_p(\sigma)$. The solid line shows the double power-law $\xi(r)$ model obtained from fitting $w_p(\sigma)$, and the dashed line is the best fit double power-law to the "true" $\xi(r)$ values (red circles). The dash-dotted line shows the mass $\xi(r)$ at $z \sim 0.7$, obtained using the non-linear $P(k)$ model of Smith et al. (2003), with the *Hubble Volume* parameters.

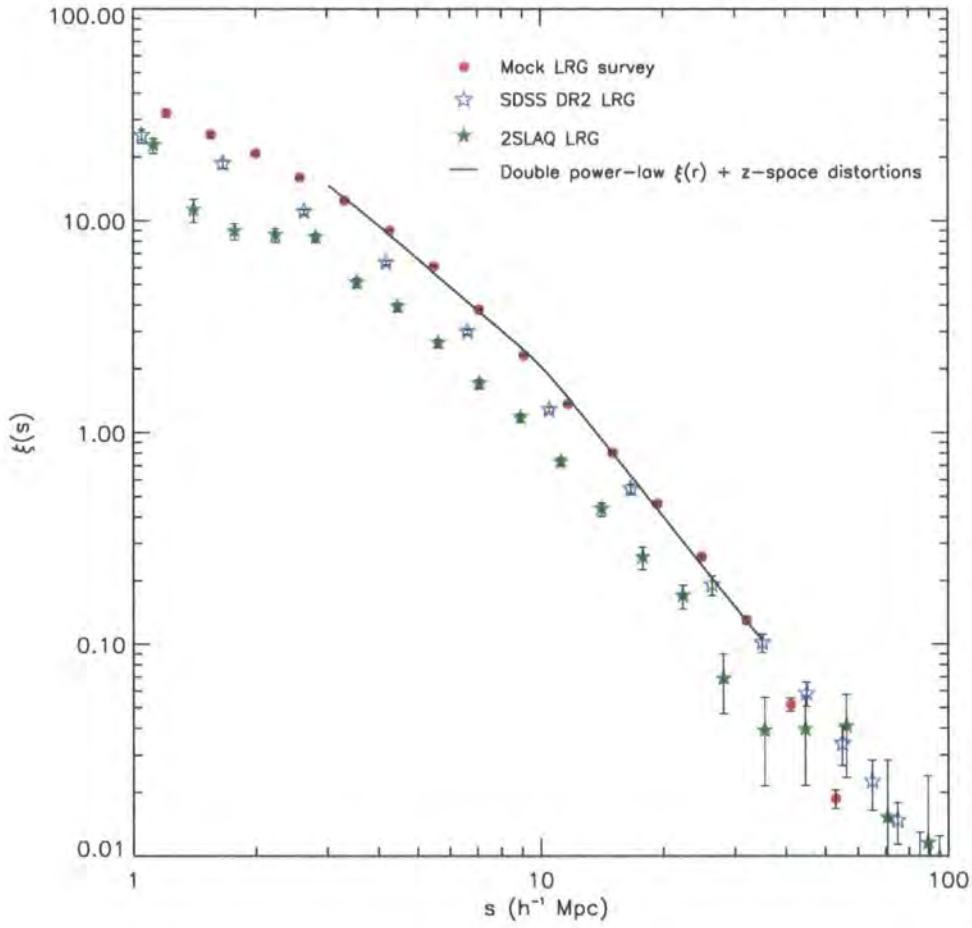

Figure 6.4: The red circles show the $\xi(s)$ measurements from the *Hubble Volume* mock LRG survey. Again, the open blue stars are the SDSS $\xi(r)$ measurements (Zehavi et al., 2005; Eisenstein et al., 2005) and the green stars the $\xi(s)$ values from the 2SLAQ LRGs (Ross et al., in prep).

in different halos (e.g. Zehavi et al., 2004; Tinker et al., 2006b).

The LRG $\xi(s)$ measurements from the mock catalogue are shown in Fig. 6.4. The symbols are the same as in Fig. 6.2 and again the error bars represent the field-to-field error from 16 mock LRG subsamples. Again, the red circles represent our measured clustering values, with associated field-to-field errors. Open blue stars are the SDSS LRG results (Zehavi et al., 2005; Eisenstein et al., 2005) and green stars the 2SLAQ LRG $\xi(s)$ results (Ross et al., in prep.). Again it is evident the higher clustering amplitude of the mock LRGs, relative to the SDSS or the 2SLAQ LRG samples.

The solid line shows the predicted $\xi(s)$ from the the best fitting $\xi(r)$ model to the $w_p(\sigma)$ values (Eq. 6.5). This was obtained by computing a $\xi(\sigma, \pi)$ model from that $\xi(r)$ parameterisation and with the dynamical distortions characterised by $< w_z^2 >^{1/2} = 600\,\mathrm{km\,s^{-1}}$ and $\beta(z) = 0.24$. The value of $< w_z^2 >^{1/2}$ is that measured directly from the biased *Hubble Volume* LRGs and the value of β is the one predicted by combining the low-z bias estimate of the 2dFGRS (Hawkins

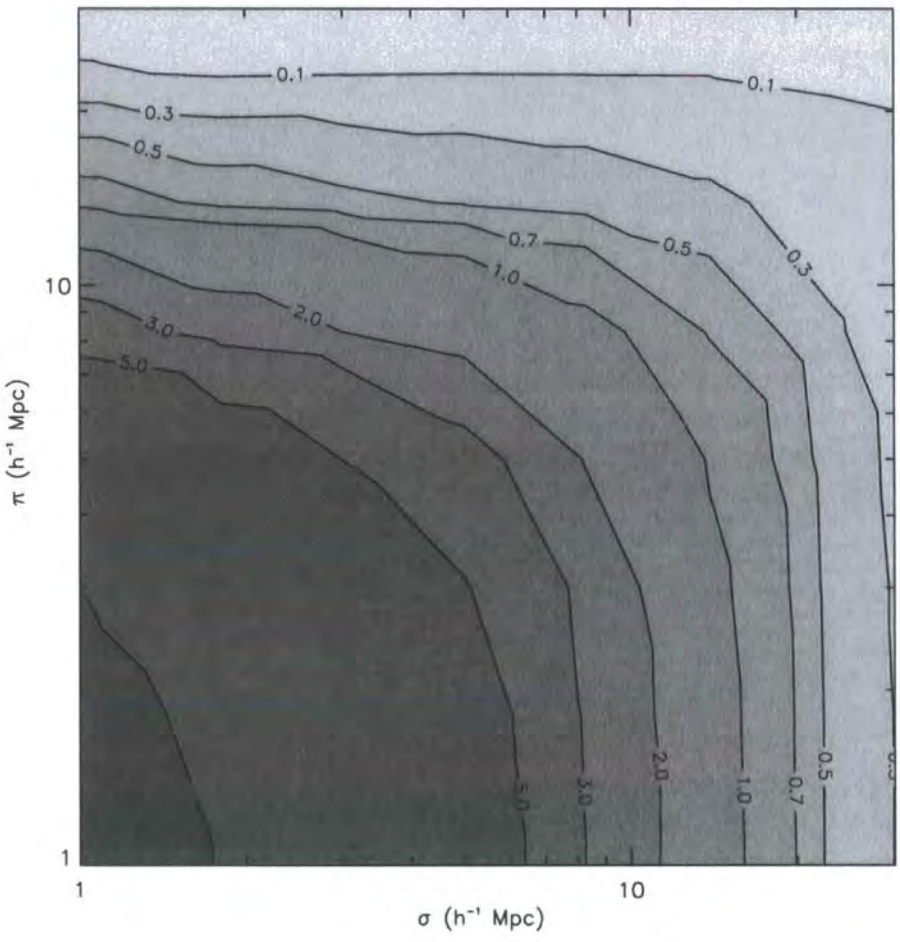

Figure 6.5: $\xi(\sigma, \pi)$ contours from the *Hubble Volume* mock LRG survey. The strong clustering of the LRGs is also evident in this plot.

et al., 2003) with the mock LRG clustering amplitude, and computing the growth factor of density perturbations (Carroll et al., 1992). The $\xi(\sigma, \pi)$ model is then spherically averaged, resulting in a $\xi(s)$ description. For details on the $\xi(\sigma, \pi)$ model see section 3.3.1 and appendix B.

The $3 - 30$ h^{-1}Mpc range over which the solid line is plotted represents the $\xi(\sigma, \pi)$ fitting range. In this range, the double power-law $\xi(r)$ model is a good description of the data. At larger scales, the clustering signal is lower than that to what expected by extrapolating this model. This is likely an effect due to our bias prescription. At lower scales the clustering measurements will be affected by the simulation resolution.

The $\xi(\sigma, \pi)$ measurements are shown in Fig. 6.5. Again, we only represent scales larger that 1 h^{-1}Mpc due to the resolution of the simulation. This will not affect our present analysis given that we are only interested in the z-space distortion effects at intermediate scales. From Fig. 6.5 it is evident the strong clustering amplitude of the mock sample.

We fitted the $\xi(\sigma, \pi)$ z-space distortions, using the double-power law $\xi(r)$ parameterisation obtained through $w_p(\sigma)$ fits (Eq. 6.5), the value of velocity dispersion measured from the simulation

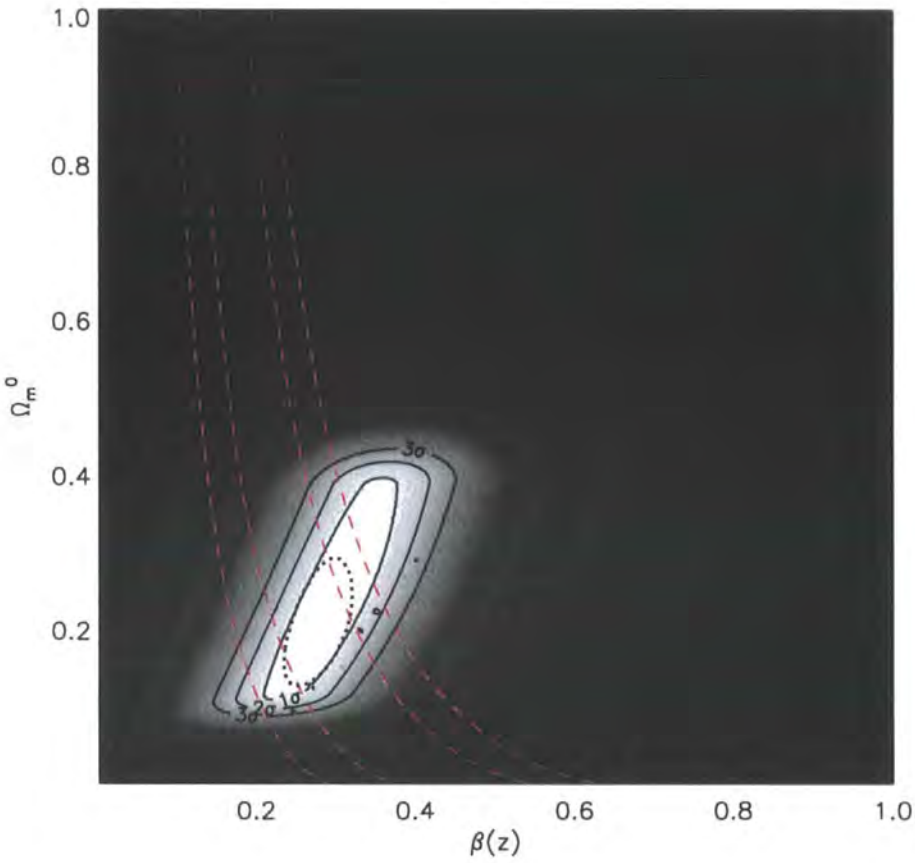

Figure 6.6: The solid contours and shaded regions represent the constraints on Ω_m^0 and β from the $\xi(\sigma,\pi)$ z-space distortion fitting of our mock data. The dashed lines are the 1σ and 2σ confidence levels from linear evolution of clustering. The dotted contour shows the 1σ joint confidence level.

($600\,\mathrm{km\,s^{-1}}$), and the fitting range shown in Fig. 6.4. The result is shown in Fig. 6.6.

The solid contours and shaded region represent the constraints obtained from the z-space distortion fitting. The best fitting parameters from this fit alone are $\Omega_m^0 = 0.25^{+0.12}_{-0.10}$, $\beta(z) = 0.30^{+0.04}_{-0.05}$, with $\chi^2_{reduced} = 1.05$ (37 d.o.f.). The reason why the best fitting value of Ω_m^0 is not exactly $\Omega_m^0 = 0.3$ is due to the uncertainty in the form of $\xi(r)$. However, that value is well within the 1σ confidence limits. The dashed lines show the 1σ and 2σ linear theory prediction of $\beta(z = 0.7)$, given the 2dFGRS results (Hawkins et al., 2003) and our $\xi(s)$ clustering amplitude. Shown as a dotted contour is the 1σ joint confidence level, which corresponds to $\Omega_m^0 = 0.21^{+0.05}_{-0.06}$, $\beta(z) = 0.28^{+0.02}_{-0.03}$. To confirm that the discrepancy between the best value of Ω_m^0 from the z-space distortion analysis alone and that expected ($\Omega_m^0 = 0.3$), we repeated the analysis using the double power-law description of the true real-space data, as measured from the mock catalogues directly. This parameterisation corresponds to the dashed line in Fig. 6.3. The result of performing the $\xi(\sigma,\pi)$ fitting using this $\xi(r)$ model as an input is shown in Fig. 6.7.

As before, constraints on Ω_m^0 and $\beta(z)$ from z-space distortion analysis alone are shown by the

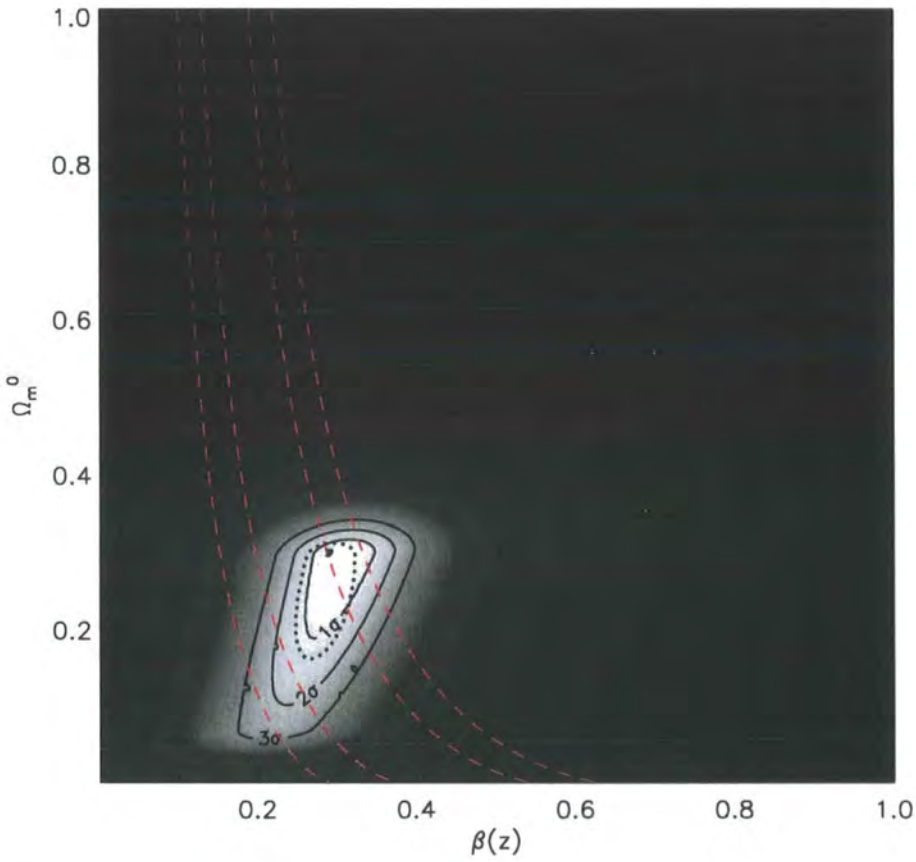

Figure 6.7: As previously, the solid contours and shaded regions are the constraints on Ω_m^0 and β from the $\xi(\sigma, \pi)$ z-space distortion analysis. Now we assume a different $\xi(r)$ parameterisation, obtained from the mock catalogue directly. The dashed lines are the 1σ and 2σ confidence levels from linear evolution of clustering and he dotted contour shows the 1σ joint confidence level.

shaded contours and solid lines. Now, the best fitting values from the z-space distortion alone are: $\Omega_m^0 = 0.30^{+0.02}_{-0.06}$, $\beta(z) = 0.31^{+0.02}_{-0.02}$ ($\chi^2_{reduced} = 1.43$). Once we combine these with linear theory predictions (dashed lines) we obtain the joint contour shown by the dotted line. The best fitting values from the combined constraints are: $\Omega_m^0 = 0.25^{+0.05}_{-0.05}$, $\beta(z) = 0.28^{+0.02}_{-0.02}$ ($\chi^2_{reduced} = 1.49$).

6.5 Conclusions

The next steps in the quest for a coherent cosmological picture will depend on the findings from the next large cosmological surveys. Large quantities of data will be used to determine the equation of state of dark energy and its (possible) redshift evolution. With this in mind, large datasets from LRG surveys are particularly wealthy, in what concerns the amount of information they carry and the precision they permit in the determination of physical quantities. Given that they are intrinsically bright and easy to identify through the pronounced $4000\AA$ spectral break (Eisenstein et al., 2001; Padmanabhan et al., 2005) and that they are strongly clustered (Zehavi et al., 2005; Padmanabhan et al., 2006), these galaxies are efficient tracers of the underlying large scale structure.

In the present work we used the *Hubble Volume* simulation to construct a mock LRG catalogue, and predict the constraints that could be obtained in Ω_m^0 and $\beta(z)$ from fitting the z-space distortions in the $\xi(\sigma, \pi)$ clustering patterns, using a method previously developed on the thesis. In particular, we constructed a mock survey with the characteristics of the AAΩ LRG survey. The size of the survey and its radial distribution make it an excellent tool for detecting the baryon signature in the correlation function at $100\,h^{-1}$Mpc, and put constraints in the equation of state of dark energy. However, constraining w demands a very tight confidence interval on the value of Ω_m^0 (Blake and Glazebrook, 2003), and we explore whether this can be achieved from the same survey, through modelling z-space distortions in the LRG $\xi(\sigma, \pi)$. z-space distortions alone do provide a tight constraint in the value of Ω_m^0, but only by combining this constraint with the orthogonal confidence levels in the $[\Omega_m^0, \beta]$ plane can we obtain the level of precision required. In particular, assuming a flat cosmology, we determine that Ω_Λ^0 can be determined with $\sim 7\%$ accuracy.

Producing estimates of the underlying form of $\xi(r)$ from fits to $w_p(\sigma)$ can lead to potential shifts in the determined values of Ω_m^0 and $\beta(z)$. However, the clustering signal of the AAΩ LRG Survey will allow precise $\xi(r)$ determinations by directly deprojecting the $w_p(\sigma)$ measurements. As for the previous cosmological surveys analysed in this thesis, given the larger size of the confidence levels in our Ω_m^0 and $\beta(z)$ estimates from the z-space distortions in the 2QZ and 2SLAQ samples (chapters 3 and 5), these potential shifts should be well within the quoted errors.

Chapter 7 | *Conclusions*

7.1 Summary and results

Over the last years redshift surveys have had a profound contribution to our knowledge and understanding of the Universe. Large cosmological datasets such as the 2dFGRS (e.g. Colless et al., 2001) or the SDSS (e.g. Loveday, 2002) have produced results with unquestionable statistical value, and tools such as correlation functions or power spectra have allowed tight constraint of cosmological scenarios. The fact that the derived cosmological constraints are in such a good agreement with those from CMB studies, in particular those of WMAP (Spergel et al., 2006) has had two repercussions in the scientific community. Firstly, there is a generalised acceptance of what we call the *Standard (or concordance) Model*, in which two thirds of the Universe is accounted by dark energy, a dynamic cosmic field characterised by a negative pressure and accounting for the accelerated expansion. The matter content accounts for one third of the total energy density, with the baryon fraction corresponding to only $\sim$ 15% of the total matter content. The second consequence of these results was the concept of *Precision Cosmology*. The joint constraint on the matter and baryon contents of the Universe from WMAP (3-year results), 2dFGRS, the Cosmic Background Imager (CBI, Pearson et al., 2003), the Arcminute Cosmology Bolometer Array Receiver (ACBAR, Kuo et al., 2004) and Lyman-α are $\Omega_m^0 = 0.23^{+0.04}_{-0.04}$, $\Omega_b^0 = 0.044^{+0.004}_{-0.004}$ (Spergel et al., 2006). This level of precision in cosmological parameters is unprecedented. However, these tight confidence levels may lead to a false sense of security: the wealth of information contained in redshift surveys has indeed proved crucial in our recent learning curve, but it has also shown us that there is much more to discover and understand. The importance of redshift surveys in the determination of cosmological parameters has been shown, for example, by Blanchard et al. (2006), who demonstrated that a EdS cosmology could still explain the WMAP observations, if one assumes a lower value of H_0 and relaxes the assumption that the primordial power-spectrum is scale-free. Only through large scale structure observations, and in particular by fitting the baryon acoustic oscillation imprint on the clustering measurements, can one exclude the possibility of a $\Omega_m^0 = 1$ cosmology.

The aim of this thesis was to contribute to our broad understanding of the Universe, by statistically analysing datasets from QSO surveys (2QZ and 2SLAQ), LBG surveys and large N-body simulations. We will here divide the main results into two groups: one of a more *cosmological* nature and another, where we will detail more *astrophysical* implications of this work.

7.1.1 Cosmology

If the standard scenario is correct, it should also explain the clustering and z-space distortions observed in our data, which spans a wide z-range. We used the 2QZ, 2SLAQ QSO and LBG samples to constrain the geometry of the Universe (by determining Ω_m^0 through the Alcock-Paczynski test) and to study the clustering of underlying dark matter and infall into local overdensities (via $\beta(z)$ estimates from modelling dynamical infall). We also use a sample of LBGs to study the effects of z-space distortions in their measured clustering pattern in orthogonal directions, and infer the potential wealth of future $z \sim 3$ surveys.

QSO clustering and z-space distortions

In chapter 2 we estimated the real-space correlation function of QSOs at $z \sim 1.4$, using the 2QZ survey. The power-law deviations seen in the z-space $\xi(s)$ measurements are unlikely to be solely due to the effects of small scale random motions, smearing the clustering signal of close QSO pairs. Fits to the sky projected correlation function suggest a double power-law parameterisation of the QSO real-space correlation function. This parameterisation is also in good agreement with the $\xi(s)$ measurements, if we assume a value of velocity dispersion suggested by previous studies. We have also verified that the double power law model is in agreement with what we expect from the ΛCDM non-linear clustering predictions (Smith et al., 2003) and what is seen in other large cosmological surveys, such as the 2dFGRS. We have also concluded that the value of $\beta(z = 1.4)$, if estimated from the $\xi(s)/\xi(r)$ ratio, depends very sensitively on the $\xi(r)$ parameterisation. Assuming a double-power law $\xi(r)$ model results in $\beta(z) = 0.32^{+0.09}_{-0.11}$.

In chapter 3 we analyse z-space distortions in the 2QZ clustering by modelling the $\xi(\sigma, \pi)$ contours. The assumed $\xi(r)$ parameterisation is of crucial importance, when modelling the effects of z-space distortions in orthogonal directions. The "spherical" change in amplitude needs to be an accurate description of $\xi(r)$, in order for deviations seen from this spherically symmetric clustering to be solely due to z-space distortions, rather than dominated by lower-order amplitude $\xi(r)$ misfits.

We compared two different dynamical distortion models and explained the differences between them. We then used one of the models to fit the z-space distortions seen in the 2QZ $\xi(\sigma, \pi)$ contours. The choice of the model to use was based in our assumption of the $\xi(s) - \xi(r)$ relation and in the need to better compare our results with other studies, namely the $\xi(\sigma, \pi)$ modelling of the 2dFGRS data. When using this model to fit the 2QZ $\xi(\sigma, \pi)$ contours we found the following best fitting parameters: $\Omega_m^0 = 0.35^{+0.19}_{-0.13}$, $\beta(z) = 0.50^{+0.13}_{-0.15}$, assuming a flat, $\Omega_m^0 = 0.3$ cosmology. These are found after combining our z-space distortion analysis with constraints from large-scale linear clustering evolution. Our results should, in the absence of noise, be independent on the assumed cosmology. As such, we have also fitted the clustering measurements in orthogonal directions in a $\Omega_m^0 = 1.0$ cosmology, having found similar constraints. The value of $\beta(z = 1.4)$ found here differs from that obtained from the $\xi(s)/\xi(r)$ analysis in chapter 2, but they are both consistent within

the 1σ confidence level.

In chapter 5 we combined the 2QZ survey data with the fainter QSO sample from the 2SLAQ survey. We found that the two samples show similar clustering results, in terms of z-space and projected correlation functions. The double-power law $\xi(r)$ parameterisation found for the 2QZ is still a good description of the 2SLAQ QSO clustering. *By fitting the z-space distortions seen in the 2QZ+2SLAQ joint sample we find* $\Omega_m^0 = 0.25^{+0.09}_{-0.07}$, $\beta(z) = 0.60^{+0.14}_{-0.11}$. Hence, by adding the 2SLAQ QSO signal, we obtain a value of $\beta(z)$ greater than that found for the 2QZ sample alone, in chapter 3. The values are still consistent however, within the 1σ confidence level. The value of Ω_m^0 is more constrained than that found previously from the 2QZ sample. This is due to the increased statistics, by having more QSO pairs at a given separation, and from the curved shape of the $\Omega_m^0 - \beta(z)$ contours from clustering evolution in linear theory, which are tighter in the Ω_m^0 space for higher values of $\beta(z)$.

Using the integrated correlated function up to 20 h^{-1}Mpc *we found evidence for an increase of QSO clustering amplitude with redshift*, in agreement with what had previously been found from the 2QZ data alone (Croom et al., 2005). As these authors, and also as found in a sample of photometrically classified SDSS DR1 QSOs (Schneider et al., 2003; Myers et al., 2006), we find that the QSO bias significantly increases with z.

z-space distortions in LBG surveys

We then apply in chapter 4 the z-space distortions analysis developed in the context of the 2QZ to a sample of distant, star-forming, $z \sim 3$ LBGs. Given the small size of the fields of view in this survey, there is not enough information in the sky direction to better constrain the real-space LBG clustering. Instead, we rely on the information along the redshift direction to obtain a $\xi(r)$ input in our $\xi(\sigma, \pi)$ fitting, especially at scales greater than $\sim 10\,h^{-1}$Mpc. This does not produce any systematic error in our z-space distortion analysis if we restrict our fitting range to scales large enough not to be significantly affected by redshift errors or small-scale peculiar velocities. By measuring $w_p(\sigma)$, we found a typical clustering length of $r_0 = 4.48^{+0.17}_{-0.18}\,h^{-1}$Mpc, with $\gamma = 1.76^{+0.08}_{-0.09}$ ($\xi(r) = (r/r_0)^{-\gamma}$), which is comparable to the values found by other studies. *The higher space density of LBGs improves our relative constraints in* Ω_m^0 *and* $\beta(z)$, relative to those that would have been obtained with a similar number of 2QZ QSOs. It was found $\Omega_m^0 = 0.55^{+0.45}_{-0.16}$, $\beta(z) = 0.25^{+0.05}_{-0.06}$. However, given the apparent lower value of $\beta(z = 3)$ of the LBGs, and the curvature of the linear clustering constraints on the $[\Omega_m^0, \beta(z = 3)]$ plane, the degeneracy between these two values, when estimated from z-space distortion analysis, is not completely lifted by the linear clustering evolution constraints. Using the *Hubble Volume* simulation to predict the gains in the Ω_m^0, $\beta(z = 3)$ confidence levels, with a survey of $\sim$ 2300 LBGs using the VLT VIMOS instrument, we show that the $\beta(z = 3)$ constraints should become tighter by a factor of ~ 2, whereas the constraint on Ω_m^0 does not improve significantly, relative to that obtained with the

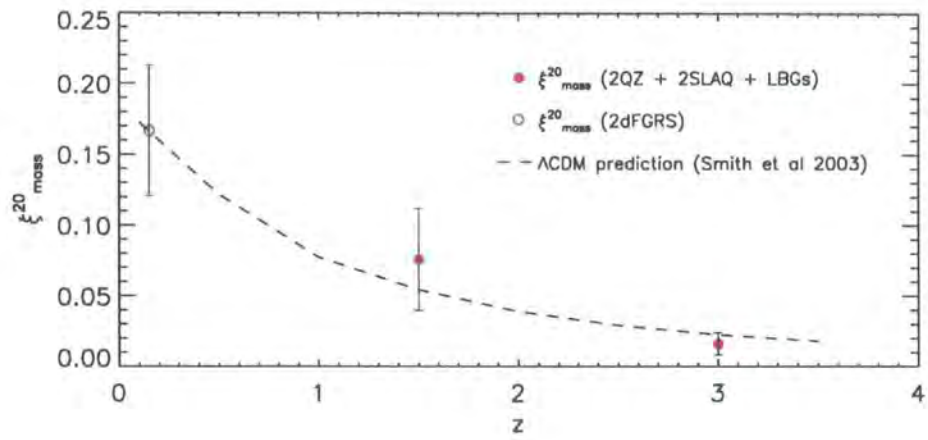

Figure 7.1: The red circles are the $\xi^{20}_{mass}(z)$ computed from the ξ_{20} measurements from the 2QZ, 2SLAQ and LBG surveys and the respective values of $\beta(z)$ from $\xi(\sigma, \pi)$ z-space distortion analysis. The open blue circle shows the ξ^{20}_{mass} computed from the 2dFGRS data. Also shown as a dashed line is the ΛCDM prediction, using the non-linear $P(k)$ model of Smith et al. (2003).

present LBG dataset.

The combination of our results allows us to study the evolution of dark matter clustering as a function of redshift. Combining or measurements of $\beta(z) = \Omega_m(z)^{0.6}/b(z)$, at $z \sim 1.5$ and $z \sim 3$ from z-space distortion analysis with those of the average spherical clustering (ξ_{20}), we can compute $\xi^{20}_{mass}(z)$, at those redshifts, and compare with what we expect from ΛCDM predictions. This is shown in Fig. 7.1. The dashed line shows the ΛCDM prediction (obtained using the Smith et al. (2003) $P(k)$ model), which is parameterised using a WMAP/2dF cosmology with $\Omega^0_m = 0.27$ and $\sigma_8 = 0.84$ (Percival et al., 2002). Shown as the open blue circle, is the $z \sim 0.15$ ξ^{20}_{mass} calculation from the 2dFGRS which, as expected, is in perfect agreement with the theoretical prediction. Our results, shown by the solid red circles, also predict values of ξ^{20}_{mass} consistent with ΛCDM predictions.

7.1.2 Astrophysics

We combined the 2QZ and 2SLAQ QSO samples in an attempt to address the possible luminosity dependence of QSO clustering. If the luminosity of the QSOs correlates with the mass of the host dark matter haloes, then QSO bias should also depend on QSO luminosity.

The black-hole – QSO connection

In chapter 5 we explore this black-hole – QSO connection. By splitting the 2QZ and 2SLAQ data into different redshift intervals, we can study the (potential) luminosity dependence of QSO clustering in each bin. *No significant luminosity dependence of QSO clustering is found.*

From the measured bias values associated to QSOs at different redshifts and luminosities we can compute the mean halo masses associated to those QSOs. This relies on the assumption of a ellipsoidal collapse model of density perturbations (Sheth et al., 2001), derived from bias calculations of Mo and White (1996), who developed the model from the Press-Schechter formalism (Press and Schechter, 1974). Our results suggest that *the mass of the dark matter haloes associated with QSOs is independent of both redshift and luminosity.*

Different dark matter halo density profiles affect differently the circular velocity of the bulge associated with the supermassive black-holes (SMBHs). Consequently, determining black hole masses from the dark matter halo masses will intrinsically depend on the form of the halo profile assumed. In addition, we also rely on our assumption of z-independent relations linking the SMBHs and their host haloes. For all the relations here assumed, our results suggest that *at a given redshift, black hole mass is approximately independent of QSO bolometric luminosity, and thus accretion efficiency. Therefore, QSOs do not appear to radiate at a fixed fraction of the Eddington luminosity.* Assuming isothermal or NFW density profiles, and a $M_{BH} - M_{DMH}$ z-independent relation, will cause the most luminous QSOs to live in a super-Eddington regime. On the other hand, the assumption of a halo density profile as suggested by lensing studies (Seljak, 2002) implies sub-Eddington accretion rates for the most luminous QSOs.

Our results corroborate and complement those of Lidz et al. (2006), whose simulation results based on the models of Hopkins et al. (2005a), Hopkins et al. (2005b), Hopkins et al. (2005c), Hopkins et al. (2005d), Hopkins et al. (2006) suggest that QSO luminosity should not be correlated with the mass of the host dark matter halo. The reason is that the same massive halos host faint and bright QSOs, and the difference in luminosity is due to the QSOs being observed in different periods of their lifetime. Another consequence is that QSO clustering should not correlate strongly with luminosity, again, just as shown by the data.

Those authors also agree with the result shown in this thesis and Croom et al. (2005), and conclude that QSO clustering and halo mass does not evolve strongly with redshift, even though QSO bias substantially increases as we move to higher z. This could hint at possible anti-hierarchical QSO formation (Merloni, 2005; Cowie et al., 2003; Lidz et al., 2006), as halos harbouring QSOs would have deeper potential wells at high-z than at low-z, leading to more luminous black holes being observed at high-z than at low-z. The reason for the rapid decrease of QSO bias with time is related to haloes of $\sim 10^{12} - 10^{13} M_{\odot}$ corresponding to rarer, high-density-contrast peaks at higher redshift. The results of those authors also predict that a large range in QSO luminosity should correspond to a very restricted range in QSO halo masses, as our observations and measurements seem to indicate.

7.2 Conclusions and future prospects

In this thesis we have seen what the clustering of QSOs and galaxies can teach us about the physics of the Universe. *The combination of the Ω_m^0 constraints from the z-space distortion $\xi(\sigma,\pi)$ fitting of the 2QZ, 2SLAQ and LBG data is* $\Omega_m^0 = 0.30^{+0.13}_{-0.05}$, slightly higher than, but consistent with, the WMAP measurements. However, we must note the number of assumptions being made when estimating Ω_m^0 and $\beta(z)$. The first one, and perhaps the most relevant, is that our $\xi(\sigma,\pi)$ z-space distortion model does not take into account a possible scale dependence of bias. It is unlikely that the bias is scale independent, as argued, for instance, by Tegmark and Peebles (1998), Mann et al. (1998), Blanton et al. (1999). However, and as shown by the first authors, this scale dependence may not be significant within the range studied here. One possible alternative would have been to perform the z-space distortion $\xi(\sigma,\pi)$ analysis withing the framework of the Halo Occupation Distribution (HOD) model (Tinker, 2006; Tinker et al., 2006b). A second assumption is that the velocity dispersion could, in principle, be implemented including a scale-dependence factor (Scoccimarro, 2004). A model including the scale dependence of the velocity dispersion has been developed by those authors, and future study could investigate the effect of introducing that additional dependence in our analysis. However, other studies concluded that including this dependence has little effect on the fitting results (e.g. Hawkins et al., 2003; Jing et al., 1998).

As discussed, many other methods for estimating Ω_m^0 and β from cosmological datasets have been developed. Selecting a given statistical tool or a data-mining algorithm to have tight constraints on these parameters is not a straightforward task. Most of the methods rely on different assumptions and are affected differently by possible systematics. We have here developed a method to constrain Ω_m^0 and β from the distortions imprinted in the clustering pattern of QSOs and galaxies via dynamical and geometrical effects. We used the autocorrelation function of the objects to determine their clustering. We found that, due to the degeneracy between the z-space anisotropies due to Ω_m^0 and β, the 1-parameter confidence levels on each parameter depend on the value of the remaining one. In other words, due to the general trend of the confidence levels on the (Ω_m^0, β) plane, the lower the value of β, the larger the uncertainty on Ω_m^0, and for low best fitting values of Ω_m^0, we should also expect a larger uncertainty on our determination of β.

Outram et al. (2004) used a similar method for constraining the same cosmological parameters, from the distortions seen in the 2QZ power-spectrum results. Their (1 σ) error on both parameters is $\Delta\beta \sim 0.10$, $\Delta\Omega_m^0 \sim 0.15$, which are similar to the values obtained in the present thesis (see chapter 3). Therefore, as we are measuring the clustering at large scales, the errors associated to the best fitting parameters are similar, using both power-spectrum or correlation function statistics. The β constraint is also comparable to that found from the 2dFGRS. Hawkins et al. (2003), for instance, by fitting the dynamical distortions on the 2dFGRS $\xi(\sigma,\pi)$, obtained $\Delta\beta \sim 0.09$.

But the constrains on these values are actually considerably stronger once one utilises datasets

such as the recent three-year WMAP release (WMAP3) or the SDSS LRG catalogue. In particular, using the WMAP3 data alone, the constraint on Ω_m^0 is $\Omega_m^0 = 0.238^{+0.030}_{-0.041}$ (Spergel et al., 2006), hence a much more precise measurement of the density of the Universe than that obtained here. Once we combine these measurements with others from large-scale structure, this constraint is even tighter: the combination of the WMAP3 constraint with that from the 2dFGRS galaxy power-spectrum, gives $\Omega_m^0 = 0.236^{+0.016}_{-0.024}$ (Spergel et al., 2006). Weak lensing results provide also an additional method to constrain Ω_m^0, as shown by Contaldi et al. (2003). Those authors used the WMAP first-year data together with the red-sequence cluster survey results (RCS, Hoekstra et al., 2002) and determined the statistical gain on the likelihood constrains on the (Ω_m^0, σ_8) plane. Including the RCS datasets reduces the uncertainty on Ω_m^0 by a factor of 2.

Tegmark et al. (2006) measured the real-space power-spectrum of the SDSS LRG survey and combined it with the WMAP results to determine cosmological parameters with a great level of accuracy. Their results yield $\Delta\Omega_m^0 \sim 0.02$. They also use the LRG $P(k)$ determinations to determine β, both though z-space distortion analysis and by determining the bias (b) from the ratio of the LRG power to the CMB power. They show that the two independent measurements are in agreement, even though the second method carries a smaller uncertainty: $\Delta\beta \sim 0.035$ for the z-space measurement and $\Delta\beta \sim 0.014$ for the power-amplitude measurement.

Similarly to our bias determinations (via estimates of β), three-point statistics such as bispectrum analyses of galaxy clustering also allow measurements of the bias. The latter are, however, independent of the cosmological model assumed. Verde et al. (2002) measured the galaxy bispectrum from the 2dFGRS survey, concluding that the non-linear bias parameter is actually very small and consistent with zero. The constraint on the linear bias is of the order of $\sim$ 10%: $b_1 = 1.04^{+0.11}_{-0.11}$. A possible future bispectrum analysis of the 2QZ and 2SLAQ samples would complement our determination of β via z-space distortions, due to its independence on geometrical effects.

Feedback mechanisms likely to occur in LBGs further motivate new, larger $z \sim 3$ surveys. In particular, our results demonstrate what can be expected from future LBG surveys, such as the VIMOS LBG Survey, in terms of $\xi_{LBG}(\sigma, \pi)$ z-space distortion analyses. Using imaging data from the MOSAIC I and II cameras at the KTNO and CTIO observatories, the VIMOS instrument will allow measurements of the LBG clustering at large angular scales, and support more reliable measurements of the LBG real-space clustering than those possible at the writing of this thesis. The real-space clustering measurements will allow the study of clustering and bias evolution scenarios and also acknowledge a better understanding of the large-scale LBG coherent infall and z-space distortions. In addition, by observing the LBGs in the foreground of distant QSOs we can probe the three dimensional distribution of the LBGs and of Lyman-α and metal systems, detected through absorption features in the QSOs' spectra. By computing LBG-Lyman-α and LBG-CIV cross-correlations we are able to probe galaxy- IGM interactions, due to the large-

scale infall of gas into the potential well caused by the galaxies, at large scales, and the effects of feedback mechanisms, such as ionisation and galactic outflows, at smaller scales. However, if we are to seriously address the LBG - IGM connection through cross-correlation techniques it is crucial to understand how dynamical (and possible geometric) processes affect the auto- and cross-clustering measurements.

Our analysis suggests a $\beta(z = 3)$ value with $\sim 20\%$ uncertainty, but the extra information from pairs at large angular separation, where z-space distortion effects are dominated by infall dynamics, should prove extremely relevant for obtaining further $\beta(z = 3)$ constraints. In addition, at the smallest scales, the survey should improve the statistics in terms of Lyman-α transmissivity at small galaxy-cloud separations. Results of Adelberger et al. (2003) suggested the existence of feedback mechanisms leading to a deficit in Lyman-α absorption at small separations from the galaxies, which would be explained by feedback mechanisms, such as supernovae winds. Later work (Adelberger et al., 2005) did not show evident signs of strong LBG feedback. Testing this hypothesis and the fact that SPH simulations still suggest that the observed absorption is lower than predicted (Adelberger et al. (2005) and references therein) also serve as additional motivations for the VIMOS LBG Survey, which will permit us to address these questions with a more statistically robust sample.

In chapter 6 we showed that large LRG surveys, such as the AAΩ LRG Survey or the VST ATLAS Survey, should provide very tight constraints on Ω_m^0 (and Ω_Λ^0), via the z-space distortion analysis here developed. The potential of these surveys is therefore unique, as *their statistical weight alone will allow tight constraints in the density of dark energy (through $\xi(\sigma, \pi)$ z-space distortions) and its equation of state (through baryon acoustic oscillations).*

In particular, we use the *Hubble Volume* simulations to build a $z \sim 0.7$ LRG mock catalogue. Using the lightcone output of the *Hubble Volume* simulation, we mocked a LRG sample similar to what is expected to be obtained with a future AAΩ LRG survey. The prime aim of this survey is to measure the equation of dark energy via baryon acoustic oscillation features in the LRGs' power-spectrum, by obtaining $\sim$ 350000 LRGs in a very large volume. However, in order to measure w accurately, one needs to have very tight constraints on the value of Ω_Λ^0. Whereas these can be obtained from the recent WMAP and 2dFGRS constraints (Spergel et al., 2006), we test if the required level of precision can be achieved from z-space distortion analysis of the LRG sample. With that in mind, we constructed a bias prescription determining the probability of forming a galaxy from the local density field.

We computed the sky-projected and z-space correlation functions and determined the real-space $\xi(r)$, both by performing parametric fits to $w_p(\sigma)$ and inverting $\xi(r)$. As such, the present analysis also serves as a test to the fitting method and $\xi(\sigma, \pi)$ model applied to the 2QZ and 2QZ+2SLAQ samples. We find that a double power law $\xi(r)$ model is a good description of the LRG $\xi(r)$, and this parameterisation leads to the following constraints: $\Omega_m^0 = 0.25^{+0.12}_{-0.10}$,

$\beta(z) = 0.30^{+0.04}_{-0.05}$. Once we combine the constraints with those found from linear clustering evolution, we obtain: $\Omega_m^0 = 0.21^{+0.05}_{-0.06}$, $\beta(z) = 0.28^{+0.02}_{-0.03}$.

$\xi(\sigma, \pi)$ z-space distortions should, in principle, also allow constraints on w, via geometrical distortions and the Alcock- Paczynski test. However, the geometrical distortions caused by w and Ω_Λ^0 are extremely degenerate, and hence to constrain the equation of state through the Alcock-Paczynski test we would need to know the value of Ω_Λ^0 (and $\beta(z)$) with a great level of accuracy. Nevertheless, this test would allow a complementary analysis to be made from the LRG sample, in terms of determining the dark energy equation of state. We also expect that z-space distortion analysis applied to datasets from the Panoramic Survey Telescope and Rapid Response System (PANSTARRS) or the Dark Energy Survey (DES) will give complementary information that can be combined with the cosmology constraints here obtained, and contribute to the dawn of the precision cosmology era that we are now witnessing.

This thesis demonstrates the importance of z-space distortions in the statistical analysis of large datasets of QSOs and galaxies. Clustering measurements and the dynamical effects superimposed on them can tell us about the dynamics of the Universe and geometry and the physics of evolution of large scale structure. A "standard scenario" theory must account for observations of large-scale structure and the clustering statistics of large datasets. So far we have shown that current observations do agree with this standard picture, but still further tests are vital. New, more complicated models for the dynamical distortions in $\xi(\sigma, \pi)$ can be developed and new, even more statistically robust, datasets of galaxies will become available. These will prove crucial not only in questioning the standard model and the actual precision of "precision cosmology" from a new perspective, but also to address more intricate questions about the physics, nature and fate of the Universe, via clustering statistics and z-space distortion analyses.

Appendix A

The two point correlation function

Statistics such as the two-point correlation-function (ξ) are used to quantify and describe the clustering and the distribution of objects.

Consider a distribution of points with density function $\rho(\mathbf{x})$. Its mean is given by:

$$\langle \rho(\mathbf{x}) \rangle = n \tag{A.1}$$

$\xi(x)$ is defined as the joint average of the density at two different locations separated by x (Peebles, 1980):

$$\xi(x) = \frac{\langle (\rho(\mathbf{r}+\mathbf{x}) - \langle \rho \rangle)(\rho(\mathbf{r}) - \langle \rho \rangle) \rangle}{\langle \rho \rangle^2} \tag{A.2}$$

or, alternatively, by defining the local overdensity as:

$$\delta(\mathbf{x}) = \frac{\rho(\mathbf{x}) - \langle \rho \rangle}{\langle \rho \rangle}, \tag{A.3}$$

we can re-write Eq. A.2 in a slightly simpler form (e.g. Bernardeau et al., 2002):

$$\xi(x) = \langle \delta(\mathbf{r}) \delta(\mathbf{r}+\mathbf{x}) \rangle \tag{A.4}$$

Another way of defining the two-point correlation function, $\xi(x)$, is by interpreting it as the excess probability (due to clustering) of finding a pair of objects at a given separation – x – relative to a Poisson (unclustered) distribution (Peebles, 1980).

$$\delta P = n \delta V (1 + \xi(x)) \tag{A.5}$$

is the probability that one has of finding an object, at separation x from a neighbour, located in a volume δV. If $\xi(x) = 0$, we have:

$$\delta P = n \delta V, \tag{A.6}$$

which is the case for uniform Poisson distribution, in which there is no correlation between the objects. If, in Eq. A.5 $\xi(x) > 0$, the objects are clustered, (positively) correlated; if $-1 < \xi(x) < 0$, the positions of the objects are said to be anticorrelated.

Defining ξ as an excess probability is by no means in contradiction with its definition in the previous subsection. In fact, we can re-write Eq. A.2 as:

$$\langle \rho(r+x)\rho(r) \rangle = n^2(1+\xi(x)) \tag{A.7}$$

which is remarkably similar to Eq. A.5. A simple way of understanding the reason why these two equation, should, in fact, be so similar, was also pointed out by Peebles (1980). Imagine that we want to populate a mock Universe with galaxies, and the spatial density of galaxies would be $\rho(r)$. The probability of finding one galaxy in a volume element δV is:

$$\delta P = \rho(r)\delta V, \tag{A.8}$$

i.e., a Poisson process where the expected number of particles is a function of position (compare with Eq. A.6). Now, the probability of finding a pair of objetcs situated at positions r_1 and r_2, in volume elements δV_1 and δV_2, respectively, is

$$\delta P = \rho_1(r)\delta V_1 \rho_2(r)\delta V_2 \tag{A.9}$$

which, if we average over our whole mock Universe, using Eq. A.7, will result:

$$\delta P = n^2(1+\xi(x))\delta V_1 \delta V_2 \tag{A.10}$$

which is the same as Eq. A.5, where we implicitly assume that our galaxies are indistinguishable objects.

Appendix B

The $\xi(\sigma,\pi)$ model for a double power-law $\xi(r)$

In Chapter 3 we introduce a $\xi(\sigma,\pi)$ z-space distortion model that was used to measure the dynamical distortions observed in the 2QZ $\xi(\sigma,\pi)$ (Model I). On chapter 4 we also use this same model to fit the distortions measured on the 2-D clustering of $z\sim 3$ LBGs. Let us remind ourselves of the equations presented in Section 3.3.1.

The 2-D z-space correlation function is given by:

$$\xi(\sigma,\pi) = \left(1+\frac{2}{3}\beta(z)+\frac{1}{5}\beta(z)^2\right)\xi_0(r)P_0(\mu) \quad \text{(B.1)}$$

$$- \left(\frac{4}{3}\beta(z)+\frac{4}{7}\beta(z)^2\right)\xi_2(r)P_2(\mu) \quad \text{(B.2)}$$

$$+ \frac{8}{35}\beta(z)^2\xi_4(r)P_4(\mu), \quad \text{(B.3)}$$

μ being the cosine of the angle between r and π and $P_l(\mu)$ the Legendre polynomials of order l. $\xi_l(r)$, $\xi_2(r)$ and $\xi_4(r)$ are the moments of order l of the linear $\xi(r)$. The form of the moments is a function of $\xi(r)$:

$$\xi_{2l}(r) = \frac{(-1)^l}{r^{2l+1}}\left(\int_0^r x dx\right)^l x^{2l}\left(\frac{d}{dx}\frac{1}{x}\right)^l x\xi(x) \quad \text{(B.4)}$$

The calculation of these moments when assuming a single power-law $\xi(r)$ model was once presented by Matsubara and Suto (1996) and, once we combine these with Eq. B.1 – B.3 and assume the usual power-law model $\xi(r)=(r/r_0)^{-\gamma}$, $\xi(\sigma,\pi)$ takes the simple form:

$$\xi(\sigma,\pi) = \xi(r)\left(1+\frac{2(1-\gamma\mu^2)}{3-\gamma}\beta(z)+\frac{\gamma(\gamma+2)\mu^4-6\gamma\mu^2+3}{(3-\gamma)(5-\gamma)}\beta(z)^2\right), \quad \text{(B.5)}$$

However, given the discussion presented previously in this thesis, we found that double power-law $\xi(r)$ models were sometimes good descriptions of the data we were studying. Therefore, the use of Eq. B.5 would be incorrect, in these cases, which led us to compute the corresponding form of $\xi(\sigma,\pi)$, for a general double power-law $\xi(r)$ form.

We here present this calculation, for future reference.

Let us consider a double power-law $\xi(r)$ model, parameterised differently before and after a given separation c:

$$\xi(r) = \begin{cases} A\, r^{-\gamma_1}, & r < c \\ B\, r^{-\gamma_2}, & r > c \end{cases} \tag{B.6}$$

Given Eq. B.4, for $l = 1$:

$$\xi_2(r) = -\frac{1}{r^3}\left(\int_0^r x dx\right) x^2 \left(\frac{d}{dx}\frac{1}{x}\right) x\, \xi(x) \tag{B.7}$$

$$= -\frac{1}{r^3}\left(\int_0^r x dx\right) x^2 \frac{d}{dx} \begin{cases} A\, x^{-\gamma_1}, & r < c \\ B\, x^{-\gamma_2}, & r > c \end{cases} \tag{B.8}$$

$$= -\frac{1}{r^3}\left(\int_0^r x dx\right) x^2 \begin{cases} -\gamma_1\, A\, x^{-\gamma_1-1}, & r < c \\ -\gamma_2\, B\, x^{-\gamma_2-1}, & r > c \end{cases} \tag{B.9}$$

$$= -\frac{1}{r^3} \begin{cases} -\gamma_1\, A \int_0^r x^{2-\gamma_1}\, dx, & r < c \\ -\gamma_1\, A \int_0^c x^{2-\gamma_1}\, dx - \gamma_2\, B \int_c^r x^{2-\gamma_2}\, dx, & r > c \end{cases} \tag{B.10}$$

$$= \begin{cases} \frac{\gamma_1 A}{3-\gamma_1} r^{-\gamma_1}, & r < c \\ \frac{\gamma_1 A}{3-\gamma_1} c^{3-\gamma_1} r^{-3} - \frac{\gamma_2 B}{3+\gamma_2}\left(r^{-\gamma_2} - c^{3-\gamma_2} r^{-3}\right), & r > c \end{cases} \tag{B.11}$$

And, for $l = 2$:

$$\xi_4(r) = \frac{1}{r^5}\left(\int_0^r x dx\right)^2 x^4 \left(\frac{d}{dx}\frac{1}{x}\right)^2 x\, \xi(x) \tag{B.12}$$

$$= \frac{1}{r^5}\left(\int_0^r x dx\right)^2 x^4 \left(\frac{d}{dx}\frac{1}{x}\right) \begin{cases} -\gamma_1 A\, x^{-\gamma_1-1}, & r < c \\ -\gamma_2 B\, x^{-\gamma_2-1}, & r > c \end{cases} \tag{B.13}$$

$$= \frac{1}{r^5}\left(\int_0^r x dx\right)^2 \begin{cases} \gamma_1 A(\gamma_1+2)\, x^{-\gamma_1+1}, & r < c \\ \gamma_2 B(\gamma_2+2)\, x^{-\gamma_2+1}, & r > c \end{cases} \tag{B.14}$$

$$= \frac{1}{r^5}\left(\int_0^r x dx\right) \begin{cases} \gamma_1 A(\gamma_1+2) \int_0^r x^{-\gamma_1+2} dx, & r < c \\ \gamma_1 A(\gamma_1+2) \int_0^c x^{-\gamma_1+2} dx + \gamma_2 B(\gamma_2+2) \int_c^r x^{-\gamma_2+2} dx, & r > c \end{cases} \tag{B.15}$$

$$= \frac{1}{r^5} \begin{cases} \frac{\gamma_1 A(\gamma_1+2)}{3-\gamma_1} \int_0^r x^{-\gamma_1+4} dx, & r < c \\ \frac{\gamma_1 A(\gamma_1+2)}{3-\gamma_1} \int_0^c x^{-\gamma_1+4} dx + \\ + \frac{\gamma_1 A(\gamma_1+2)}{3-\gamma_1} c^{3-\gamma_1} \int_c^r x dx + \\ + \frac{\gamma_2 B(\gamma_2+2)}{3-\gamma_2}\left(\int_c^r x^{-\gamma_2+4} dx - c^{3-\gamma_2} \int_c^r x dx\right), & r > c \end{cases} \tag{B.16}$$

$$= \begin{cases} \frac{\gamma_1 A(\gamma_1+2)}{(3-\gamma_1)(5-\gamma_1)} r^{-\gamma_1}, & r < c \\ \frac{\gamma_1 A(\gamma_1+2)}{3-\gamma_1}\left(\frac{c^{5-\gamma_1}}{5-\gamma_1} + \frac{1}{2}(-c^{5-\gamma_1} r^{-5} + c^{3-\gamma_1} r^{-3})\right) + \\ + \frac{\gamma_2 B(\gamma_2+2)}{3-\gamma_2}\left(-\frac{c^{5-\gamma_2}}{5-\gamma_2} r^{-5} + \frac{r^{-\gamma_2}}{5-\gamma_2} - \frac{1}{2}(-c^{5-\gamma_2} r^{-5} + c^{3-\gamma_2} r^{-3})\right), & r > c \end{cases} \tag{B.17}$$

When $A = B$ and $\gamma_1 = \gamma_2$, it can easily be seen that the expressions for $r > c$ simplify to those when $r < c$. To obtain $\xi(\sigma,\pi)$ we substitute these expressions in Eqs. B.1 – B.3. The Legendre polynomials are given by:

$$P_0(\mu) = 1 \tag{B.18}$$

$$P_2(\mu) = \frac{1}{2}(3\mu^2 - 1) \tag{B.19}$$

$$P_4(\mu) = \frac{1}{8}(35\mu^4 - 30\mu^2 + 3) \tag{B.20}$$

Bibliography

K. L. Adelberger, A. E. Shapley, C. C. Steidel, M. Pettini, D. K. Erb, and N. A. Reddy. The Connection between Galaxies and Intergalactic Absorption Lines at Redshift 2¡˜z¡˜3. ApJ, 629: 636–653, Aug 2005.

K. L. Adelberger and C. C. Steidel. A Possible Correlation between the Luminosities and Lifetimes of Active Galactic Nuclei. ApJ, 630:50–58, Sept 2005.

K. L. Adelberger, C. C. Steidel, A. E. Shapley, and M. Pettini. Galaxies and Intergalactic Matter at Redshift z˜3: Overview. ApJ, 584:45–75, Feb 2003.

J. K. Adelman-McCarthy, M. A. Agüeros, S. S. Allam, K. S. J. Anderson, S. F. Anderson, J. Annis, N. A. Bahcall, I. K. Baldry, J. C. Barentine, A. Berlind, M. Bernardi, M. R. Blanton, W. N. Boroski, H. J. Brewington, J. Brinchmann, J. Brinkmann, R. J. Brunner, T. Budavári, L. N. Carey, M. A. Carr, F. J. Castander, A. J. Connolly, I. Csabai, P. C. Czarapata, J. J. Dalcanton, M. Doi, F. Dong, D. J. Eisenstein, M. L. Evans, X. Fan, D. P. Finkbeiner, S. D. Friedman, J. A. Frieman, M. Fukugita, B. Gillespie, K. Glazebrook, J. Gray, E. K. Grebel, J. E. Gunn, V. K. Gurbani, E. de Haas, P. B. Hall, F. H. Harris, M. Harvanek, S. L. Hawley, J. Hayes, J. S. Hendry, G. S. Hennessy, R. B. Hindsley, C. M. Hirata, C. J. Hogan, D. W. Hogg, D. J. Holmgren, J. A. Holtzman, S.-i. Ichikawa, Ž. Ivezić, S. Jester, D. E. Johnston, A. M. Jorgensen, M. Jurić, S. M. Kent, S. J. Kleinman, G. R. Knapp, A. Y. Kniazev, R. G. Kron, J. Krzesinski, N. Kuropatkin, D. Q. Lamb, H. Lampeitl, B. C. Lee, R. F. Leger, H. Lin, D. C. Long, J. Loveday, R. H. Lupton, B. Margon, D. Martínez-Delgado, R. Mandelbaum, T. Matsubara, P. M. McGehee, T. A. McKay, A. Meiksin, J. A. Munn, R. Nakajima, T. Nash, E. H. Neilsen, Jr., H. J. Newberg, P. R. Newman, R. C. Nichol, T. Nicinski, M. Nieto-Santisteban, A. Nitta, W. O'Mullane, S. Okamura, R. Owen, N. Padmanabhan, G. Pauls, J. J. Peoples, J. R. Pier, A. C. Pope, D. Pourbaix, T. R. Quinn, G. T. Richards, M. W. Richmond, C. M. Rockosi, D. J. Schlegel, D. P. Schneider, J. Schroeder, R. Scranton, U. Seljak, E. Sheldon, K. Shimasaku, J. A. Smith, V. Smolčić, S. A. Snedden, C. Stoughton, M. A. Strauss, M. SubbaRao, A. S. Szalay, I. Szapudi, P. Szkody, M. Tegmark, A. R. Thakar, D. L. Tucker, A. Uomoto, D. E. Vanden Berk, J. Vandenberg, M. S. Vogeley, W. Voges, N. P. Vogt, L. M. Walkowicz, D. H. Weinberg, A. A. West, S. D. M. White, Y. Xu, B. Yanny, D. R. Yocum, D. G. York, I. Zehavi, S. Zibetti,

and D. B. Zucker. The Fourth Data Release of the Sloan Digital Sky Survey. ApJS, 162:38–48, Jan 2006.

C. Alcock and B. Paczynski. An evolution free test for non-zero cosmological constant. Nature, 281:358–+, Oct 1979.

R. Antonucci. Unified models for active galactic nuclei and quasars. ARA&A, 31:473–521, 1993.

M. Baes, P. Buyle, G. K. T. Hau, and H. Dejonghe. Observational evidence for a connection between supermassive black holes and dark matter haloes. MNRAS, 341:L44–L48, June 2003.

W. E. Ballinger, A. F. Heavens, and A. N. Taylor. The real-space power spectrum of IRAS galaxies on large scales and the redshift distortion. MNRAS, 276:L59–L63, Oct 1995.

W. E. Ballinger, J. A. Peacock, and A. F. Heavens. Measuring the cosmological constant with redshift surveys. MNRAS, 282:877–+, Oct 1996.

J. M. Bardeen, J. R. Bond, N. Kaiser, and A. S. Szalay. The statistics of peaks of Gaussian random fields. ApJ, 304:15–61, May 1986.

S. Basilakos and M. Plionis. Cosmological Evolution of Linear Bias. ApJ, 550:522–527, Apr 2001.

S. Basilakos and M. Plionis. Modelling the two-point correlation function of galaxy clusters in the Sloan Digital Sky Survey. MNRAS, 349:882–888, Apr 2004.

C. M. Baugh. The real-space correlation function measured from the APM Galaxy Survey. MNRAS, 280:267–275, May 1996.

G. D. Becker, W. L. W. Sargent, and M. Rauch. Large-Scale Correlations in the Lyα Forest at z = 3-4. ApJ, 613:61–76, Sept 2004.

C. Belfiore, M. Brescia, M. Capaccioli, O. Caputi, G. Castiello, F. Cortecchia, L. Ferragina, D. Fierro, V. Fiume, D. Mancini, G. Mancini, G. Marra, L. Marty, G. Mazzola, L. Parisi, L. Pellone, F. Perrotta, V. Porzio, P. Schipani, G. Sciarretta, G. Spirito, M. Valentino, and G. Sedmak. VST - VLT Survey Telescope Integration Status. *ArXiv Astrophysics e-prints*, Jan 2005.

C. L. Bennett, M. Halpern, G. Hinshaw, N. Jarosik, A. Kogut, M. Limon, S. S. Meyer, L. Page, D. N. Spergel, G. S. Tucker, E. Wollack, E. L. Wright, C. Barnes, M. R. Greason, R. S. Hill, E. Komatsu, M. R. Nolta, N. Odegard, H. V. Peiris, L. Verde, and J. L. Weiland. First-Year Wilkinson Microwave Anisotropy Probe (WMAP) Observations: Preliminary Maps and Basic Results. ApJS, 148:1–27, Sept 2003.

A. A. Berlind, D. H. Weinberg, A. J. Benson, C. M. Baugh, S. Cole, R. Davé, C. S. Frenk, A. Jenkins, N. Katz, and C. G. Lacey. The Halo Occupation Distribution and the Physics of Galaxy Formation. ApJ, 593:1–25, Aug 2003.

F. Bernardeau, S. Colombi, E. Gaztañaga, and R. Scoccimarro. Large-scale structure of the Universe and cosmological perturbation theory. Phys. Rep., 367:1–3, Sept 2002.

S. Bharadwaj. Non-linear redshift distortions: the two-point correlation function. MNRAS, 327: 577–587, Oct 2001.

C. Blake and K. Glazebrook. Probing Dark Energy Using Baryonic Oscillations in the Galaxy Power Spectrum as a Cosmological Ruler. ApJ, 594:665–673, Sept 2003.

C. Blake, D. Parkinson, B. Bassett, K. Glazebrook, M. Kunz, and R. C. Nichol. Universal fitting formulae for baryon oscillation surveys. MNRAS, 365:255–264, Jan 2006.

A. Blanchard, M. Douspis, M. Rowan-Robinson, and S. Sarkar. Large-scale galaxy correlations as a test for dark energy. A&A, 449:925–928, Apr 2006.

M. Blanton, R. Cen, J. P. Ostriker, and M. A. Strauss. The Physical Origin of Scale-dependent Bias in Cosmological Simulations. ApJ, 522:590–603, Sept 1999.

R. G. Bower, A. J. Benson, R. Malbon, J. C. Helly, C. S. Frenk, C. M. Baugh, S. Cole, and C. G. Lacey. Breaking the hierarchy of galaxy formation. MNRAS, pages 659–+, July 2006.

B. J. Boyle, T. Shanks, S. M. Croom, R. J. Smith, L. Miller, N. Loaring, and C. Heymans. The 2dF QSO Redshift Survey - I. The optical luminosity function of quasi-stellar objects. MNRAS, 317:1014–1022, Oct 2000.

M. O. Calvão, J. R. de Mello Neto, and I. Waga. Probing the Dark Energy with Quasar Clustering. *Physical Review Letters*, 88(9):091302–+, March 2002.

S. M. Carroll, W. H. Press, and E. L. Turner. The cosmological constant. ARA&A, 30:499–542, 1992.

S. Cole, K. B. Fisher, and D. H. Weinberg. Fourier Analysis of Redshift Space Distortions and the Determination of Omega. MNRAS, 267:785–+, Apr 1994.

S. Cole, S. Hatton, D. H. Weinberg, and C. S. Frenk. Mock 2dF and SDSS galaxy redshift surveys. MNRAS, 300:945–966, Nov 1998.

S. Cole, W. J. Percival, J. A. Peacock, P. Norberg, C. M. Baugh, C. S. Frenk, I. Baldry, J. Bland-Hawthorn, T. Bridges, R. Cannon, M. Colless, C. Collins, W. Couch, N. J. G. Cross, G. Dalton, V. R. Eke, R. De Propris, S. P. Driver, G. Efstathiou, R. S. Ellis, K. Glazebrook, C. Jackson, A. Jenkins, O. Lahav, I. Lewis, S. Lumsden, S. Maddox, D. Madgwick, B. A. Peterson, W. Sutherland, and K. Taylor. The 2dF Galaxy Redshift Survey: power-spectrum analysis of the final data set and cosmological implications. MNRAS, 362:505–534, Sept 2005.

M. Colless, G. Dalton, S. Maddox, W. Sutherland, P. Norberg, S. Cole, J. Bland-Hawthorn, T. Bridges, R. Cannon, C. Collins, W. Couch, N. Cross, K. Deeley, R. De Propris, S. P.

Driver, G. Efstathiou, R. S. Ellis, C. S. Frenk, K. Glazebrook, C. Jackson, O. Lahav, I. Lewis, S. Lumsden, D. Madgwick, J. A. Peacock, B. A. Peterson, I. Price, M. Seaborne, and K. Taylor. The 2dF Galaxy Redshift Survey: spectra and redshifts. MNRAS, 328:1039–1063, Dec 2001.

C. R. Contaldi, H. Hoekstra, and A. Lewis. Joint Cosmic Microwave Background and Weak Lensing Analysis: Constraints on Cosmological Parameters. *Physical Review Letters*, 90(22): 221303–+, June 2003.

A. Cooray, W. Hu, D. Huterer, and M. Joffre. Measuring Angular Diameter Distances through Halo Clustering. ApJ, 557:L7–L10, Aug 2001.

L. L. Cowie, A. J. Barger, M. W. Bautz, W. N. Brandt, and G. P. Garmire. The Redshift Evolution of the 2-8 keV X-Ray Luminosity Function. ApJ, 584:L57–L60, Feb 2003.

S. Cristiani and R. Vio. The composite spectrum of quasars. A&A, 227:385–393, Jan 1990.

S. M. Croom, B. J. Boyle, N. S. Loaring, L. Miller, P. J. Outram, T. Shanks, and R. J. Smith. The 2dF QSO Redshift Survey - IX. A measurement of the luminosity dependence of QSO clustering. MNRAS, 335:459–464, Sept 2002.

S. M. Croom, B. J. Boyle, T. Shanks, R. J. Smith, L. Miller, P. J. Outram, N. S. Loaring, F. Hoyle, and J. da Ângela. The 2dF QSO Redshift Survey - XIV. Structure and evolution from the two-point correlation function. MNRAS, 356:415–438, Jan 2005.

S. M. Croom, T. Shanks, B. J. Boyle, R. J. Smith, L. Miller, N. S. Loaring, and F. Hoyle. The 2dF QSO Redshift Survey - II. Structure and evolution at high redshift. MNRAS, 325:483–496, Aug 2001.

S. M. Croom, R. J. Smith, B. J. Boyle, T. Shanks, L. Miller, P. J. Outram, and N. S. Loaring. The 2dF QSO Redshift Survey - XII. The spectroscopic catalogue and luminosity function. MNRAS, 349:1397–1418, Apr 2004.

J. da Ângela, P. J. Outram, and T. Shanks. Constraining $\beta(z)$ and Ω_m^0 from redshift-space distortions in z˜ 3 galaxy surveys. MNRAS, 361:879–886, Aug 2005.

J. da Ângela, P. J. Outram, T. Shanks, B. J. Boyle, S. M. Croom, N. S. Loaring, L. Miller, and R. J. Smith. The 2dF QSO Redshift Survey- XV. Correlation analysis of redshift-space distortions. MNRAS, 360:1040–1054, July 2005.

M. Davis, G. Efstathiou, C. S. Frenk, and S. D. M. White. The evolution of large-scale structure in a universe dominated by cold dark matter. ApJ, 292:371–394, May 1985.

M. Davis, S. M. Faber, J. Newman, A. C. Phillips, R. S. Ellis, C. C. Steidel, C. Conselice, A. L. Coil, D. P. Finkbeiner, D. C. Koo, P. Guhathakurta, B. Weiner, R. Schiavon, C. Willmer, N. Kaiser, G. A. Luppino, G. Wirth, A. Connolly, P. Eisenhardt, M. Cooper, and B. Gerke.

Science Objectives and Early Results of the DEEP2 Redshift Survey. In P. Guhathakurta, editor, *Discoveries and Research Prospects from 6- to 10-Meter-Class Telescopes II. Edited by Guhathakurta, Puragra. Proceedings of the SPIE, Volume 4834, pp. 161-172 (2003).*, pages 161–172, Feb 2003.

M. Davis and M. J. Geller. Galaxy Correlations as a Function of Morphological Type. ApJ, 208: 13–19, Aug 1976.

M. Davis and P. J. E. Peebles. A survey of galaxy redshifts. V - The two-point position and velocity correlations. ApJ, 267:465–482, Apr 1983.

P. de Bernardis, P. A. R. Ade, J. J. Bock, J. R. Bond, J. Borrill, A. Boscaleri, K. Coble, B. P. Crill, G. De Gasperis, P. C. Farese, P. G. Ferreira, K. Ganga, M. Giacometti, E. Hivon, V. V. Hristov, A. Iacoangeli, A. H. Jaffe, A. E. Lange, L. Martinis, S. Masi, P. V. Mason, P. D. Mauskopf, A. Melchiorri, L. Miglio, T. Montroy, C. B. Netterfield, E. Pascale, F. Piacentini, D. Pogosyan, S. Prunet, S. Rao, G. Romeo, J. E. Ruhl, F. Scaramuzzi, D. Sforna, and N. Vittorio. A flat Universe from high-resolution maps of the cosmic microwave background radiation. Nature, 404:955–959, Apr 2000.

J. S. Dunlop, R. J. McLure, M. J. Kukula, S. A. Baum, C. P. O'Dea, and D. H. Hughes. Quasars, their host galaxies and their central black holes. MNRAS, 340:1095–1135, Apr 2003.

D. J. Eisenstein. Dark energy and cosmic sound [review article]. *New Astronomy Review*, 49: 360–365, Nov 2005.

D. J. Eisenstein, J. Annis, J. E. Gunn, A. S. Szalay, A. J. Connolly, R. C. Nichol, N. A. Bahcall, M. Bernardi, S. Burles, F. J. Castander, M. Fukugita, D. W. Hogg, Ž. Ivezić, G. R. Knapp, R. H. Lupton, V. Narayanan, M. Postman, D. E. Reichart, M. Richmond, D. P. Schneider, D. J. Schlegel, M. A. Strauss, M. SubbaRao, D. L. Tucker, D. Vanden Berk, M. S. Vogeley, D. H. Weinberg, and B. Yanny. Spectroscopic Target Selection for the Sloan Digital Sky Survey: The Luminous Red Galaxy Sample. AJ, 122:2267–2280, Nov 2001.

D. J. Eisenstein, I. Zehavi, D. W. Hogg, R. Scoccimarro, M. R. Blanton, R. C. Nichol, R. Scranton, H.-J. Seo, M. Tegmark, Z. Zheng, S. F. Anderson, J. Annis, N. Bahcall, J. Brinkmann, S. Burles, F. J. Castander, A. Connolly, I. Csabai, M. Doi, M. Fukugita, J. A. Frieman, K. Glazebrook, J. E. Gunn, J. S. Hendry, G. Hennessy, Z. Ivezić, S. Kent, G. R. Knapp, H. Lin, Y.-S. Loh, R. H. Lupton, B. Margon, T. A. McKay, A. Meiksin, J. A. Munn, A. Pope, M. W. Richmond, D. Schlegel, D. P. Schneider, K. Shimasaku, C. Stoughton, M. A. Strauss, M. SubbaRao, A. S. Szalay, I. Szapudi, D. L. Tucker, B. Yanny, and D. G. York. Detection of the Baryon Acoustic Peak in the Large-Scale Correlation Function of SDSS Luminous Red Galaxies. ApJ, 633: 560–574, Nov 2005.

Ø. Elgarøy and O. Lahav. Neutrino masses from cosmological probes. *New Journal of Physics*, 7: 61–+, Feb 2005.

Ø. Elgarøy, O. Lahav, W. J. Percival, J. A. Peacock, D. S. Madgwick, S. L. Bridle, C. M. Baugh, I. K. Baldry, J. Bland-Hawthorn, T. Bridges, R. Cannon, S. Cole, M. Colless, C. Collins, W. Couch, G. Dalton, R. de Propris, S. P. Driver, G. P. Efstathiou, R. S. Ellis, C. S. Frenk, K. Glazebrook, C. Jackson, I. Lewis, S. Lumsden, S. Maddox, P. Norberg, B. A. Peterson, W. Sutherland, and K. Taylor. New Upper Limit on the Total Neutrino Mass from the 2 Degree Field Galaxy Redshift Survey. *Physical Review Letters*, 89(6):061301–+, July 2002.

A. E. Evrard, T. J. MacFarland, H. M. P. Couchman, J. M. Colberg, N. Yoshida, S. D. M. White, A. Jenkins, C. S. Frenk, F. R. Pearce, J. A. Peacock, and P. A. Thomas. Galaxy Clusters in Hubble Volume Simulations: Cosmological Constraints from Sky Survey Populations. ApJ, 573: 7–36, July 2002.

L. Ferrarese. Beyond the Bulge: A Fundamental Relation between Supermassive Black Holes and Dark Matter Halos. ApJ, 578:90–97, Oct 2002.

L. Ferrarese and D. Merritt. A Fundamental Relation between Supermassive Black Holes and Their Host Galaxies. ApJ, 539:L9–L12, Aug 2000.

K. B. Fisher, M. Davis, M. A. Strauss, A. Yahil, and J. Huchra. Clustering in the 1.2-Jy IRAS Galaxy Redshift Survey. I - The redshift and real space correlation functions. MNRAS, 266: 50–+, Jan 1994.

S. Folkes, S. Ronen, I. Price, O. Lahav, M. Colless, S. Maddox, K. Deeley, K. Glazebrook, J. Bland-Hawthorn, R. Cannon, S. Cole, C. Collins, W. Couch, S. P. Driver, G. Dalton, G. Efstathiou, R. S. Ellis, C. S. Frenk, N. Kaiser, I. Lewis, S. Lumsden, J. Peacock, B. A. Peterson, W. Sutherland, and K. Taylor. The 2dF Galaxy Redshift Survey: spectral types and luminosity functions. MNRAS, 308:459–472, Sept 1999.

S. Foucaud, H. J. McCracken, O. Le Fèvre, S. Arnouts, M. Brodwin, S. J. Lilly, D. Crampton, and Y. Mellier. The Canada-France deep fields survey-II: Lyman-break galaxies and galaxy clustering at z ˜ 3. A&A, 409:835–850, Oct 2003.

C. S. Frenk, A. E. Evrard, S. D. M. White, and F. J. Summers. Galaxy Dynamics in Clusters. ApJ, 472:460–+, Dec 1996.

K. Gebhardt, R. Bender, G. Bower, A. Dressler, S. M. Faber, A. V. Filippenko, R. Green, C. Grillmair, L. C. Ho, J. Kormendy, T. R. Lauer, J. Magorrian, J. Pinkney, D. Richstone, and S. Tremaine. A Relationship between Nuclear Black Hole Mass and Galaxy Velocity Dispersion. ApJ, 539:L13–L16, Aug 2000.

K. Glazebrook and C. Blake. Measuring the Cosmic Evolution of Dark Energy with Baryonic Oscillations in the Galaxy Power Spectrum. ApJ, 631:1–20, Sept 2005.

E. J. Groth and P. J. E. Peebles. Statistical analysis of catalogs of extragalactic objects. VII - Two- and three-point correlation functions for the high-resolution Shane-Wirtanen catalog of galaxies. ApJ, 217:385–405, Oct 1977.

A. H. Guth. Inflationary universe: A possible solution to the horizon and flatness problems. Phys. Rev. D, 23:347–356, Jan 1981.

M. G. Haehnelt and G. Kauffmann. The correlation between black hole mass and bulge velocity dispersion in hierarchical galaxy formation models. MNRAS, 318:L35–L38, Nov 2000.

D. Hale-Sutton. *Ph.D. Thesis, University of Durham*, 1990.

A. J. S. Hamilton. Measuring Omega and the real correlation function from the redshift correlation function. ApJ, 385:L5–L8, Jan 1992.

A. J. S. Hamilton. Omega from the anisotropy of the redshift correlation function in the IRAS 2 Jansky survey. ApJ, 406:L47–L50, Apr 1993a.

A. J. S. Hamilton. Toward Better Ways to Measure the Galaxy Correlation Function. ApJ, 417: 19–+, Nov 1993b.

A. J. S. Hamilton, P. Kumar, E. Lu, and A. Matthews. Reconstructing the primordial spectrum of fluctuations of the universe from the observed nonlinear clustering of galaxies. ApJ, 374: L1–L4, June 1991.

E. Hawkins, S. Maddox, S. Cole, O. Lahav, D. S. Madgwick, P. Norberg, J. A. Peacock, I. K. Baldry, C. M. Baugh, J. Bland-Hawthorn, T. Bridges, R. Cannon, M. Colless, C. Collins, W. Couch, G. Dalton, R. De Propris, S. P. Driver, G. Efstathiou, R. S. Ellis, C. S. Frenk, K. Glazebrook, C. Jackson, B. Jones, I. Lewis, S. Lumsden, W. Percival, B. A. Peterson, W. Sutherland, and K. Taylor. The 2dF Galaxy Redshift Survey: correlation functions, peculiar velocities and the matter density of the Universe. MNRAS, 346:78–96, Nov 2003.

A. F. Heavens and A. N. Taylor. A spherical harmonic analysis of redshift space. MNRAS, 275: 483–497, July 1995.

H. Hoekstra, H. K. C. Yee, and M. D. Gladders. Constraints on Ω_m and σ_8 from Weak Lensing in Red-Sequence Cluster Survey Fields. ApJ, 577:595–603, Oct 2002.

P. F. Hopkins, L. Hernquist, T. J. Cox, T. Di Matteo, P. Martini, B. Robertson, and V. Springel. Black Holes in Galaxy Mergers: Evolution of Quasars. ApJ, 630:705–715, Sept 2005a.

P. F. Hopkins, L. Hernquist, T. J. Cox, T. Di Matteo, B. Robertson, and V. Springel. Luminosity-dependent Quasar Lifetimes: A New Interpretation of the Quasar Luminosity Function. ApJ, 630:716–720, Sept 2005b.

P. F. Hopkins, L. Hernquist, T. J. Cox, T. Di Matteo, B. Robertson, and V. Springel. Luminosity-dependent Quasar Lifetimes: Reconciling the Optical and X-Ray Quasar Luminosity Functions. ApJ, 632:81–91, Oct 2005c.

P. F. Hopkins, L. Hernquist, T. J. Cox, T. Di Matteo, B. Robertson, and V. Springel. A Unified, Merger-driven Model of the Origin of Starbursts, Quasars, the Cosmic X-Ray Background, Supermassive Black Holes, and Galaxy Spheroids. ApJS, 163:1–49, March 2006.

P. F. Hopkins, L. Hernquist, P. Martini, T. J. Cox, B. Robertson, T. Di Matteo, and V. Springel. A Physical Model for the Origin of Quasar Lifetimes. ApJ, 625:L71–L74, June 2005d.

F. Hoyle. *Ph.D. Thesis, University of Durham*, 2000.

F. Hoyle, P. J. Outram, T. Shanks, B. J. Boyle, S. M. Croom, and R. J. Smith. The 2dF QSO Redshift Survey - VII. Constraining cosmology from redshift-space distortions via ξ (σ , π). MNRAS, 332:311–324, May 2002.

G. Huetsi. Power spectrum of the SDSS luminous red galaxies: constraints on cosmological parameters. *ArXiv Astrophysics e-prints*, Apr 2006.

H. K. Jassal, J. S. Bagla, and T. Padmanabhan. WMAP constraints on low redshift evolution of dark energy. MNRAS, 356:L11–L16, Jan 2005.

A. Jenkins, C. S. Frenk, F. R. Pearce, P. A. Thomas, J. M. Colberg, S. D. M. White, H. M. P. Couchman, J. A. Peacock, G. Efstathiou, and A. H. Nelson. Evolution of Structure in Cold Dark Matter Universes. ApJ, 499:20–+, May 1998.

Y. P. Jing, H. J. Mo, and G. Boerner. Spatial Correlation Function and Pairwise Velocity Dispersion of Galaxies: Cold Dark Matter Models versus the Las Campanas Survey. ApJ, 494:1–+, Feb 1998.

N. Kaiser. On the spatial correlations of Abell clusters. ApJ, 284:L9–L12, Sept 1984.

N. Kaiser. Clustering in real space and in redshift space. MNRAS, 227:1–21, July 1987.

G. Kauffmann and M. Haehnelt. A unified model for the evolution of galaxies and quasars. MNRAS, 311:576–588, Jan 2000.

J. Kormendy and D. Richstone. Inward Bound—The Search For Supermassive Black Holes In Galactic Nuclei. ARA&A, 33:581–+, 1995.

C. L. Kuo, P. A. R. Ade, J. J. Bock, C. Cantalupo, M. D. Daub, J. Goldstein, W. L. Holzapfel, A. E. Lange, M. Lueker, M. Newcomb, J. B. Peterson, J. Ruhl, M. C. Runyan, and E. Torbet. High-Resolution Observations of the Cosmic Microwave Background Power Spectrum with ACBAR. ApJ, 600:32–51, Jan 2004.

O. Lahav, P. B. Lilje, J. R. Primack, and M. J. Rees. Dynamical effects of the cosmological constant. MNRAS, 251:128–136, July 1991.

S. D. Landy and A. S. Szalay. Bias and variance of angular correlation functions. ApJ, 412:64–71, July 1993.

S. D. Landy and A. S. Szalay. An Inversion Method for Measuring β in Large-Redshift Surveys. ApJ, 579:76–82, Nov 2002.

I. J. Lewis, R. D. Cannon, K. Taylor, K. Glazebrook, J. A. Bailey, I. K. Baldry, J. R. Barton, T. J. Bridges, G. B. Dalton, T. J. Farrell, P. M. Gray, A. Lankshear, C. McCowage, I. R. Parry, R. M. Sharples, K. Shortridge, G. A. Smith, J. Stevenson, J. O. Straede, L. G. Waller, J. D. Whittard, J. K. Wilcox, and K. C. Willis. The Anglo-Australian Observatory 2dF facility. MNRAS, 333:279–299, June 2002.

L. Liberato and R. Rosenfeld. Dark energy parameterizations and their effect on dark halos. *ArXiv Astrophysics e-prints*, Apr 2006.

A. Lidz, P. F. Hopkins, T. J. Cox, L. Hernquist, and B. Robertson. The Luminosity Dependence of Quasar Clustering. ApJ, 641:41–49, Apr 2006.

P. B. Lilje and G. Efstathiou. The cross-correlation of Abell clusters with the Lick galaxy counts. MNRAS, 231:635–655, Apr 1988.

E. N. Ling, J. D. Barrow, and C. S. Frenk. Uncertainties in the cluster-cluster correlation function. MNRAS, 223:21P–27P, Dec 1986.

J. Loveday. The Sloan Digital Sky Survey. *Contemporary Physics*, 43:437–449, June 2002.

J. Loveday, G. Efstathiou, S. J. Maddox, and B. A. Peterson. The Stromlo-APM Redshift Survey. III. Redshift Space Distortions, Omega, and Bias. ApJ, 468:1–+, Sept 1996.

P. Madau, H. C. Ferguson, M. E. Dickinson, M. Giavalisco, C. C. Steidel, and A. Fruchter. High-redshift galaxies in the Hubble Deep Field: colour selection and star formation history to z˜4. MNRAS, 283:1388–1404, Dec 1996.

S. J. Maddox, G. Efstathiou, W. J. Sutherland, and J. Loveday. Galaxy correlations on large scales. MNRAS, 242:43P–47P, Jan 1990.

D. S. Madgwick, E. Hawkins, O. Lahav, S. Maddox, P. Norberg, J. A. Peacock, I. K. Baldry, C. M. Baugh, J. Bland-Hawthorn, T. Bridges, R. Cannon, S. Cole, M. Colless, C. Collins, W. Couch, G. Dalton, R. De Propris, S. P. Driver, G. Efstathiou, R. S. Ellis, C. S. Frenk, K. Glazebrook, C. Jackson, I. Lewis, S. Lumsden, B. A. Peterson, W. Sutherland, and K. Taylor. The 2dF Galaxy Redshift Survey: galaxy clustering per spectral type. MNRAS, 344:847–856, Sept 2003.

J. Magorrian, S. Tremaine, D. Richstone, R. Bender, G. Bower, A. Dressler, S. M. Faber, K. Gebhardt, R. Green, C. Grillmair, J. Kormendy, and T. Lauer. The Demography of Massive Dark Objects in Galaxy Centers. AJ, 115:2285–2305, June 1998.

R. G. Mann, J. A. Peacock, and A. F. Heavens. Eulerian bias and the galaxy density field. MNRAS, 293:209–+, Jan 1998.

A. Marconi and L. K. Hunt. The Relation between Black Hole Mass, Bulge Mass, and Near-Infrared Luminosity. ApJ, 589:L21–L24, May 2003.

T. R. Marsh, L. Morales-Rueda, D. Steeghs, P. Maxted, U. Kolb, B. Boyle, S. Croom, N. Loaring, L. Miller, P. Outram, T. Shanks, and R. Smith. A first look at cataclysmic variable stars from the 2dF QSO survey. In *ASP Conf. Ser. 261: The Physics of Cataclysmic Variables and Related Objects*, pages 200–+, Jan 2002.

T. Matsubara and Y. Suto. Cosmological Redshift Distortion of Correlation Functions as a Probe of the Density Parameter and the Cosmological Constant. ApJ, 470:L1+, Oct 1996.

R. J. McLure and J. S. Dunlop. The cosmological evolution of quasar black hole masses. MNRAS, 352:1390–1404, Aug 2004.

A. Merloni. Anti-hierarchical Growth of Supermassive Black Holes and QSO Lifetimes. In A. Merloni, S. Nayakshin, and R. A. Sunyaev, editors, *Growing Black Holes: Accretion in a Cosmological Context*, pages 453–458, 2005.

L. Miller, W. J. Percival, and S. M. Croom. The Cosmological History of Accretion onto Supermassive Black Holes. *ArXiv Astrophysics e-prints*, June 2005.

H. J. Mo and S. D. M. White. An analytic model for the spatial clustering of dark matter haloes. MNRAS, 282:347–361, Sept 1996.

A. W. Moore, A. J. Connolly, C. Genovese, A. Gray, L. Grone, N. I. Kanidoris, R. C. Nichol, J. Schneider, A. S. Szalay, I. Szapudi, and L. Wasserman. Fast Algorithms and Efficient Statistics: N-Point Correlation Functions. In A. J. Banday, S. Zaroubi, and M. Bartelmann, editors, *Mining the Sky*, pages 71–+, 2001.

M. S. Movahed and S. Rahvar. Observational constraints on a variable dark energy model. Phys. Rev. D, 73(8):083518–+, Apr 2006.

A. Myers. *Ph.D. Thesis, University of Durham*, 2003.

A. D. Myers, R. J. Brunner, G. T. Richards, R. C. Nichol, D. P. Schneider, D. E. Vanden Berk, R. Scranton, A. G. Gray, and J. Brinkmann. First Measurement of the Clustering Evolution of Photometrically Classified Quasars. ApJ, 638:622–634, Feb 2006.

J. F. Navarro, C. S. Frenk, and S. D. M. White. A Universal Density Profile from Hierarchical Clustering. ApJ, 490:493–+, Dec 1997.

P. Norberg, C. M. Baugh, E. Hawkins, S. Maddox, D. Madgwick, O. Lahav, S. Cole, C. S. Frenk, I. Baldry, J. Bland-Hawthorn, T. Bridges, R. Cannon, M. Colless, C. Collins, W. Couch, G. Dalton, R. De Propris, S. P. Driver, G. Efstathiou, R. S. Ellis, K. Glazebrook, C. Jackson, I. Lewis, S. Lumsden, J. A. Peacock, B. A. Peterson, W. Sutherland, and K. Taylor. The 2dF Galaxy Redshift Survey: the dependence of galaxy clustering on luminosity and spectral type. MNRAS, 332:827–838, June 2002.

P. Norberg, C. M. Baugh, E. Hawkins, S. Maddox, J. A. Peacock, S. Cole, C. S. Frenk, J. Bland-Hawthorn, T. Bridges, R. Cannon, M. Colless, C. Collins, W. Couch, G. Dalton, R. De Propris, S. P. Driver, G. Efstathiou, R. S. Ellis, K. Glazebrook, C. Jackson, O. Lahav, I. Lewis, S. Lumsden, D. Madgwick, B. A. Peterson, W. Sutherland, and K. Taylor. The 2dF Galaxy Redshift Survey: luminosity dependence of galaxy clustering. MNRAS, 328:64–70, Nov 2001.

A. Nusser. The Alcock-Paczyński test in redshifted 21-cm maps. MNRAS, 364:743–750, Dec 2005.

P. J. Outram, F. Hoyle, T. Shanks, S. M. Croom, B. J. Boyle, L. Miller, R. J. Smith, and A. D. Myers. The 2dF QSO Redshift Survey - XI. The QSO power spectrum. MNRAS, 342:483–495, June 2003.

P. J. Outram, T. Shanks, B. J. Boyle, S. M. Croom, F. Hoyle, N. S. Loaring, L. Miller, and R. J. Smith. The 2dF QSO Redshift Survey - XIII. A measurement of Λ from the quasi-stellar object power spectrum, $P^S(k_{parallel;}, k_?)$. MNRAS, 348:745–752, March 2004.

N. D. Padilla and C. M. Baugh. Cluster correlations in redshift space. MNRAS, 329:431–444, Jan 2002.

N. Padmanabhan, T. Budavári, D. J. Schlegel, T. Bridges, J. Brinkmann, R. Cannon, A. J. Connolly, S. M. Croom, I. Csabai, M. Drinkwater, D. J. Eisenstein, P. C. Hewett, J. Loveday, R. C. Nichol, K. A. Pimbblet, R. De Propris, D. P. Schneider, R. Scranton, U. Seljak, T. Shanks, I. Szapudi, A. S. Szalay, and D. Wake. Calibrating photometric redshifts of luminous red galaxies. MNRAS, 359:237–250, May 2005.

N. Padmanabhan, D. J. Schlegel, U. Seljak, A. Makarov, N. A. Bahcall, M. R. Blanton, J. Brinkmann, D. J. Eisenstein, D. P. Finkbeiner, J. E. Gunn, D. W. Hogg, Z. Ivezic, G. R. Knapp, J. Loveday, R. H. Lupton, R. C. Nichol, D. P. Schneider, M. A. Strauss, M. Tegmark, and D. G. York. The Clustering of Luminous Red Galaxies in the Sloan Digital Sky Survey Imaging Data. *ArXiv Astrophysics e-prints*, May 2006.

T. Padmanabhan. Dark Energy: Mystery of the Millennium. *ArXiv Astrophysics e-prints*, March 2006.

J. A. Peacock. *Cosmological Physics.* Cosmological Physics, by John A. Peacock, pp. 704. ISBN 052141072X. Cambridge, UK: Cambridge University Press, January 1999., Jan 1999.

J. A. Peacock and S. J. Dodds. Non-linear evolution of cosmological power spectra. MNRAS, 280: L19–L26, June 1996.

F. R. Pearce, A. Jenkins, C. S. Frenk, S. D. M. White, P. A. Thomas, H. M. P. Couchman, J. A. Peacock, and G. Efstathiou. Simulations of galaxy formation in a cosmological volume. MNRAS, 326:649–666, Sept 2001.

T. J. Pearson, B. S. Mason, A. C. S. Readhead, M. C. Shepherd, J. L. Sievers, P. S. Udomprasert, J. K. Cartwright, A. J. Farmer, S. Padin, S. T. Myers, J. R. Bond, C. R. Contaldi, U.-L. Pen, S. Prunet, D. Pogosyan, J. E. Carlstrom, J. Kovac, E. M. Leitch, C. Pryke, N. W. Halverson, W. L. Holzapfel, P. Altamirano, L. Bronfman, S. Casassus, J. May, and M. Joy. The Anisotropy of the Microwave Background to l = 3500: Mosaic Observations with the Cosmic Background Imager. ApJ, 591:556–574, July 2003.

P. J. E. Peebles. The Gravitational-Instability Picture and the Nature of the Distribution of Galaxies. ApJ, 189:L51+, Apr 1974a.

P. J. E. Peebles. The Nature of the Distribution of Galaxies. A&A, 32:197–+, May 1974b.

P. J. E. Peebles. Test of the use of n-point galaxy correlation functions to discriminate among clustering models. MNRAS, 189:89–94, Oct 1979.

P. J. E. Peebles. *The large-scale structure of the universe.* Research supported by the National Science Foundation. Princeton, N.J., Princeton University Press, 1980. 435 p., 1980.

P. J. E. Peebles. Tests of cosmological models constrained by inflation. ApJ, 284:439–444, Sept 1984.

W. J. Percival. Cosmological constraints from galaxy clustering. *ArXiv Astrophysics e-prints*, Jan 2006.

W. J. Percival, W. Sutherland, J. A. Peacock, C. M. Baugh, J. Bland-Hawthorn, T. Bridges, R. Cannon, S. Cole, M. Colless, C. Collins, W. Couch, G. Dalton, R. De Propris, S. P. Driver, G. Efstathiou, R. S. Ellis, C. S. Frenk, K. Glazebrook, C. Jackson, O. Lahav, I. Lewis, S. Lumsden, S. Maddox, S. Moody, P. Norberg, B. A. Peterson, and K. Taylor. Parameter constraints for flat cosmologies from cosmic microwave background and 2dFGRS power spectra. MNRAS, 337:1068–1080, Dec 2002.

S. Perlmutter, G. Aldering, G. Goldhaber, R. A. Knop, P. Nugent, P. G. Castro, S. Deustua, S. Fabbro, A. Goobar, D. E. Groom, I. M. Hook, A. G. Kim, M. Y. Kim, J. C. Lee, N. J. Nunes, R. Pain, C. R. Pennypacker, R. Quimby, C. Lidman, R. S. Ellis, M. Irwin, R. G. McMahon, P. Ruiz-Lapuente, N. Walton, B. Schaefer, B. J. Boyle, A. V. Filippenko, T. Matheson, A. S.

Fruchter, N. Panagia, H. J. M. Newberg, W. J. Couch, and The Supernova Cosmology Project. Measurements of Omega and Lambda from 42 High-Redshift Supernovae. ApJ, 517:565–586, June 1999.

M. Pettini, S. A. Rix, C. C. Steidel, K. L. Adelberger, M. P. Hunt, and A. E. Shapley. New Observations of the Interstellar Medium in the Lyman Break Galaxy MS 1512-cB58. ApJ, 569: 742–757, Apr 2002.

C. Porciani, M. Magliocchetti, and P. Norberg. Cosmic evolution of quasar clustering: implications for the host haloes. MNRAS, 355:1010–1030, Dec 2004.

W. H. Press, B. P. Flannery, and S. A. Teukolsky. *Numerical recipes. The art of scientific computing.* Cambridge: University Press, 1986, 1986.

W. H. Press and P. Schechter. Formation of Galaxies and Clusters of Galaxies by Self-Similar Gravitational Condensation. ApJ, 187:425–438, Feb 1974.

A. Ratcliffe. *Ph.D. Thesis, University of Durham*, 1996.

A. Ratcliffe, T. Shanks, Q. A. Parker, and R. Fong. The Durham/UKST Galaxy Redshift Survey - IV. Redshift-space distortions in the two-point correlation function. MNRAS, 296:191–205, May 1998.

M. J. Rees. Mechanisms for biased galaxy formation. MNRAS, 213:75P–81P, Apr 1985.

G. T. Richards, S. M. Croom, S. F. Anderson, J. Bland-Hawthorn, B. J. Boyle, R. De Propris, M. J. Drinkwater, X. Fan, J. E. Gunn, Ž. Ivezić, S. Jester, J. Loveday, A. Meiksin, L. Miller, A. Myers, R. C. Nichol, P. J. Outram, K. A. Pimbblet, I. G. Roseboom, N. Ross, D. P. Schneider, T. Shanks, R. G. Sharp, C. Stoughton, M. A. Strauss, A. S. Szalay, D. E. Vanden Berk, and D. G. York. The 2dF-SDSS LRG and QSO (2SLAQ) Survey: the $z < 2.1$ quasar luminosity function from 5645 quasars to g= 21.85. MNRAS, 360:839–852, July 2005.

D. Richstone, E. A. Ajhar, R. Bender, G. Bower, A. Dressler, S. M. Faber, A. V. Filippenko, K. Gebhardt, R. Green, L. C. Ho, J. Kormendy, T. R. Lauer, J. Magorrian, and S. Tremaine. Supermassive black holes and the evolution of galaxies. Nature, 395:A14+, Oct 1998.

H. P. Robertson. Kinematics and World-Structure. ApJ, 82:284–+, Nov 1935.

R. H. Sanders. Observational Cosmology. *LNP Vol. 653: The Physics of the Early Universe*, 653: 105–+, 2005.

W. Saunders, M. Rowan-Robinson, and A. Lawrence. The spatial correlation function of IRAS galaxies on small and intermediate scales. MNRAS, 258:134–146, Sept 1992.

E. Scannapieco, A. Ferrara, and P. Madau. Early Enrichment of the Intergalactic Medium and Its Feedback on Galaxy Formation. ApJ, 574:590–598, Aug 2002.

D. J. Schlegel, D. P. Finkbeiner, and M. Davis. Maps of Dust Infrared Emission for Use in Estimation of Reddening and Cosmic Microwave Background Radiation Foregrounds. ApJ, 500:525–+, June 1998.

M. Schmidt, D. P. Schneider, and J. E. Gunn. Spectrscopic CCD Surveys for Quasars at Large Redshift.IV.Evolution of the Luminosity Function from Quasars Detected by Their Lyman-Alpha Emission. AJ, 110:68–+, July 1995.

D. P. Schneider, X. Fan, P. B. Hall, S. Jester, G. T. Richards, C. Stoughton, M. A. Strauss, M. SubbaRao, D. E. Vanden Berk, S. F. Anderson, W. N. Brandt, J. E. Gunn, J. Gray, J. R. Trump, W. Voges, B. Yanny, N. A. Bahcall, M. R. Blanton, W. N. Boroski, J. Brinkmann, R. Brunner, S. Burles, F. J. Castander, M. Doi, D. Eisenstein, J. A. Frieman, M. Fukugita, T. M. Heckman, G. S. Hennessy, Ž. Ivezić, S. Kent, G. R. Knapp, D. Q. Lamb, B. C. Lee, J. Loveday, R. H. Lupton, B. Margon, A. Meiksin, J. A. Munn, H. J. Newberg, R. C. Nichol, M. Niederste-Ostholt, J. R. Pier, M. W. Richmond, C. M. Rockosi, D. H. Saxe, D. J. Schlegel, A. S. Szalay, A. R. Thakar, A. Uomoto, and D. G. York. The Sloan Digital Sky Survey Quasar Catalog. II. First Data Release. AJ, 126:2579–2593, Dec 2003.

R. Scoccimarro. Redshift-space distortions, pairwise velocities, and nonlinearities. Phys. Rev. D, 70(8):083007–+, Oct 2004.

R. Scranton, D. Johnston, S. Dodelson, J. A. Frieman, A. Connolly, D. J. Eisenstein, J. E. Gunn, L. Hui, B. Jain, S. Kent, J. Loveday, V. Narayanan, R. C. Nichol, L. O'Connell, R. Scoccimarro, R. K. Sheth, A. Stebbins, M. A. Strauss, A. S. Szalay, I. Szapudi, M. Tegmark, M. Vogeley, I. Zehavi, J. Annis, N. A. Bahcall, J. Brinkman, I. Csabai, R. Hindsley, Z. Ivezic, R. S. J. Kim, G. R. Knapp, D. Q. Lamb, B. C. Lee, R. H. Lupton, T. McKay, J. Munn, J. Peoples, J. Pier, G. T. Richards, C. Rockosi, D. Schlegel, D. P. Schneider, C. Stoughton, D. L. Tucker, B. Yanny, and D. G. York. Analysis of Systematic Effects and Statistical Uncertainties in Angular Clustering of Galaxies from Early Sloan Digital Sky Survey Data. ApJ, 579:48–75, Nov 2002.

U. Seljak. Constraints on galaxy halo profiles from galaxy-galaxy lensing and Tully-Fisher/Fundamental Plane relations. MNRAS, 334:797–804, Aug 2002.

U. Seljak and M. Zaldarriaga. A Line-of-Sight Integration Approach to Cosmic Microwave Background Anisotropies. ApJ, 469:437–+, Oct 1996.

T. Shanks, A. J. Bean, R. S. Ellis, R. Fong, G. Efstathiou, and B. A. Peterson. The clustering of galaxies in a complete redshift survey. ApJ, 274:529–533, Nov 1983.

T. Shanks and B. J. Boyle. QSO Clustering - Part One - Optical Surveys in the Redshift Range 0.3<Z<2.2. MNRAS, 271:753–+, Dec 1994.

R. Sharp, W. Saunder, G. Smith, V. Churilov, D. Correll, J. Dawson, T. Farrel, G. Frost, R. Haynes, R. Heald, A. Lankshear, D. Mayfield, L. Waller, and D. Whittard. Performance of AAOmega: the AAT multi-purpose fibre-fed spectrograph. *ArXiv Astrophysics e-prints*, June 2006.

R. K. Sheth, H. J. Mo, and G. Tormen. Ellipsoidal collapse and an improved model for the number and spatial distribution of dark matter haloes. MNRAS, 323:1–12, May 2001.

G. A. Shields, K. Gebhardt, S. Salviander, B. J. Wills, B. Xie, M. S. Brotherton, J. Yuan, and M. Dietrich. The Black Hole-Bulge Relationship in Quasars. ApJ, 583:124–133, Jan 2003.

G. A. Shields, K. L. Menezes, C. A. Massart, and P. Vanden Bout. The Black Hole-Bulge Relationship for QSOs at High Redshift. ApJ, 641:683–688, Apr 2006a.

G. A. Shields, S. Salviander, and E. W. Bonning. Evolution of the Black Hole - Bulge Relationship in QSOs. *ArXiv Astrophysics e-prints*, Jan 2006b.

R. E. Smith, J. A. Peacock, A. Jenkins, S. D. M. White, C. S. Frenk, F. R. Pearce, P. A. Thomas, G. Efstathiou, and H. M. P. Couchman. Stable clustering, the halo model and non-linear cosmological power spectra. MNRAS, 341:1311–1332, June 2003.

D. N. Spergel, R. Bean, O. Dore', M. R. Nolta, C. L. Bennett, G. Hinshaw, N. Jarosik, E. Komatsu, L. Page, H. V. Peiris, L. Verde, C. Barnes, M. Halpern, R. S. Hill, A. Kogut, M. Limon, S. S. Meyer, N. Odegard, G. S. Tucker, J. L. Weiland, E. Wollack, and E. L. Wright. Wilkinson Microwave Anisotropy Probe (WMAP) Three Year Results: Implications for Cosmology. *ArXiv Astrophysics e-prints*, March 2006.

D. N. Spergel, L. Verde, H. V. Peiris, E. Komatsu, M. R. Nolta, C. L. Bennett, M. Halpern, G. Hinshaw, N. Jarosik, A. Kogut, M. Limon, S. S. Meyer, L. Page, G. S. Tucker, J. L. Weiland, E. Wollack, and E. L. Wright. First-Year Wilkinson Microwave Anisotropy Probe (WMAP) Observations: Determination of Cosmological Parameters. ApJS, 148:175–194, Sept 2003.

C. C. Steidel, K. L. Adelberger, M. Dickinson, M. Giavalisco, M. Pettini, and M. Kellogg. A Large Structure of Galaxies at Redshift Z approximately 3 and Its Cosmological Implications. ApJ, 492:428–+, Jan 1998.

C. C. Steidel, K. L. Adelberger, A. E. Shapley, M. Pettini, M. Dickinson, and M. Giavalisco. Lyman Break Galaxies at Redshift z ˜ 3: Survey Description and Full Data Set. ApJ, 592: 728–754, Aug 2003.

N. Sugiyama. Cosmic Background Anisotropies in Cold Dark Matter Cosmology. ApJS, 100: 281–+, Oct 1995.

N. R. Tanvir, H. C. Ferguson, and T. Shanks. The Cepheid distance to M96 and the Hubble constant. MNRAS, 310:175–188, Nov 1999.

M. Tegmark et al. Cosmological Constraints from the SDSS Luminous Red Galaxies. *ArXiv Astrophysics e-prints*, Aug 2006.

M. Tegmark and P. J. E. Peebles. The Time Evolution of Bias. ApJ, 500:L79+, June 1998.

M. Tegmark, M. A. Strauss, M. R. Blanton, K. Abazajian, S. Dodelson, H. Sandvik, X. Wang, D. H. Weinberg, I. Zehavi, N. A. Bahcall, F. Hoyle, D. Schlegel, R. Scoccimarro, M. S. Vogeley, A. Berlind, T. Budavari, A. Connolly, D. J. Eisenstein, D. Finkbeiner, J. A. Frieman, J. E. Gunn, L. Hui, B. Jain, D. Johnston, S. Kent, H. Lin, R. Nakajima, R. C. Nichol, J. P. Ostriker, A. Pope, R. Scranton, U. Seljak, R. K. Sheth, A. Stebbins, A. S. Szalay, I. Szapudi, Y. Xu, J. Annis, J. Brinkmann, S. Burles, F. J. Castander, I. Csabai, J. Loveday, M. Doi, M. Fukugita, B. Gillespie, G. Hennessy, D. W. Hogg, Ž. Ivezić, G. R. Knapp, D. Q. Lamb, B. C. Lee, R. H. Lupton, T. A. McKay, P. Kunszt, J. A. Munn, L. O'Connell, J. Peoples, J. R. Pier, M. Richmond, C. Rockosi, D. P. Schneider, C. Stoughton, D. L. Tucker, D. E. vanden Berk, B. Yanny, and D. G. York. Cosmological parameters from SDSS and WMAP. Phys. Rev. D, 69(10):103501–+, May 2004.

T. Theuns, H. J. Mo, and J. Schaye. Observational signatures of feedback in QSO absorption spectra. MNRAS, 321:450–462, March 2001.

T. Theuns, M. Viel, S. Kay, J. Schaye, R. F. Carswell, and P. Tzanavaris. Galactic Winds in the Intergalactic Medium. ApJ, 578:L5–L8, Oct 2002.

J. L. Tinker. Redshift-Space Distortions with the Halo Occupation Distribution II: Analytic Model. *ArXiv Astrophysics e-prints*, Apr 2006.

J. L. Tinker, P. Norberg, D. H. Weinberg, and M. S. Warren. On the Luminosity Dependence of the Galaxy Pairwise Velocity Dispersion. *ArXiv Astrophysics e-prints*, March 2006a.

J. L. Tinker, D. H. Weinberg, and Z. Zheng. Redshift-space distortions with the halo occupation distribution - I. Numerical simulations. MNRAS, 368:85–108, May 2006b.

S. Tremaine, K. Gebhardt, R. Bender, G. Bower, A. Dressler, S. M. Faber, A. V. Filippenko, R. Green, C. Grillmair, L. C. Ho, J. Kormendy, T. R. Lauer, J. Magorrian, J. Pinkney, and D. Richstone. The Slope of the Black Hole Mass versus Velocity Dispersion Correlation. ApJ, 574:740–753, Aug 2002.

D. Tytler, D. Kirkman, J. M. O'Meara, N. Suzuki, A. Orin, D. Lubin, P. Paschos, T. Jena, W.-C. Lin, M. L. Norman, and A. Meiksin. Cosmological Parameters σ_8, the Baryon Density Ω_b, the Vacuum Energy Density Ω_Λ, the Hubble Constant and the UV Background Intensity from a Calibrated Measurement of H I Lyα Absorption at z=1.9. ApJ, 617:1–28, Dec 2004.

L. Verde, A. F. Heavens, W. J. Percival, S. Matarrese, C. M. Baugh, J. Bland-Hawthorn, T. Bridges, R. Cannon, S. Cole, M. Colless, C. Collins, W. Couch, G. Dalton, R. De Propris, S. P. Driver, G. Efstathiou, R. S. Ellis, C. S. Frenk, K. Glazebrook, C. Jackson, O. Lahav,

I. Lewis, S. Lumsden, S. Maddox, D. Madgwick, P. Norberg, J. A. Peacock, B. A. Peterson, W. Sutherland, and K. Taylor. The 2dF Galaxy Redshift Survey: the bias of galaxies and the density of the Universe. MNRAS, 335:432–440, Sept 2002.

H. Von Zeipel. Catalogue de 1571 etoiles contenues dan l'amas globulaire Messier 3 (N. G.C. 5272). *Annales de l'Observatoire de Paris*, 25:F1+, 1908.

A. G. Walker. On the formal comparison of Milne's kinematical system with the systems of general relativity. MNRAS, 95:263–269, Jan 1935.

J. S. B. Wyithe and A. Loeb. Calibrating the Galaxy Halo-Black Hole Relation Based on the Clustering of Quasars. ApJ, 621:95–103, March 2005a.

J. S. B. Wyithe and A. Loeb. Constraints on the Process that Regulates the Growth of Supermassive Black Holes Based on the Intrinsic Scatter in the $M_{bh} - \sigma_{sph}$ Relation. ApJ, 634:910–920, Dec 2005b.

J. S. B. Wyithe and T. Padmanabhan. Properties of high-redshift quasars - I. Evolution of the supermassive black hole to halo mass ratio. MNRAS, 366:1029–1036, March 2006.

D. G. York, J. Adelman, J. E. Anderson, Jr., S. F. Anderson, J. Annis, N. A. Bahcall, J. A. Bakken, R. Barkhouser, S. Bastian, E. Berman, W. N. Boroski, S. Bracker, C. Briegel, J. W. Briggs, J. Brinkmann, R. Brunner, S. Burles, L. Carey, M. A. Carr, F. J. Castander, B. Chen, P. L. Colestock, A. J. Connolly, J. H. Crocker, I. Csabai, P. C. Czarapata, J. E. Davis, M. Doi, T. Dombeck, D. Eisenstein, N. Ellman, B. R. Elms, M. L. Evans, X. Fan, G. R. Federwitz, L. Fiscelli, S. Friedman, J. A. Frieman, M. Fukugita, B. Gillespie, J. E. Gunn, V. K. Gurbani, E. de Haas, M. Haldeman, F. H. Harris, J. Hayes, T. M. Heckman, G. S. Hennessy, R. B. Hindsley, S. Holm, D. J. Holmgren, C.-h. Huang, C. Hull, D. Husby, S.-I. Ichikawa, T. Ichikawa, Ž. Ivezić, S. Kent, R. S. J. Kim, E. Kinney, M. Klaene, A. N. Kleinman, S. Kleinman, G. R. Knapp, J. Korienek, R. G. Kron, P. Z. Kunszt, D. Q. Lamb, B. Lee, R. F. Leger, S. Limmongkol, C. Lindenmeyer, D. C. Long, C. Loomis, J. Loveday, R. Lucinio, R. H. Lupton, B. MacKinnon, E. J. Mannery, P. M. Mantsch, B. Margon, P. McGehee, T. A. McKay, A. Meiksin, A. Merelli, D. G. Monet, J. A. Munn, V. K. Narayanan, T. Nash, E. Neilsen, R. Neswold, H. J. Newberg, R. C. Nichol, T. Nicinski, M. Nonino, N. Okada, S. Okamura, J. P. Ostriker, R. Owen, A. G. Pauls, J. Peoples, R. L. Peterson, D. Petravick, J. R. Pier, A. Pope, R. Pordes, A. Prosapio, R. Rechenmacher, T. R. Quinn, G. T. Richards, M. W. Richmond, C. H. Rivetta, C. M. Rockosi, K. Ruthmansdorfer, D. Sandford, D. J. Schlegel, D. P. Schneider, M. Sekiguchi, G. Sergey, K. Shimasaku, W. A. Siegmund, S. Smee, J. A. Smith, S. Snedden, R. Stone, C. Stoughton, M. A. Strauss, C. Stubbs, M. SubbaRao, A. S. Szalay, I. Szapudi, G. P. Szokoly, A. R. Thakar, C. Tremonti, D. L. Tucker, A. Uomoto, D. Vanden Berk, M. S. Vogeley, P. Waddell, S.-i. Wang, M. Watanabe, D. H. Weinberg, B. Yanny, and N. Yasuda. The Sloan Digital Sky Survey: Technical Summary. AJ, 120:1579–1587, Sept 2000.

K. Yoshikawa, Y. P. Jing, and G. Börner. Spatial and Dynamical Biases in Velocity Statistics of Galaxies. ApJ, 590:654–663, June 2003.

I. Zehavi, D. J. Eisenstein, R. C. Nichol, M. R. Blanton, D. W. Hogg, J. Brinkmann, J. Loveday, A. Meiksin, D. P. Schneider, and M. Tegmark. The Intermediate-Scale Clustering of Luminous Red Galaxies. ApJ, 621:22–31, March 2005.

I. Zehavi, D. H. Weinberg, Z. Zheng, A. A. Berlind, J. A. Frieman, R. Scoccimarro, R. K. Sheth, M. R. Blanton, M. Tegmark, H. J. Mo, N. A. Bahcall, J. Brinkmann, S. Burles, I. Csabai, M. Fukugita, J. E. Gunn, D. Q. Lamb, J. Loveday, R. H. Lupton, A. Meiksin, J. A. Munn, R. C. Nichol, D. Schlegel, D. P. Schneider, M. SubbaRao, A. S. Szalay, A. Uomoto, and D. G. York. On Departures from a Power Law in the Galaxy Correlation Function. ApJ, 608:16–24, June 2004.